Communication and Energy Delivery Architectures for Personal Medical Devices

by

Patrick Philip Mercier

B.Sc. in Electrical and Computer Engineering, University of Alberta, 2006
S.M. in Electrical Engineering and Computer Science, Massachusetts Institute of Technology, 2008

Submitted to the Department of Electrical Engineering and Computer Science
in partial fulfillment of the requirements for the degree of

Doctor of Philosophy

at the

MASSACHUSETTS INSTITUTE OF TECHNOLOGY

June 2012

Author .....
Department of Electrical Engineering and Computer Science
May 21, 2012

Certified by .....
Anantha P. Chandrakasan
Joseph F. and Nancy P. Keithley Professor of Electrical Engineering
Thesis Supervisor

Accepted by .....
Leslie A. Kolodziejski
Chair, Department Committee on Graduate Students

Communication and Energy Delivery Architectures for Personal Medical Devices

by

Patrick Philip Mercier

Submitted to the Department of Electrical Engineering and Computer Science
on May 21, 2012, in partial fulfillment of the
requirements for the degree of
Doctor of Philosophy

Abstract

Advances in sensor technologies and integrated electronics are revolutionizing how humans access and receive healthcare. However, many envisioned wearable or implantable systems are not deployable in practice due to high energy consumption and anatomically-limited size constraints, necessitating large form-factors for external devices, or eventual surgical re-implantation procedures for *in-vivo* applications.

Since communication and energy-management sub-systems often dominate the power budgets of personal biomedical devices, this thesis explores alternative use-cases, system architectures, and circuit solutions to reduce their energy burden. For wearable applications, a system-on-chip is designed that both communicates and delivers power over an eTextiles network. The transmitter and receiver front-ends are at least an order of magnitude more efficient than conventional body-area networks.

For implantable applications, two separate systems are proposed that avoid re-implantation requirements. The first system extracts energy from the endocochlear potential, an electrochemical gradient found naturally within the inner-ear of mammals, in order to power a wireless sensor. Since extractable energy levels are limited, novel sensing, communication, and energy management solutions are proposed that leverage duty-cycling to achieve enabling power consumptions that are at least an order of magnitude lower than previous work. Clinical measurements show the first system demonstrated to sustain itself with a mammalian-generated electrochemical potential operating as the only source of energy into the system. The second system leverages the essentially unlimited number of re-charge cycles offered by ultra-capacitors. To ease patient usability, a rapid wireless capacitor charging architecture is proposed that employs a multi-tapped secondary inductive coil to provide charging times that are significantly faster than conventional approaches.

Thesis Supervisor: Anantha P. Chandrakasan
Title: Joseph F. and Nancy P. Keithley Professor of Electrical Engineering

Acknowledgments

It has been quite the journey. A journey that began as a fresh incoming graduate student trying to figure out how the MIT building numbering system makes sense (hint: it doesn't). A journey that culminates in the submission of a Ph.D. thesis, but encompasses so much more than just the contents of this document. My time in graduate school has been exciting, challenging, and rewarding not only for my own professional development, but also for my own personal growth.

I've been very fortunate to have a lot of help and inspiration to guide me along the way. I am indebted to my advisor, Anantha Chandrakasan, for providing me with the inspiration to push the boundaries of research and state-of-the-art design. Your advice, not only on technical issues, but also on topics of funding, industry relations, organization, and logistics have been invaluable. You have taught me that a successful researcher is not only inventive and thoughtful, but also sincere, cooperative, and respectful (and generously cites the work of others!). I would also like to extend my sincerest gratitude to my Ph.D. thesis committee members for all their contributions and support: Joel Dawson, Konstantina (Tina) Stankovic, and Charlie Sodini. I would especially like to thank Tina for the exciting energy, ideas, and clinical expertise brought into the inner-ear related work.

Naturally, none of this work could have been accomplished without the generous support of funding partners. I would like to thank Intel Corporation, the Center for Circuit and System Solutions (C2S2), the Interconnect Focus Center (IFC), and the Natural Sciences and Engineering Research Council of Canada (NSERC) for providing me with fellowship, assistantship, and scholarship support.

I often get asked what the best thing about MIT is. I've come to learn that the answer is incredibly easy – it's the people. It's not the buildings, the infrastructure, the equipment, or the location that makes MIT such a great place to learn and discover – it's the people in the MIT community. Faculty members and visiting scientists such as Vladimir Stojanovic, Dina Katabi, Muriel Medard, Dana Weinstein, and Dennis Buss have taught me that collaborations across various disciplines and industries can

lead to powerful concepts and results. Student collaborators are equally important – I would like to acknowledge Saurav Bandyopadhyay for co-designing the energy harvesting chip, and Andrew Lysaght for performing guinea pig surgeries. We spent many long hours in that hot chamber, but the results were certainly worth it! I'd like to thank Phillip Nadeau and Arun Paidimarri for the invigorating discussions on RF circuits and successful implementations of multi-channel FBAR-based radios – it has been a pleasure working with you and I learned a lot throughout the process. Tapeouts can always be difficult, especially with a new PDK – working in parallel with Jose Bohorquez and Marcus Yip made this process much more bearable. I'd also like to acknowledge Sushmit Goswami and Benjamin Tay for valuable discussions and pre-initial-prototype developments of the wireless energy transfer project. Co-chairing the MTL Annual Research Conference with Priya Jadhav was a wonderful experience, and I'd like to thank the entire steering committee, especially Debb Hodges-Pabon, for all their ideas, help, and hard work.

I've had the luxury of sharing my time here with many other incredibly insightful and fun people. Michael Georgas – we had a great time interning in Oregon, and our recent tradition of getting coffee or lunch has been most welcome. Denis Daly – I learned an incredible amount from you as a mentor, as a friend, and as an ice-hockey teammate. Jose Bohorquez – it's been a pleasure spending time with you and your family; your research insight and suggestions have been extremely valuable. Marcus Yip – thank you for being a great cube-mate and introducing me to some fantastic craft-brewed wheat-based beverages. To the golf crew: Fred Chen, Michael Georgas, Jose Bohorquez, David Tax, Marcus Yip, and Al Avestruz – I hope one of us finds that ever elusive hole-in-one someday! I'd also like to thank Ranko Sredojevic, Robert Pilawa, Willie Sanchez, Eric Winokur, David He, David Shirokoff, Fergus Hurley, Byungsub Kim, and many others for being wonderful friends and colleagues.

Past and present members of *ananthagroup* have had a significant impact on my personal and professional development. I'd like to thank Manish Bhardwaj, David Wentzloff, Brian Ginsburg, Naveen Verma, Nathan Ickes, Yogesh Ramadass, Daniel Finchelstein, Joyce Kwong, Vivienne Sze, Nigel Drego, Payam Lajervardi, Alexan-

dra Kern, Jae Lee, and Chih-Chi Cheng for being excellent mentors and colleagues. Mahmut Ersin Sinangil, Masood Qazi, and I all arrived in *ananthagroup* at roughly the same time – it's hard to believe where the time has gone. I still vividly remember taking our first few classes together, working on projects primarily with Mahmut. It's also exciting to see the next generation of students join and continue the excellent legacy of *ananthagroup*: Georgios, Kailian, Nachiket, Dina, Sungjae, Bonnie, Sunghyuk, Michael, Priyanka, Rahul, Yildiz, Mehul, and Frank. Margaret Flaherty most certainly an acknowledgment here for being on-top of everything and keeping 38-107 running so smoothly!

Finally, but certainly not least, I'd like to thank my family for their love, support, and encouragement throughout this entire process. To my parents, Angie and Maurice: your steadfast belief in me has been an inspiration. I only hope I can instill some of the values you have taught me to the next generation. To my beautiful wife, Chelcé: although it was difficult living 2073.6 miles apart from each other for the majority of my time at MIT, it was without question worth the wait. The last two years have been the best of my life, and I can't wait to share the rest of my years with you at my side.

Contents

List of Figures

List of Tables

Chapter 1

Introduction

Semiconductor process scaling has been fueling the growth of the computer and electronics industries for decades. Since the invention of the integrated circuit (IC) by Jack Kilby and Robert Noyce in the late 1950s, process scaling has faithfully followed Moore's Law, which states that the number of transistors on a single chip will double every two years. To put this into perspective, Moore famously said "if the auto industry advanced as rapidly as the semiconductor industry, a Rolls Royce would get a half a million miles per gallon, and it would be cheaper to throw it away than to park it" [1].

Integrated circuits following Moore's Law have been transformational when it comes to the computer industry. A vacuum-tube-based computer that weighed more than 30 tons and consumed 20 kW of power in 1946 is easily surpassed in performance by small, hand held devices today [2]. To put this in perspective, consider that the General Purpose Computer (GPC) on board NASA's space shuttles in the 1970s had roughly the same computational throughput as a circa 1980s IBM 5150 processor with 500 kB of memory [3][1]. An Xbox 360 has 20,000 times the processing horsepower.

However, as all technologies mature, the theory of diffusion of innovations suggest they tend to become commoditized [4]. By creating new or disrupting existing application spaces, the microelectronics industry has shown remarkable agility in finding

[1]Remarkably, NASA continued to use essentially the same computer until the Space Transportation System program was shut down in 2011. This is a classic example of "don't fix it unless it's broken".

new growth opportunities. As shown in Figure 1-1, new areas of growth have consistently been exposed every decade over the past forty years. For example, after a very long period of exponential growth, margins in the personal computer (PC) market are at all-time lows, which is the direct result of desktop and laptop computers becoming commoditized. Advances in integrated radio-frequency (RF) circuits using cheaply available CMOS technologies propelled the communication markets in the 2000s, and together with miniaturized computers, have created the currently expanding portable consumer electronics market.

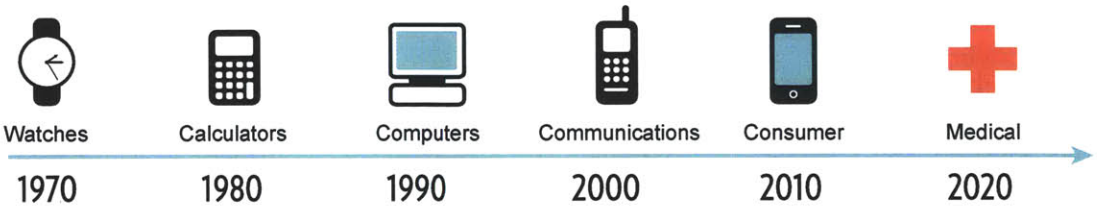

Figure 1-1: Industries disrupted by microelectronics. Courtesy of MEDRC/Mara Karapetian.

Due to significant growth opportunities, personal medical electronics has been identified by many as the next market ripe for disruption by microelectronics. For example, a report by Parks Associates suggests that digital home-based healthcare is projected to grow from an already large $1.7 billion market in 2010 to a $5.7 billion market in 2015, with anticipated exponential growth following this [5]. Given such economic projections, there is much activity beginning to develop in this area.

However, with the exception of certain key applications, the personal medical electronics market has been largely untapped until very recently. Not surprisingly, biomedical electronic devices that have been on the market for a while have typically been used in applications where circuits are simple and there is sufficient volume to support the resulting system. For example, artificial cardiac pacemakers, first designed in the 1960s, are low-complexity oscillators that have the luxury to fit in a 60 mm diameter and 10mm thick disc. Even when consuming 10 μA, a 600 mAh battery (which could, even in the 1960s, fit in such a package) allowed for up to 5

years of operation before surgical replacement was necessary [6]. In 2002, there were 3 million people with implanted artificial cardiac pacemakers worldwide, with 600,000 additional devices being implanted per year [7]. Similarly, cochlear implants, which help deaf patients re-create the sensation of sound through neural stimulation, have been implanted in over 219,000 people worldwide as of December 2010 [8,9].

So if integrated electronics and Moore's law have enabled these particular applications, in some cases decades ago, why is it only now that significant industry-wide activity is being seen in the biomedical electronics area? While there are undoubtedly many reasons, there are two significant interrelated societal factors that make now a good time for investment in research and development:

- **Aging Population**: The US baby-boomer generation consists of approximately 76 million people. In 2006, approximately 12% of the US population was over the age of 65. By 2030, when the last of the baby boomers are expected to retire, the number of Americans over the age of 65 will increase to roughly 20% of the population [10]. Consequently, the number of people needing frequent access to basic healthcare services is expected to increase significantly.

- **Healthcare Costs**: In 2010, the United States spent $2.6 trillion on healthcare, which is roughly 17.9% of the country's GDP. By 2020, healthcare costs in the United States are expected to outpace economic growth and comprise 19.8% of GDP, or $4.6 trillion [11]. Similarly, total Medicare expenditures were $523 billion in 2010, which is roughly 3.6% of GDP. Left unchecked, Medicare expeditures are projected to grow to 10.7% of GDP in 2085 [12]. Regardless of the accuracy of these predictions, it is clear that any advances in biomedical electronics that offer the potential for reduced healthcare costs will be a boon not only to human health, but also to the economy.

Additionally, there are three significant technological factors that are beginning to enable this emerging biomedical electronics market:

- **Semiconductor Scaling**: Continued process scaling is not necessarily required for the design of implanted or body-worn devices. In fact, many implants are designed in standard 0.18 μm Complimentary Metal Oxide Semiconductor (CMOS) processes or older, mostly due to their excellent analog properties and low-leakage characteristics. Instead, continued semiconductor process scaling facilitates higher-performance *external* computational resources, which can be used to process biological data for monitoring applications and closed-loop actuation systems, or can be used for advanced modeling of biological processes. These computations are typically not performed on the implant or wearable device itself, but are instead performed by a high performance processor located on a smart phone, PC, or a remote server farm in the cloud. Examples include machine learning algorithms to detect seizures in epilepsy patients [13], or neuromorphic electronics deriving inspiration from neural networks for accelerated biological simulations or processing [14].

- **Clinical Understanding**: With improved computational resources and biomedical electronic devices, clinicians are able to perform new experiments and analyze larger and more complex data sets, creating an environment well suited to expand basic scientific knowledge of underlying biological processes. With expanded understanding, it is possible to better identify where and why sensing or actuation of biomedical electronic interfaces can be beneficial, and consequently, how biomedical electronic devices can be improved.

- **Miniaturization**: Unlike PCs, which can be as large as necessary (within reasonable limits), personal medical electronic devices necessitate small form factors due to aesthetics and, more fundamentally, anatomy. Although process scaling has typically been the trump card for miniaturization of microelectronics, battery technology has not followed suit. Consequently, *energy efficiency* and/or *energy autonomy* together with advanced packaging technologies are the most promising method of reducing biomedical electronic device volume. This is of particular importance to implanted and body-worn devices, where, in

sharp contrast to PCs, total system volume (including all peripheral electronics and energy storage elements) must be on the order of anywhere from a few cubic centimeters to a few cubic millimeters. Energy efficient designs based on techniques and technologies developed at universities and industrial research and development centers are beginning to enable very interesting and beneficial biomedical electronic systems such as artificial pancreases [15] or epileptic seizure monitoring systems [16], that can approach the size of cubic millimeters [17].

The high-level goal of the research presented in this thesis is to explore the personal biomedical electronics design space, with an emphasis on increasing energy efficiency and autonomy metrics in order to create devices that are sufficiently miniaturized to fit within the anatomical constraints typical of biomedical applications. Pushing such energy metrics for wearable and implantable devices beyond the state-of-the-art requires innovation and optimization not only at the circuit level, but also, and perhaps more importantly, at the system level.

Regardless of the specific application, many personal wearable or implantable biomedical monitoring or actuation devices share four common requirements. The first and most obvious requirement is that such devices must interface in some manner with the underlying biological process. For example, an electrocardiography (ECG) monitoring patch must capture the inherent electrical activity of the heart, while an artificial cardiac pacemaker must electrically stimulate the heart if the natural electrical conduction system is damaged. The second requirement is that most such devices must communicate with the outside world. Communication is required in order to transmit sensed data, for example from an ECG monitoring patch, or to receive commands, for example to change the pacing frequency of an implanted pacemaker. Thirdly, such devices must process and manage their energy effectively. Battery management circuits and efficient power converters are required to make the most of limited energy budgets. Finally, many, but not all biomedical electronic systems also require some on-board signal processing. In some cases a trade-off exists where processing and compression of data can substantially reduce communication

requirements, thereby altering the system energy allocation budget [16]. A generalized biomedical electronic system featuring these requirements is shown in Figure 1-2.

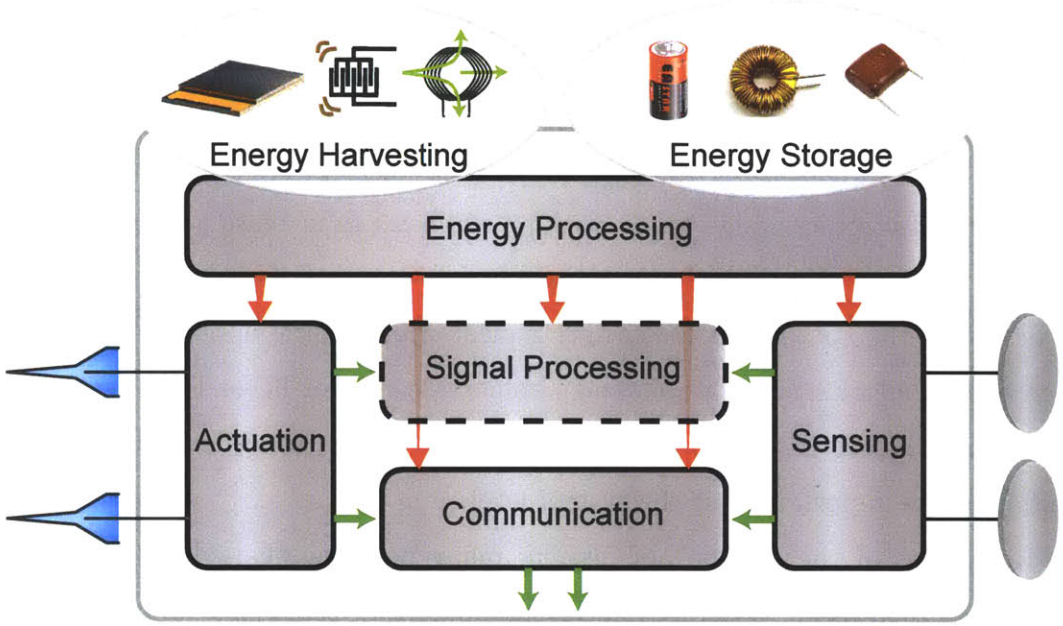

Figure 1-2: A generalized wearable or implantable biomedical electronics platform for personalized monitoring or actuation. On-board signal processing (shown in the dashed box) may be extremely beneficial in many cases but is not required for all applications.

Typically, communication circuits dominate the power budget of such nodes [18]. Consequently, efficiency improvements of communication sub-systems together with their corresponding energy management circuits can directly lead to increased miniaturization through the use of smaller energy storage or harvesting elements. As a result, the more specific goal of this thesis is to investigate communication and energy delivery sub-systems in order to maximize energy efficiency. Both wearable and implantable application spaces will be explored.

1.1 System Design Philosophy

The research and design philosophy used throughout this thesis relies on a three-pronged approach to achieve anatomical miniaturization through energy efficiency and energy autonomy. This philosophy spans multiple layers of design, from low-level transistor optimization to high-level system considerations.

1. *Use-case engineering*: The most powerful way to achieve miniaturization or advance functionality is by considering the use-case of the system. Careful consideration as to *how* a patient may use a particular system can lead to new design approaches at the circuit, algorithmic, and architectural levels. In some cases, the use-case and resulting system implementation is straightforward, and no further design insight is gained. However, in other cases it may be possible to *slightly* change the use-case in a manner that does not negatively affect overall system experience, with dramatic implications in terms of system size or functionality. For example, Chapter 4 of this thesis discusses a change in the user experience that eliminates the requirement of a semi-permanent external wireless energy source used to power an implant. Instead, a fast once-a-day charging paradigm is proposed, permitting a fully implanted system that does not have the aesthetic or practical concerns of a relatively large semi-permanent external attachment.

2. *Architectural optimizations*: After system usability is carefully considered, the resulting system architecture should be optimized to fit the modified use-case. In some cases, a modified use-case lends itself directly to novel architectural requirements with implications in energy, size, or usability. In other cases, architectural transforms are inherently necessary to achieve energy efficiency, independent of the specific use-case. For example, the work presented in Chapter 2 discusses an electronic textiles system for communication of sensor data around the human body. Since communication is achieved over a two-wire interface, the transceiver architecture can be modified to further permit power

delivery over the very same network, enabling capacitively-buffered, energy autonomous sensor nodes of minimal size.

3. *Circuit techniques*: Classical circuit optimizations are also required to maximize system integration and energy efficiency. Such optimizations include device selection, transistor sizing, layout considerations, wire engineering, passive design, and sub-block topological design. Chapter 3, for example, describes how very careful analysis of transistor leakage characteristics, together with an extremely duty-cycled energy buffering architecture, can enable the design of an ultra-low-power radio transmitter that can operate on sub-nanowatt power budgets.

In many cases, two additional steps can be employed to further system efficiency or functionality. Applications of advanced algorithms for both communication [19] and data analysis/compression [16], as well as device engineering can substantially increase overall system energy efficiency. These topics will not, however, be discussed in detail in this thesis.

1.2 Wearable Bio-Monitoring Devices

One current thrust in the area of personal medical devices is to transition medical monitoring operations away from expensive hospital environments and move them towards the home. So-called *telemedicine* or *connected health* systems employ the use of body-worn sensor nodes for remote monitoring of vital signs or other physiological signals [20–23], as illustrated in Figure 1-3. Monitoring of this nature is not only useful for patients with chronic conditions, but can also be valuable to those at high risk of medical emergencies (e.g. a monitoring system could alert an ambulance at the onset of a heart attack), or those undergoing physical stress (e.g. monitoring dehydration in athletes or soldiers).

From a patient's perspective, a key metric for such wearable devices is *operational* lifetime; that is, the length of time the device can operate before its energy storage element (e.g. a battery) must be completely re-charged. As previously discussed,

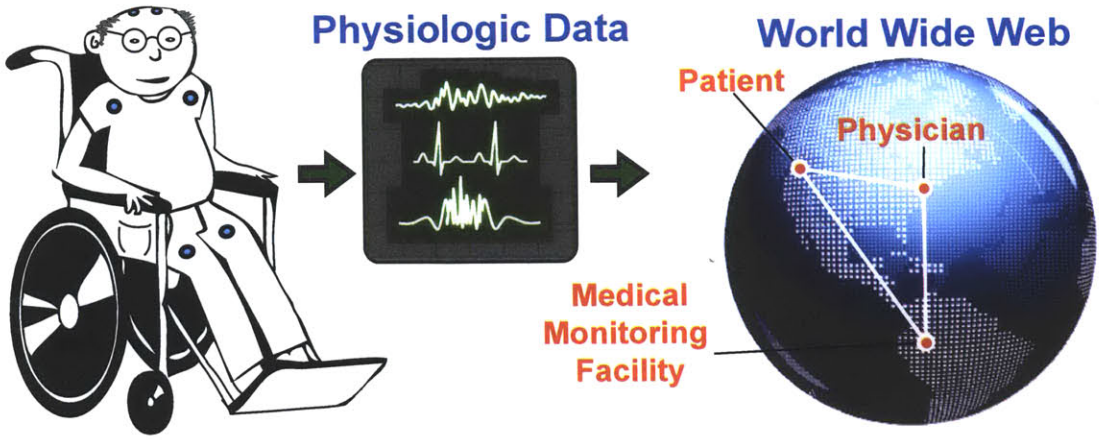

Figure 1-3: A typical medical monitoring system, where a patient's physiologic signals are transmitted to the Internet for examination by a physician or a remote monitoring server.

communication circuits often dominate the power budget of sensor nodes, thereby limiting the achievable operational lifetime per unit battery weight. This is particularly evident when using wireless circuits for communication distances in excess of 10 m, where power amplifier (PA) power consumption scales directly with transmit distance and ends up dominating the entire system power budget [24].

From a system perspective, it makes sense to push complexity away from locations where weight and volume (and as a result, energy) are constrained, and move this complexity to locations where energy is more abundant. Thus, rather than having each sensor node communicate directly over a cellular or WiFi-type of network, it is beneficial to have body-worn sensor nodes communicate over a local body-area network (BAN), as illustrated in Figure 1-4. This limits communication distances to under a few meters, pushing the bulk of the transmit power requirements to an energy-rich local relay (e.g. a cellular phone or pager-type device). This also permits BAN users to self-monitor, provided the local relay has a display or other notification mechanism.

Unfortunately, even when communication distances are on the order of one meter, communication circuit power still often dominates the power budget of sensor nodes. Due to short transmit distances (and therefore limited required radiated power), the

power budget is not completely dominated by the transmitter's PA in this situation; instead, the receiver front-end constitutes a large fraction of system power [25].

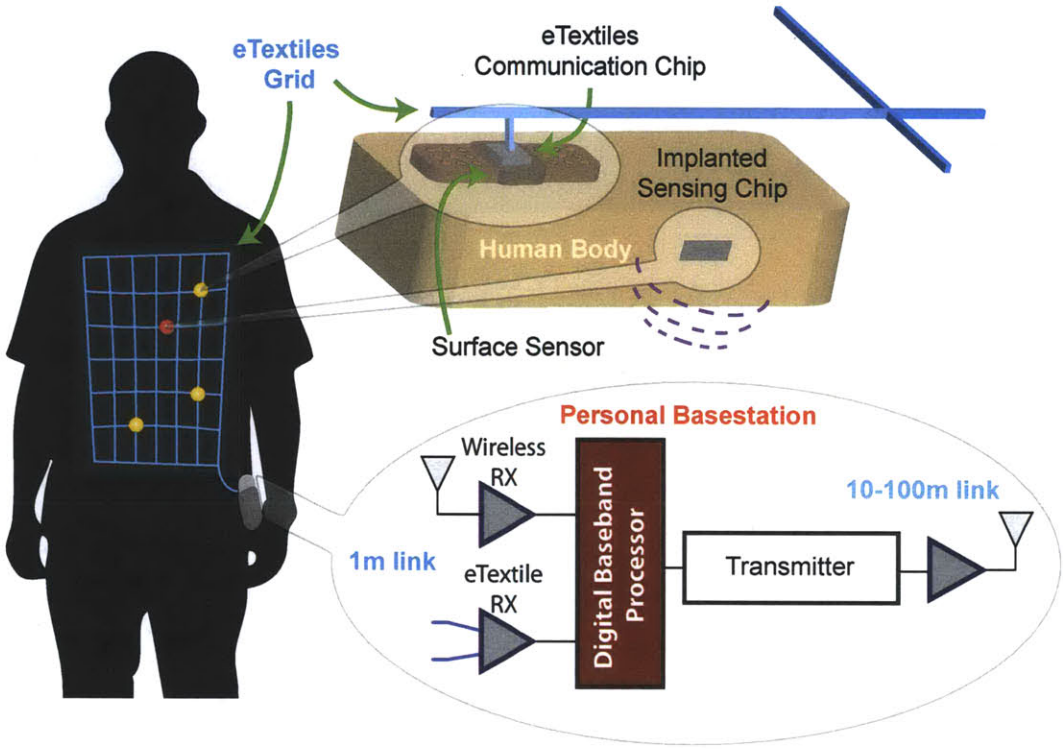

Figure 1-4: A body-area network for local communication of sensor data using both wired eTextiles and wireless RF circuits.

As a result, it is still imperative to increase the energy efficiency of communication circuits in order to achieve the desired goal of small, long-lasting body-worn sensor nodes, even in the limit of short transmit distances. The proposed work addresses this requirement by exploring the use of eTextiles as a communication medium for body-area networks, also shown in Figure 1-4. Since nodes are effectively coupled together via a wired link, extreme efficiency is possible for both data communication and energy delivery, ultimately permitting smaller nodes that have longer operational lifetimes. A system-on-chip (SoC) was built to communicate and deliver energy over a network-on-shirt, and is described in Chapter 2.

1.3 Implantable Bio-Monitoring Devices

Patients with implanted devices are most certainly concerned with operational lifetimes.[2] However, often times a metric of greater importance is implanted *device* lifetime. In this case, implanted device lifetime refers specifically to how long the device can function before surgery is required to replace the implant, typically because a battery has been depleted of energy or has exceeded the recommended number of re-charging cycles.

Fortunately, reducing the energy consumption of implanted circuits addresses both operational *and* device lifetime concerns. However, it is not always possible to simply reduce energy consumption. Electrical stimulation of nerve fibers, for example, requires a fixed amount of power that appears to be fundamentally limited by neural strength-duration curves [26]. Similarly, sensing of physiologic signals such as electroencephalography (EEG) or ECG waveforms require instrumentation amplifiers that consume current that is fundamentally limited by noise constraints [27,28]. Since it is not possible to reduce energy consumption below certain fundamental limits, the only way to increase operational and device lifetime is by either increasing the size of the energy storage element, or by extracting and harvesting energy from locally available sources.

Many of today's implanted devices such as retinal implants and deep brain stimulators rely on continuous wireless power transfer from an external source [29, 30]. Constant wireless power delivery is particularly relevant when the implant does not permit the installation of a battery, either through anatomical volume constraints, or because it is not practical to perform additional surgeries[3] when the battery eventually fails. In this case, the implanted *device* lifetime is essentially infinite - the implant potentially never needs to be surgically replaced. However, the *implant operational* lifetime is essentially zero - an external energy source must always be present. Furthermore, the external energy source must be much larger than an equivalent implanted energy source by at least a factor of $1/\eta$, where η is the wireless power transfer

[2] As a reminder, operational lifetime is the span of time a device lasts between re-charge cycles.
[3] For example, due to a build-up of scar tissue or additional risk of infection.

efficiency, for equivalent *system operational* lifetime. Since η's are generally very poor for these types of schemes (often much less than 50%), external energy sources, which must be worn at all times, can become uncomfortably large for patients. Additionally, such semi-permanent external sources often have poor aesthetics, and prevent patients from undertaking certain activities[4] without losing access to the implant's functionality.

To address the latter problems, one solution is to install an implanted battery and rely on a once-per-day charging use-case. This allows the patient to use or access the implant's functionality without requiring a semi-permanent externally-worn power source. However, there are two significant issues with such an approach. First, as previously alluded to, a battery has a limited number of recharge cycles before its internal electrochemical cells wear out. Consequently, implanted *device* lifetime is limited, and surgical re-implantation will eventually be required to replace the battery. Second, batteries require a relatively long time to charge. For example, standard lithium-ion batteries typically require at least an hour to fully charge, regardless of the battery size [31, 32]. This charging time can be a major inconvenience for patients. Since approximately 50% of patients do not even follow their medication plans properly [33], it is imperative to make implantable devices as easy to use as possible. A shorter charging time would alleviate this particular inconvenience.

This thesis proposes two separate energy delivery and communication schemes to ease operational use of implanted devices. Significant changes over conventional implants at the use-case and architectural levels are proposed in order to increase both implant and system operational lifetimes, while keeping an essentially unlimited *device* lifetime. The first scheme relies on energy harvesting techniques to continuously power an implant without the requirement of a battery. Specifically, energy is extracted from an *in-vivo* electrochemical potential that exists naturally within the inner-ear of mammals. A fully-functional system prototype is presented in Chapter 3, which includes a description of the energy management and load circuitry. Since the available power from this energy source is extremely small, its use is limited to sensing

[4]Taking a shower or going swimming, for example.

and communication applications of slowly-varying biological signals. As discussed in Sections 3.6 and 5.2, these applications can be extremely important and perhaps even transformational for patient diagnostics, monitoring, or basic scientific research.

For applications requiring higher power or energy density than is available from the source described in Chapter 3, a second power management scheme is proposed that relies on once-per-day charging of an implanted ultra-capacitor. The benefit of using an ultra-capacitor as an energy storage element is that charging times can be orders of magnitude faster than batteries – minutes rather than hours, for example. So although the energy density of ultra-capacitors may be smaller than comparable-sized batteries, rapid charging enables the once-per-day charging use-case without significantly affecting patient usability. Additionally, since ultra-capacitors can be re-charged upwards of 1,000,000 times without a significant degradation in performance [34], system *device* lifetimes can last the duration of a patient's lifetime, never requiring surgical re-implantation. Chapter 4 presents a prototype wireless charger geared toward such a fully-implanted system.

1.4 Thesis Contributions

Broadly, this thesis examines the design of communication and energy management technologies for personalized biomedical devices. The ultimate goal of this work is to design systems that are suitably miniaturized to fit within the anatomical constraints of typical biomedical applications. This is primarily accomplished by increasing energy efficiency, in some cases in combination with energy harvesting, in order to eliminate the requirement of large energy storage devices. The main contributions of this thesis are in the following four areas:

1. *Electronic textiles system-on-chip* – An eTextiles transceiver that communicates over electronic textiles as an alternative, energy-efficient communication medium for BAN applications is presented in Chapter 2. The proposed eTextiles network architecture consists of a two-wire conductive yarn medium, body-worn nodes, and a basestation used for data collection and medium-access control.

The eTextiles transceiver employs supply-rail-coupled differential signaling to efficiently time-share the eTextiles medium between communication and remote charging activities. Remote charging achieves up to 96% power transfer efficiency over ohmic network and switch losses when a basestation battery is used to charge remote capacitors, which are used as the power supplies of body-worn nodes. Fabricated in 0.18 μm CMOS and operating at 0.9 V, the receiver and transmitter front-ends together consume 3.2 pJ/bit over 1 m at 10 Mbps, which is at least 20X more efficient than conventional BAN (i.e., wireless) receiver front-ends. The transceiver also contains an integrated digital baseband and medium access controller, which, together with the receiver front-end, consumes 110 μW during continuous operation.

2. *Ultra-low power wireless implanted radio design* – Due to anatomical volume limitations, implanted electronics are severely power constrained. However, not all implantable applications require frequent measurements or actuations. Such applications present an opportunity to design electronics that can be deeply duty-cycled, spending most of their time in ultra-low-power sleep states. Chapter 3 presents the design of a minimal-complexity 2.4 GHz radio transmitter that is designed specifically with aggressive duty-cycling in mind. Fabricated in a 0.18 μm CMOS process, the transmitter achieves a standby-mode power consumption of 39.7 pW, which is the lowest reported to date. In active mode, the transmitter requires 38 pJ to transmit a bit of information at an instantaneous data rate of 5 Mbps. When operating at a duty-cycle of 0.0001% by wirelessly relaying 128-bit packets every minute up to a distance of 1 m, the transmitter requires only 83 pW, which is over 100X lower than previously published work.

3. *System demonstration of energy extraction from the inner ear* – The endocochlear potential is an electrochemical gradient naturally found within the inner ear of mammals. Due to limited extractable power, it has never before been used as an energy source for electronics. Chapter 3 of this thesis presents clinical measurement results of the first system demonstrated to sustain itself

with a mammalian-generated electrochemical potential operating as the only source of energy into the system. This was enabled in part through the aforementioned energy efficiency transmitter, which was integrated together with a boost converter, antenna, and three passives into a 9 mm by 11 mm chip-on-board package. Clinical results were obtained using the endocochlear potential of a guinea pig as the system power source over an experiment duration of five hours.

4. *Rapid wireless ultra-capacitor charger* – There are many additional implant applications that have larger power requirements than what is harvestable *in-vivo* in mammals. As a result, implantable energy storage elements are required. Since batteries take too long to charge, Chapter 4 proposes a once-per-day charging use-case that employs an ultra-capacitor as the implanted energy storage element. Unlike conventional chronic wireless power delivery systems which endeavor to maximize efficiency, the goal of this work is to minimize charging time for patient ease-of-use. This new problem formulation requires a re-investigation of standard inductive coupling theory in order to identify opportunities to improve charging time. Based on this investigation, Chapter 4 presents the design of a rapid wireless capacitor charger that uses a multi-tap secondary coil that dynamically alters the characteristic inductive coupling equations in order to deliver the maximum amount of transient energy to the ultra capacitor. The proposed technique enables charging times that are up to 3.7X faster than conventional approaches. Alternatively, the usable transcutaneous coil separation range can be increased by 2.5X. Although developed primarily for rapid charging, the results presented in this thesis can also be applied to maximize power transfer efficiency.

Chapter 2

Electronic Textiles for Body-Area Networks

Recent advances in sensor technologies are fueling new possibilities in personal health monitoring, where data is sensed and communicated away from the body for remote telehealth applications, as introduced in Section 1.2. For patient usability, sensing nodes must be small and light, thereby limiting the size of energy storage elements and requiring circuit and system solutions that are extremely energy efficient. Rather than directly interacting with a long-range wireless network, it is beneficial from an energy perspective for individual sensor nodes to communicate over a local body-area network (BAN), as illustrated in Figure 1-4. A dedicated local relay, such as a smart phone, can then collect sensor data to be transmitted over a long-range network to the Internet for monitoring purposes.

This chapter describes a system solution for not only communicating information around the human body, but also for delivering power to sensor nodes, obviating the need for a large battery. Both communication and power delivery is performed extremely efficiently through the use of a transceiver system-on-chip employing a wired electronic textiles (eTextiles) clothing network.

2.1 One-Meter BAN Communication

This section describes various means of achieving 1m body-area network communication, and examines the strengths and weaknesses of each approach.

2.1.1 Wireless Communication

From a user's perspective, the untethered mobility gained by wireless communications can, in certain cases, significantly improve freedom of patient movement. Unfortunately, wireless communication suffers from several drawbacks which ultimately require high energy consumption, necessitating large form factor devices that as a result can restrict freedom of movement.

Broadcasting

The broadcasting nature of wireless communication is simultaneously a strength and weakness when referring to BAN applications. On the one hand, omni-directional radiation of information encoded within electromagnetic (EM) waves is extremely convenient for the design of a single network in isolation. For instance, a transmitter and receiver do not need any *a priori* knowledge of their respective locations for successful communication, so long as they are within a pre-described distance of each other. Additionally, RF nodes are free to change their relative positions over time with little increase in processing overhead, so long as the rate of change of movement is slower than the duration of a single packet (which is generally true for human body movement).

On the other hand, broadcasting sensitive information over a wireless network raises significant privacy, security, and reliability concerns. To overcome these issues, the BAN must be designed to be robust to eavesdroppers (privacy), malicious attackers (security), and interference from other users (reliability).[1] As an example to combat privacy concerns, an advanced encryption standard (AES) engine could be

[1]Many other possible scenarios potentially affecting a wireless network exist and should be considered [35].

used to encrypt data before transmission, at the cost of increased circuit complexity and energy consumption [36].

Finally, broadcasting of EM waves is an inherently single-ended process. Because of this, common-mode interference (such as from a broadcast tower) can easily corrupt the original signal, making correct digital reception difficult. Communication schemes which permit differential signaling on the other hand, can easily attenuate common-mode interference by designing differential amplifiers.

Path Loss

The second major drawback of wireless communication is the significant path-loss faced by EM waves. The Friis transmission equation can be used to predict path loss and is given by Equation 2.1.

$$P_{loss} = G_t + G_r + 20\log_{10}\frac{\lambda}{4\pi R} \tag{2.1}$$

Here, G_t and G_r are the antenna gains in dB at the transmitter and receiver, respectively, λ is the carrier wavelength, and R is the physical distance between the transmitter and receiver. In free space, the Friis equation predicts a 40 dB path loss over a distance of one meter at 2.4 GHz, using a theoretically perfect isotropic antenna [37].[2] Naturally, radiated EM waves around the human body face more obstacles, resulting in measured path losses that are not only higher on average (up to 100 dB at 2.4 GHz), but can also vary with body movement [38,39].

A BAN system employing wireless communication must therefore amplify signals, either at the transmit or receive side, to compensate for the dramatic path loss and its variation. Unfortunately for sensor node size considerations, RF amplification is typically power-expensive and inefficient, especially if good noise performance is required [40]. For example, typical RF front-ends require hundreds of picojoules to hundreds of nanojoules to receive a single bit of information over communication distances of several meters [41,42].

[2]The Friis transmission equation predicts that at further distances, the radiated energy falls off with distance squared.

2.1.2 Body-Coupled Communication

Another technique for BAN communication that has been gaining recent popularity employs the human body as a communication medium. This scheme, termed body-coupled communication (BCC), uses near-field electrostatic coupling to transmit information between nodes that are on or near the human body [43].

Such a technique is a good solution to some of the broadcasting issues associated with traditional wireless techniques, since only a small amount of electromagnetic radiation is generated when carrier frequencies are sufficiently low. Instead, only electric fields remain, whose energy falls off with distance cubed. Thus, eavesdroppers need to be physically very close, or perhaps even touching, before the network can be accessed. Note that this inherent security comes even though BCC nodes locally broadcast their information over the body. That is, this scheme retains one of the benefits of wireless broadcasting - sensor nodes can be placed at arbitrary locations, so long as they are on or very near the body (which is suitable for BAN applications).

It has been experimentally shown that the path loss of BCC systems generally decrease with carrier frequencies up to 150 MHz [44]. However, the human body begins to act as an antenna at these higher frequencies, producing undesired EM radiation. Thus, an optimal point can be reached as a compromise between these conflicting conditions. At near-optimal frequencies (30-120 MHz), the path loss of BCC systems is on the same order as 1m wireless systems [44, 45], thereby requiring power-hungry transmit and/or receive amplification. Additionally, since the human body acts as a receiving antenna at these frequencies, the inherently single-ended BCC signaling scheme is particularly susceptible to common-mode interference (for example, from FM radio stations). This requires designs that transition away from low-complexity modulation schemes (such as digital NRZ) [46], and towards more complex interference-robust schemes (such as correlation-based schemes, or frequency-shift keying (FSK) with channel-hopping [25, 47, 48]). Increased communication and modulation scheme complexity invariably require increased power consumption, which may not be at sufficiently low levels for small sensor nodes with long operational

lifetimes.

2.1.3 Electronic Textiles

A dramatic improvement in energy efficiency can be achieved over wireless and BCC techniques by carefully considering the application use-case. By considering recent advances in flexible conductors and conductive fabrics, an electronic textiles, or eTextiles system is proposed as a body-area network communication system. The change in use-case here involves requiring a patient to wear a specific type of under-shirt when personal sensing is desired. If such an approach can sufficiently miniaturize sensor nodes to the point where they are not noticeable, for many patients this will be a welcome alternative to otherwise bulky wireless sensor nodes.

Electronic textiles specifically refers to the integration of electronics with clothing using conductive fabrics. Such fabrics are often much more flexible and/or stretchable than traditional wires, easing integration into clothing that can be worn during daily-use activities. The salient advantage of conductive fabrics over wireless and BCC systems is that they provide a direct wired link with essentially zero path loss, permitting the design of extremely energy-efficient communication front-ends. Such fabrics are also relatively cheap to manufacture, and they can potentially survive many washing cycles [49]. Figure 2-1 presents several common conductive materials such as stainless-steel filament yarn ($< 0.1\ \Omega/\text{cm}$), silver-coated lycra-like nylon ($< 1\ \Omega/\square$), copper and tin-plated nylon ($< 0.1\ \Omega/\square$), and metal-clad polymer fibers ($< 0.1\ \Omega/\text{cm}$). Electronic textiles have previously been used in several applications, including wearable motherboards [50], LED-based fashion [51], and biomedical sensing [52,53]. It is also naturally possible to use eTextile wires purely for BAN purposes, for example as short-range inductive links or direct node-to-node wiring [54, 55].

Compared to wireless and BCC systems, which are inherently single-ended, a wired eTextiles link also provides an opportunity to use multiple parallel wires. As discussed in sections 2.3 and 2.4, this permits the use of low-complexity two-wire differential modulation schemes that are robust to common-mode interference, further reducing communication circuit power consumption. At the architectural level, such a two-

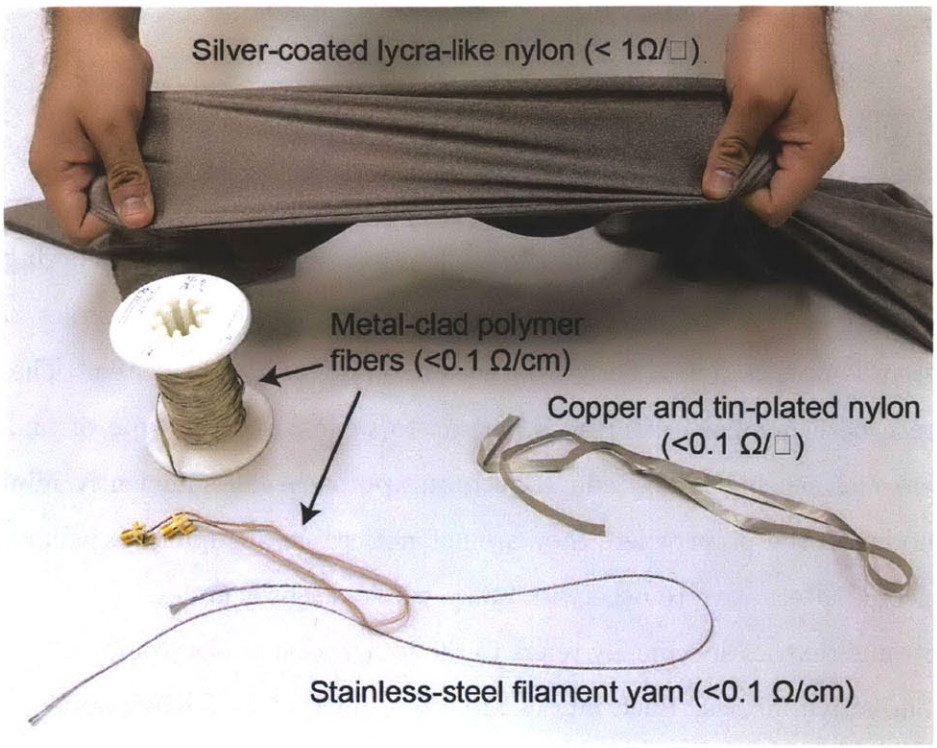

Figure 2-1: Various conductive fabrics for use as eTextiles communication mediums.

wire interface can also be re-purposed as a vehicle to transfer energy between storage elements at extremely high efficiencies.

By virtue of these advantages, this work employs an eTextiles network as a communication and power delivery medium for BAN applications. Unlike [54] and [55], which optimize the efficiency of communication and power transfer *between* clothing layers (using wireless cm-range inductive links), the goal of this work is to optimize the efficiency over a *single* clothing layer for much longer distances (e.g. 1 m).

2.2 System Architecture

2.2.1 Network-on-Shirt Architecture

The implemented eTextiles-based body-area network system is shown in Fig. 2-2 [56]. The eTextiles network-on-shirt consists of stainless-steel filament yarn sewn into an argyle pattern on a plain cotton T-shirt. The pattern is designed such that there

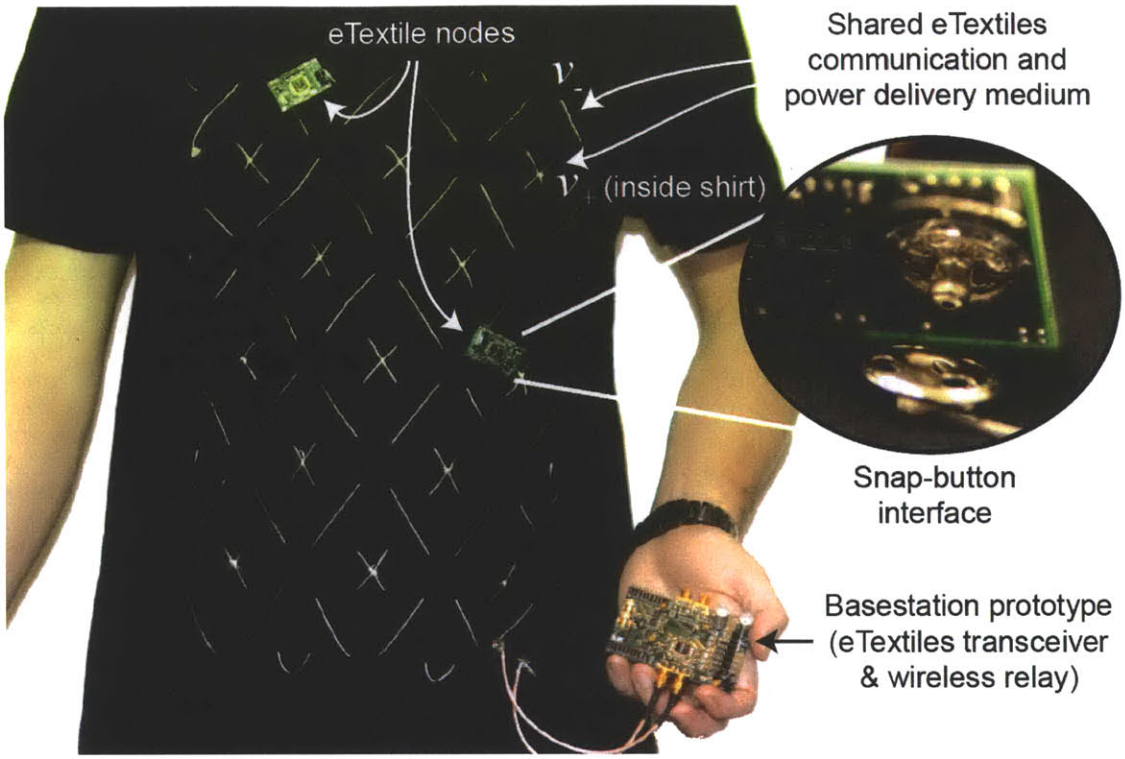

Figure 2-2: Implemented eTextiles-based body-area network system using conductive yarn as a time-shared communication and remote charging medium.

are two conducting grids: an exterior grid (the visible diamond-patterned wires) and an interior grid (the visible X-patterned wires), corresponding to nodes v_- and v_+, respectively.[3] If the shirt were worn inside-out, the overall pattern would appear the same, with the X and diamond patterns instead corresponding to nodes v_+ and v_-, respectively. The use of two separate conductive channels permits the use of low-complexity differential signaling and high-efficiency remote charging.

The X-crossing locations are electrically connected using conductive epoxy to ensure conductivity throughout the grid. The resistance between X-crossings is measured to be 1.8 Ω. The maximum resistance between any two points on the shirt is measured to be 3.1 Ω.

Body-worn sensor nodes (henceforth referred to as "sensor nodes") attach to the grid using metallic button-snaps that are commonly found in fabric stores. One half

[3]This is a very simple pattern; it is certainly feasible to design more complex patterns with multiple layers in future work.

of each button is electrically connected to the grid using conductive epoxy, while the other half is soldered to a standard printed circuit board (PCB). As a result, sensor nodes can only reside in fixed locations. However, it is relatively simple and easy to manufacture eTextile shirts with buttons located in various common locations.

Sensor nodes directly broadcast ternary digits (or trits) over the entire grid network. This broadcasting approach further eases snap button placement restrictions.[4] Although this increases the loading on each sensor node, broadcasting is used to provide fault-tolerance by means of redundancy. For instance, consider the case of having a sensor node's metallic button located on an X intersection of the eTextiles grid. If one of the wires breaks its electrical connection, there are at least three other paths for the signal to take in order to get to its destination.

A basetation node is electrically connected to the network-on-shirt, and is the primary destination for sensor node transmissions. The basestation controls medium access using a time-domain multiple-access (TDMA) scheme by ensuring all sensor nodes strictly adhere and are synchronized to the packet structure shown in Figure 2-3. Section 2.5.2 discusses the medium access scheme in more detail.

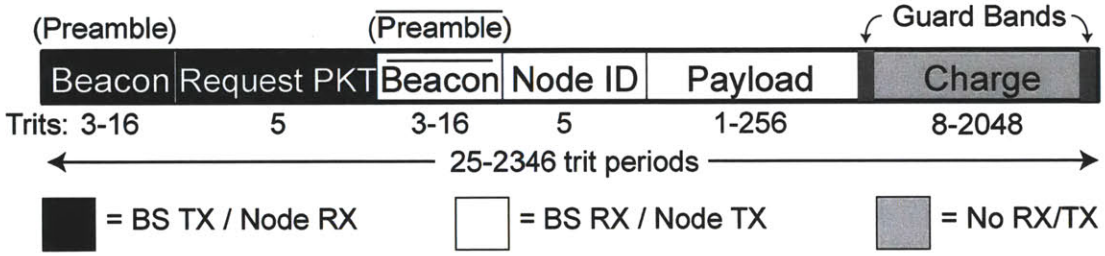

Figure 2-3: Packet diagram indicating when sensor nodes and the basestation transmit, receive, and enter the remote charging phase.

[4]Future work could involve replacing snap buttons with cm-range wireless inductive links for the sensor node-to-eTextiles link, as is done in [55], to further ease sensor node location restrictions. Once data is on the eTextiles network, the proposed transceiver could be used as an efficient way to move information and energy across the 1m BAN.

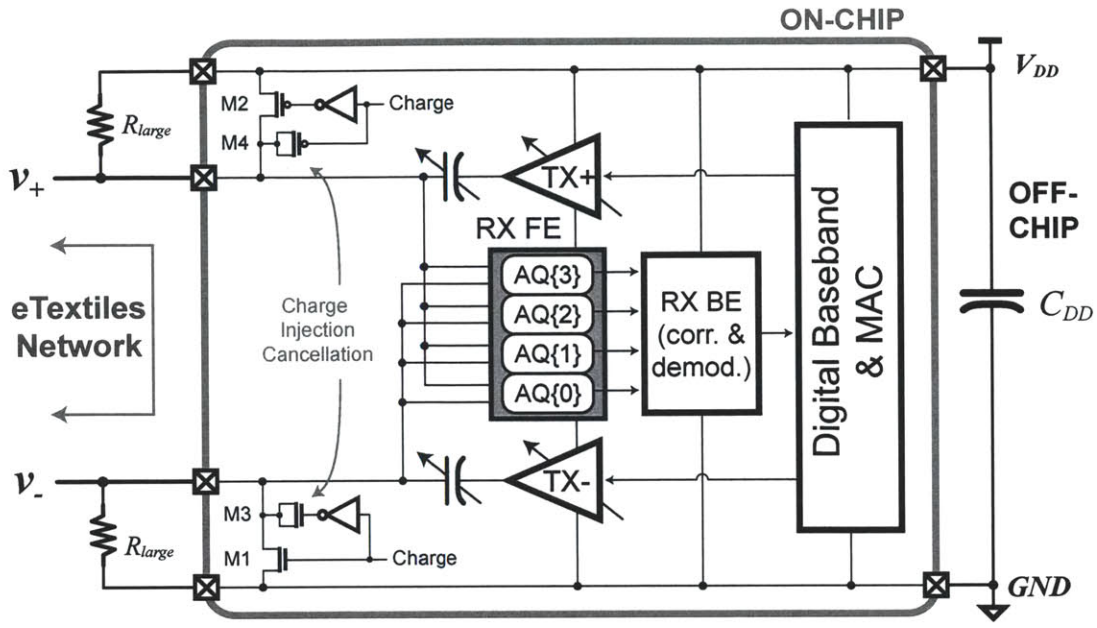

Figure 2-4: eTextiles transceiver block diagram.

2.2.2 Transceiver Architecture

Communication and remote charging is performed by an eTextiles transceiver chip, whose block diagram is shown in Figure 2-4. Depending on the configuration, the chip will serve as either a sensor node or basestation.

The two main I/O nodes, v_+ and v_-, connect to two metallic snap buttons soldered to the PCB, which then connect to the two-wire eTextiles network. Signaling on the network is performed differentially and directly at baseband, using NRZ ternary digits (trits) as data symbols {'+1', '0', '−1'}. As discussed in Section 2.5, trits are used in the preamble to improve synchronization performance, while binary payload data is mapped to trits using the following convention: '0'→'−1' and '1'→'+1' (ternary '0' is a "don't care" when decoding binary data).

On-chip, nodes v_+ and v_- feed directly into the receiver front-end, consisting of four time-interleaved acquisition (AQ) blocks. Each AQ block contains a sample and hold network, a 1.5 bit ADC, and a ternary encoder. The AQ outputs feed two separate receiver back end (RX BE) blocks: a correlation module, used for packet synchronization, and a demodulation module, used for decoding ternary payloads

into bits. An on-chip digital baseband controls the flow of trits and bits from the receiver back end, and an on-chip medium access controller (MAC) ensures the chip is synchronized to the packet diagram enforced by the basestation node. Nodes v_+ and v_- are also the output of differential capacitively-coupled transmitters. Since the receiver inputs are naturally high impedance when turned off and the transmitter outputs are capacitively coupled, no explicit transmit/receive switch is required.

At the end of the communication phase of a packet, nodes v_+ and v_- are effectively left floating. Remote charging is enabled at this point by turning on charging transistors M1 and M2, which connect nodes v_+ and v_- to the supply terminals of each chip on the network. Each sensor node chip is equipped with a large capacitor, C_{DD}, across its supply terminals (no battery is used). The network is synchronized such that the basestation, which does have a battery across its supply terminals, turns on its charging transistors at the same time as the sensor nodes, thereby remotely charging C_{DD}. Thus, remote charging is time-multiplexed with communication.[5]

The required size of C_{DD} is ultimately dictated by the length of time during any potential power outages (for example, the time required between programming the node off of the network, and when the node is placed and synchronized to the network). Related the the capacitor size, the absolute amount of time dedicated to remote charging is set by the basestation during network configuration, and is dictated by the amount of time spent in the communication packet phases (i.e the duty cycle between communication and remote charging), the power consumption of the chip during the active and charging states, the effective resistance between battery terminals and the C_{DD} terminals, the relative sizes of various C_{DD}s on the network (usually set for the worst-case), and the acceptable amount of voltage droop during the active phase. For system demonstration purposes (i.e. Figure 2-2), a 0.47 F (300 mm^3) ultra capacitor is used, allowing for many minutes of node operation during basestation power outages or off-network programming. Alternatively, a much

[5]Simultaneous power delivery and communication could have instead been achieved by up-converting communication signals to a higher carrier frequency, similar to powerline communication networks [57, 58]. However, high-frequency radiation effects and large RF-blocking filters limit the feasibility of such a technique.

smaller 100 μF capacitor can be used, providing several seconds of node operation during basestation power outages. A charging/communication duty cycle of 80% is typically used, resulting in a remote charging period of approximately 100 μs. The efficiency of remote charging can be thought of in a similar fashion to the efficiency of a low-dropout regulator (LDO) working with nearly equal input and output voltages. For example, a voltage droop of 37 mV between remote charging cycles results in a 96% charging efficiency.

Since nodes v_+ and v_- are nominally set to V_{DD} and GND, respectively[6], transmission gates are not required to pass charge. Instead, PMOS-only and NMOS-only pass transistors are used for nodes v_+ and v_-, respectively. The pass transistors are sized to be large in order to minimize the effective charging resistance. Since the eTextiles network is again left floating after the remote charging phase, charge injection effects can potentially disrupt the floating voltage on the network. Half-sized charged-injection-cancellation transistors, M3 and M4, are used to attenuate this effect.

The primary design goal of the eTextiles transceiver is to minimize the energy required to communicate over the BAN for personal sensing applications. Such applications can have data rate requirements ranging from 1 bps to 1 Mbps. Given multiple sensors per network, in addition to coding and remote charging overhead, an instantaneous data rate of 10 Mbps is chosen for the transceiver to provide sufficient communication bandwidth. Should the given application require less bandwidth, duty-cycling can be employed.

2.3 Transmitter Front-End

The transmitter front-end is shown in Figure 2-5, and is comprised of entirely digital circuits. Two separate driver blocks, $TX_+\{6:0\}$ and $TX\_\{6:0\}$, are used to generate differential signals on the eTextiles network. Unlike wireless and BCC systems,

[6]Large resistors help keep v_+ and v_- at these potentials during network start up and during sleep periods. These resistors are sized such that they will not substantially affect the network potential during long strings of consecutive '+1's and '−1's over the course of a 256-bit payload.

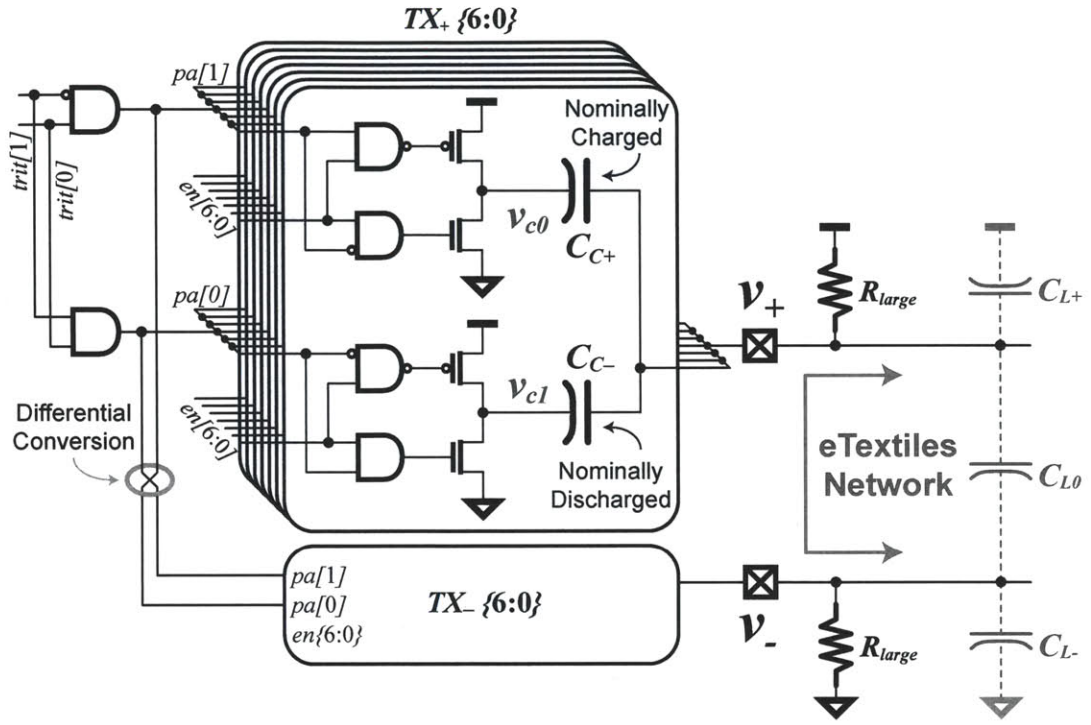

Figure 2-5: Supply-rail-coupled differential ternary transmitter front-end.

differential signaling permits direct digital modulation schemes that have inherent resilience to common-mode interferers. Up-conversion of the 10 Mbps baseband signal to a higher frequency is not performed, since this would require increased power consumption due to oscillator and mixers stages. Additionally, frequencies above 100 MHz have wavelengths approaching the physical size of the eTextiles network, potentially producing undesired EM radiation and multi-path effects.

To save CV^2 energy, low-swing digital transmissions are used. Specifically, capacitive-driving is employed, permitting the use of simple tri-state inverter drivers to couple signals on to the network [59,60]. There are several advantages to this approach. For instance, a second voltage supply is not necessary to generate the low-swing waveforms; instead, the resulting output swings seen on the network are proportional to the capacitive divider ratios between the coupling capacitors, C_{C+} and C_{C-}, and the parasitic eTextiles network capacitance, C_{L+}, C_{L0}, and C_{L-}. For the design in Figure 2-2, C_{L0} is measured to be 35 pF, with ± 5 pF variation when the user moves

around. Since C_{L0} is bound to differ amongst different users, the voltage swing can be made programmable by simply varying the coupling capacitor sizes. In this implementation, seven parallel sets of binary-weighted coupling capacitors are driven by binary-weighted inverters in each differential transmitter, resulting in 7-bits of output swing programmability. The parallel drivers are individually enabled through an on-chip configuration register which sets the $en\,[6:0]$ signals. To overcome any capacitance variation induced by user motion, the output swing must be configured with sufficient margin in order to guarantee reliable communication.[7] The output voltage swing can be programmed to very between 6–260 mV over a 1 m eTextiles network. Since the maximum voltage swing is limited to well under a diode drop, no forward biasing of parasitic diodes will be encountered.

Capacitive-driving also permits the use of smaller, more efficient drivers, since the effective load seen by each driver is not the entire eTextiles network, but is rather the load of the much smaller coupling capacitor; this allows for reduced parasitic CV^2 switching power in the driver buffer circuits. When the tri-state inverters are disabled, their output impedances are very high, thereby ensuring that the loading of the network by unused drivers is dominated by the parasitic capacitance at nodes v_{c0} and v_{c1}, instead of the much larger coupling capacitance, C_{C+} and C_{C-}.

Another benefit of using capacitively-coupled transmitters is that the network can more efficiently switch between remote charging and communication states by using *supply-rail-coupled* differential signaling. To illustrate, first recall that the eTextiles medium is left floating after the remote charging phase. Specifically, nodes v_+ and v_- are left floating at V_{DD} and GND, respectively. Conventional differential signaling schemes are designed to operate over a pair of wires centered at the same potential (nominally GND); disrupting the floating voltage on the eTextiles network by discharging v_+ to GND would require consuming unnecessary CV^2 energy. Since the transmitter outputs are capacitively-coupled onto the network, nodes v_+ and v_- can

[7]Real-time output swing calibration could be performed in future work by adding an ADC on the output node and feeding back swing information. This would likely contribute minimal parasitic capacitance relative to the existing network capacitance, and can be aggressively duty-cycled to minimize power.

instead be left floating at their prior DC potentials throughout a packet.

By using two coupling capacitors, C_{C+} and C_{C-} that are normally charged and discharged, respectively, the proposed supply-rail-coupled technique can additionally permit bipolar signaling.[8] This technique can be used to generate ternary data, which aids in receiver synchronization.

The transmitter generates bipolar signals as follows. Ternary digits are generated in the digital back-end, and are sent to the transmitter in a 2-bit two's complement binary representation ($trit\,[1:0]$). The trits are applied to the input of the driving tri-states, ultimately changing the voltages at nodes v_{c0} and v_{c1}. As shown in Figure 2-6, for an input ternary value of '0', or $trit\,[1:0]$ ='00', node $v_{c0} = GND$ and $v_{c1} = V_{DD}$ for transmitter TX_+. Since node v_+ is nominally at V_{DD}, capacitors C_{C+} and C_{C-} are nominally charged and discharged, respectively.

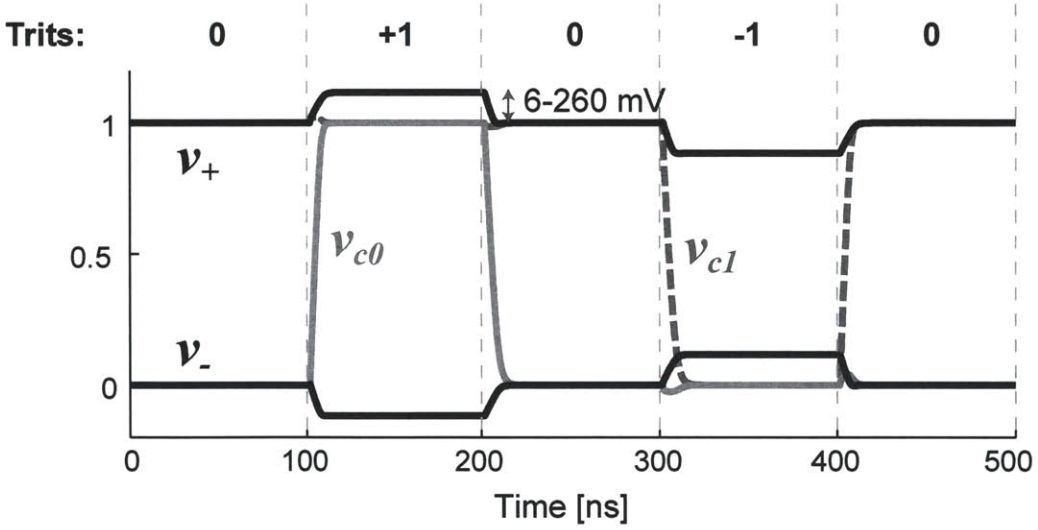

Figure 2-6: Simulated supply-rail-coupled transmitter timing diagram for transmitter TX_+.

In order to transmit a ternary '+1' ($trit\,[1:0]$ ='01'), v_{c0} is pulled up to V_{DD}, thereby discharging capacitor C_{C+}, and creating a small positive voltage swing on the output node v_+. Node v_{c1} is left unchanged here. To get back to a zero state, capacitor C_{C+} is recharged by de-asserting v_{c0}. In order to transmit a ternary '-1'

[8] A similar technique was first proposed and utilized in an ultra-wideband transmitter that I had published in 2009 [61].

($trit\,[1:0]$ ='11'), v_{c1} is pulled down to GND. This charges capacitor C_{C-} (which is nominally discharged), creating a small negative voltage swing on the output node v_+. Node v_{c0} is left unchanged here. Again, to get back to a zero state, capacitor C_{C-} is re-discharged by asserting v_{c1}. A similar arrangement is made for TX_-, thereby completing the generation of supply-rail-coupled differential ternary signals.

Although the proposed high-impedance supply-rail-coupled network can be affected by interference, differential signaling provides an energy-efficient mean to reject such common-mode signals. A low-impedance open-drain architecture could have alternatively been used with less interference effects, at the cost of increased transmit power due to static bias currents and increased drive strengths.

2.4 Receiver Front-End

A block diagram of the receiver architecture is shown in Figure 2-7. Since the path loss across the eTextiles medium is effectively zero, low-noise pre-amplification is not required. Supply-rail-coupled differential signals are instead directly sampled and digitized by four time-interleaved acquisition (AQ) blocks in the receiver front-end. Each AQ block contains dedicated sample-and-hold units and 1.5-bit ternary analog-to-digital converters (ADCs). Depending on the packet phase, output samples of the AQ blocks either flow into a synchronization module, used to select the optimal set of AQ front-end units, or into a demodulator, used to decode payload bits. No circuits in the receiver require static bias currents; as a result, only CV^2 switching and subthreshold leakage energy is consumed.

2.4.1 Supply-Rail-Coupled Sampling

A schematic of the AQ block sample-and-hold unit is shown in Figure 2-8. The sampler consists of PMOS- and NMOS-only transistors as sampling switches for nodes v_+ and v_-, respectively, exploiting the fact that the differential supply-rail-coupled signals are biased at opposite supply rails (otherwise, transmission gates would be required). The top-plate sampling switch is implemented as a transmission gate

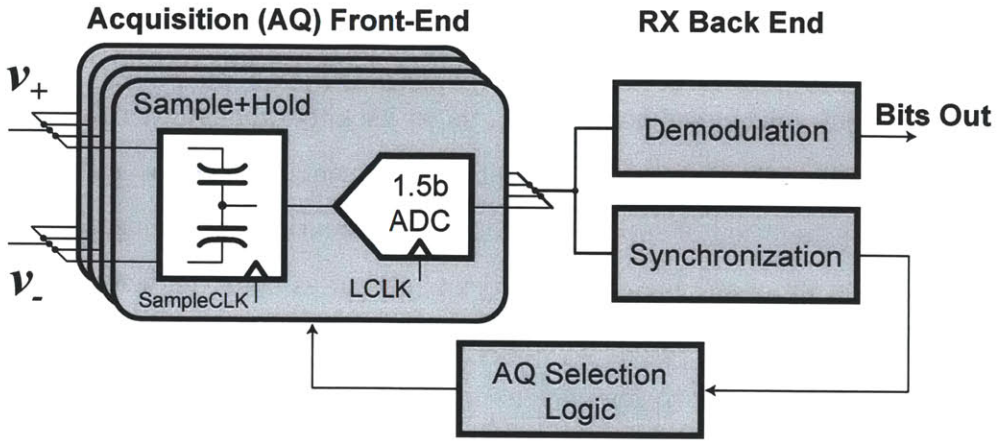

Figure 2-7: Block diagram of the eTextiles receiver.

since, as will be shown shortly, the capacitor top plates are nominally at half-supply. When operating at supply voltages below 1 V, it is necessary to boost the gate of the NMOS sampling switch device to a larger voltage in order to maintain a sufficiently low overall on-resistance; this is accomplished using the charge-pump circuit shown in Figure 2-9, such that a second dedicated supply voltage is not required [41].

The left side of Figure 2-8 shows a model of the supply-rail-coupled input signals, v_+ and v_-:

$$\begin{aligned} v_+ &= V_{DD} + v_{CMI} + v_{in}/2 \\ v_- &= GND + v_{CMI} - v_{in}/2, \end{aligned}$$

where v_{CMI} is a common-mode interference signal that may have coupled onto the eTextiles network.

Simulated waveforms illustrating the sampling procedure are shown in Figure 2-10, using a supply voltage of $V_{DD} = 0.9$ V, and, for this illustration, $v_{CMI} = 0$.

At the beginning of packet reception, the sampling capacitors, C_{S+} and C_{S-}, are purged of their charge by shorting their respective terminals to a fixed supply rail. Purging must be performed semi-occasionally, as the passively-set capacitor top-plate voltage will eventually be disrupted by leakage currents. Experimental results show that over 5000 bit cycles are required before bit errors start to accrue because of this effect. For reasonably-sized packets (e.g. in this case, payloads of 256 bits), leakage

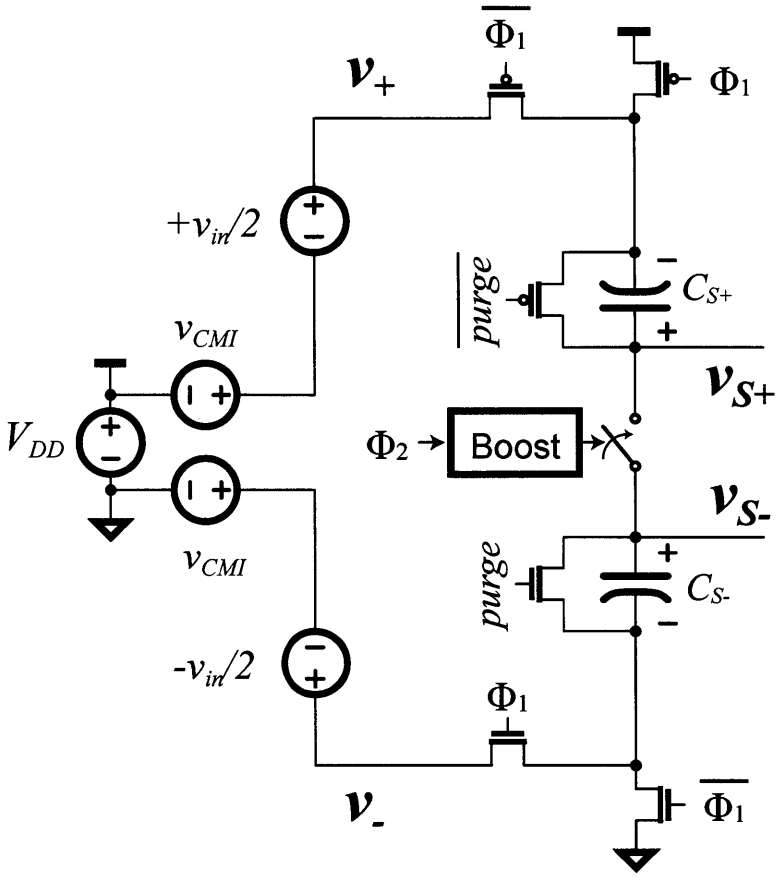

Figure 2-8: Common-mode independent supply-rail-coupled sample-and-hold schematic diagram.

has minimal effect on the bit error rate (BER); as a result, it is sufficient to perform purging only at the beginning of every packet.

During normal sampling operation, the sample-and-hold circuit cycles through four stages: preset, sample, hold, and latch. During the preset phase, $\Phi_1 = 0$ and $\Phi_2 = 1$, thus connecting the bottom capacitor plates to opposite rails while connecting their top plates together. As a result, a potential $\alpha V_{DD} = [C_{S+}/(C_{S+} + C_{S-})] \cdot V_{DD}$ is developed at nodes v_{S+} and v_{S-}. If C_{S+} and C_{S-} are matched, $\alpha = 0.5$, leaving equal and opposite amounts of charge on each sampling capacitor:

$$\begin{aligned} Q_{S+} &= -C_{S+}(\alpha V_{DD}) \\ Q_{S-} &= C_{S-}(\alpha V_{DD}). \end{aligned}$$

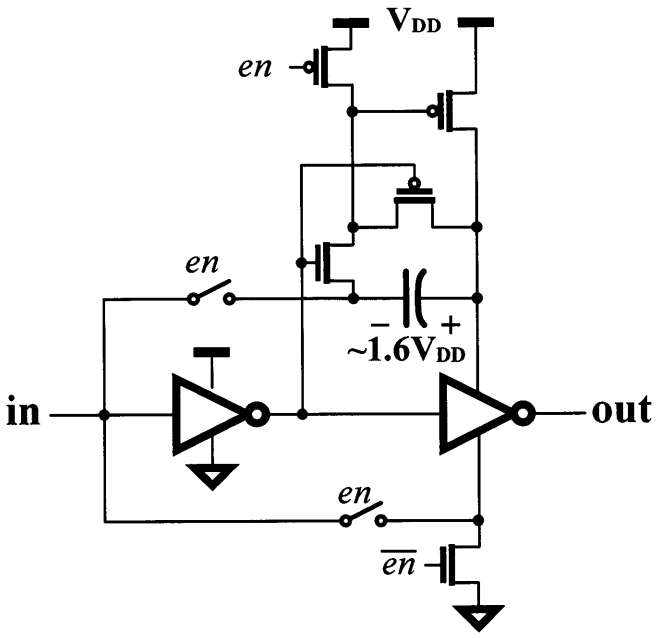

Figure 2-9: Sampling switch boosting circuit, enabled when operating at supply voltages below 1V.

During the sample phase, Φ_1 is asserted, connecting the bottom capacitor plates directly to the eTextiles network. Since the top capacitor plates remain tied together, and the differential supply-rail-coupled signals move in equal and opposite directions, differential-mode charge is accumulated on the capacitors:

$$\begin{aligned} Q_{S+} = &\quad -C_{S+}((1-\alpha)V_{DD} + v_{in}/2 + v_{CMI}) \\ Q_{S-} = &\quad C_{S-}(\alpha V_{DD} + v_{in}/2 - v_{CMI}). \end{aligned}$$

Note that the top plate potentials, v_{S+} and v_{S-}, remain at αV_{DD} during this phase.

The hold phase begins by de-asserting Φ_1 and Φ_2, connecting the bottom plates back to the supplies and opening the top plate switch. The top plate switch is designed to open before the bottom plate switches by passing Φ_1 through a four-stage inverter-based delay chain with non-minimum length devices. This timing is important for two main reasons. First, this avoids the scenario where the sampled charge would be disrupted by the supply rails (if the bottom plates were connected to the supplies before the top plate switch was opened). Second, since the bottom plate switches

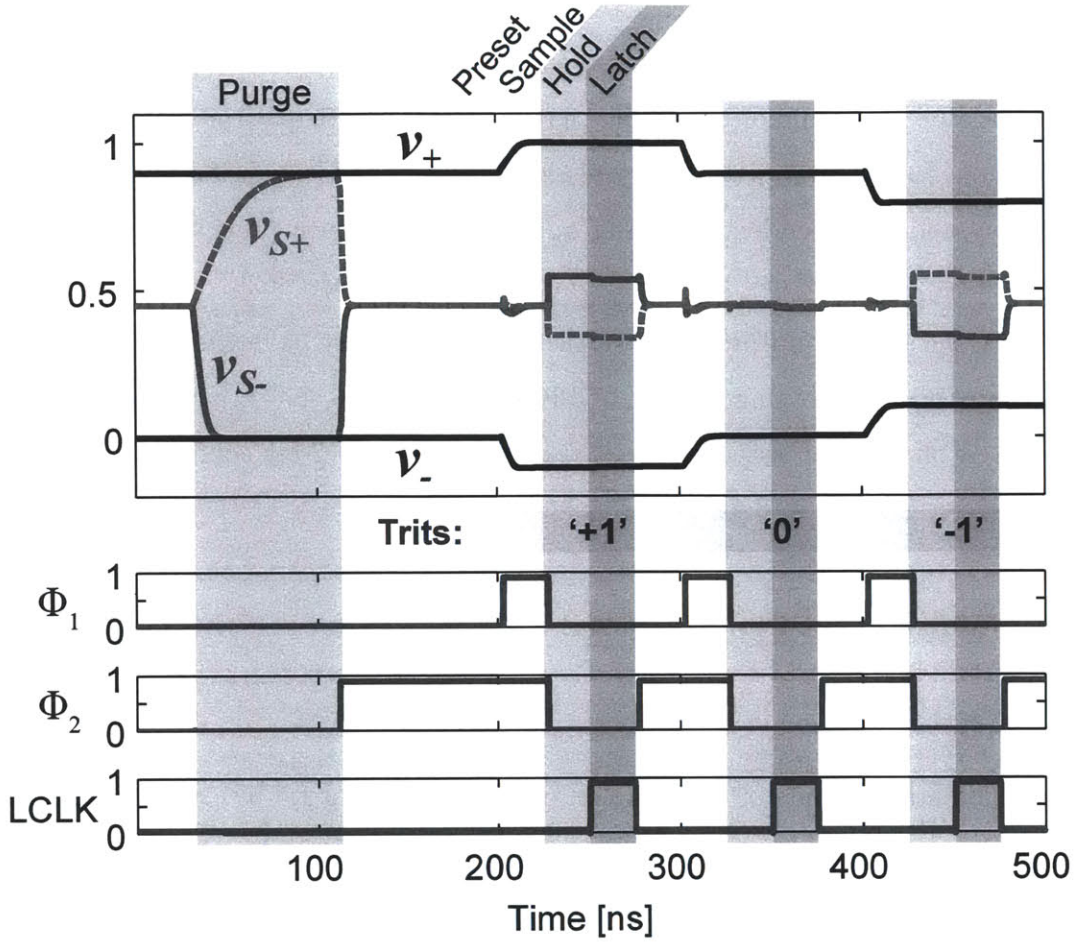

Figure 2-10: Simulated supply-rail-coupled sampling transient waveforms.

are sized such that the total impedance is symmetric around the top plate nodes, the channel charge accumulated in the top-plate switch ideally distributes evenly across both sampling capacitors, resulting in only common-mode charge-injection effects [62].

After the hold phase and into the latch phase, the charge on the sampling capacitors remains the same as in the sampling phase. However, after some settling time, the bottom capacitor plates are now referenced to the supplies, rather than the eTextiles network. This creates the desired differential voltages on the top plate nodes:

$$\begin{aligned} v_{S+} &= \alpha V_{DD} - v_{in}/2 - v_{CMI} \\ v_{S-} &= \alpha V_{DD} + v_{in}/2 - v_{CMI}. \end{aligned}$$

The salient features of this approach are that the top plate voltages are automatically centered at DC potentials suitable for the ensuing comparator inputs, and, taken differentially, the common-mode interference terms and capacitor mismatch terms cancels out ($v_{S+} - v_{S-} = -v_{in}$, regardless of the value of V_{CMI} or if $\alpha = 0.5$). Similar common-mode independent sampling approaches have been previously proposed in ADC design, albeit without supply-rail-coupled input biases [62].

Once the sampler outputs have settled, the results may be latched by the ensuing ternary ADC on the rising edge of LCLK. Timing signals Φ_1, Φ_2, and LCLK are all generated off of the master system clock using a simple 2-bit counter consisting of dual-edge-triggered flip-flops [63].

2.4.2 Ternary ADC

ADC Design

The differential outputs of the sampler feed directly into a 1.5-bit ternary ADC. The ADC, shown in Figure 2-11, consists of two regenerative clocked comparators followed by some simple encoding logic.

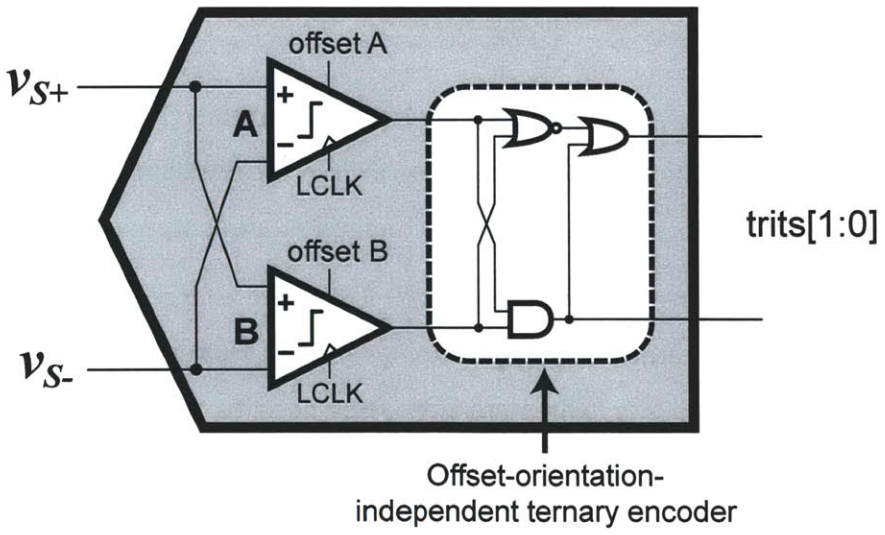

Figure 2-11: Block diagram of the 1.5-bit flash-like ternary ADC.

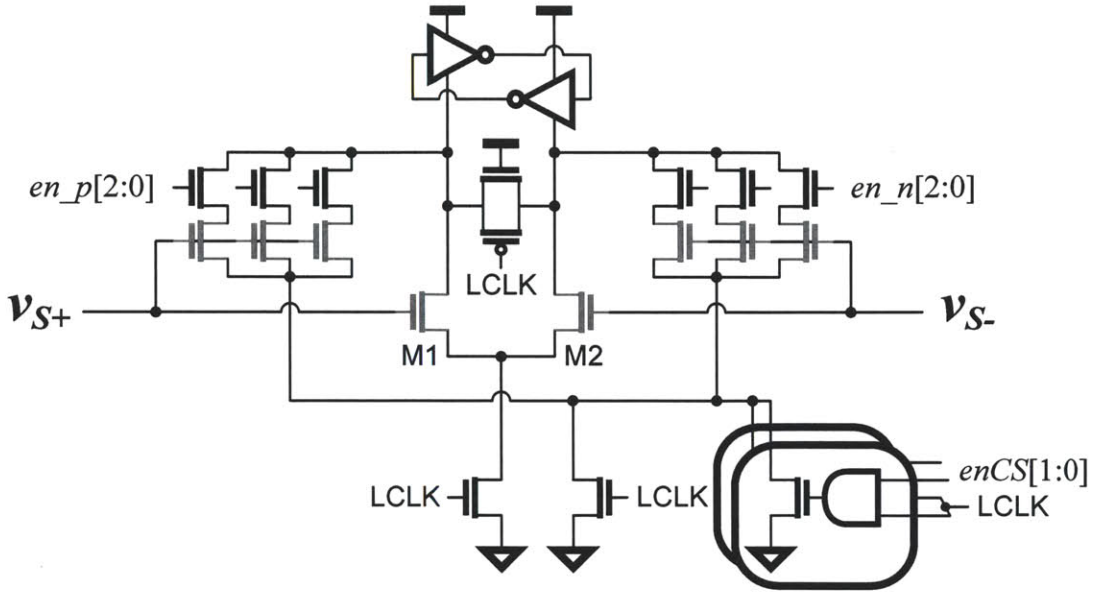

Figure 2-12: Programmable-offset comparator (pre-charge transistors not shown).

The comparator, shown in Figure 2-12, is a Strong-ARM inspired sense amplifier with a primary differential input pair consisting of transistors M1 and M2 [64]. The primary devices are sized for a nominal 3σ input-referred offset voltage of 25 mV and have a common-mode input range of 0.35–0.9 V. Offset tuning is attained using weighted supplementary differential input devices, controlled by six enable signals, $en\_p\,[2:0]$ and $en\_n\,[2:0]$, similar to [65]. However, unlike [65], these supplementary input devices use a separate, tunable tail current source, configured with 2-bits of tuning signals $enCS\,[1:0]$. This expands the overall tuning range by varying the strength of the supplementary devices relative to the primary devices, for a total of eight tuning bits. Capacitive trimming could have been used to achieve the large desired tuning range [66], however at the expense of additional CV^2 switching energy. The tuning calibration routine is discussed in more detail in the following subsection.

The ADC is flash-like, in the sense that the input signal is applied in parallel to the comparators, which are intentionally configured to have equal and opposite non-zero offsets. A sampled signal whose differential amplitude falls below the absolute offset level (i.e. has low amplitude) is converted to ternary '0'. On the other hand, if the

differential input voltage $|v_{S+} - v_{S-}|$ is greater than the comparator offset voltage, the output will be a ternary '+1' or '-1', depending on the sign of the input signal.

The conversion between the comparator outputs and the 2-bit binary-coded ternary signals is performed by an offset-orientation-independent ternary encoder. Consisting of a few simple logic gates, the encoder permits the comparator pair to swap roles. That is, if during calibration it is found that comparator A is better suited to be configured with a negative offset than comparator B[9], then the two comparators may be configured as such without requiring any additional configuration of the encoder. The measured benefits of this type of comparator configuration redundancy are discussed in the following subsection.

Since the comparators are programmed to have equal and opposite offsets, any metastable states would only occur at transitions between ternary values. In other words, the differential input voltage would have to *exactly* equal one of the comparator input-referred offset voltages. This would affect only a single comparator. The encoder is designed such that valid logic levels should propagate in case this unlikely scenario is encountered.

Comparator Calibration

For reliable system operation, the absolute comparator offsets are typically set to be slightly less than the absolute voltage swing on the network. For example, given ± 15 mV voltage swings, comparators might be configured to have ± 10 mV offsets. In this implementation, offsets are configured manually at start-up.[10] To configure each comparator with a specific offset, it is first necessary to characterize the offset profile of each comparator across all of its tuning bits. This is accomplished using an offline characterization routine, where for each comparator setting, an external voltage ramp is applied to the input and the comparator trip points are recorded.

[9] In this case, comparators A and B are normally configured with positive and negative offsets, respectively.

[10] Future work could involve a heavily-duty-cycled feedback ADC to measure incoming voltage swings, permitting once-per-packet offset configuration based on a fixed voltage-swing/offset ratio. As discussed in Section 2.3, such an ADC could also be re-used to dynamically configure the transmitter voltage swings.

Figure 2-13 shows an example offset profile for two comparators located in the same AQ unit. In this case, the two comparators achieve an 8-bit offset tuning range of ± 60 mV at a supply voltage of 0.9 V.

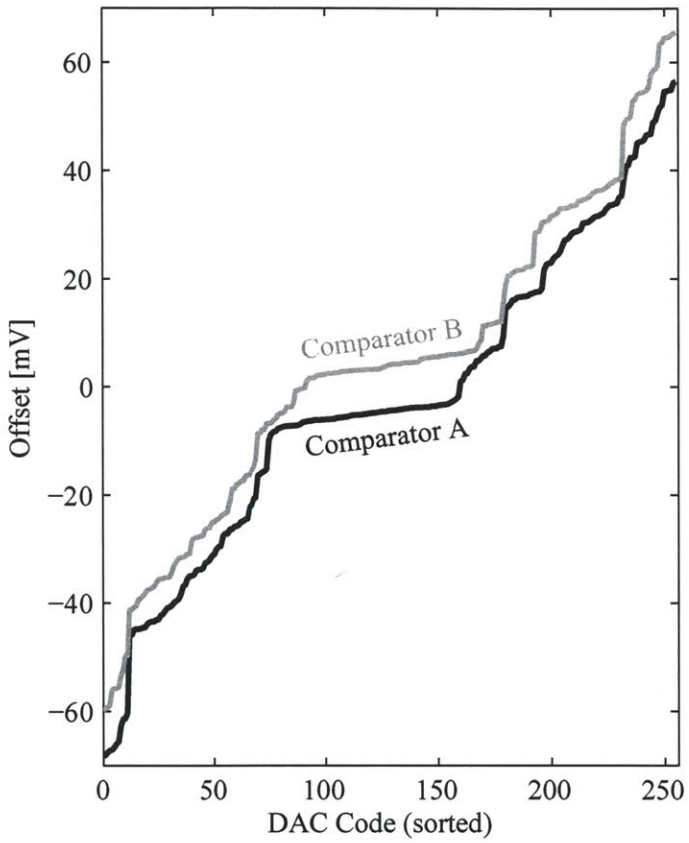

Figure 2-13: Measured offset profile of two comparators in an AQ unit.

Calibration is performed by sorting the offset profiles, and configuring each comparator with the tuning code that most closely results in the desired offset. In the un-optimized case, comparators A and B (Figure 2-12) are always programmed to have positive and negative offsets, respectively. This results in the offset error distribution, measured as the difference between the best attainable offset and the desired offset, shown in Figure 2-14.

In some instances, comparators A and B might be better suited to have negative and positive offsets, respectively. The offset-independent ternary encoder enables the

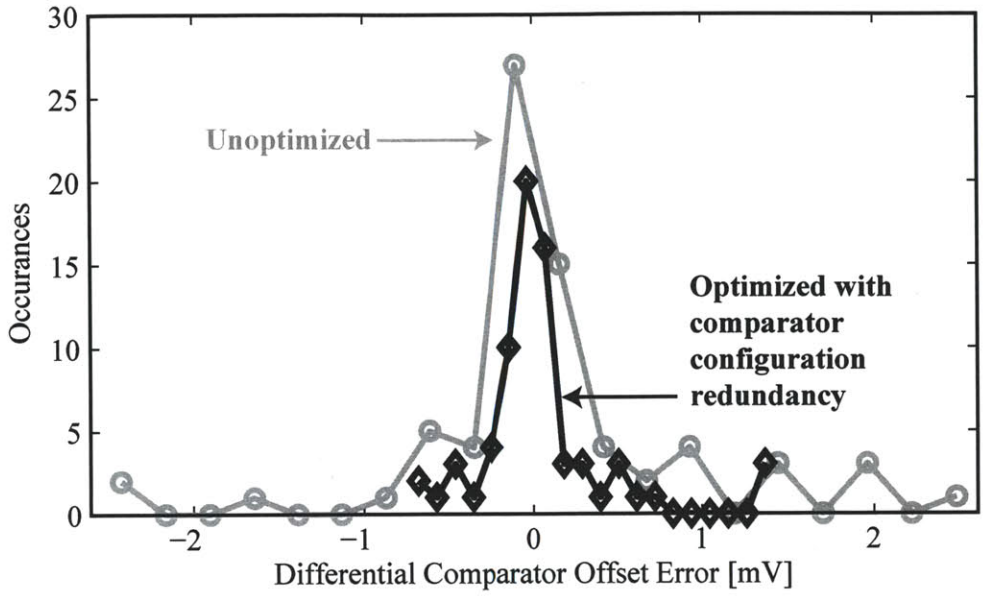

Figure 2-14: Offset error distribution of 72 different comparators, measured across 9 different chips. The comparator configuration redundancy improves the standard deviation of offset errors by 2.1X in this case.

comparators to swap roles as such, with no extra configuration required. Thus, the calibration routine can leverage this inherent comparator redundancy in its optimization search: for instance, it can try to minimize the RMS offset error between the two comparators. Figure 2-14 illustrates the optimized offset error distribution when the calibration routine minimizes the largest offset error. After calibration optimization, the standard deviation of offset errors is improved by 1.5-to-2.5X depending on the optimization criterion. Since two comparators are necessary for proper operation regardless of the optimization, no area overhead is incurred. Post-factory calibration can be performed by observing the difference in bit-error rates of training packets between the two comparator configurations for reduced-voltage swing transmissions. Note that similar types of comparator redundancy schemes have been proposed for ADCs and SRAM applications [41, 67].

2.5 Digital Baseband and Medium Access Controller

2.5.1 Synchronization

As in most communication systems, synchronization between the transmitter and receiver is essential for overall system performance. In this work, synchronization more precisely refers to three separate steps: 1) *detection* of valid incoming signals; 2) *phase-synchronization* to align clocks between the transmitter and receiver; and 3) *packet-synchronization* to align the demodulator with the beginning of the payload. The computations for these three steps are performed simultaneously in the receiver back-end, shown in Figure 2-15, during the beacon (preamble) phase of the packet (Figure 2-3).

As described in Section 2.4.1 and illustrated in Figure 2-16, each AQ block samples for one half clock period every two cycles. For data reception at the 10 MHz system clock (SCLK) frequency, two time-interleaved AQ blocks, spaced apart by one clock cycle, are required.

When only two time-interleaved AQ blocks are used, input signals are still only sampled for one half clock period every cycle. If a transmitter and receiver are phase-aligned, this situation is sufficient for payload demodulation. However, such alignment is not guaranteed (nor expected) at the beginning of every packet. Thus, phase-synchronization is required in order to accurately align transmitter and receiver clocks. This is accomplished by using an extra pair of AQ blocks, such that sampling covers the entire clock period.

Synchronization is accomplished by correlating input samples from all four AQ blocks with a pre-determined code; the AQ block that registers the highest correlation value determines the implied phase- and packet-synchronization, provided the correlation value exceeds a pre-programmed threshold (for detection purposes). The use of ternary signaling introduces some softness (i.e., an additional quantization level) in the data and decision making process.

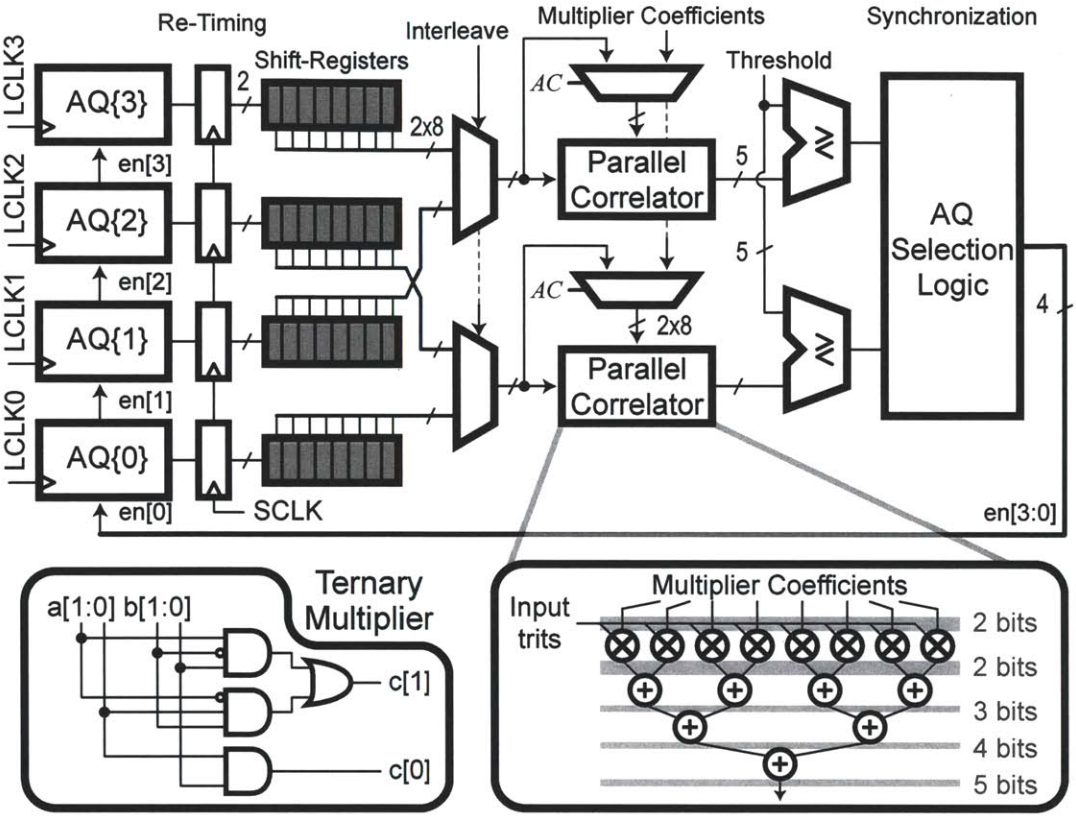

Figure 2-15: Receiver back-end used for synchronization between the transmitter and receiver.

During the synchronization phase, the basestation's transmitter broadcasts a beacon code across the network. For example, the code used in Figure 2-16 is a 7-trit sequence, S_1, that is interleaved with a second code, S_0, which in this case consists entirely of erasures (i.e. ternary '0's) for illustrative purposes[11], to create the following 14-trit sequence:

$$S_b = [+1\ \ 0\ +1\ \ 0\ +1\ \ 0\ -1\ \ 0\ -1\ \ 0\ +1\ \ 0\ -1\ \ 0].$$

Since AQ units sample for one half clock period every two cycles, each AQ unit effectively only observes every second trit in the overall beacon code, S_b. To illustrate,

[11] S_0 should ideally be a code with the greatest Hamming distance to S_1; this would, however, unnecessarily complicate this illustrative example.

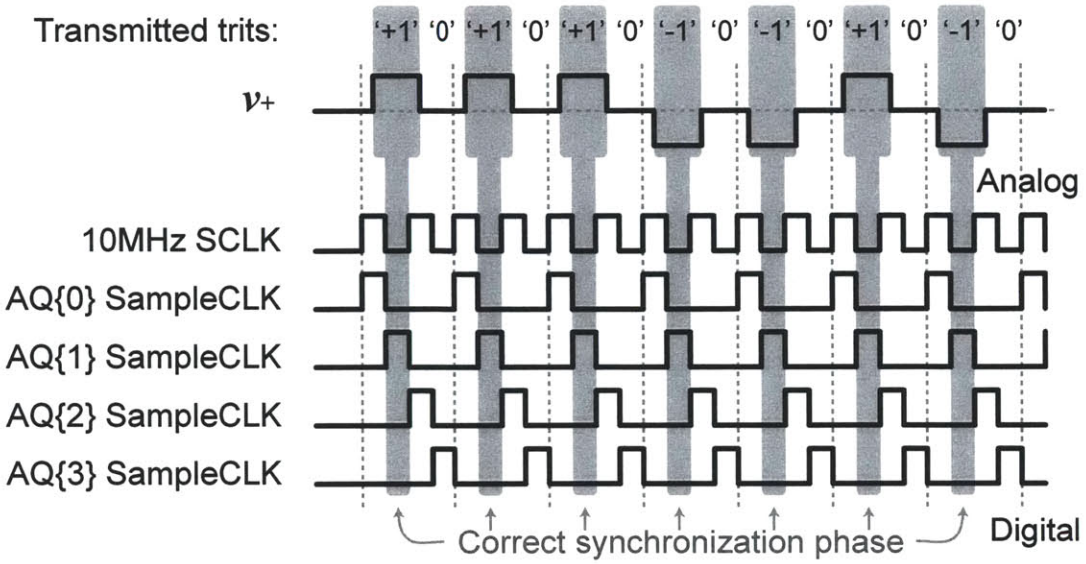

Figure 2-16: An illustrative beacon transmission and the corresponding interleaved sampling clocks. Since each AQ unit samples for one half clock period every two cycles, two beacon codes are interleaved such that only a single AQ unit captures the appropriate data.

AQ{1} in Figure 2-16 correctly samples the desired 7-trit code S_1, while AQs{3 : 2} sample 7 consecutive erasures (code S_0). In this illustration, AQ{0} ideally also has a chance of correctly sampling S_0. However, the period of data covered by its sampling window is beyond the specifications of the system; as a result, decoding errors may occur, likely resulting in a lower correlation value than AQ{1}. Due to finite transmitter rise times, this is rarely an issue in practice. However, extra precaution could be added into the system by using non-overlapping sampling clocks or adding very small guard-bands to each non-zero ternary transmission.

The actual correlations are performed as follows. Ternary symbols from the AQ blocks, which are clocked using different phases, are re-timed to SCLK, and then shifted into serial-to-parallel registers every time new symbols are available, as shown in Figure 2-15. Once the registers are full, the parallel data is then interleaved into two parallel correlators. The correlators multiply the parallel input trits with up to eight parallel ternary multiplier coefficients (with the example code, S_b as used in

Figure 2-16, only seven coefficients are required). Since ternary multiplication has several "don't care" results, a custom multiplication structure is used, saving 2-bits in each ensuing adder stage over a traditional two's complement implementation. If one of the correlation results crosses a pre-programmed threshold, detection is achieved. The AQ selection logic block then feeds back control signals to the receiver front-end for phase synchronization purposes, indicating which pair of AQ blocks to gate for the remainder of the packet. Immediately after the threshold is exceeded, the receiver waits for a fixed number of clock cycles until the payload begins, thereby achieving packet synchronization.

2.5.2 Medium Access

The basestation controls medium access using a TDMA scheme by acting as the master node on the star-configured eTextiles network. Sensor nodes are configured as slave devices, each pre-programmed with a unique 5-trit ID code.

Communication on the eTextiles network strictly follows the protocol outlined in the packet state diagrams, shown in Figure 2-17. Sensor nodes do not change their internal wake-up schedule while connected to the network, unless directed to do so by the basestation (e.g. if a new node is added to the network and additional charging time is required). Synchronization is performed by each node once per packet. Since the signaling scheme is directly at baseband, active clock phase and frequency tracking is not required between nodes. For example, up to 50 ns of phase error can be tolerated between a transmitter and receiver before trit errors occur. When operating off of a 10 MHz crystal with 30 ppm accuracy, this occurs after 50,000 clock cycles (5 ms). The maximum packet length is 29.8 μs – well within these bounds.

The basestation begins each regular communication packet at the exact same time by broadcasting a beacon signal across the network, after which the receivers of all sensor nodes are synchronized with the basestation's transmitter. Immediately following the beacon, the basestation transmits a 5-trit request code, containing the ID code of a particular sensor node. The sensor nodes who do not receive their

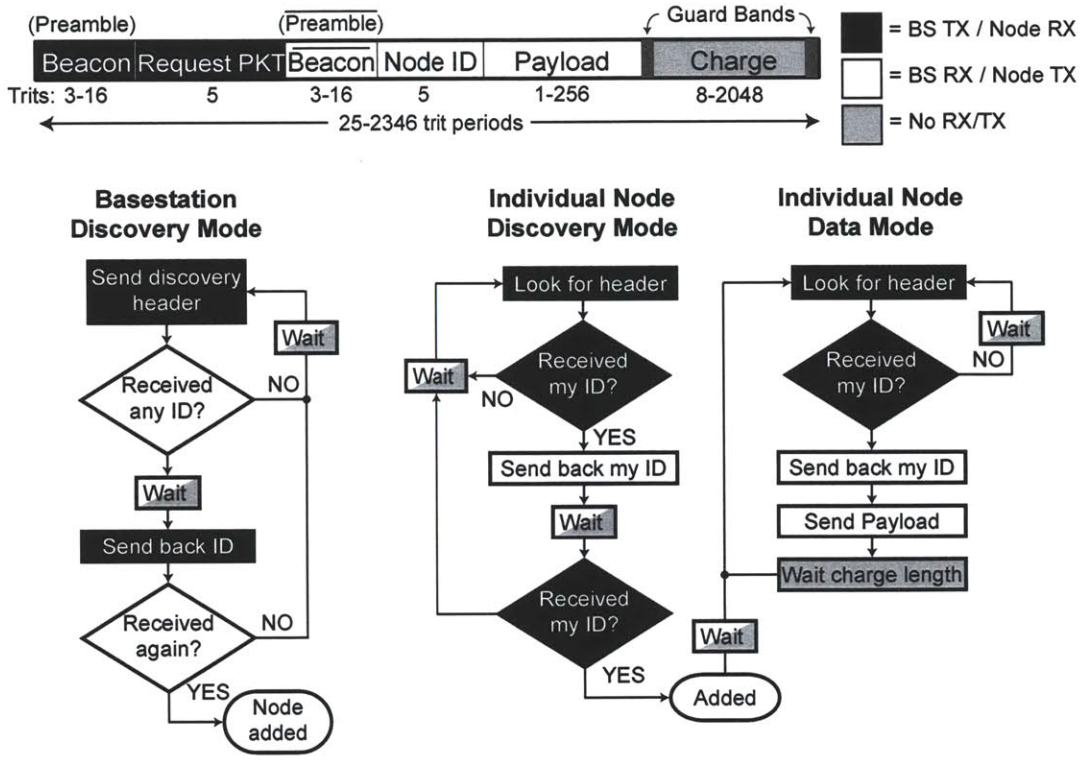

Figure 2-17: System medium access protocol with packet diagram repeated for convenience.

own ID codes at this point enter a sleep mode. The sensor node that does receive its ID code and is in its data mode, proceeds to re-transmit an inverted beacon across the network, followed again by its own ID code. This is done to ensure the basestation's receiver is synchronized to the sensor node's transmitter, as well as to provide an additional means of false packet detection (for instance, if the wrong node ID is sent back to the basestation). The sensor node then transmits its payload to the basestation. Following the payload, all nodes on the network wake up from sleep using their watchdog timers and enter the remote charging phase, as described in Section 2.2.2. Small guard bands are inserted at this point to avoid charging contention on the network, and ease the synchronization procedure.

Sensor nodes can be dynamically added to the network at any time through individual discovery modes. Upon initial power up, each sensor node IC alternates

between synchronization and sleep states until it synchronizes with the beacon. However, the basestation does not know the node has been added to the network, and as a result, will not request any packets from it. To add new nodes to the basestation queue, the basestation will periodically enter its own discover mode and broadcast a special request code following the beacon, called the *welcome request* code. Any node on the network who has not yet been recognized will attempt to respond to the welcome request code by following the standard packet convention: broadcasting an inverted beacon, followed by its ID code, and an empty payload. To avoid contention on the network, sensor nodes in this state only respond with a certainly probability, similar to a $p-$persistance scheme. At this point, the basestation and sensor nodes handshake over the next two packets, formally adding the sensor node to the network.

In the absence of a master basestation node, the sensor nodes can instead be programmed to use a carrier-sense multiple-access (CSMA) MAC with collision avoidance. Network activity is sensed in the the receiver back end (Figure 2-15) by asserting the AC signal, turning the correlators into auto-correlators.[12] If the auto-correlation result is sufficiently low (i.e. the network is quiet), the sensing node proceeds to transmit a beacon and payload, again using $p-$persistence to avoid contention.

2.6 Experimental Results

The eTextiles transceiver chip is fabricated in a 0.18 μm process, and occupies a core area of 0.83 mm^2; a die photo is shown in Figure 2-18. Both digital and analog circuits are designed to operate down to voltages as low as 0.9 V while being clocked at 10 MHz. Table 2.1 summarizes the chip results while comparing the results to other 1 m BAN solutions.

Figure 2-19 presents measured transient results across the network shown in Figure 2-2, demonstrating both transceiver and network operation. The measurement directly probes nodes v_+ and v_- on the eTextiles network, as well as the demodulated

[12]This is another important reason for using ternary data; autocorrelation results are more robust on ternary data than on binary data.

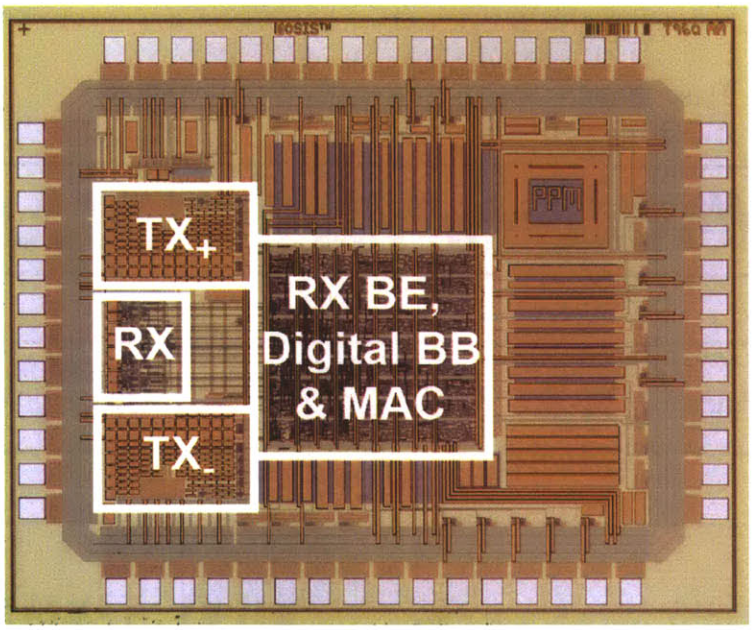

Figure 2-18: Die photograph of the eTextiles transceiver.

data stream from the basestation's receiver back end.

With 7-bits of binary weighted coupling capacitors, the transmitter achieves voltage swings ranging from 6–260 mV across a 1 m eTextiles network.[13] This results in a transmitter front-end energy consumption of 0.7–18 pJ per transmitter bit. The receiver front-end consumes 2 pJ/bit, regardless of the input signal amplitude. As shown in Table 2.1, these results are up to 35X more efficient than an already very efficient wireless ultra-wideband (UWB) receiver [68], greater than 100X more efficient than comparable BCC systems [47, 48], and on the same order as a wireless eTextiles approach that operates over 1.2 cm distances [54]. Due to the energy-efficient front-end combined with low-voltage digital baseband operation, the chip consumes 110 μW during full receive-mode duty cycle (including receiver front-end, back-end, digital baseband, and I/O power), which is at least 20X lower than other fully integrated receiver systems (Table 2.1), including the wired portion of the eTexiles transceiver in [54]. Unlike wireless and BCC approaches which operate over inherent

[13] A 1m eTextiles link was used, as this facilitates reasonable comparison to other BAN approaches, and is also a good length for a generic size-medium t-shirt. Longer and/or shorter designs are certainly possible.

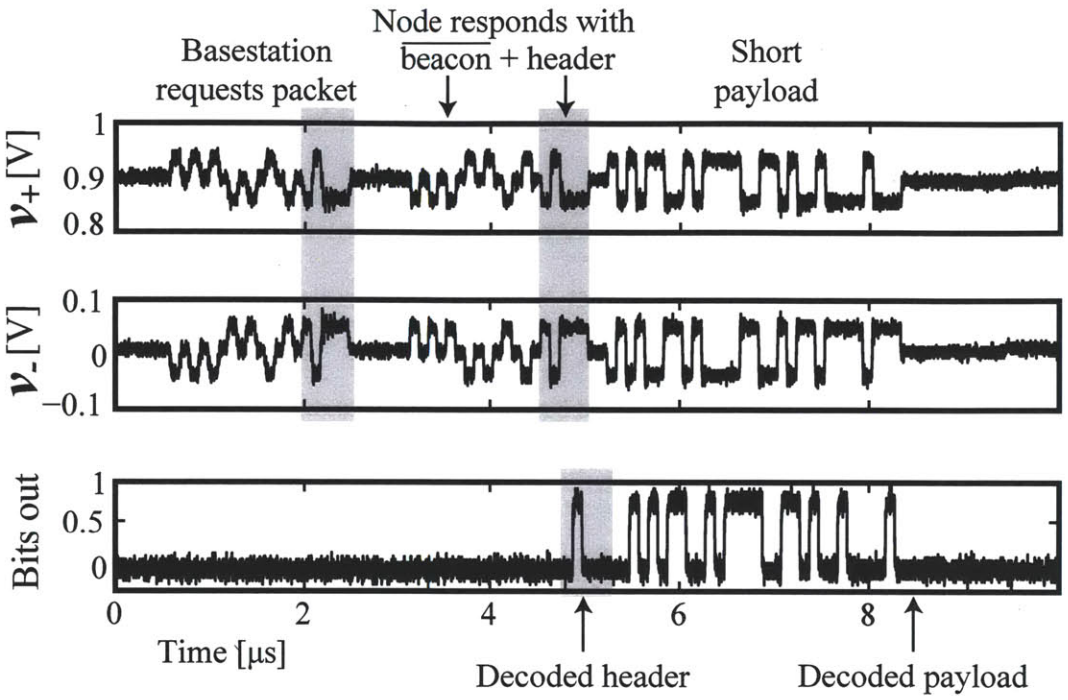

Figure 2-19: Measured transient response across the eTextiles network, illustrating a typical packet request by the basestation.

media, the proposed transceiver does, however, require the use of an eTextiles network which must be worn during operation.

To quantify the communication performance of the system, the receiver BER is characterized with respect to varying transmitter voltage swings for both differential and single-ended operation across a 1 m eTextiles network. Measurement results, taken in a noisy lab environment with significant RF (e.g. AM and FM radio, 802.11, cellular, etc.) and powerline interference, are shown in Figure 2-20. Note that single-ended measurements were made with double the transmitted voltage swing to facilitate fair comparisons to the differential results. To achieve a BER of 10^{-3} typically required in wireless systems, the differential case requires 15 mV, while the single-ended case requires 42 mV. This 2.8X difference illustrates the communication advantage of differential signaling in noisy environments. The right axis of Figure 2-20 also shows the combined receiver and transmitter energy consumption in dif-

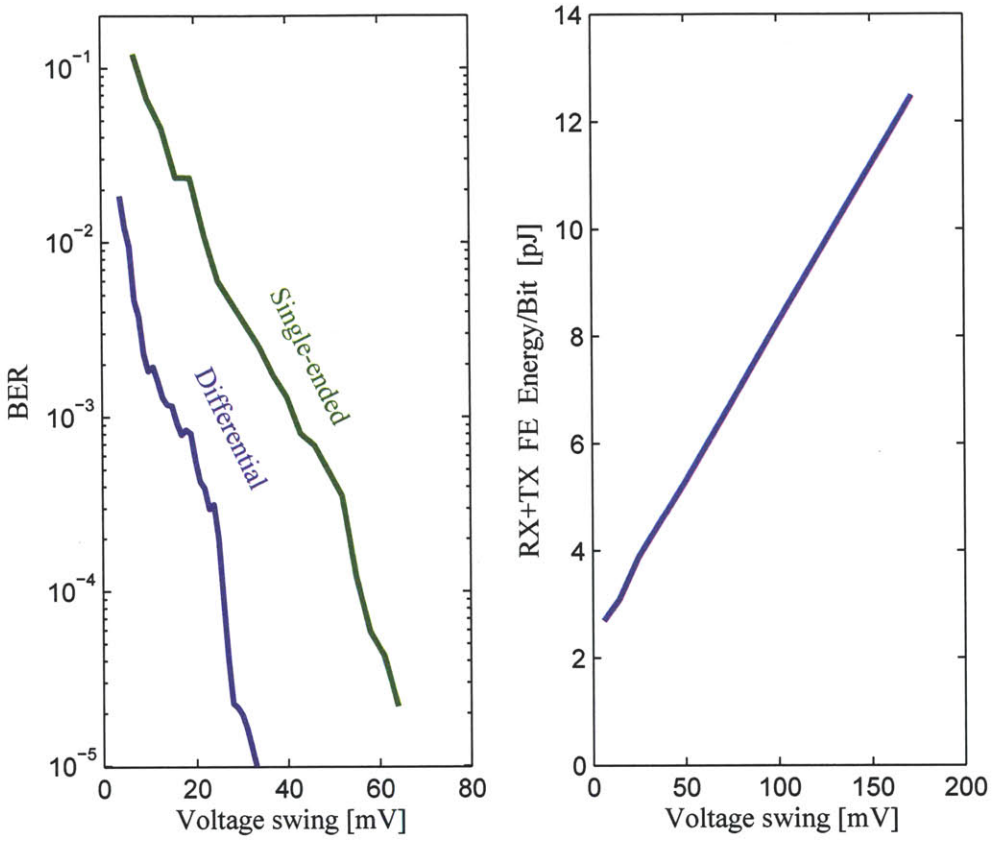

Figure 2-20: Measured receiver bit error rate (BER) curves and combined receiver and transmitter front-end energy consumption as a function of the effective differential voltage swing seen on the 1m eTextiles network.

ferential operation. At the receiver sensitivity of 15 mV, the transmitter consumes 1.2 pJ/bit, resulting in a total front-end energy consumption of 3.2 pJ/bit.

Although the sensitivity of the receiver could potentially be improved by adding linear amplification in front of the comparators, this would likely come with an overall system energy penalty. For instance, adding linear amplification would increase the energy consumption of the receiver front-end, increasing its sensitivity, thereby requiring lower transmitter voltage swings. However, since the receiver already constitutes a large fraction of the total front-end energy consumption, marginally decreasing the transmitter energy consumption while raising the increasingly dominant receiver energy consumption would not likely result in overall energy savings.

Table 2.1: Comparison of Body-Area Network Communication Systems

	[68]	[69]	[48]	[54]	[54]	**This work**
Type	Wireless UWB	Wireless MICS	BCC	Wireless eTextiles	Wired eTextiles	Wired eTextiles
Range [m]	10	2	1.8	0.012	0.85	1
Technology [nm]	130	90	180	250	250	180
Supply [V]	1.2/0.95	0.7	1.0/1.5	2.5/3.3	2.5/3.3	0.9
Data Rate [Mbps]	39.1	0.12	10	10	10	10
RX FE energy [pJ/bit]	69	10,000	225	1.1	–	2
TX FE energy [pJ/bit]	–*	2900	90	2.9	–	0.7-18
RX & baseband power [mW]	4.2	–*	3.7	>0.17*	2.7	0.11

*transmitter, digital baseband, and/or network controller not included.

When operating at a charging/communication duty cycle of 80%, the remote charging scheme achives 96% power transfer efficiency, measured over a 1m distance as the ratio of power going into the sensor node storage capacitor over the basestation's output power. As alluded to earlier, this is similar to the measurement of LDO efficiency. At a 50% duty cycle, 91% power transfer efficiency is achieved. Existing wireless power transfer schemes achieve upwards of 55% power transfer efficiencies over much shorter distances [54].

2.7 Summary

To address the broadcasting and/or path loss issues of wireless and BCC systems, an eTextiles transceiver is proposed in an inherently secure and private communication system. The designed eTextiles transceiver uses supply-rail-coupled differential signaling to efficiently time-share the eTextiles medium between communication and remote-charging circuits. Fabricated in 0.18μm CMOS technology and operating at 0.9 V, the resulting transmitter and receiver front-ends together consume 3.2 pJ/bit, which is at least 20X more efficient than conventional 1m BAN approaches. At 100% receive-mode duty cycle operating at a data rate of 10 Mbps, the transceiver consumes 110 μW, including the power from an integrated digital baseband. Remote charging, where a basestation's battery is directly connected to a sensor node's power supply through the eTextiles network and remote charging transistors, achieves up to 96% power transfer efficiency, thereby enabling small sensor nodes which last for a long time between charges. Several exciting future research directions resulting from this work are discussed at the conclusion of this thesis in Section 5.2.

Chapter 3

In-vivo Energy Harvesting: Extracting Energy from the Endocochlear Potential

The design of implanted devices is generally an exceedingly difficult task. Such devices must be sized according to anatomical constraints, must interface with the underlying biological process with long-term bio-compatibility, and must wirelessly communicate data in and/or out. All these requirements must be met while also maximizing *device* lifetime in order to avoid costly and invasive surgical re-implantations. Since current battery technologies have limited number of recharge cycles and often do not provide sufficient energy density given underlying anatomical size constraints, system-level optimizations involving energy are required to meet these difficult implantable system requirements.

Specifically, this chapter investigates the design of an energy harvesting system to provide energy and functional autonomy to implanted systems. There are many different ways to harvest energy from the environment to power such systems. One of the more popular approaches is to extract energy from available far-field electromagnetic energy. This idea encompasses the radio frequency identification (RFID) application space, where a local reader node radiates high-power RF signals, which is then rectified by the smaller implanted, or "tag" device [70, 71]. Since an implanted

device must always be in the vicinity of a high-output-power node, this approach does not fully qualify as being completely autonomous to the patient – that is, a patient must conscientiously always be within the range of a suitable RF field. By requiring sufficient exposure to certain wavelengths of light, photovoltaic energy harvesting technologies share the same autonomy pitfalls.

On the other hand, the human body stores and actively consumes a tremendous amount of energy. Since all patients are required to re-fuel themselves by ingesting food and nutrients, energy extraction from natural biological processes offer an opportunity to power electronic devices both autonomously and indefinitely.[1] As a result, Section 3.1 of this chapter begins by investigating extractable sources of energy located within the human body. However, most current demonstrated energy extraction systems offer low output power, are inherently intermittent, or have not yet been demonstrated in *in-vivo* applications. As a result, the specific aim of this chapter is to investigate an *in-vivo* source of energy that has never before been used to power electronic devices - the endocochlear potential (EP).

3.1 Harvesting Energy from the Human Body: an Overview

The human body is an absolutely astounding factory of energy. To quantify this, consider that 1g of fat contains approximately 38 kJ of energy [72]. Putting this in perspective, a human of average size stores approximately the same amount of energy in fat alone as a 1000 kg battery [73–75]. In terms of power, the human body consumes energy at rates ranging between 80 W and 1.6 kW while sleeping and sprinting, respectively [72]. Since implanted medical devices often have power budgets on the order of microwatts (or less), it should be possible to extract a small fraction of this energy and use it to power electronic devices. Importantly, this should occur without affecting natural physiology.

This section will provide a brief overview of some of the possible techniques for

[1] Well, at least for the lifetime of the patient.

extracting energy from the human body from both external (i.e. wearable) and *in-vivo* (i.e. implantable) perspectives. An overview of such harvestable sources is shown in Figure 3-1.

3.1.1 External Sources of Extractable Energy

Even though externally worn energy harvesters by definition do not operate *in-vivo* to the human body, such devices can still in fact be useful for implanted electronics. For example, if sufficient energy can be harvested at the appropriate location external to the body, a simple wireless near-field link as described in Chapter 4 can transfer this generated power to an implant.

There are many ways to extract energy from the body, in an environment external to the body. Hand-crank generators are a classic example of precisely this: turning stored energy in the human body into useful electrical energy through active muscle movement. Such generators have applications in flashlights [76], cellular phones [77], laptops [78]. Of course, this type of energy conversion relies on active human input - a patient must exert physical effort in order to generate power. In other words, this technique does not generate energy autonomous to human interaction. As discussed in Section 1.3, patient compliance is a significant and real issue. Consequently, it is worthwhile investigating other methods to harvest energy from the human body that do not require active patient participation.

Many autonomous or semi-autonomous energy harvesting devices often draw inspiration from classic hand-crank generators - that is, they generate electricity based on motion resulting from muscle actuation. In general, such energy harvesting techniques are based on induction (i.e. geared motion into a generator) or piezoelectricity (i.e. pressure or vibrational motion of a piezoelectric material). In this case, rather than having patients actively actuate muscles, energy is instead scavenged from motion that a patient would naturally perform during the course of a typical day. For example, the human body consumes an additional 47 W by walking instead of sitting [72]. As a result, there have been several attempts to extract energy from this naturally occurring motion, in the form of heel-strike harvesters [79,80] or leg mounted

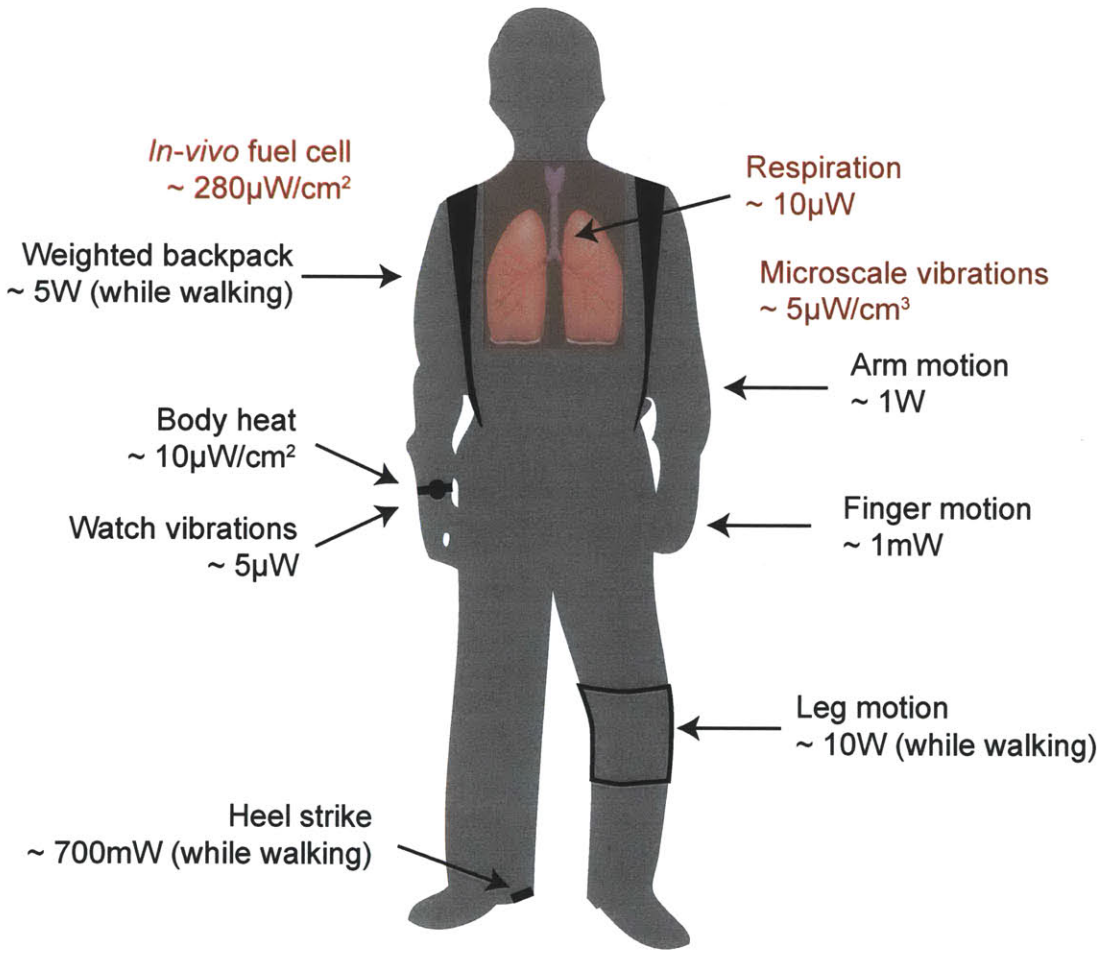

Figure 3-1: Various energy harvesting sources located external (black) or *in-vivo* (red) to the body. Scalable solutions use power density estimates, while non-scalable solutions use total extractable power estimates.

devices [75]. Such heel-strike and leg-mounted devices have been demonstrated to extract on the order of hundreds of milliwatts to single-digit watts, respectively. This is a significant amount of power, sufficient for operating or charging a cellular phone. However, such generated power either requires relatively large, obtrusive, and low-cosmesis externally-worn devices, or is generated at locations that are physically inconvenient to autonomously share with wireless wearable or implantable medical devices. A promising alternative approach involves integrating nanogenerators into clothing to tap into microscale human vibrations [81], though such an approach has not yet been shown for large-scale (i.e. clothing-size) implementations.

An alternative to motion-based energy harvesting is to extract energy based on temperature differences, relying on the thermoelectric effect. Since ambient room temperature is much lower than the temperature of the human body, which is actively regulated to 37°C, such a naturally occurring temperature gradient is a logical choice for autonomous energy harvesting. Many others have investigated such systems, typically as a wrist-watch type of device [82–85]. In contrast to vibrational techniques however, thermoelectric harvesting has substantially lower extractable power, in part due to low Carnot efficiencies and limited device surface areas. For example, the Carnot efficiency from the human body temperature of 37°C to room temperature of 20°C is only 5.5% [86]. Consequently, such harvesters can only be used to operate simple, low-power surface-worn devices, as it is exceedingly difficult to generate sufficient power to operate a near-field wireless power transfer link to an implanted device. In addition, any externally generated power would be at least $1/\eta$ times lower by the time it reaches the implant, where η is the efficiency of wireless power transfer.

3.1.2 *In-vivo* Sources of Extractable Energy

In contrast to external energy harvesting, energy extraction *in-vivo* to the human body is at least semi-autonomous, will not require obtrusive wearable elements, and will not suffer the power loss due to the finite efficiency of a wireless power transfer link. For these reasons, together with the pitfalls of implanted batteries as described in this chapter's introduction, developing *in-vivo* energy harvesting technologies can

thus be a significant boon for implanted biomedical devices.

Since the temperature of the human body is actively regulated to 37°C, there are no significant opportunities to harvest thermal energy *in-vivo*.[2] As a result, most *in-vivo* energy harvesting techniques are similar to their most common external counterparts, in that they rely on piezoelectric devices to extract energy from vibrations. However, unlike their external counterparts, there are far less opportunities to extract energy from *in-vivo* movement. In addition, the range of internal motion is typically far more limited than what is available externally, resulting in much lower extractable power. For example, one of the few systems described for *in-vivo* deployment scavenges energy from respiration motion; it was estimated to extract on the order of microwatts with air flow speeds of approximately 1 m/s [87].

A promising alternative approach to vibrational harvesting relies on *in-vivo* electrochemistry. Such systems draw inspiration from the way energy is consumed throughout the body by extracting energy from glucose that is naturally found in blood. To accomplish such a feat requires the development of implantable biofuel cell technology. There are two different types of biofuel cells described in the literature: microbial [88, 89] and enzymatic [90, 91]. Since microbial fuel cells require the use of precious metals and whole-cells as catalysts, their bio-compatibility is limited, and their application spaces are typically reserved for large-scale power plant-type operations. On the other hand, enzymatic biofuel cells use enzymes as a catalyst, and glucose or other sugars are well suited fuels. Consequently, there is much promise in miniaturizing enzyme-based fuel cells for implantable applications [92]. For example, others have described extracting energy from biofuel cells implanted in insects [93], rats [94], and snails [95]. However, with the exception of the latter reference, no such biofuel cells have been demonstrated in fully *in-vivo* conditions. Since snails do not have the same level of oxygen concentration in hemolymph[3] as mammals do in blood, there is still much work required before *in-vivo* mammalian experiments are

[2]One possible exception may be in the vicinity of the lungs, but the temperature difference there will likely not be sufficiently large to extract useful amounts of power.

[3]Hemolymph is somewhat analogous to a combination of blood and interstitial fluid as found in mammals.

attainable.

As a result of these concerns, this thesis explores an alternative method to extract energy naturally *in-vivo* to the human body, relying on the electrochemical properties of the inner ear. A summary of harvestable energy sources is shown in Table 3.1, partially based on the summaries provided in [86, 96].

Table 3.1: Comparison of various energy harvesting sources.

Source	**Power density (scalable sources) or total available power (non-scalable sources)**	**Notes**
External-only applications		
Leg motion [75]	10 W	While walking
Heel strike [79]	700 mW	While walking
Thermoelectric [86]	60 μW/cm^2	$\Delta T = 5°C$
External or *in-vivo* applications		
Piezoelectric microbender [97]	< 20 μW/cm^3	$f \approx 800$ Hz, 2.25 m/s^2
Ambient RF [98]	< 1 μW/cm^2	Unless in close proximity to a transmitter
in-vivo-only applications		
Glucose fuel cell [99]	280 μW/cm^2	Not demonstrated *in-vivo*
Hemolymph fuel cell [95]	30 μW/cm^2	Demonstrated in a snail
Lung air-flow [87]	10 μW	Not demonstrated *in-vivo*, air speed of 1 m/s
Endocochlear potential (this work)	1 nW	Conveniently located near the ear, eye, and brain

3.2 Inner-ear Physiology and the Generation of the Endocochlear Potential

3.2.1 General Auditory Physiology

The mammalian ear is a tremendously complicated organ that transduces acoustic waves into electrical impulses that are interpreted by the brain as sound. Viewed as an engineering system, the human ear attains absolutely tremendous specifications. The electrochemical, nanofluidic, mechanically actuated system has a dynamic range of approximately 120 dB, a power supply voltage of up to 150 mV, a power consumption of a few microwatts, and a 1 dB loudness discrimination [100]. At the threshold of hearing, the human ear can detect ear drum and middle ear bone vibrations on the order of 5 pm and 100 pm[4], respectively [100, 101]. To put this in perspective, recall that the Bohr radius (i.e. the distance between the proton and electron in a hydrogen atom) is around 53 pm.

The mammalian ear, illustrated in Figure 3-2, operates in the following manner. Acoustic sound pressure waves enter the pinna (outer ear), travel through the auditory canal, and mechanically vibrate the tympanic membrane (ear drum). This membrane is physically connected to a series of three middle ear bones – the malleus, incus, and stapes. These bones are often referred to as the ossicles, which occupy the tympanic cavity and comprise the middle ear. The primary purpose of the ossicles is to impedance match sound pressure waves traveling in a low impedance environment (air) to a higher impedance environment (cochlear fluid). By translating a force distributed over a large surface area of the malleus to a much smaller, concentrated area at the end of the stapes, a mechanical pressure amplification is also attained, though only for specific frequencies.[5] The stapes, which also happens to be both the smallest and strongest bone in the human body, then acts as a piston, which mechanically

[4]Yes, that is not a typo - picometers is the correct unit here.

[5]To elucidate, the resonant frequency of the middle ear bones is around 1 kHz, which also happens to correspond nicely to the main frequency found in speech. At this frequency, a gain of 26.6 dB was observed, while a gain of 23 dB was observed below 1 kHz, and little to no gain was found beyond 7 kHz [102].

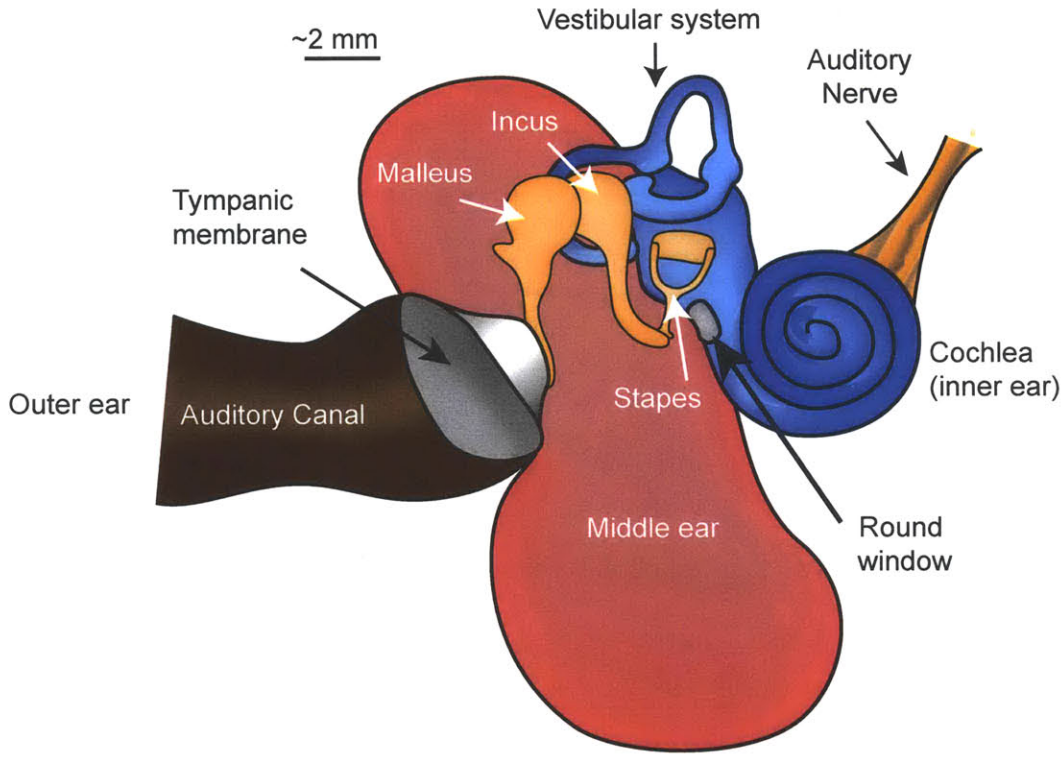

Figure 3-2: Diagram of the outer, middle, and inner ear. The ossicles (middle ear bones) are highlighted in white text.

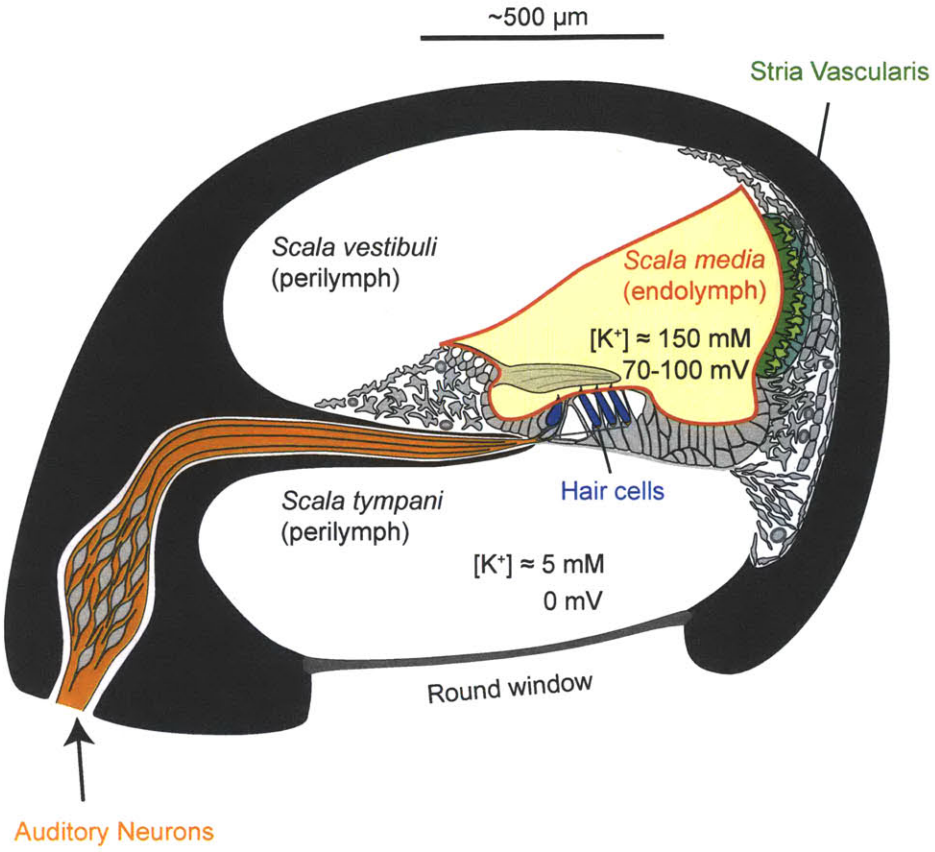

Figure 3-3: Illustrative diagram of the cross section of a single turn of the cochlea.

plunges fluid that exists inside the cochlea (inner ear) through a membrane called the oval window.

The cochlea is a spiral-shaped cavity enclosed by bone, which internally consists of three separate chambers of fluid: the *scala vestibuli*, the *scala tympani*, and the *scala media*. The *scala vestibuli* and *scala tympani* both contain a fluid called perilymph, which is similar in composition to cerebrospinal fluid. The third chamber, the *scala media*, contains a fluid called endolymph. Figure 3-3 illustrates a cross section of a single turn of the cochlea, showing these three separate chambers. The *scala vestibuli* and *scala media* fluidic chambers are separated by a thin membrane called Reissner's membrane. The *scala tympani* is separated from the other chambers by the much thicker basilar membrane.

Vibrating fluid, actuated by the stapes which mechanically displaces the oval window membrane, send sound pressure waves down the *scala vestibuli* and *scala media* chambers. The Organ of Corti, a cellular layer following the basilar membrane, consist of sensory hair cells that are mechanically actuated by these vibrations. An outer layer of hair cells act as a mechanical preamplifier which can be configured by the brain to increase their gain during low-volume hearing. Mechanically actuated inner hair cells, shown in Figure 3-4 then open up gated ion channels, which allow ionic current to flow. This ionic current, which mostly consists of potassium ions, depolarizes the hair cell, which opens up voltage-gated calcium channels. Incoming calcium ions cause the release of neurotransmitters, which diffuse toward afferent nerve fibers, ultimately triggering action potentials that are sent along the auditory nerve to the brain, creating the sensation of sound [103]. This essentially completes the mechanotransduction process of converting air-based sound waves to electrical activity within the nervous system.

For frequency discrimination, the cochlea performs spectrum analysis by converting frequency information into distance information. Specifically, low-frequency waves propagate to the end of the cochlea's apex, while high frequency waves terminate quickly (i.e. closer to the oval window).[6] The brain decodes this frequency information by associating the location of a specific hair cell along the basilar membrane with a particular frequency.

3.2.2 Generation of the Endocochlear Potential

Ionic hair cell currents are necessary to ultimately create the action potentials necessary for proper perception of hearing. As with all natural systems, energy is required to perform work – in this case to circulate ionic currents during mechanical hair cell actuation. This energy is derived from a concentration gradient found naturally in the mammalian inner-ear. Specifically, this gradient is found between endolymphatic and perilymphatic chambers, where the concentration of potassium ions changes from

[6]This is similar to the behavior of an electric transmission line. In fact, an interesting spectrum analyzer design has been reported in [104] whose architecture was inspired by the cochlea.

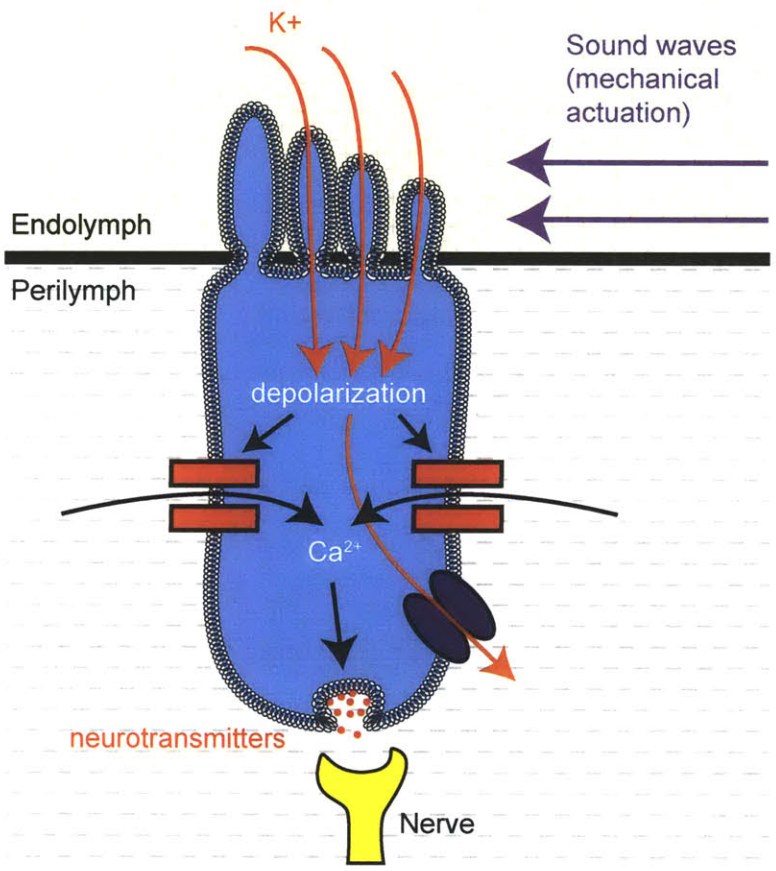

Figure 3-4: Detailed illustration of the operation of a single hair cell. Ionic currents, consisting mostly of potassium ions, depolarize the hair cell, opening voltage-actuated calcium channels, which cause the release of neurotransmitters, which elicit action potential firings in afferent nerves.

approximately 150 mM to 5 mM, respectively. For continuous hearing functionality, this concentration gradient is actively maintained and stabilized.

Since these two chambers are physically and electrically separated, this arrangement is in principal a concentration cell battery.[7] In fact, probing these two chambers with appropriately-sized electrodes reveals a potential difference! Despite being an over simplification, to a first approximation this potential can be calculated using the Nernst equation [105]:

$$V = \frac{RT}{zF} \ln \frac{[K^+_{endolymph}]}{[K^+_{perilymph}]}, \tag{3.1}$$

where R is the universal gas constant, T is absolute temperature, z is the number of moles of electrons transferred in the cell reaction, F is the Faraday constant, and $[K^+]$ is the concentration of potassium ions in the respective chambers. Plugging in the appropriate numbers leads to a potential difference of 90 mV.

This sort of biologic battery was first discovered by Georg von Békésy in 1952, and is termed the endocochlear potential (EP) [106, 107].[8] Depending on the animal, the endocochlear potential ranges anywhere from 70–100mV. This potential is the largest DC voltage found in the human body.

Due to its inherent and actively maintained stability, *in-vivo* location, and proximity to important organs, the endocochlear potential appears to be a well suited choice to power implantable medical electronics in the vicinity of the ear, eye, and brain. This is especially relevant, considering there are no other reported or demonstrated sources of body energy harvesting in this vicinity. However, even though the endocochlear potential was discovered almost exactly 60 years ago, it has never before been used as a power source for electronics. Thus, before energy extraction can occur, it is necessary to understand in more detail how the endocochlear potential is generated in order to better appreciate the associated challenges and limitations.

Ever since its discovery, the method of generation of the endocochlear potential

[7]This is in contrast to the much more popular Galvanic cell battery (i.e., a normal battery), which generates electrical energy from chemical energy based on two different metallic electrodes, electrolytes, and a connecting salt bridge.

[8]Interestingly, Georg von Békésy won the Nobel Prize in Physiology or Medicine in 1961 for his research on the ear, part of which was the discovery of the endocochlear potential.

has been a topic of much discussion and some amount of controversy. In 1959, it was first discovered that the stria vascularis[9] is the source of generation [108]. While this has subsequently been independently confirmed, the intricate details of generating the unusually high concentration of potassium ions within the endolymphatic space by the stria vascularis is still not entirely understood. The most common explanation invokes the multi-layered physical structure, which is described by a five-compartment (two-cell) model [109–114]. This model is summarized and simplified in Figure 3-5.

Although there is a lot of detail in Figure 3-5, the basic concept of EP generation is fairly simple. Perilymphatic potassium ions, which exist in "normal" concentration levels of 5 mM, enter fibrocytes via Na^+/K^+-ATPase and Na-K-Cl cotransporter proteins. With the help of energy, in this case adenosine triphosphate (ATP), these potassium ions are pumped against a concentration gradient, after which the ions pass through gap junctions and strial basal and intermediate cells, until they enter the intra-strial space via KCNJ10 rectifying channels. The potential difference between the intra-strial space and perilymph is close to the absolute value of the endocochlear potential.[10] However this intra-strial space is small, and with the help of additional energy from ATP, potassium ions are again pumped against a concentration gradient into strial marginal cells, and are then released into endolymph at concentration levels of around 150 mM. Due to the large concentration gradient, potassium ions in endolymph have significant potential energy and want to re-enter the perilymphatic space. This can and does occur via leakage pathways through surrounding tissues or tight junction networks. The more important mechanism for potassium ions to re-enter the perilymphatic space, however, is through hair cells. Mechanical actuation of hair cells open up previously gated ion channels, allowing potassium ions to flow. This ionic current depolarize the hair cells, eventually creating the actions potentials that are sent to the brain, creating the sensation of sound.

This circulating potassium current is essential to human hearing. Consequently, the concentration gradient comprising the endocochlear potential is actively main-

[9]The location of the stria vascularis within the cochlea is shown in Figure 3-3.
[10]In fact, it's slightly higher than the EP.

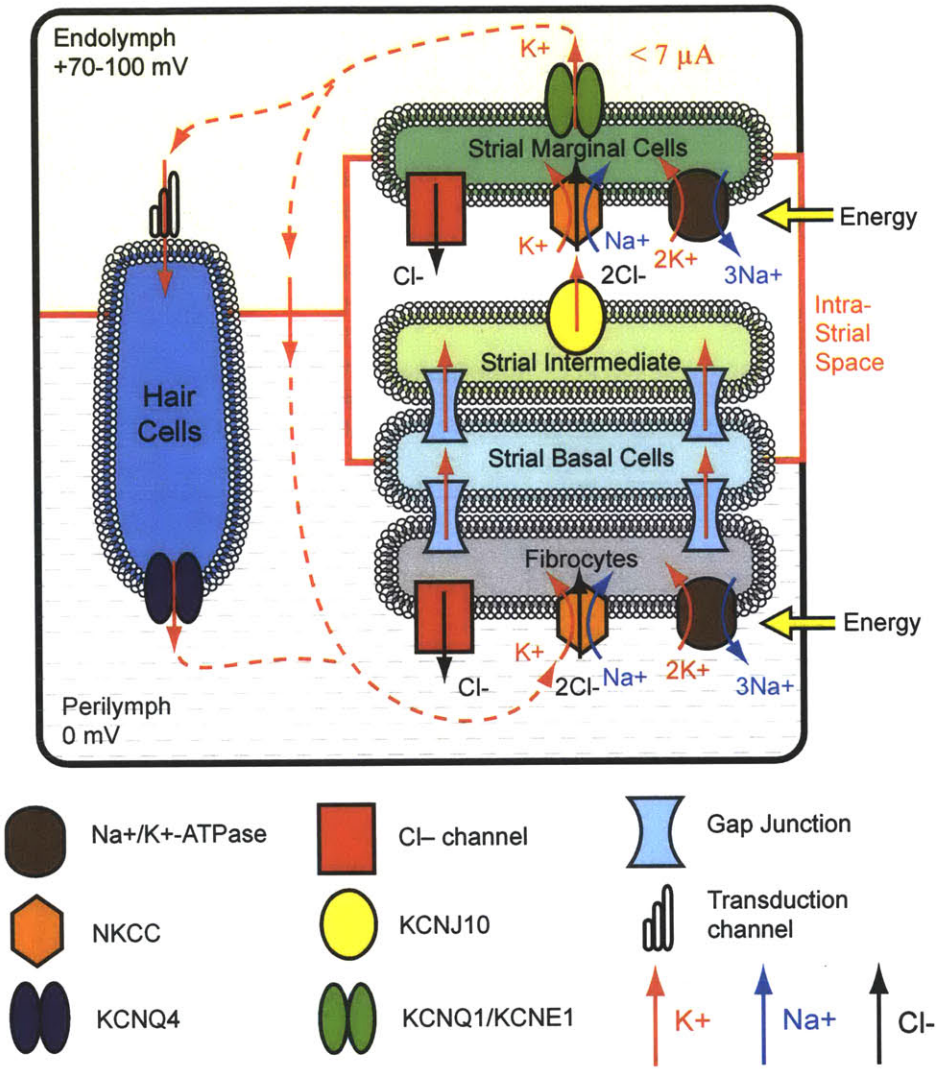

Figure 3-5: Detailed illustration of the ionic flow occurring inside the cochlea.

tained by natural physiology. As an *in-vivo* energy source, this sounds fantastic: a biologic battery that does not deplete itself over a patient's lifetime.[11]

To better understand how to extract energy from the endocochlear potential, it is worthwhile modeling its generation with an electronic circuit. Figure 3-6 illustrates a simple, yet appropriate circuit model, based on some of the work in [116]. Specifically, leakage current through tight junction networks is modeled as a simple resistor, while leakage current through mechanically actuated hair cells is modeled as a resistor in series with a capacitor. Inherent microelectrode impedance is also modeled as a resistor, and will be discussed in more detail in Section 3.3.2.

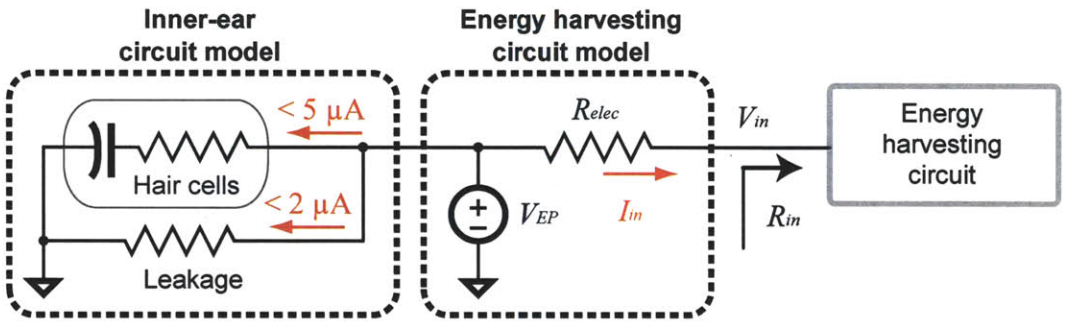

Figure 3-6: Circuit model of circulating potassium current as generated by the endocochlear potential.

Potassium current flow through the hair cells of a guinea pig, whose anatomy and physiology is similar to humans, range between 1–4 μA at quiet to maximal sound intensities, respectively [117–119]. Leakage currents through nonsensory cells and tight junctions are on the lower end of that range [120]. Thus, currents upwards of 7 μA naturally flow in the cochlea, resulting in a maximum power consumption of approximately 0.7 μW. This places a fundamental limit on the total extractable power from the endocochlear potential.

[11] To be fair, it has been experimentally shown in gerbils that the endocochlear potential does decrease slightly with age, though the amount is not large [115].

3.3 Endoelectronics System Challenges

There are three significant technological challenges associated with extracting energy from the endocochlear potential:

1. **Voltage**: the actual measured voltage of the endocochlear potential is too small to directly power CMOS electronics.

2. **Power:** the amount of extractable power is *extremely* limited and must not interfere with natural physiology.

3. **Size:** the designed system must be miniaturized to fit within the anatomical size constraints of the ear.

The following subsections will discuss each of these challenges in more detail.

3.3.1 Ultra-Low-Voltage Challenges

The 70–100 mV endocochlear potential is generally too low to directly power standard CMOS electronics. In fact, early IC work in the 1970s suggested that the minimum supply voltage for an inverter to have greater than unity gain was around 200 mV [121]. Greater than unity gain is a necessary condition to propagate digital logic values, or design a start-up circuit (based on a ring-oscillator, for example). Recent work has achieved operation at voltages down to 120 mV using standard CMOS technologies [122, 123]. Lower supply voltages down to 85 mV are achievable with body biasing, however, the supply voltage for the body biasing itself is often larger than the nominal supply voltage, limiting the usefulness of this technique in certain situations [124]. Others have also described interesting start-up circuits that operate to as low as 40 mV, albeit requiring additional CMOS post-processing [125] or a large external transformer [126]. Finally, a very promising 65 mV standard cell library based on Schmitt trigger logic was described in [127]. However, as described in Section 3.3.2, energy extraction from the endocochlear potential must actually occur at voltages down to 35 mV. Additionally, the Schmitt trigger devices were sized to be extremely large, which may surpass the power budget described in Section 3.3.2.

These low-voltage issues can be addressed by simply boosting the endocochlear potential to a higher voltage that is suitable for powering CMOS devices. This can be accomplished using a switching boost converter, described in Section 3.4.2. Of course, this technique does not address the start-up concern: the boost converter switches must operate from a supply voltage higher than the EP, which must be present before the converter can operate in the first place.

Use-case engineering can help address the start-up issue. Because the endocochlear potential is a stable source of energy, once the boost converter starts up it should, in theory, be able to operate over the lifetime of the patient. Consequently, any start-up solution should only have to occur once. As a result, the efficiency of the start-up solution is inconsequential – so long as it works. In other words, an inefficient or cumbersome use-case is still an acceptable one. Next, considering that this is an implanted system, it will require some form of wireless communication in order to transmit (receive) sensed data (actuation commands) to (from) the outside world. The proposed solution is then to re-use the communication antenna for a circuit that receives wireless energy from an external wireless power source.[12] This energy can be used to initialize the boost converter supply voltage; once this occurs, the external power source can be removed, and the boost converter will self-replenish its supply voltage. The wireless energy receiver circuit is described in Section 3.4.5.

3.3.2 Low-Power Challenges and Safety

The absolute amount of extractable power from the endocochlear potential is extremely limited. Because the physical anatomy of the *scala media* and *scala tympani* chambers and their surrounding cellular structures are very small, any interfacing microelectrodes must also be small. Ideally, the diameter of these electrodes should be comparable or smaller than the size of a single cell – on the order of 1 μm. In practice, this proves to be extremely difficult. Although metallic electrodes may offer sufficiently low impedances at these dimensions, further research is required to select and design metallic electrodes that have the appropriate electrochemical compati-

[12]This idea was developed in parallel with the system demonstrated in [128].

bility with inner-ear fluids while also eliminating junction potentials. On the other hand, electrolyte-filled glass electrodes have good bio-compatibility with negligible junction potentials. However, such glass electrodes suffer from high impedances at these dimensions – often on the order of tens or hundreds of megaohms. Since this is generally too high, tip diameters of approximately 10 μm are instead used for this initial prototype, resulting in impedances on the order of 500 kΩ per microelectrode. Unfortunately there is a risk of cellular damage with such electrodes dimensions; further research on low-impedance metal electrodes will be necessary to overcome this challenge. Section 5.2 briefly discusses future electrode directions.

Due to the resulting high electrode impedances, it is worthwhile to form a maximum power transfer circuit. Specifically, the input impedance of the energy harvesting circuit, R_{in} should be designed to be equal in magnitude to the electrode impedance, R_{elec}. In this situation, we have a simple voltage divider, where due to the equal impedances, V_{in} of Figure 3-6 is equal to $V_{EP}/2$. The maximum extractable power under this condition is given by Equation 3.2.

$$P_{in} = \frac{V_{in}^2}{R_{in}} = \frac{V_{EP}^2}{4R_{elec}} \tag{3.2}$$

Using two electrodes comprising a total impedance of 1 MΩ, the maximum extractable power with endocochlear potentials ranging from 70–100 mV is 1.2–2.5 nW. This is a minuscule amount of power. To put this in perspective, the lowest quiescent power boost converter published in the literature requires 330 nA at a supply voltage of several volts, which is orders of magnitude higher than the amount of extractable power from the EP [129].

To overcome this challenge, circuits that consume near-zero leakage power are required together with an energy buffering architecture. In this architecture, any extracted energy in excess of the continuous quiescent power consumption is buffered up onto an energy storage element. Once there is sufficient energy available (i.e. sufficient time has passed and a large reservoir of energy is available), a useful task can be accomplished (e.g., a radio transmission). The proposed energy buffering

architecture is discussed in more detail in Section 3.4.

Importantly, any power extraction from the endocochlear potential should additionally not interfere with natural physiology. That is, it should not cause hearing damage. Since the maximum extractable current is roughly three orders of magnitude lower than the natural power consumption of the cochlea itself, a proposed hypothesis is that the body can easily supplement the additional potassium ions by the ingestion of food, and no hearing damage is caused.[13] Although this appears to be a good hypothesis, it should most certainly be verified experimentally in future work.

3.3.3 Miniaturization Challenges

The endocochlear potential is attractive as an energy harvesting source, since it is available fully *in-vivo* to the human body and is in close proximity to important human systems, such as the vestibular organs, facial nerve, carotid artery, and the temporal lobe of the brain, all of which are within millimeters of the cochlea. To take advantage of this favorable placement, all necessary electronics should be miniaturized to fit within the fundamental anatomical size constraints in this vicinity.

Fortunately, the human mastoid cavity, or the bulla cavity of cats or gerbils contains sufficient room to fit a circuit board of up to several millimeters on either side [130]. To accomplish this, the resulting design must be tightly integrated. By combining the boost converter and radio transmitter on a single chip, using a compact packaging technology, minimal number of external passives, and sharing the antenna between the radio and wireless energy receiver, it will be possible to fit all the required functionality within the space constraints.

3.4 Endoelectronics Chip and System Design

A block diagram of the endoelectronics chip is shown in Figure 3-7. At the maximum power transfer condition, the input into the boost converter, V_{in}, ranges between

[13] Alternatively, by periodically swapping the electrical polarity of the input to the boost converter, potassium ions can instead be made to circulate.

35–50 mV, or half of the endocochlear potential. Transistor M1 and M2 are activated by timer, control, and charge pump circuits in order to extract energy from V_{in}. Any residual energy is used to increase the voltage, V_{DD}, on capacitor C_{DD}. Once sufficient energy has buffered onto C_{DD}, a radio transmitter is activated and a wireless packet is quickly delivered to an external receiver up to 1 m away. The radio shares an antenna with the one-time start-up rectifier circuit, which is used to initialize the charge on C_{DD} during system start-up. The following sections discuss the design of each block in more detail.

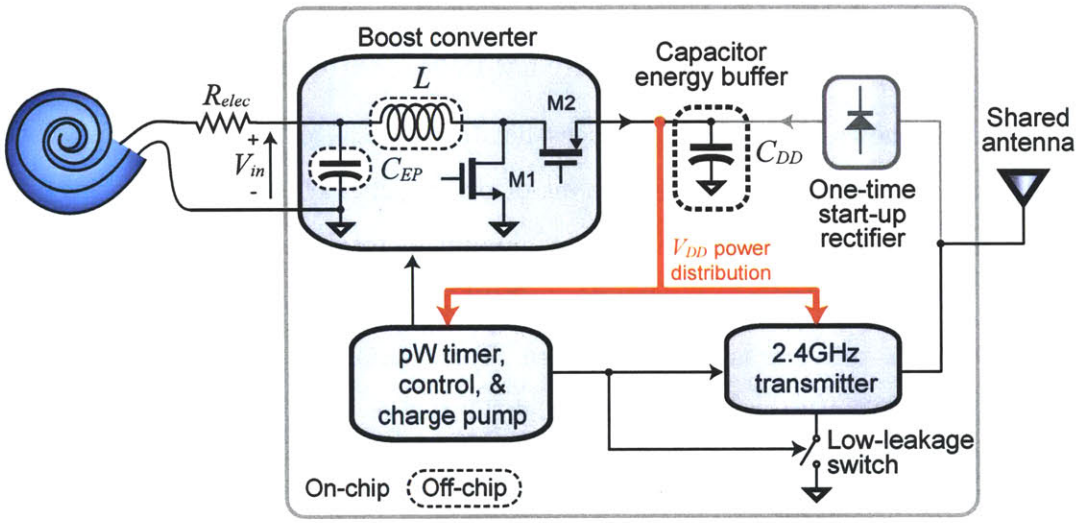

Figure 3-7: Block diagram of the endoelectronics chip.

3.4.1 CMOS Leakage Analysis Applied to Transistor Sizing

The leakage (i.e. standby) power constraints of any system used to extract energy from the endocochlear potential are extreme. To offer any amount of functionality, the leakage power of the system must be much less than the low-end of extractable power (i.e. less than 1.2 nW) if there is to be any power left to perform useful tasks. Consequently, it is imperative to limit transistor leakage power.

Through judicious use of power gating devices and good practice low-leakage design, others have described excellent work in sub-nW standby-mode microcontrollers

& sensor interfaces [17, 131], and sub-10 nW standby-mode radios [17]. However, there have been no fully integrated systems with the requisite functionality demonstrated to operate under the extreme power budgets imposed by the EP harvesting system. Specifically, there is no published work using a large step-up boost converter and meter-range radio at these power levels.

To realize a fully functional system at such extreme power budgets therefore requires additional device leakage considerations, given a particular CMOS technology. In this work, a 0.18 μm technology was chosen due to its sufficient RF performance up to and beyond 2.4 GHz, as well as the availability of thick-oxide high threshold voltage (V_t) devices that offer sufficiently low leakage currents.

It is well-known that high-V_t devices have larger I_{on} to I_{off} ratios than low-V_t devices sized to deliver the same amount of on-current. Thus, a design using high-V_t devices will generally offer the lowest amount of total leakage power. However, choosing a high-V_t device over a low-V_t device has consequences in regards to device size, and as a result, parasitic capacitance. For example, parasitic capacitance can increase by 3-10X between low-V_t and high-V_t devices in this technology. Thus, if such circuits additionally need to operate at high speeds (for example, in the radio front-end), more careful consideration is required.

For low-frequency, non-performance limited circuits, operating at the lowest supply voltage and using high-V_t devices is most appropriate, as the absolute amount of leakage power is minimum in this case. To a first order, Equation 3.3 can be used to predict the amount of leakage current through a device, while also giving some insight in how to further minimize this current.

$$I_D \approx I_{D0}\frac{W}{L}e^{\frac{qV_{GS}}{nkT}} \tag{3.3}$$

Here, I_{D0} is the pre-exponential current, W is the device width, L is the device length, and kT/q is the thermal voltage (approximately 26 mV at room temperature). After transistor types and power supplies have been selected, the only variable left to the designer is its sizing. To minimize leakage current, Equation 3.3 suggests creating a

small-width, large-length device.

However, most deep sub-micron technologies (including the chosen 0.18 μm technology) employ the use of shallow trench isolation (STI), which is a technique used to isolate adjacent transistor leakage effects (older technologies had made use of local oxidation of silicon (LOCOS)). As the transistor width gets narrower, the electric field at the edge of the trench becomes enhanced, creating a slightly stronger inversion layer, which ultimately causes a drop in threshold voltage. This is called the inverse narrow width effect (or the reverse short channel effect), and causes device leakage to be higher for very small width devices [132–134]. This effect is illustrated in Figure 3-8 for a representative NMOS device. In this example, leakage can be reduced by up to 50% through proper sizing. Interestingly, low-V_t PMOS devices in this process do not suffer from the inverse narrow width effect. Reference [133] hypothesizes this is due to a boron puddle that is created during device manufacturing.

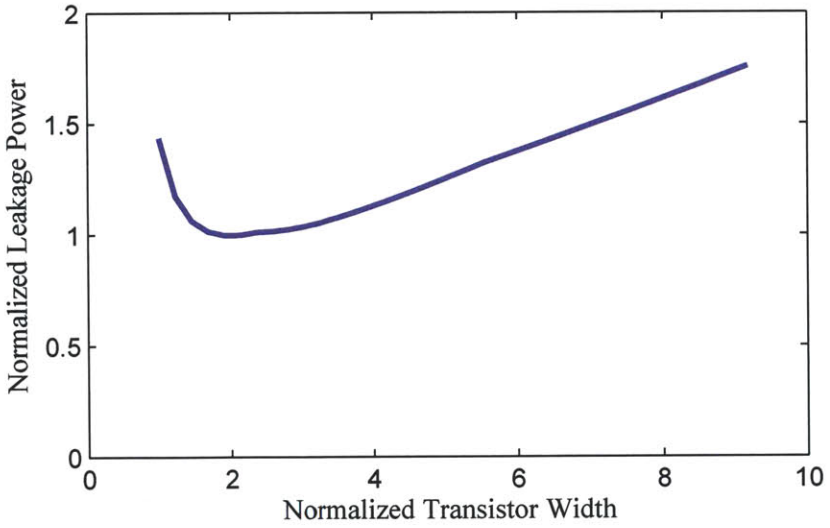

Figure 3-8: Leakage performance of a representative NMOS device plotted versus the device width. Clearly, the lowest leakage current is found with a greater-than-minimum width.

With the optimal transistor width selected for low leakage performance, the only other variable is transistor length. Fortunately, increasing the length of a transistor also increases its threshold voltage due to the V_t rolloff effect [134], further reducing the leakage current. However, the V_t rolloff effect quickly plateaus, reducing the

impact of increasing device lengths beyond a few integer multiples of the minimum length.

Figure 3-9 summarizes these results by plotting the simulated maximum device frequency[14] versus leakage power for NMOS and PMOS devices of various lengths, all sized with optimal widths to minimize leakage. The data is normalized to different values for NMOS and PMOS devices for technology confidentiality reasons. Here, the negative effects of extremely long transistors become readily apparent. Particularly for NMOS devices, long transistors do not offer much leakage benefits, but instead substantially increase parasitic capacitance, and therefore switching speed and energy per operation. As a balance between performance and leakage, sizing NMOS devices near the knee of this curve (somewhere between 2 and 3X minimum length) is a good starting point.

3.4.2 Boost Converter Design

The boost converter is used to extract energy from the endocochlear potential while simultaneously processing it to be at a higher voltage for CMOS utility. Typically, the 35–50 mV input voltage is boosted to 0.8–1.1 V, which is at least a 1:22 up-conversion ratio. A block diagram of the converter is shown in Figure 3-10. The converter was primarily designed by Saurav Bandyopadhyay.[15] Design of the control circuits follow the guidelines outlined in Section 3.4.1 for minimum leakage power.

The converter operates in discontinuous conduction mode (DCM) at a frequency of 12.5 Hz. Unlike traditional converters that endeavor to regulate the output voltage, this converter does not have any output regulation control. The converter is designed to instead extract maximum energy from the source, as a form of *input* voltage regulation. Since the source is resistance-limited, and since the resistance of the microelectrodes do not change, the maximum power point tracking (MPPT) condition only requires the *average* input impedance of the converter to be matched to the impedance of the microelectrodes. In other words, active MPPT is not required –

[14]Calculated using a fan-out of four delay.

[15]I assisted with architectural considerations and system design.

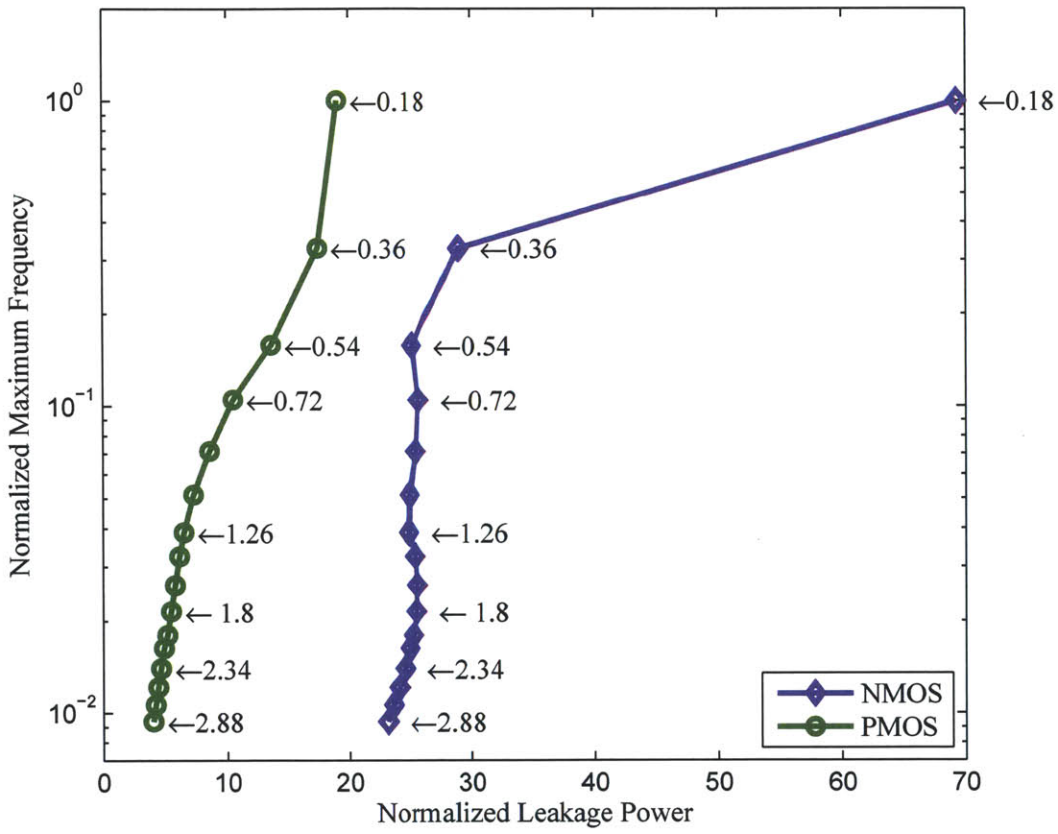

Figure 3-9: The maximum frequency of NMOS and PMOS devices whose widths are optimally sized, plotted for various lengths (in μm) versus normalized leakage power.

MPPT requires only a one-time calibration for every set of microelectrodes. At the matched condition, V_{in} will approximately equal $V_{EP}/2$. At this point, any excess energy will buffer up onto capacitor C_{DD}, thereby increasing its voltage.

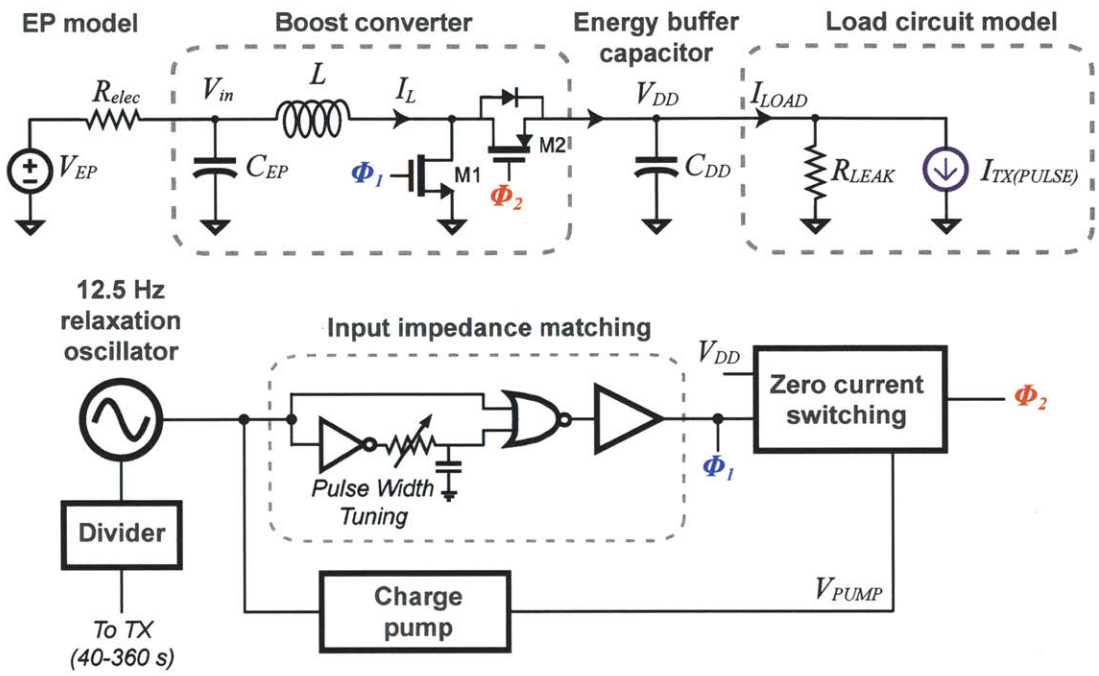

Figure 3-10: Schematic diagram of the boost converter power train and its simplified control logic.

The boost converter operates as follows. A relaxation oscillator generates a 12.5 Hz clock that is used to generate the signals that control transistors M1 and M2. For example, the clock is passed through a pulse generator, creating signal Φ_1 that directly controls M1. When Φ_1 is high, current through inductor L is ramped up, as illustrated in Figure 3-11. Other than resistive losses in the inductor and switch, no energy is wasted here; rather, energy is being stored in the magnetic field of the inductor. When M1 is turned off, M2 is immediately turned on by de-asserting Φ_2. During this phase, the energy stored on inductor L is transfered to capacitor C_{DD}, thereby increasing its voltage. Since the converter is operated in discontinuous conduction mode, the inductor current will ramp down to zero and M2 will shut off. This requires the use of a zero current switching (ZCS) controller to ensure Φ_2 is toggled

at the correct time. The average input impedance of the boost converter is set by controlling the pulse width of control signal Φ_1.

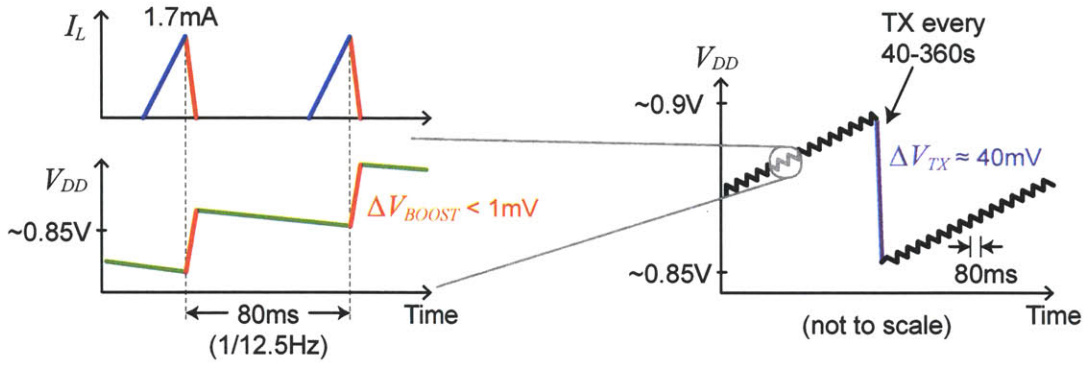

Figure 3-11: Timing diagram of the boost converter power train illustrating overall system power supply behavior.

This process repeats itself every 80 ms. During the period when M2 is not on, any energy stored on capacitor C_{DD} will leak away, as modeled by the load resistor R_{LEAK}. As long as the energy coming from the input causes a larger ΔV on capacitor C_{DD} than the leakage component, the desired energy buffering behavior will occur. Once there is sufficient energy stored on capacitor C_{DD}, the radio is activated and a quick packet is transmitted. This causes a large ΔV drop on the supply voltage V_{DD}. The total amount of energy consumed by the transmitter through the duration of a wireless packet will determine this voltage drop. So long as the transmitter's packet energy consumption is less than or equal to the buffered up energy since the last transmission, the system will sustain itself.

The transmitter is activated every 40–360 seconds by the relaxation oscillator through a twelve-stage digital register-based clock divider. Since the transmitter is activated at regular, programmable intervals (and is not controlled with respect to the amount of energy on capacitor C_{DD}), any energy imbalance in the system will be worked out through a DC shift in V_{DD}. For example, if the packet interval is large and the amount of input power is large, there will be more energy coming into the system than will be dissipated. Thus, V_{DD} will begin to rise. However, as V_{DD} rises, the constituent system leakage power also increases. A natural settling point will be

achieved at some intermediate value of V_{DD} where the combination of leakage and active power exactly cancels out the incoming harvested power. For safety reasons, a built-in diode-based clamp is used to prevent any excessive increases in V_{DD} in the event that the available input power becomes unwieldy large.

To increase converter efficiency, transistor M2 is not driven by a signal at voltage V_{DD}. Instead, it is driven by a signal at voltage V_{PUMP}, which is designed to be roughly double V_{DD} as provided by the charge pump circuit. The reason for this is to limit the amount of reverse leakage through M2 during the long periods of time when M2 is turned off. The charge pump schematic is shown in more detail in Figure 3-12. It uses a simple cross-coupled inverter-based pumping topology, with 18 pF pumping capacitors. The V_{PUMP} supply is decoupled by an on-chip 360 pF capacitor. Note that the charge pump supply is used by several other circuits in both the boost converter and in the radio transmitter. Since the nominal chip power supply is less than 1 V and the maximum tolerated supply in the 0.18 μm process is 2 V, there are no gate oxide reliability or safety issues.

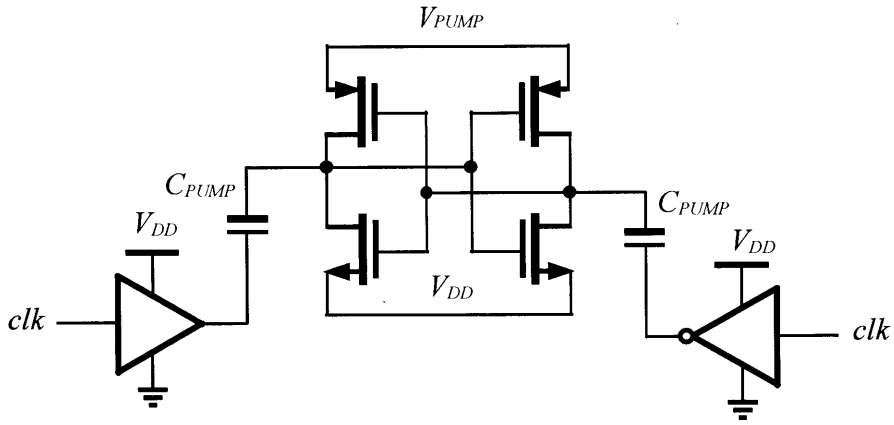

Figure 3-12: Schematic diagram of the charge-pump circuit.

3.4.3 Radio Transmitter and Wireless Energy Receiver Architectural Considerations

The application use-case for this design is to use the endocochlear potential as an energy source to autonomously power a wireless implant. Since it is not desired (or required!) to have a semi-permanent external wireless source powering and interrogating the implant, transmission of information from the implant should have sufficient reach to communicate with a device at least a meter away. For example, this external device can be a smart phone, which could locally process the data or re-transmit over a WiFi or cellular network to the cloud for analysis or storage. This setup permits the design of a functionally autonomous system, with zero patient involvement required.[16]

Another benefit of using a smart phone as the receiver is that the concept of body-area networking can be leveraged. Since the energy available to power the implant is extremely limited, it makes sense to push as much communication complexity away from the implant as possible. Cellular phones transmit on the order of watts, requiring significant investment in battery capacity. Consequently, a cellular phone has more than sufficient battery capacity to power a very sensitive receiver capable of detecting weak, low-power transmissions from the implant. Particularly if the implant transmits very infrequently, the energy overhead to the cellular phone for implementing this receiver can be essentially negligible. In this regard, designing a low-complexity, low-output power radio is a reasonable direction, and perhaps the only direction that will produce a radio operating with sufficiently low power consumption.

Specifically, the average power consumption of the radio transmitter should be less than 250 pW for system self-sustainability, as discussed in Section 3.5.1. Since the transmitter will be extremely duty-cycled, its average power consumption is not determined solely by its active or leakage performance, but by a combination of both. More precisely, the average power consumption can be modeled by Equation 3.4.

[16] Other than keeping their phone nearby, which is a reasonable assumption today.

$$P_{TX,avg} = P_{TX,leak} + \frac{E_b N}{T_{pkt,int}} \quad (3.4)$$

Average power	Leakage power	Active energy averaged over packet interval

Here, E_b defines the energy required to transmit a single bit, N is the number of bits per packet, and $T_{pkt,int}$ is the time interval between packets (in this case, programmable between 40–360 s). So not only must the transmitter have extremely low leakage power, it also must be very energy efficient, or the effective bit rate (i.e. $N/T_{pkt,int}$) will be forced to be very low. In this particular application, transmitting approximately one packet per minute, where each packet contains on the order of 100-bits, would be appropriate. This results in an average data rate on the order of 1 bps. Information will of course be packetized, and transmitted instantaneously at a much higher data rate (for example at 1 Mbps). This results in an extreme duty ratio of approximately 0.0001% between active transmission and sleep modes.

There are many examples of very energy efficient transmitter designs in the literature. Narrowband transmitters, which modulate data on top of continuous wave (CW) RF signals, are used in almost every modern wireless communication system today. Previous chips have attained energy efficiencies on the order of 140–2900 pJ/bit for output power ranging from -16 dBm to 0 dBm at instantaneous data rates under 5 Mbps [69, 135–140]. However, none of these systems are optimized for ultra-low standby power. On the other hand, work in references [17,141] were indeed optimized for low leakage power, consuming 675 pW and 3.3 nW in standby power modes, respectively. Unfortunately, neither of these results meet the specification of the EP harvesting system, particularly when their actives transmission modes are taken into account. For example, the two separate chips require 27 nJ/bit and 4.7 nJ/bit, result-

ing in average power consumptions of 46 nW and 11 nW, respectively.[17] Additionally, both chips have very low radiated output power (e.g., −45 dBm), limiting their range to below 1 m. A summary of previously published narrowband work is provided in Section 3.5.1.

On the other hand, ultra-wideband (UWB) radios, which communicate using very short duration impulses at RF, offer promising results in terms of energy efficiency.[18] In particular, the energy efficiency of UWB transmitters using non-coherent signaling can be much lower than their narrowband counterparts, due in part to relaxed frequency tolerances and internationally regulated output power limits. For example, Figure 3-13 shows the block diagram of a UWB transmitter that I had previously designed, which consumed 17 pJ/pulse in only 0.07 mm^2 of die area without any off-chip components other than the antenna [61].

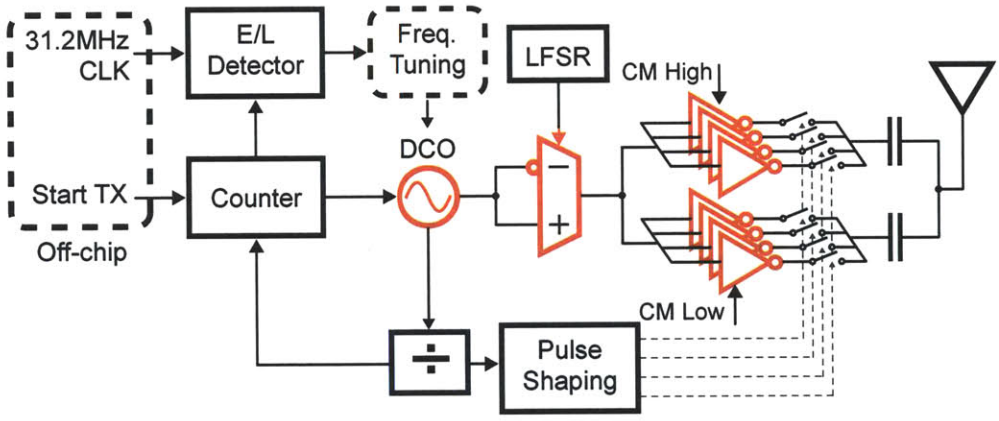

Figure 3-13: Block diagram of a typical energy-efficient UWB transmitter.

At first glance, a transmitter like this looks like a good choice for the EP harvesting system due to its ultra-low active energy consumption and minimal size. However, the complexity of the transmitter is fairly large, and highlighted in red in Figure

[17]This is calculated using each radio's nominal instantaneous data rate, for 100-bit packets transmitted once per minute.

[18]In this thesis, UWB specifically refers to impulse radio ultra-wideband (IR-UWB). There are competing UWB architectures that rely on more traditional narrowband techniques such as orthogonal frequency-division multiplexing (OFDM), but spread over a wide bandwidth. Although such systems also offer promising energy efficiencies, their active power consumptions are far too high to be considered in this application.

3-13 are blocks that need to operate at radio frequencies. Blocks that operate at RF generally require low-V_t transistors in order to switch sufficiently fast to generate power in the 3.1–10.6 GHz UWB bands. Such blocks have naturally high amounts of leakage that are difficult to effectively power gate down to the requisite levels in this particular application. Additionally, as an implanted system, energy loss through skin and tissue layers becomes increasingly important at high radiated frequencies, reducing the overall system radiation efficiency.[19]

For these reasons, it is necessary to reduce the overall transmitter complexity by limiting the number of RF blocks while pushing all possible communication complexity to the energy-abundant external smart-phone-based receiver. Taking the simplified architecture concept to a logical extreme, the transmitter proposed in this thesis radiates information through the use of a direct-RF power oscillator (PO) design, based on the work in [69]. A simplified block diagram of the transmitter is shown in Figure 3-14.

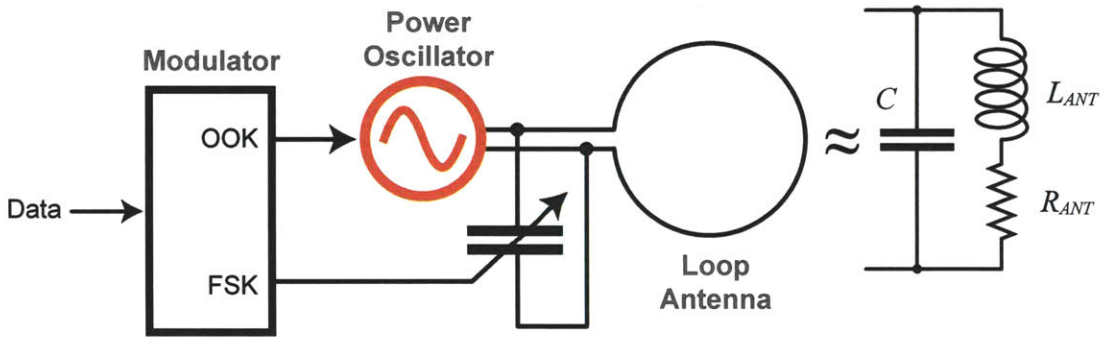

Figure 3-14: Simplified block diagram of the proposed direct-RF power oscillator transmitter.

The transmitter generates RF at a frequency of 2.4 GHz as a compromise between tissue losses, antenna efficiency, and circuit power consumption. A more thorough discussion of this trade-off is found in Section 3.4.4. A loop antenna is chosen as the radiative element, as it offers sufficient radiation conversion efficiency, has a high

[19]Recent work has challenged the conventional wisdom on this topic, though the results only apply for millimeter-sized implants operating somewhere in between the near- and far-field electromagnetic regimes for wireless power transfer [142, 143].

quality factor, and is naturally well suited to receive wireless power for system initialization. Due to anatomical size constraints, the physical size of the antenna will be much smaller than its radiating wavelength, resulting in an electrically small design. An electrically small magnetic loop antenna can be modeled as an inductor in series with a resistor, which is well suited to serve as part of the resonant network of the power oscillator. The oscillator itself performs automatic impedance matching, resulting in a very low-complexity, low-area, and energy efficient design. Data modulation can be achieved by turning on or off the entire oscillator for on-off keying (OOK) modulation, or the resonant capacitors can be dynamically switched for frequency-shift keying (FSK) modulation. Since OOK modulation generally requires half the power consumption (as the power oscillator is only on half the time), FSK should only be used when communication channel conditions are poor.

The following sections describe the design of the transmitter and wireless energy receiver circuits in more detail.

3.4.4 Antenna Design

As one of the few external system components to go along with the boost converter inductor and off-chip decoupling capacitors, the antenna should be sized to fit within the anatomical constraints of the middle ear. Specifically, the antenna should not be larger than a few millimeters on either side. Since the radiated wavelength at 2.4 GHz is 125 mm in free space, the antenna can be considered to be electrically small.[20] As briefly mentioned in the preceding section and illustrated in Figure 3-14, an electrically small loop antenna can be modeling as an inductor, L_{ANT}, in series with a resistor, R_{ANT}. A circular loop antenna's inductance can be approximated by Equation 3.5.

$$L_{ANT} = \frac{\mu}{2} D \left[\ln(8D/d) - 2\right] \tag{3.5}$$

[20]There are various rules of thumb as to what constitutes "electrically small". The typical requirement is that the diameter and circumference of the antenna must be approximately ten and three times less than the wavelength, respectively [144].

Here, μ is the permeability of the surrounding environment, D is the diameter of the loop, and d is the diameter of the constituent wire. There are also expressions for the inductance of loop antennas of various different shapes – refer to [144] for more information.

The antenna's series resistance, R_{ANT}, is made up of two components: R_{RAD} is the radiation resistance, and models the conversion of energy to useful electromagnetic radiation; R_{LOSS} is the loss resistance, which models energy dissipated as heat. The radiation efficiency, η_{RAD}, of an antenna is a metric that essentially describes how efficient the process of radiating EM waves is. Radiation efficiency can be calculated using Equation 3.6.

$$\eta_{RAD} = \frac{R_{RAD}}{R_{RAD} + R_{LOSS}} \tag{3.6}$$

The radiation resistance can be approximated by Equation 3.7.

$$R_{RAD} = \sqrt{\mu\epsilon}\frac{8\pi^3}{3}\left(\frac{A}{\lambda^2}\right)^2 \tag{3.7}$$

Here, ϵ is permittivity, A is the antenna's area in units of m^2, and λ is the operational wavelength. The loss resistor, R_{LOSS} can be calculated in the usual way from metallic conduction properties, taking into account the skin effect. The skin depth is given by Equation 3.8, and the associated per-unit-length resistance, $R_{LOSS,pu}$, is given by Equation 3.9.

$$\delta_s = \sqrt{\frac{1}{\pi f \mu \sigma}} \tag{3.8}$$

$$R_{LOSS,pu} = \frac{1}{\sigma d_p \delta_s} \tag{3.9}$$

Here, σ is the metallic conductance and d_p is the distance around the perimeter of the wire. Note that Equation 3.9 only applies when any cross sectional dimension of the wire is at least six skin-depths deep. For flat copper traces on a circuit board, this may not be a good approximation. Instead, the per-unit loss resistance can be calculated via Equation 3.10.

$$R_{LOSS,pu} = \frac{1}{\sigma d_W \delta_s} \tag{3.10}$$

Here, d_W is the width of the PCB trace.

Given the application size constraints, how should the antenna be optimized? To answer this question, recall the application use-case. The antenna is shared between the radio transmitter and the wireless energy receiver. Since reception of wireless energy only needs to occur once at system start-up, its efficiency is essentially irrelevant. To the extent that the wireless energy reception circuit works (i.e. the system can be initialized by an external wireless energy source), it is of little consequence the energy demands of the external source. As a result, it makes sense to optimize the antenna for maximum transmitter radiation efficiency, given the power-oscillator architecture and application size requirements.

Table 3.2 shows the calculated radiation efficiency, quality factor, and inductance of a representative 3×4 mm^2 antenna in free-space, using 8 mil, 2-oz copper traces at various Industrial, Scientific, and Medical (ISM) band frequencies. Also shown in Table 3.2 are simulated results from the the same antenna on a 1.6 mm-thick FR-4 PCB substrate with a finite ground plane in air. For completeness, the same antenna is additionally simulated in a realistic implanted environment using both FR-4 and Rogers substrates, while coated with 0.1 mm of bio-compatible parylene and being surrounded on the underside by bone and brain, and on the top side by 3 mm of fat tissue and 2 mm of skin. Antenna electromagnetic simulations were performed in Mentor Graphics IE3D, a fully 3D method-of-moments simulator. A picture of the biological tissue simulation setup is shown in Figure 3-15.

The calculated and simulated results in air are in good agreement at 400 MHz. At higher frequencies, losses associated with the FR-4 substrate increase the effective R_{LOSS}, thereby decreasing Q and the radiation efficiency compared to ideal calculated results. At 5.8 GHz, the loop antenna has crossed its self-resonant point and no longer looks inductive.

Although the medical implant communication service (MICS) specification in the 400 MHz ISM band is specifically designated for medical implant communications, the radiation efficiencies are simply too low to be useful for implants with limited antenna sizes. To put this in perspective, a transmitter consuming 1 mW of power

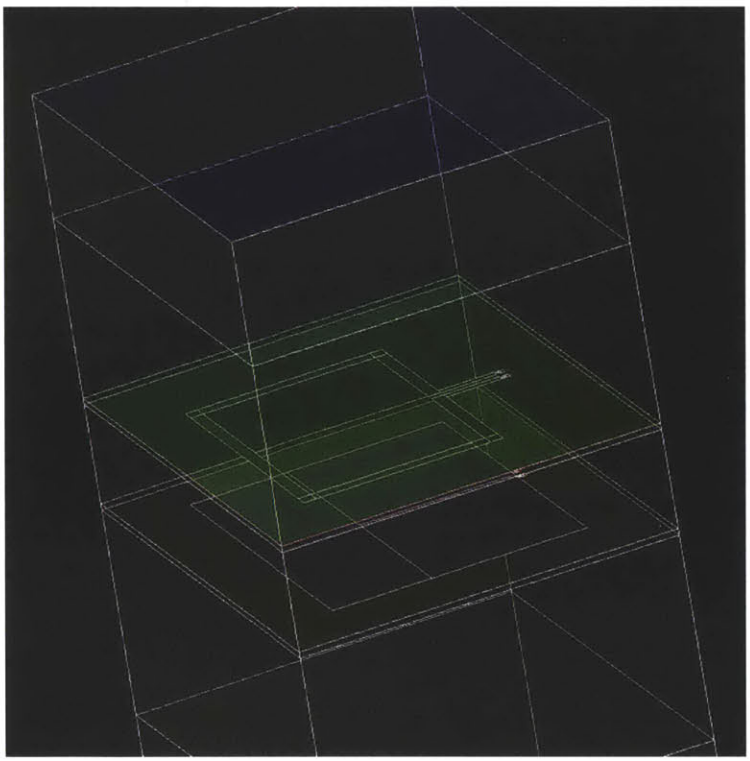

Figure 3-15: Electromagnetic simulation setup in IE3D. The various rectangular layers represent different substrates or tissues.

Table 3.2: Calculated and simulated 3×4 mm^2 loop antenna in free space and biological tissue environments at various ISM band frequencies.

	400 MHz			900 MHz		
	η_{rad}	Q	L [nH]	η_{rad}	Q	L [nH]
Calculated (air)	0.004%	77	9.5	0.08%	115	9.5
Simulated (air/FR-4)	0.003%	91	10.5	0.04%	124	10.6
Simulated (bio/FR-4)	0.00004%	75	10.3	0.006%	90	10.6
Simulated (bio/Rogers)	0.00004%	76	10.3	0.006%	98	10.5
	2.4 GHz			5.8 GHz		
	η_{rad}	Q	L [nH]	η_{rad}	Q	L [nH]
Calculated (air)	2.4%	184	9.5	32%		
Simulated (air/FR-4)	0.8%	105	12.6	6%	No longer	
Simulated (bio/RF-4)	0.05%	33	14.6	2%	inductive	
Simulated (bio/Rogers)	0.05%	46	13.6	2%		

could, at its theoretically optimal point, only radiate -44 dBm in air or -64 dBm in an implanted environment at 400 MHz. In contrast, the same antenna operating at 2.4 GHz would ideally radiate -21 dBm in air or -33 dBm in an implanted environment. Since non-power-constrained receivers can realistically achieve sensitivities down to -100 dBm, and 1 m path loss can vary from 40–60 dB [38, 39], it makes more sense to communicate at a higher frequency and reduce the circuit (and therefore radiated) power proportionally when constrained by extreme implant power requirements.

Operating at an even higher frequency, for example at 5.8 GHz, may be beneficial for many applications with small implanted antennas. However, there are several pitfalls when choosing such an approach under such extreme power budgets. Because the antenna no longer looks inductive (in fact, it looks capacitive), inductor-based tuning would be required. Due to implanted area constraints, a low-Q on-chip inductor would be required. Additionally, because the radiation and loss resistances of the

antenna are higher, such an approach precludes the design of a single-stage power oscillator architecture. Since the presented load to an oscillator would be substantial, a more traditional oscillator-buffer-PA architecture would instead be required. It would ultimately be exceedingly difficult to power-gate the additional blocks down to acceptable standby power limits, considering the additional fact that they must also operate at a much higher frequency that pushes the limits of 0.18 μm technology. As a result of these considerations, a frequency of 2.4 GHz was chosen to comply with the simplified architecture philosophy and extreme power gating possibilities. Additionally, this provides an opportunity to communicate in the uncrowded Medical Body Area Network (MBAN) band at 2360-2395 MHz recently allocated by the Federal Communications Commission (FCC) and supported by the recently-passed IEEE 802.15.6 standard [145].

In terms of sizing optimization, the antenna has restrictions not only from anatomy, but also from a resonant frequency perspective. Equation 3.7 suggests that the radiation resistance will increase with the square of the area of the antenna, while the loss resistance only increases linearly with area. It would then of course be beneficial to size the antenna as large as possible given the anatomical constraints for maximum radiation efficiency. However, increasing the antenna size also increases its inductance according to Equation 3.5. When performing any optimization, it is important to keep in mind that the antenna must interface with the on-chip transmitter. The interface between the antenna and chip will involve bondwires and bondpads; additionally, the on-chip interface will involve electrostatic discharge (ESD) protection diodes and functional transistors. All of these interface elements have parasitic capacitances that are essentially fixed during antenna optimization. As a result, the maximum resonant frequency,

$$f_{c,max} = \frac{1}{2\pi\sqrt{L_{ANT}C_{parasitic}}}, \tag{3.11}$$

decreases with increasing antenna size. Figure 3-16 presents electromagnetic simulation of a rectangular antenna where the antenna height is swept from 2 mm to 7 mm, for a fixed width of 3 mm at 2.45 GHz in air with an FR-4 substrate. The

maximum center frequency was calculated based on the simulated inductance, and an estimated parasitic capacitance of 300 fF. This parasitic capacitance assumption was initially calculated from extracted layout simulations; it was later corroborated with measurement results.

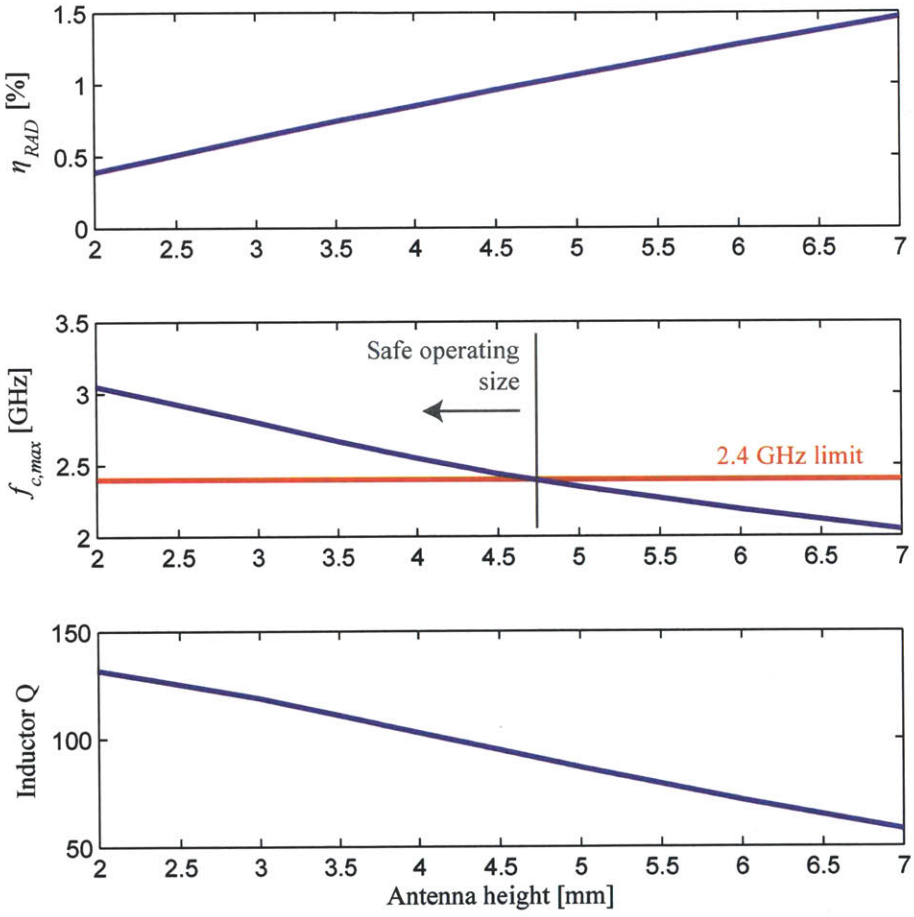

Figure 3-16: Electromagnetic simulation results for varying the antenna height for a fixed, 3 mm antenna width.

As predicted, radiation efficiency does indeed increase with antenna size. However, the maximum parasitic-limited resonant frequency decreases; 2.4GHz resonance is not achievable beyond an antenna height of 4.5 mm. This places a functional upper bound on the antenna size given the requirement to radiate in the 2.4 GHz ISM band. Note

that since Q also decreases with antenna size, lower active power operation can be achievable for reduced antennas sizes. To a first order this makes sense, since although L_{ANT} increases super-linearly with antenna area, radiation resistance increases with the square of area. However, this will limit achievable radiated output power; careful consideration of the system link budget is needed to justify smaller antennas.

Based on the preceding analysis, an antenna size of 3×4 mm^2 is chosen for this design in order to maximize radiation efficiency given both the anatomical and resonant frequency size constraints. For completeness, Figure 3-17 shows the simulated 3D radiation pattern of the designed antenna.

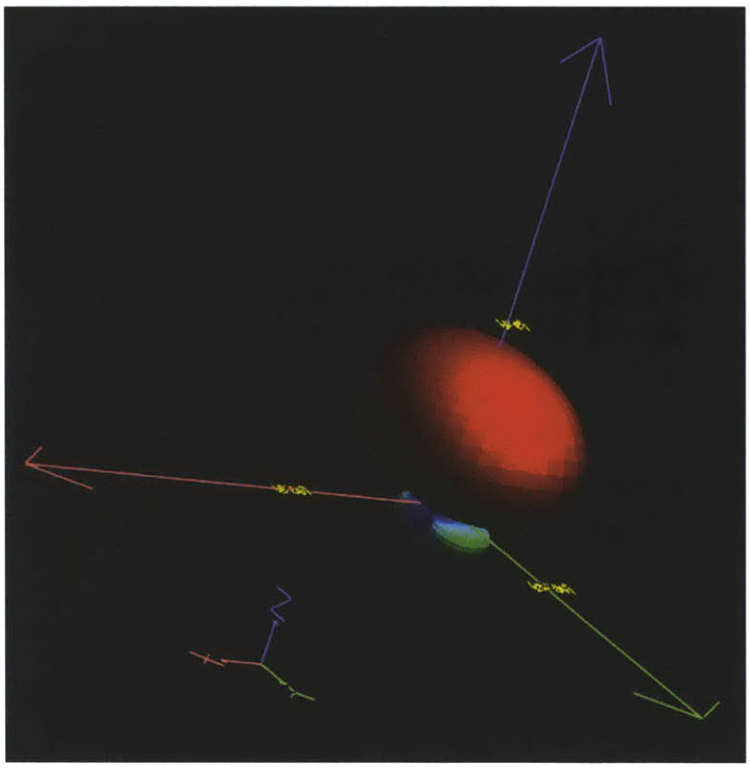

Figure 3-17: Radiation pattern of the 3×4 mm^2 loop antenna embedded in biological tissue.

Finally, Figure 3-18 shows the simulated gain when delivering wireless power to the implant from an external 10 mm diameter loop antenna spaced 13 mm away from the implant. Under a simultaneous conjugate match [146], the simulated maximum gains in air and in tissue are -13 dB at 1.7 GHz, and -15.5 dB at 1.45 GHz, respectively. At 2.4 GHz, the gain falls to -16 dB and -17.5 dB in air and tissue, respectively.

This simulation result shows that it is possible to achieve reasonable wireless power transfer results at the antenna's resonant frequency of 2.4 GHz. Since the efficiency of this power transfer is not critically important, no further optimization is performed.

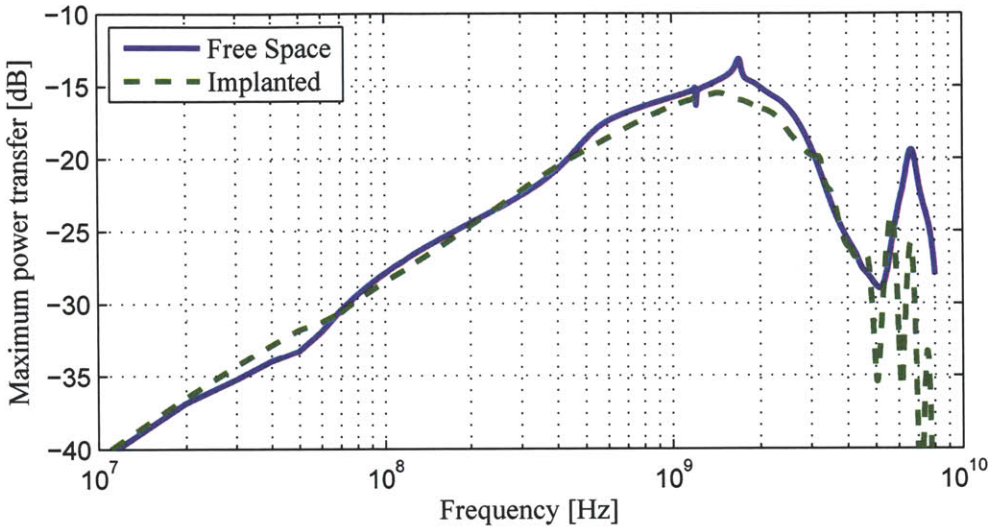

Figure 3-18: Electromagnetic simulation results for wireless power transfer to the implant for initial programming under a simultaneous conjugate matching condition.

3.4.5 Transmitter and Wireless Energy Receiver Circuit Design

The transmitter architecture was already shown at a high level in Figure 3-14. A more detailed circuit schematic is shown in Figure 3-19. The following subsections describe the individual transmitter blocks.

Power Oscillator

The core of the transmitter is the power-oscillator, comprising the cross-coupled pair of transistors (M1 and M2), a capacitive tuning digital-to-analog converter (DAC), and the aforementioned loop antenna. As shown in Figure 3-19, the loop antenna can be modeled as an inductor, though the parasitic series resistance is not shown for simplicity. The loop antenna has a center-tap, which is connected to the system

power supply in order to properly bias the power oscillator transistors. Since the loop antenna is already centered over a DC-biased metallic patch, adding a symmetrically-centered tap does not affect the antenna characteristics, and the patch can easily be biased at V_{DD} instead of ground.

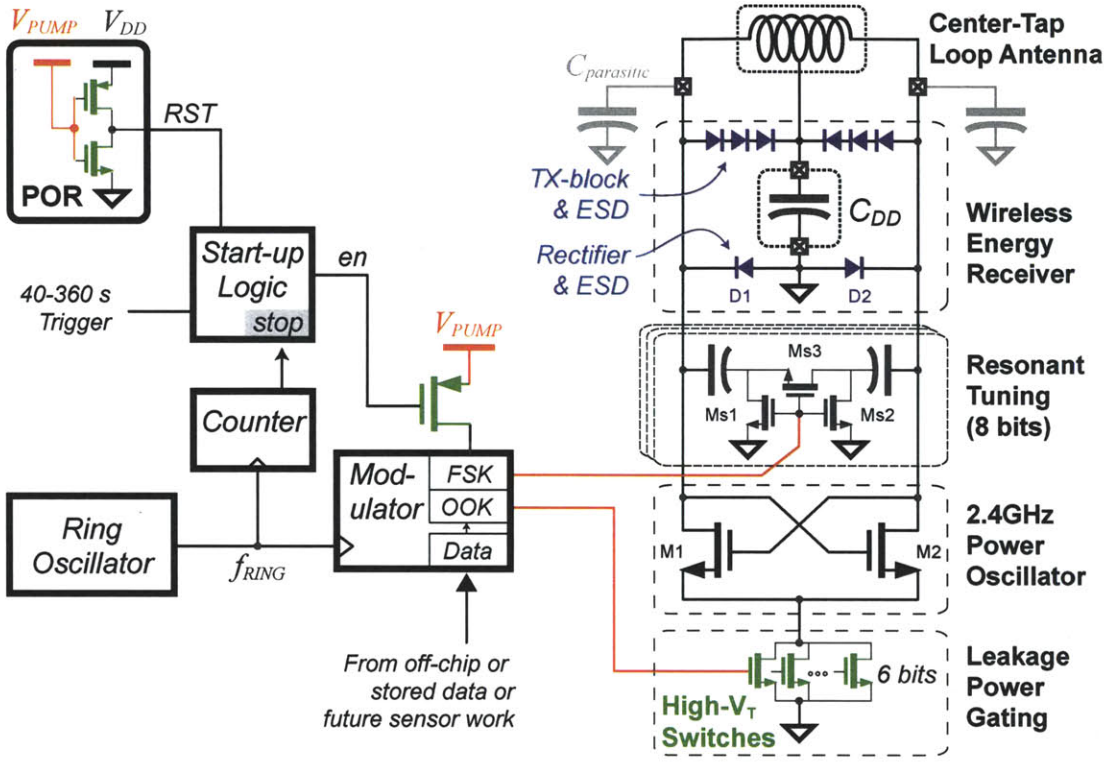

Figure 3-19: Detailed circuit schematic of the 2.4 GHz radio transmitter with integrated wireless energy receiver. High-V_t switches are shown in green, and signals operating from the charge pump supply are shown in red.

Since the transmitter draws fairly significant amounts of power, it is not suited to operate off of the on-chip decoupled charge pump supply, V_{PUMP}. As a result, the cross-coupled devices are implemented using low-V_t devices in order to reduce parasitic drain capacitance compared to high-V_t devices sized for equivalent on-conduction. The use of low-V_t devices decreases parasitic capacitance from 2.8 pF to 280 fF, which is a factor of 10X. The reduced capacitance permits a significantly larger antenna as discussed in Section 3.4.4. As a result, the antenna radiation efficiency is much larger than if high-V_t devices were instead used. During OOK modulation, the capacitance

at the source terminals of the cross-coupled NMOS pair only switch at the data rate frequency and not at RF. Consequently, the power oscillator can be biased using high-V_t NMOS transistors without any recourse to operational speed. This permits standby-mode leakage currents that are 33X lower for equivalent on-conduction. To further reduce active energy consumed per transmitted bit, the high-V_t NMOS devices are enabled by full-swing signals operating at V_{PUMP}, which decreases the associated parasitic capacitance (and therefore active switching energy) by 28X. The biasing circuit specifically consists of six binary weighted devices in order to control the amount of on-current for output amplitude swing control, or dynamic pulse shaping in a future implementation. To be clear, the biasing transistor gates are not driven by an intermediate voltage as set by a current reference, but rather they are driven by full-swing digital signals at V_{PUMP} in order to maximize I_{on} to I_{off} ratios.

Resonant tuning is implemented primarily using a 5-bit binary-weighted metal-insulator-metal (MIM) capacitive DAC, totaling approximately 300 fF. A separate 3-bit sub-ranging DAC using custom-designed metal-oxide-metal (MOM) capacitors is used to provide fine frequency control, with 0.25 fF switchable at the least significant bit (LSB) [147]. The sub-DAC is specifically used to achieve minimal bandwidth FSK modulation. For example, minimum-shift keying (MSK), which requires the theoretically smallest amount of FSK bandwidth for a given data rate, requires approximately 0.5 fF of switchable capacitance at 2.4 GHz when communicating at an instantaneous data rate of 5 Mbps. The tuning range of the resonant circuit, simulated in Cadence using extracted antenna s-parameters from IE3D and extracted circuit models from layout, is shown in Figure 3-20(a). The DAC is dynamically activated using differential switches, which according to the simulation result shown in Figure 3-21, reduces the parasitic switch capacitance by 2X for a capacitor quality factor of approximately 50.[21] Note that the parasitic capacitance here is essentially seen at the power oscillator output, as the series combination of the MIM or MOM capacitors with the non-activated transistors will ultimately be dominated by the parasitic switch capacitance. The differential switches are sized to maintain or exceed

[21] A differential design uses transistor Ms3 in addition to transistor Ms1 as shown in Figure 3-19.

an overall tank quality factor of 50. At small capacitance levels, switch on-resistance becomes negligible next to the capacitive reactance and therefore Q becomes large, as shown in Figure 3-20(b).

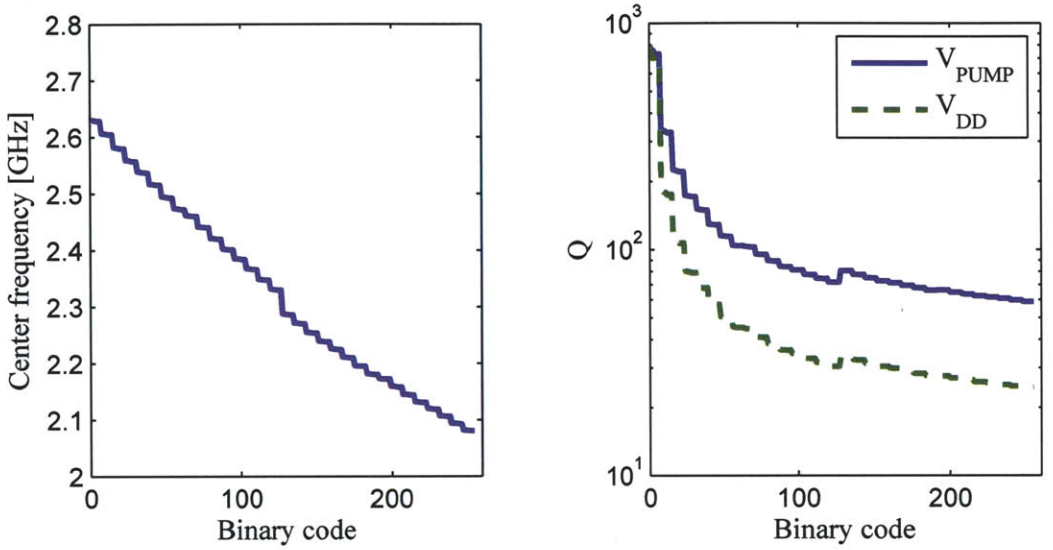

(a) Tuning range of the DAC

(b) Quality factor of the DAC using V_{DD} and V_{PUMP} activation signals across the tuning range.

Figure 3-20: Simulated results of the resonant tuning capacitive DAC together with the fixed inductive loop antenna.

Ring Oscillator, Modulator, and Control

For this initial prototype, transmitted data either comes from off-chip (for example, from a digital sensor interface), or consists of a string of alternating '1's and '0's. The modulating frequency that clocks in this data (or goes directly through the modulator in the latter case) is generated by an on-chip ring oscillator, shown in Figure 3-22. The oscillator is a five-stage current-starved inverter-based design. To minimize active CV^2 switching power, the inverter devices use low-V_t transistors. However, overall current is dictated by 6-bits of NMOS and PMOS degeneration devices, separated into two groups of control: *coarse* and *fine*. Since generating an on-chip current reference would consume excessive static power, current starving devices are instead sized to operate as resistive elements (i.e. in the triode regime) when driven by full-

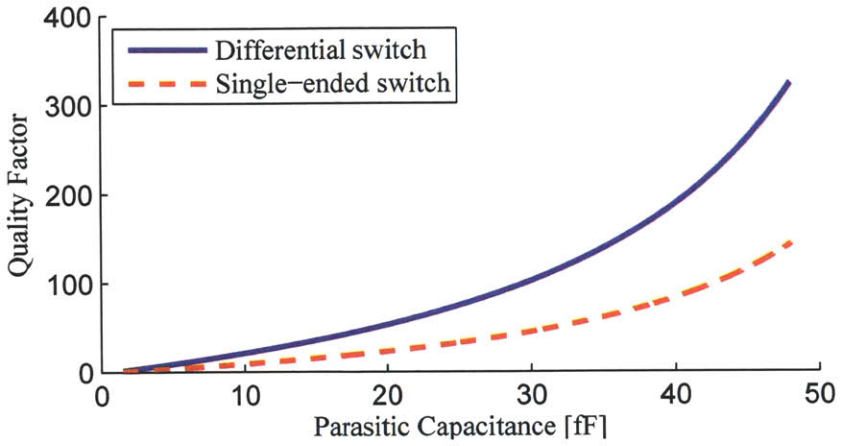

Figure 3-21: Simulated capacitor quality factor versus parasitic switch capacitance for single-ended and differential switches.

swing input signals (i.e. at V_{DD}). The NMOS $fine[0]$ control signal for example uses a stack of two high-V_t transistor that each have a W/L of 0.22/7 μm. For manufacturing and operational reliability, the ring oscillator is designed to operate from 100 kHz to 10 MHz across process corners and V_{DD} variation. To achieve the high-end frequencies in slow process corners, low-V_t devices are used for the $coarse[2]$ control signal. To achieve low-end frequencies at fast process corners, two-bits of capacitive tuning are included in each inverter delay element. To minimize active CV^2 energy consumption, these extra capacitors should not be activated unless it is necessary to achieve the desired operational frequency. During standby mode, the oscillator is put into a low-leakage state by gating the output and gating all current starving elements.

The data modulator consists of digital logic that is hand-designed using a mix of custom high-V_t and low-V_t-based standard cells. It accepts a digital clock from the ring oscillator and can accept stored data or externally driven serial data. To decrease the standby current of the power oscillator biasing devices for a given on-current, the modulator output signals are driven from the V_{PUMP} supply (a similar effect is arranged for the capacitive DAC to increase their quality factors). Level-conversion to the higher voltage is achieved using a standard cross-coupled level shifter circuit [148]. Since the output is single-ended, a dummy driver load is installed for edge transition

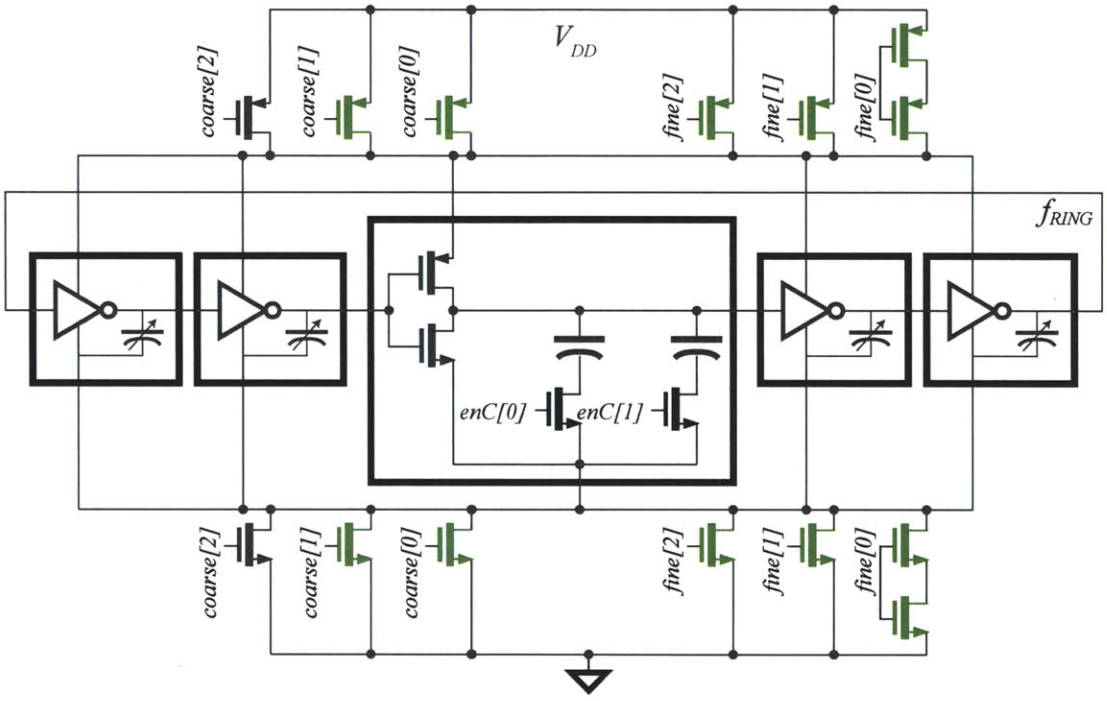

Figure 3-22: Current-starved ring oscillator schematic. High-V_t devices are shown in green.

matching purposes. The entire modulator is power gated by PMOS devices, saving upwards of 4,000X in leakage power from the V_{DD} supply and 20X from the V_{PUMP} supply.

The output of the ring oscillator also clocks a counter and comparator that are used to set the number of bits transmitted in a single packet. The counter, whose schematic is shown in Figure 3-23, uses a ripple-carry frequency divider for the first two registers. The final two counter stages use a synchronous design that is pre-scaled to reduce the critical path, enabling sufficiently fast operation at low voltages using low-leakage devices [149, 150]. Although the counter itself is a 7-bit design, only the final 5-bits are applied to the comparator, as the utility of transmitting 1–4-bit packets is limited. Furthermore, rather than designing a full 5-bit adder to count to arbitrary 5-bit packet lengths, a simple 5-bit power-of-two comparator is used, enabling counting intervals ranging between 8 and 128 in powers of two only. This substantially reduces the gate count, resulting in a low-complexity, low-leakage design. The counter is power gated by a single PMOS device, nominally saving 18X in standby power. Since the circuit operates using the V_{DD} supply, it is possible to gate the PMOS device with the V_{PUMP} supply, forcing the transistor into super cut-off, and saving an additional 2.6X in leakage, or 48X in total.

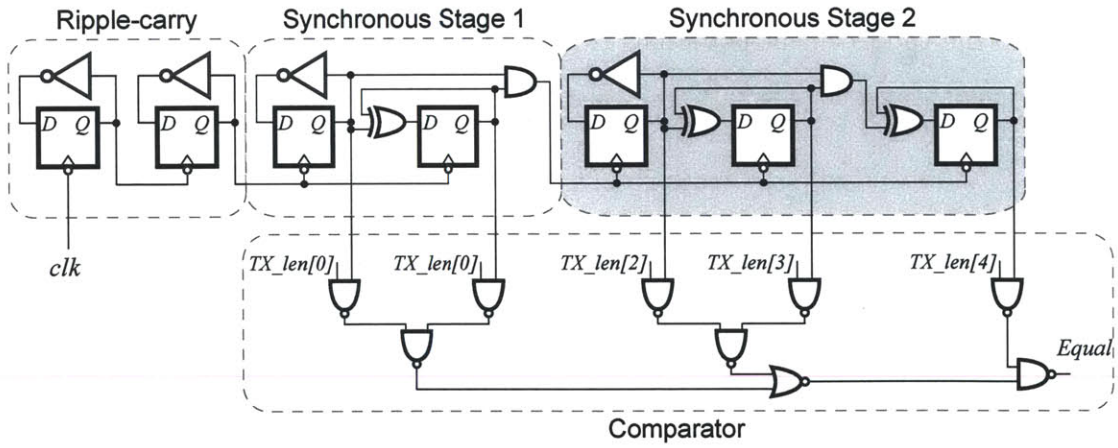

Figure 3-23: Circuit schematic of the 7-bit (5-bit output) counter, with the 5-bit comparator used to set the transmitted packet length.

The transmitter is activated every 40–360 seconds by the output of the boost converter's divided timing signal. A start-up logic block is designed to receive this signal, disable the appropriate power gating devices, and initialize the ring oscillator and modulator. Since the start-up block itself cannot be power gated, it is designed using almost exclusively high-V_t devices for minimal leakage power consumption.

Wireless Sensor

Although the transmitter only accepts external digital data for wireless transmission, given the described architecture, the endoelectronics chip in fact contains a built-in sensor whose information is inherently communicated! Recall the energy buffering behavior: maximum energy is extracted from the endocochlear potential, given the electrode impedance constraints. If V_{EP} goes up, then more energy will come into the system, thereby increasing V_{DD} (and vice-versa for a lower V_{EP}). Additionally, note that the ring oscillator's power supply is not regulated - it is in fact directly connected to V_{DD}, as re-iterated in Figure 3-24. It is well known that a ring oscillator frequency varies with its supply voltage, as shown in Figure 3-25. Thus, the following relation holds:

$$\text{Data rate} = f_{RING} \propto V_{DD} \propto V_{in} \approx \frac{V_{EP}}{2}. \tag{3.12}$$

This relationship indicates that the instantaneous transmitter data rate is proportional to the endocochlear potential. A wireless receiver can easily keep track of this varying instantaneous data rate and use it to infer relative changes in the endocochlear potential.

Wireless Energy Receiver and Power-on Reset

The wireless energy receiver circuit design is already included in Figure 3-19. In fact, since the antenna can be modeled as an inductor that has a center tap, creating a full bridge rectifier is as simple as placing two diodes between the two ends of the inductor, connected to ground (diodes D1 and D2 in Figure 3-19). Diodes D1 and D2 alternate conduction modes, depending on the phase of the incoming waveform.

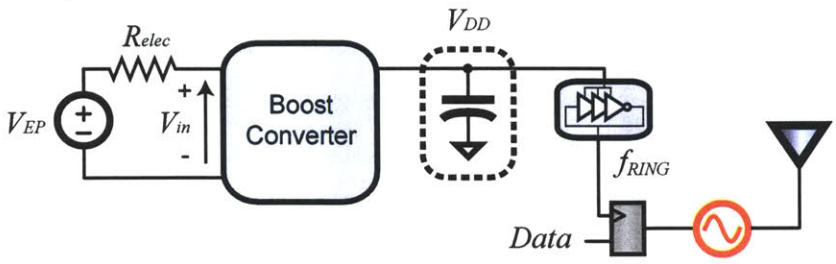

Figure 3-24: Schematic diagram illustrating the relationship between the endocochlear potential and the instantaneous output data rate. This relationship can be exploited to create a built-in wireless endocochlear potential sensor.

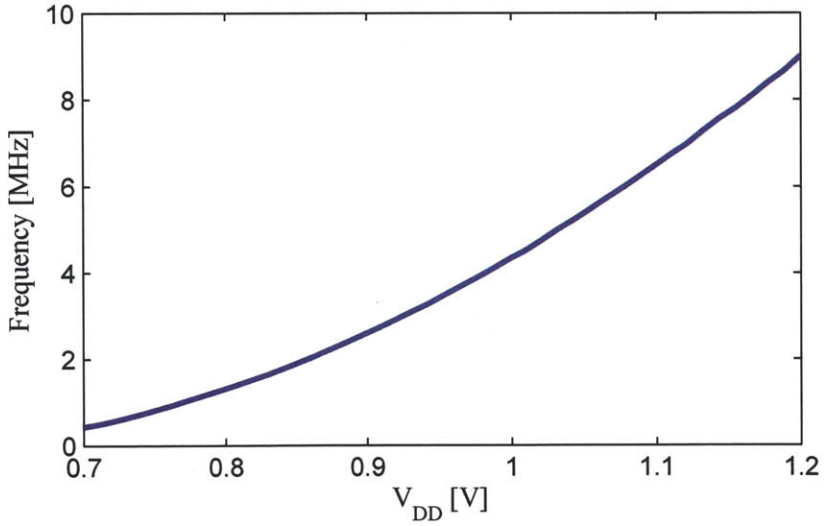

Figure 3-25: Measured relationship between the ring oscillator power supply and its characteristic frequency.

Of critical importance here is that these diodes are in fact already required for ESD protection. Thus, adding wireless power transfer functionality does not add any additional complexity and, more importantly, does not add any additional parasitic capacitance on the sensitive antenna interface nodes. As described in Section 3.4.4, reduced parasitics on these nodes permit the design of a larger, more efficient antenna given a resonant frequency requirement of 2.4 GHz. Naturally, diodes D1 and D2 only protect the ground supply; additional diodes are required to protect the positive (i.e. V_{DD}) supply. However, since the antenna is center-tapped and biased at V_{DD}, the power oscillator output RF signals naturally swing symmetrically above and below V_{DD}. If only a single set of diodes were placed to protect V_{DD}, these RF voltage swings would be limited to a single diode drop. The simple solution here is to instead stack three diodes in series, as shown in Figure 3-19.

Following wireless energy delivery to the endoelectronics chip for the purposes of initializing V_{DD}, it is of critical importance to ensure the chip is reset to a known-good state. If, for example, the power oscillator gating switches were somehow enabled after the external wireless energy source was removed, the on-current would be large enough to catastrophically collapse the V_{DD} supply. To avoid such an event, a reliable power-on-reset (POR) is required. Fortunately, creating a POR signal can be achieved in a very low-complexity, low-leakage manner. Since the charge pump supply, V_{PUMP}, requires 600 ms seconds to initialize following V_{DD} initialization[22], a simple inverter structure can be used to generate the requisite POR signal, as shown in Figure 3-19. Specifically, an inverter with V_{PUMP} as the input powered from the V_{DD} supply will nominally output a logic high value until V_{PUMP} crosses the inverter threshold. The inverter is designed with high-V_t transistors, since there is no opportunity to power-gate the initialization logic. The leakage impact of this inverter is negligible, however, since after the reset signal has been deactivated, the leakage of the inverter is set by the PMOS device which in this case is biased in super cut-off due to the presence of V_{PUMP} as its input.

[22]The charge pump circuit is self-governing and does not require a reset signal.

Summary

With careful design, a low-complexity architecture, and extensive use of leakage-mitigation techniques employing high-V_t transistors, the simulated power consumption of the transmitter meets and even exceeds the requirements set out in Section 3.5.1 across V_{DD} and process corner variation. Note that temperature effects are not considered here, due to the natural temperature regulation of the human body and the fact that the endoelectronics chip consumes such little power that self-heating effects are entirely negligible. Table 3.3 outlines a representative sample of the simulated results, obtained in Cadence/Spectre using extracted layouts and very high Spectre error tolerances. Interestingly, the dominant power consumers are the ring oscillator and charge-pump power supplies. The single NMOS/PMOS pair of low-V_t current-starving transistors are primarily responsible for the high leakage current in the ring oscillator, while a non-power-gated level shifter in the start-up block is primarily responsible for the high leakage power on the digital supply. The latter device is essential for system start-up, though the former pair of transistors may not be necessary in future implementations if process variability can be tightly controlled.[23]

Table 3.3: Simulated transmitter power breakdown across process corners and voltage variation.

		Standby power consumption [pW]				
V_{DD} [V]	Corner	PO	Ring Osc.	Digital	V_{PUMP}	**Total**
0.8	TT	0.6	7.8	1.0	9.1	**18.7**
0.8	SS	0.4	1.6	0.4	3.0	**5.6**
0.8	FF	1.3	27.2	3.3	29.4	**61.4**
0.9	FF	1.6	31.5	3.8	33.0	**70.2**
1.0	FF	2.0	36.0	4.4	38.0	**80.8**

[23]The low-V_t transistors were designed to ensure operation up to 10 MHz at slow corners. In a future revision, this could instead be achieved using a much larger sized, though much lower leakage high-V_t device.

3.5 Measurement Results

The boost converter, radio transmitter, and wireless energy receiver circuit were integrated together on a single chip and fabricated in a 0.18 μm process. The chip occupies a total area of 2.4 $\times$ 2.4 mm^2; a die photo is shown in Figure 3-26. Since the chip must self-configure upon system start-up, and there is no room in the power budget to add non-volatile memory for wake-up programming, all digital configuration bits are routed to unique bond-pads. For implantable systems, programming is performed during packaging, where digital bits are either directly wire-bonded to V_{DD} or ground planes. As a result of this design decision, the chip is extremely pad-limited. For example, out of the 108 total pads on the chip, 81 are digital configuration bits. The core area of the design occupies 1.2 mm^2, and represents a lower bound on the size of the chip in future iterations.

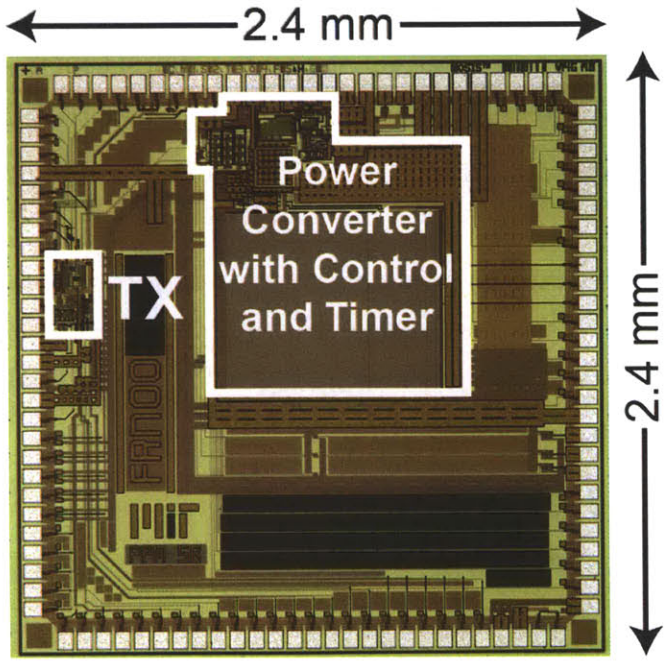

Figure 3-26: Microphotograph of the endoelectronics chip. The core area occupies 1.2 mm^2.

To minimize packaging parasitics (specifically with the radio transmitter performance in mind), the chip is directly wire-bonded to a PCB using chip-on-board packaging technology. Exposed copper pads on the PCB are finished with 80 mi-

croinches of soft gold over 250 microinches of nickel for wirebonding compatibility. Wirebonding was performed by VLSIP Technologies Inc, Richardson, TX, and the chip was subsequently encapsulated with non-conductive epoxy for mechanical and environmental stability. Two separate boards were prepared: one for prototyping and initial testing, and another miniaturized for implantation and clinical testing; both used FR-4 substrates. The prototyping and testing board, shown in Figure 3-27, was manufactured by Advanced Circuits, Aurora, CO, and was designed to allow external digital control of every programmable bit on the chip. Specifically, the board was designed as a daughter card, which interfaces to a mainboard housing an FPGA for programming and testing purposes. The miniaturized board, shown in Figure 3-28, was manufactured by DDi, Anaheim, CA. This board is currently small enough to fit within the human mastoid cavity, or in the bulla cavity of cats, gerbils, or chinchillas [130]. With further optimizations, the size of the board could be reduced by approximately 50%.

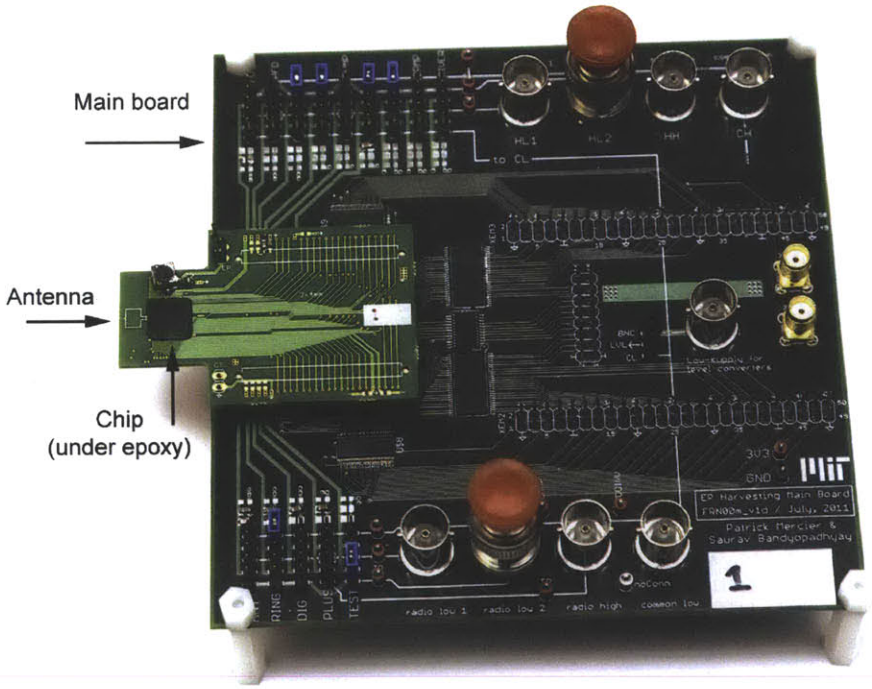

Figure 3-27: Photograph of the endoelectronics testing and prototyping platform, showing the daughter card containing the chip and the main board hosting the FPGA interface.

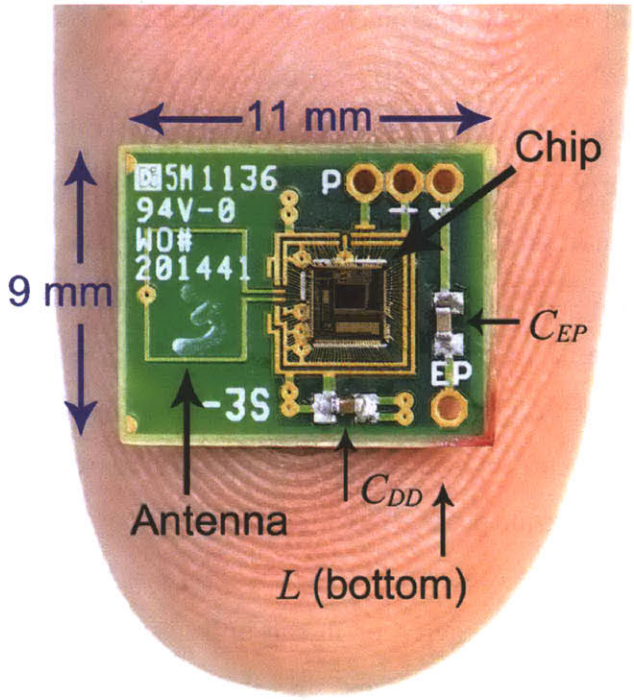

Figure 3-28: Photograph of the miniaturized endoelectronics chip-on-board on a human index finger. Dam-and-fill epoxy encapsulation is not shown for clarity.

The following two subsections describe and discuss measurement results performed in a standard electronics laboratory environment, as well as in a clinical environment.

3.5.1 Laboratory Measurements

Boost Converter

Due to vary careful leakage management following the transistor sizing methodology outlined in Section 3.4.1, together with a compact, low-complexity architecture, the quiescent power consumption of the boost converter timer, control, and charge pump circuits was measured to be between 490 pW and 590 pW for supply voltages (i.e. V_{DD}) between 0.8 V and 0.9 V, respectively. Low-current measurements were performed using 2602 and 6430 sourcemeters together with low-loss tri-axial cables from Keithley Instuments, Cleveland, OH. Table 3.4 breaks down the power consumption of each block in the converter for two different operating voltages.

Table 3.4: Measured quiescent power breakdown of various blocks in the boost converter.

	Quiescent power consumption [pW]			
V_{DD} [V]	Timer	Control	Charge pump	**Total**
0.8	301	87	57	**490**
0.9	353	104	70	**590**

When operating with a Keithley Instruments 2400 source meter modeling the endocochlear potential, and a discrete resistor modeling the electrode impedance, the boost converter power train achieves 35% to 55% efficiency, as shown in Figures 3-29(a) and 3-29(b). These plots are generated by changing τ_1 in the boost converter in order to change its effective input impedance. Clearly, operation using the 47 μH inductor offers substantially better performance, in part due to its lower effective series resistance (ESR), though at the cost of 15 additional square millimeters in board area.

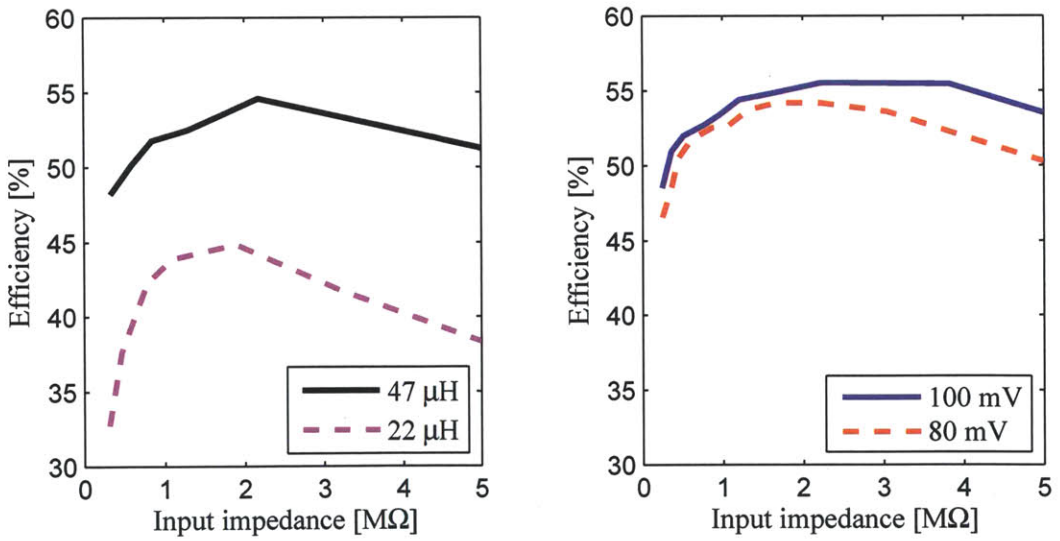

(a) Measurement conditions: R_{elec} = 0.75MΩ, V_{DD} = 0.9 V, V_{EP} = 80 mV, two different inductors.

(b) Measurement conditions: R_{elec} = 1MΩ, V_{DD} = 0.9 V, L = 47 μH, endocochlear potential variable.

Figure 3-29: Measured efficiency of the boost converter power train as the input impedance of the boost converter is swept.

The total amount of output power available to the load can be calculated as follows. First, multiply the available power from the endocochlear potential by the boost converter power train efficiency. The available input power ranges from 1.6 nW to 3.3 nW in this case study for endocochlear potentials and electrode impedances of 80 mV and 1 MΩ at the low end to 100 mV and 0.75 MΩ at the high end, respectively. This gives the total extracted power at the output of the boost converter power stage. Then, subtract the quiescent power consumption of the timer, control, and charge pump circuits to find the total power available to any attached load circuit at the given supply voltage. Such results are plotted in Figures 3-30(a) and 3-30(b).

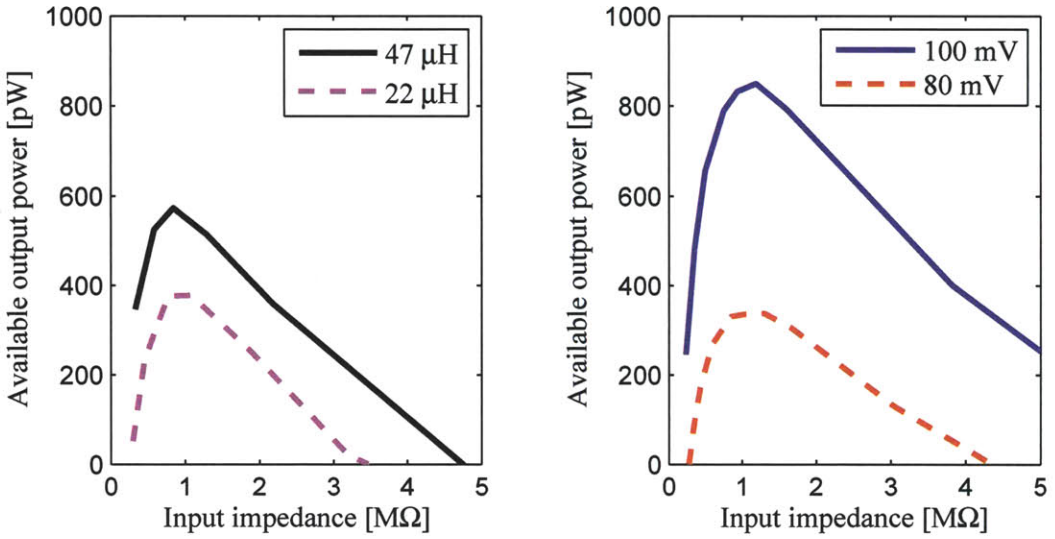

(a) Measurement conditions: R_{elec} = 0.75MΩ, V_{DD} = 0.9 V, V_{EP} = 80 mV, two different inductors.

(b) Measurement conditions: R_{elec} = 1MΩ, V_{DD} = 0.9 V, L = 47 μH, endocochlear potential variable.

Figure 3-30: Amount of output power available to any load circuit powered by the boost converter, harvesting energy from a circuit model of the endocochlear potential.

Fortunately, the available output power is positive! That is, it is possible to extract more energy from the endocochlear potential circuit model than is required to perform the extraction in the first place. This is the first boost converter demonstrated to be operational at quiescent power levels this low, and the first to show net positive energy extraction from a circuit model of the endocochlear potential. Figure 3-30 also shows that maximum power is indeed achieved at approximately the correct

input impedances. For low endocochlear potentials, and factoring in some amount of maximum power transfer matching accuracy, the minimum amount of power available to the load is 250 pW.

Radio Transmitter

Since the antenna is part of the resonant network of the power oscillator, it was not possible to directly test or probe the output power of the transmitter. Instead, wireless testing was typically performed by placing a 2.4 GHz, $\lambda/4$ whip antenna as close as possible to the on-board loop antenna while measuring the received power on an MXA N9020A spectrum analyzer from Agilent Technologies, Santa Clara, CA. The distance from the center conductor of the whip antenna to the loop antenna was measured to be approximately 5 mm. Testing the radio transmitter with this setup in a typical indoor environment revealed that the maximum wirelessly received power was -21.9 dBm when operating with $V_{DD} = 1.0$ V and the maximum current setting in the power oscillator. Figure 3-31 reveals measurements for additional supply voltages across all power oscillator tuning bits. When placing the whip antenna at a distance of 1 m from the loop antenna, the maximum wirelessly received power was measured to be approximately -60 dBm in the indoor environment. These measurements suggest that the maximum output power of the transmitter is approximately -20 dBm.

Figure 3-32 shows the consumed power of the transmitter when in active mode under the same conditions as was shown in Figure 3-31. For energy efficiency reasons, if there is room in the link budget to spare, it is beneficial to not operate the transmitter at maximum output power, but rather at some intermediate back-off point. Figure 3-33 shows the measured transmitter output efficiency, taken as the ratio of radiated output power versus total consumed transmitter power. At high bit configurations (i.e. high current consumption), the power oscillator began to approach the non-linear voltage limiting property typical of cross-coupled oscillators [40]. In other words, additional current at these configurations do not proportionally increase radiated output power. Thus, an optimal point can be found that maximizes the transmitter output power efficiency. Interestingly, the maximum output power effi-

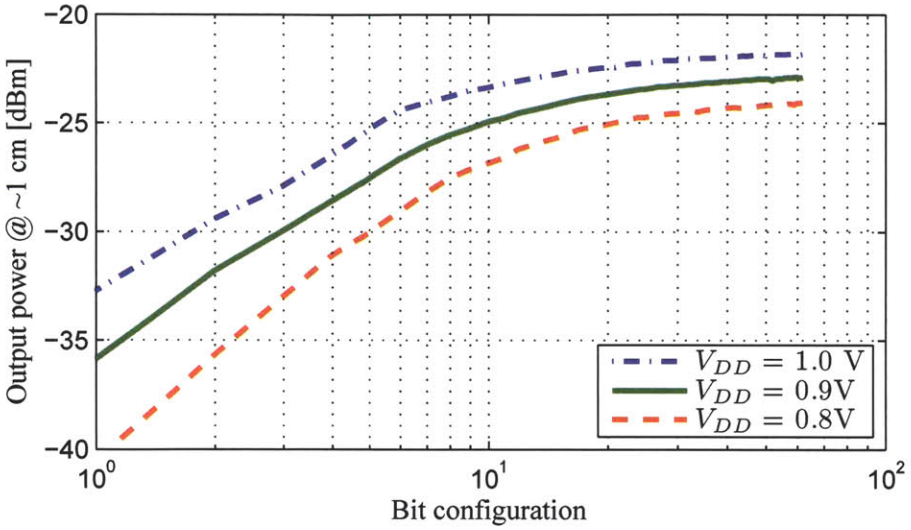

Figure 3-31: Active-mode output power of the radio transmitter measured from a 2.4 GHz $\lambda/4$ whip antenna with 2 dBi gain placed approximately 5 mm from the on-board loop antenna, plotted versus power oscillator current configuration settings. Actual radiated power is expected to be higher than these results, though it is not possible to measure this directly.

ciency, achieved near a bit configuration value of 13, is around 0.68%, depending on V_{DD}. This is close to the simulated antenna radiation efficiency of 0.8% described in Section 3.4.4. Although the actual radiated output power is difficult to precisely measure, a 0.68% transmitter efficiency indicates the transmitter is 85% efficient at actually driving the antenna.

To minimize the energy required to transmit a bit of information, it is additionally worthwhile to operate at some intermediate back-off point. For example, at $V_{DD} = 0.8$ V, a data rate of 5 Mbps, and an output power of at least -26 dBm or -29 dBm,[24] the transmitter consumes 374 μW or 191 μW for FSK and OOK modulations, respectively. This results in a energy efficiency of 75 pJ/bit or 38 pJ/bit for FSK and OOK, respectively. A power breakdown of these two operating points is shown in Table 3.5.

Clearly, the active mode power is completely dominated by the power oscillator. Since the power consumption of the ring oscillator, digital logic, and V_{PUMP}-powered

[24]Output powers were measured using a whip antenna placed 5 mm from the loop antenna. Actual radiated output power is expected to be higher than these numbers.

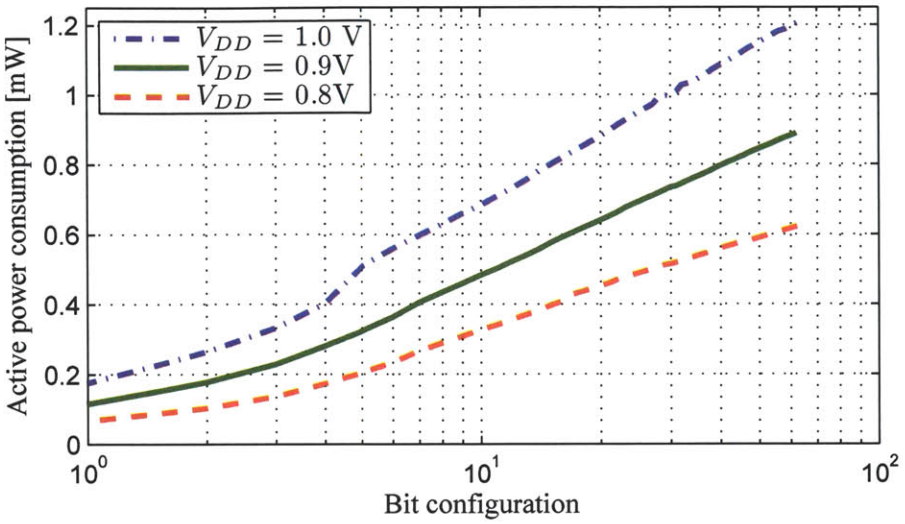

Figure 3-32: Measured active-mode power consumption of the transmitter plotted versus power oscillator current configuration settings.

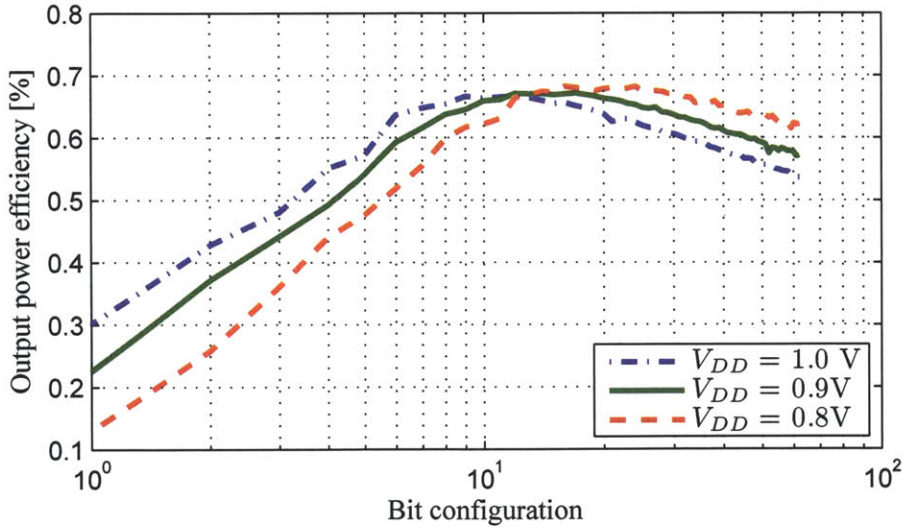

Figure 3-33: Transmitter radiated efficiency, measured as the ratio of radiated output power over total consumed power in the transmitter, plotted versus power oscillator current configuration settings. The actual transmitter efficiency is expected to be higher, due to the uncertainty in output power measurements.

Table 3.5: Measured active-mode power breakdown of various blocks in the radio transmitter operating at 0.8 V and at a frequency of 2.48 GHz.

		Active-mode power consumption [μW]				
Modulation	Output Power	PO	Ring Oscillator	Digital	V_{PUMP}	**Total**
OOK	> -29 dBm	191	0.1	0.1	0.3	**191**
FSK	> -26 dBm	374	0.1	0.2	0.2	**374**

blocks are negligible during active mode, the total active power consumption of the transmitter does not appreciably change with data rate. Thus, the most efficient operating point (i.e. the lowest energy per transmitted bit) occurs at the highest achievable data rate. For the simple modulation formats supported in this chip (i.e. OOK and FSK), operating at data rates beyond 10 Mbps can have limited utility, as the bandwidth requirements are large, and therefore the received signal is much more easily susceptible to reduced bit error rates due to interferers in overlapping or closely adjacent channels. The entire MBAN band contains only 40 MHz of total bandwidth, for example. Figures 3-34(a) and 3-34(b) show measured OOK spectral results modulated by random externally-derived bits at data rates of 1 Mbps and 10 Mbps, respectively. Achieved -3 dB bandwidths and energy per bits for 1 Mbps and 10 Mbps data rates are 620 kHz and 2 MHz, and 191 pJ/bit and 19 pJ/bit, respectively. For completeness, Figures 3-35(a) and 3-35(b) show measured spectra using FSK and near-MSK modulation, respectively. Since FSK is a constant-envelope modulation format, its total output power is typically double that of OOK. Consequently, it is a good modulation choice in limited SNR communication channels, particularly those with common-mode interference. However, the energy consumed per bit is also approximately double that of OOK, so in this work, OOK is the primary choice of modulation formats.

The transmitter is capable of starting up in 180 ns, as shown in Figure 3-36. This permits the rapid duty cycling necessary to maintain energy efficiencies down to low average data rates. A transient measurement of wirelessly-received 5 Mbps OOK data is shown in Figure 3-37. Transient measurements were performed by again placing a

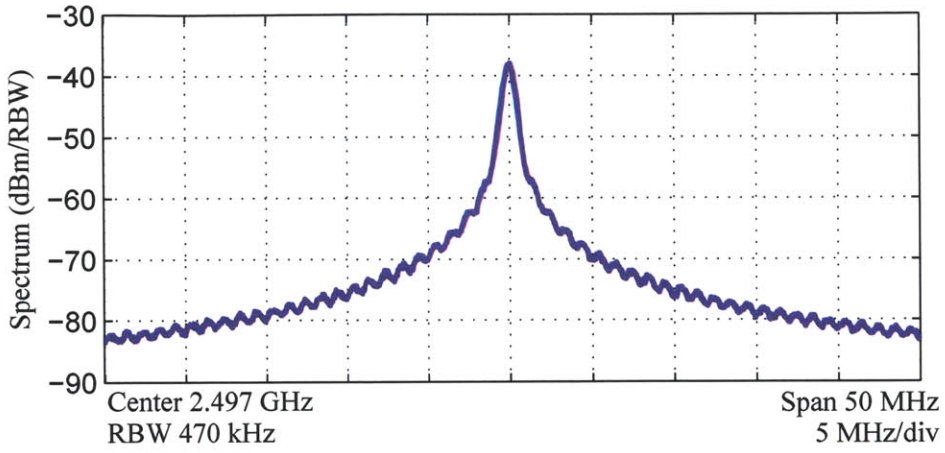

(a) Data rate = 1 Mbps.

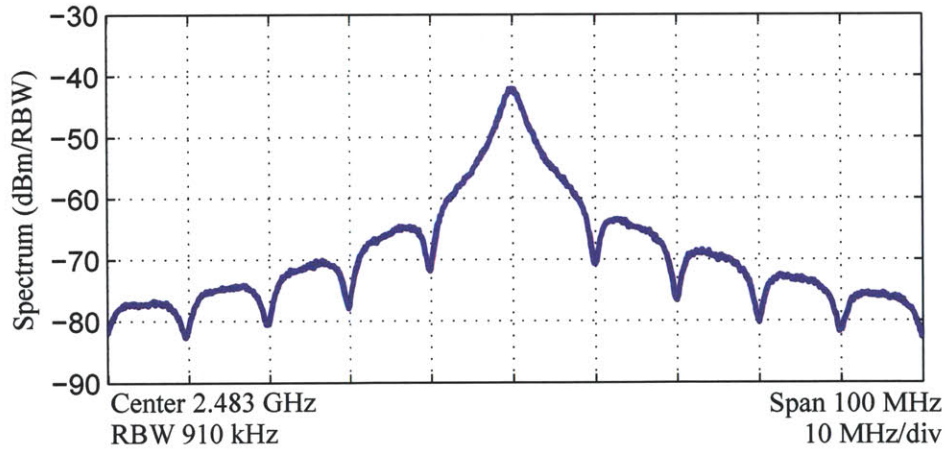

(b) Data rate = 10 Mbps.

Figure 3-34: Measured OOK spectra taken using a $\lambda/4$ whip antenna a few centimeters from the on-board loop antenna.

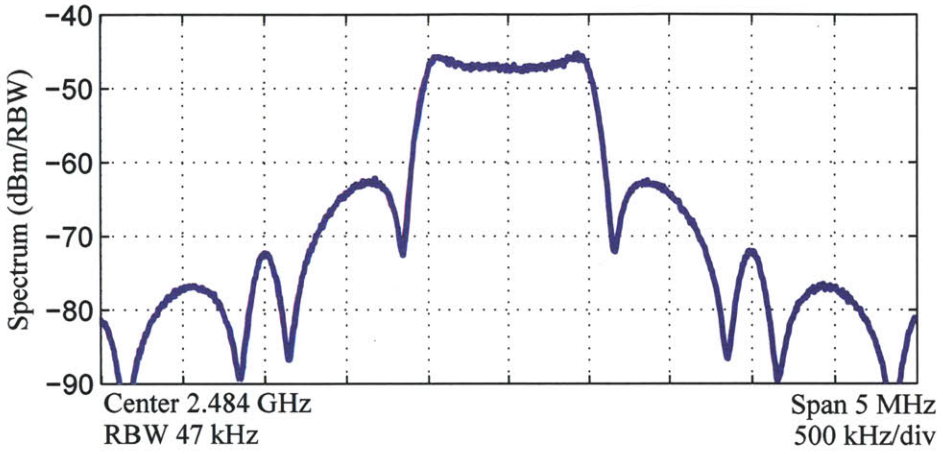

(a) FSK, data rate = 1 Mbps.

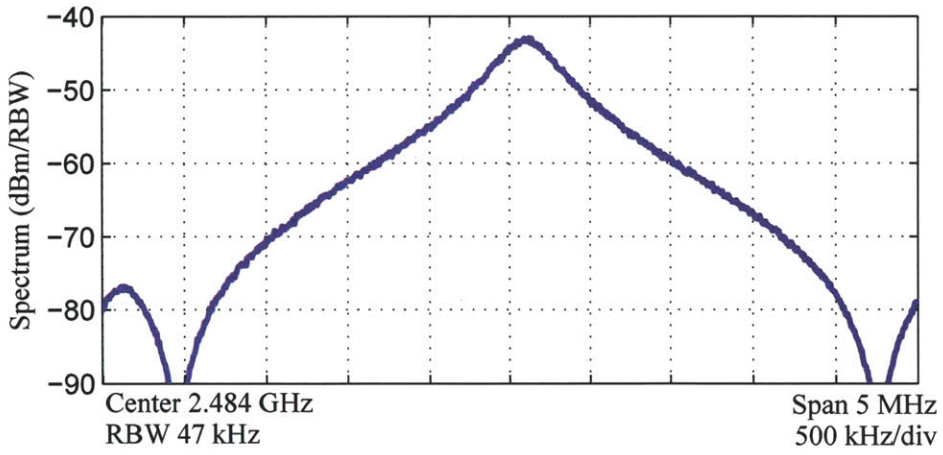

(b) Near-MSK, data rate = 2.5 Mbps.

Figure 3-35: Measured FSK spectra taken using a $\lambda/4$ whip antenna a few centimeters from the on-board loop antenna. Here, $\Delta f = 0.7$ MHz.

whip antenna close to the loop antenna. In this case, external amplification, provided by a cascade of ZX60-272LN Mini-Circuits amplifiers, was used to provide sufficient voltage swing to an Agilent DSO90254A oscilloscope that recorded the measurement.

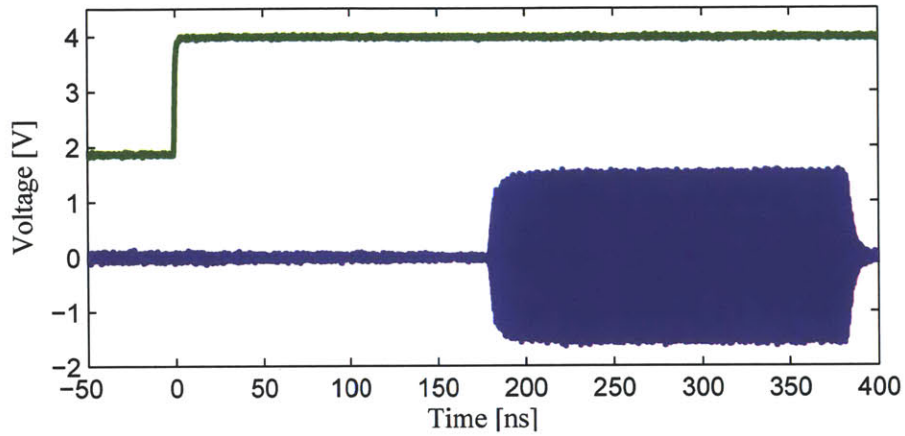

Figure 3-36: Measured wirelessly-received transient waveform, illustrating a startup time of 180 ns.

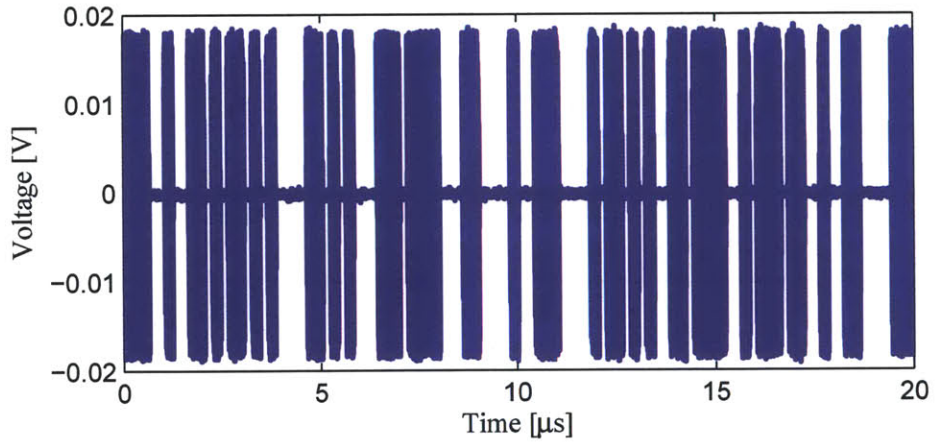

Figure 3-37: Measured wirelessly-received transient waveforms of the transmitter with randomly-modulated 5 Mbps OOK data.

The power oscillator achieves a frequency tuning range from 2.1 GHz to 2.54 GHz across the 8-bit capacitive DAC when resonating with the on-board 3×4 mm^2 inductive loop antenna. Electromagnetic simulation results together with extracted on-chip parasitics match measurement results well: the maximum simulated resonant

frequency was found to be 2.55 GHz. Figure 3-38(a) shows the measured resonant frequency with increasing tuning capacitance. Monotonicity is guaranteed, although step sizes are not equal by design. For instance, the smallest frequency step size is typically around several kilohertz, as shown in Figure 3-38(b). The two most significant bits (MSBs) of the DAC are sized proportionally larger than the remaining bits to achieve a sufficiently wide tuning range in the event the loop antenna's inductance turned out to be smaller than expected. For completeness, the power oscillator achieves a phase noise of -105 dBc/Hz at a 1 MHz offset, as shown in Figure 3-39.

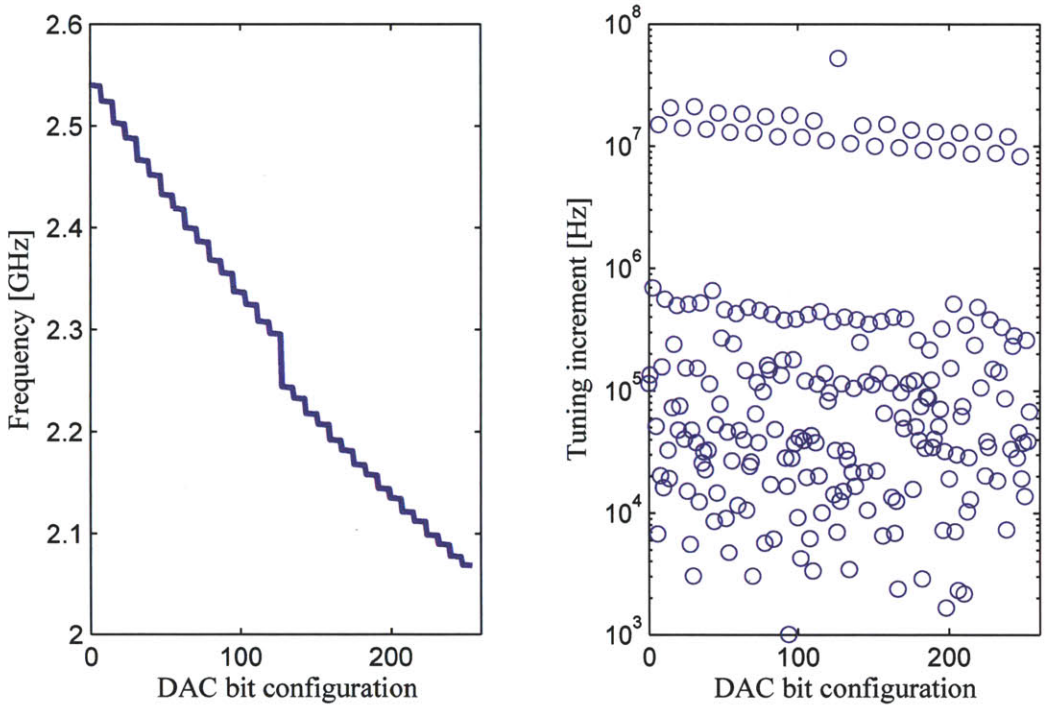

(a) Achievable transmitter frequencies.

(b) Tuning steps between capacitive DAC bit configuration settings.

Figure 3-38: Measured frequency response of the capacitive DAC tuning range.

For constant power oscillator current levels, the amount of radiated output power will change with frequency due to antenna radiation efficiency effects. Recall Equation 3.7, which shows that the antenna's radiation resistance increases with frequency to the fourth power. Since the radiation resistance is such a small portion of the total antenna resistance (i.e. radiation efficiency is small), the total consumed power will

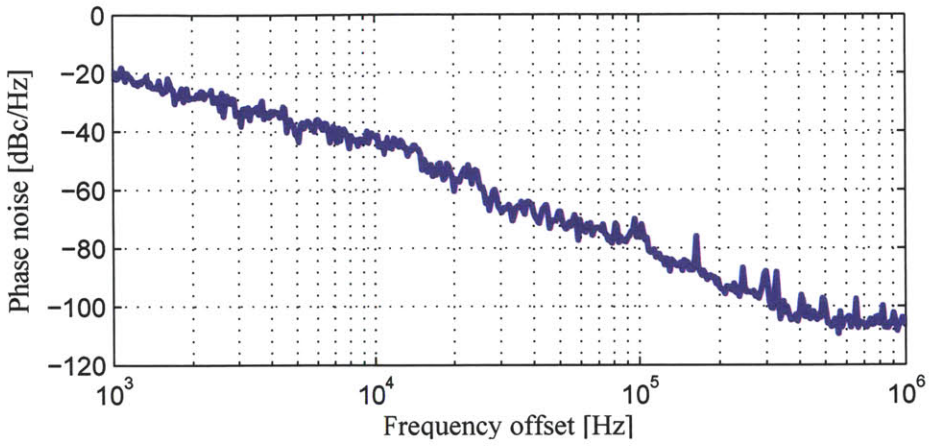

Figure 3-39: Measured phase noise of the power oscillator output. At 1 1MHz offset, the phase noise is -105 dBc/Hz.

not significantly change with frequency. However, as shown in Figure 3-40, radiated output power increases at the rate of approximately 40 dB per decade.[25] This matches predicted behavior, based on the $R_{RAD} \propto f^4$ relationship. It is thus slightly more efficient to operate near the high edge of the 2.4 GHz ISM band if the environment permits it.

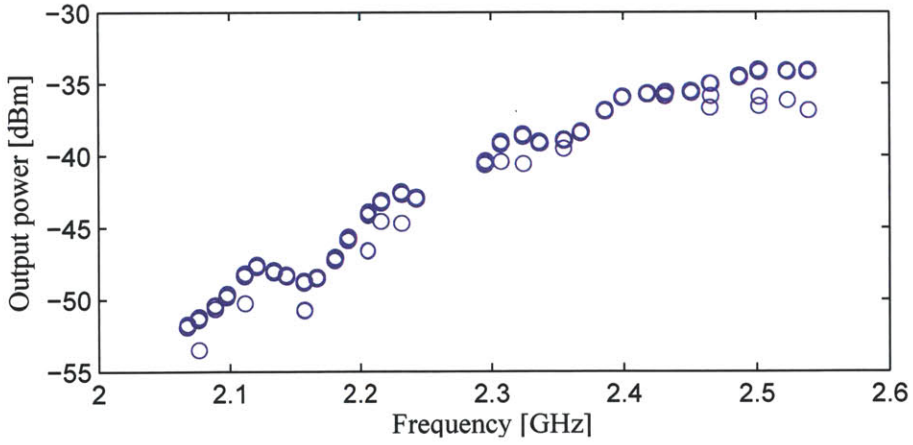

Figure 3-40: Measured radiated output power plotted versus resonant frequency as the capacitive DAC tuning bits are varied.

By tuning the current starving and capacitive loading bits, the ring oscillator was

[25]This assumption is roughly valid until approximately 2.4 GHz. Beyond this level, non-linear effects of the power oscillator prevent proportional increases in radiated output power (i.e., due to supply rail limited voltage swings).

measured to generate clock frequencies from below 100 kHz to at least 100 MHz across supply voltages ranging from 0.7 V to 1.0 V, as shown in Figure 3-41(a). At at supply voltage of 1.0 V, the lowest achievable frequency was measured to be 800 kHz, while the highest achievable frequency at a supply voltage of 0.7 V was measured to be at least 10 MHz. Depending on V_{DD}, testing of higher output frequencies was limited by the bandwidth of off-chip level converters. It could be inferred, however, that the oscillator could achieve higher on-chip frequencies than is reported in Figure 3-41(a) based on observing the ring oscillator power consumption. The extended tuning range of the ring oscillator was designed to support the wide range of supply voltages in the presence of process variation. Although the tuning range was measured to be very large, this amount of configurability was required to be able to generate, for instance, a 5 MHz signal at 0.7 V in a slow process corner.

The power consumption of the ring oscillator across the entire measured frequency span ranges from 14 nW at 0.7 V, to 19 μW at 1.0 V. Figure 3-41(b) shows these power results, sorted in the same order of ascending frequencies as in Figure 3-41(a). The power consumption curves are non-monotonic in this case, as there is overlap in terms of frequency achievability between capacitively and non-capacitively loaded stages. To expand on this point, Figure 3-42 shows the measured energy required per output cycle, plotted versus achievable frequencies. Here, it is clear to see four distinct zones of energy consumption – a result of the four capacitive loading options, $enC[1:0]$. Although the ring oscillator consumes a small fraction of the total transmitter active energy budget, its energy efficiency is clearly minimized at the lowest capacitive loading setting.

By implementing a low-complexity architecture together with the low-leakage sizing and design considerations outlined in Section 3.4.1, the transmitter standby power consumption was measured to be 39.7 pW at a supply voltage of 0.8 V. Table 3.6 summarizes the measured transmitter standby power at several different voltages and compares the results to simulated results at 0.8 V. Somewhat surprisingly, the simulated results fairly closely matched the measured results, with the measured chip likely

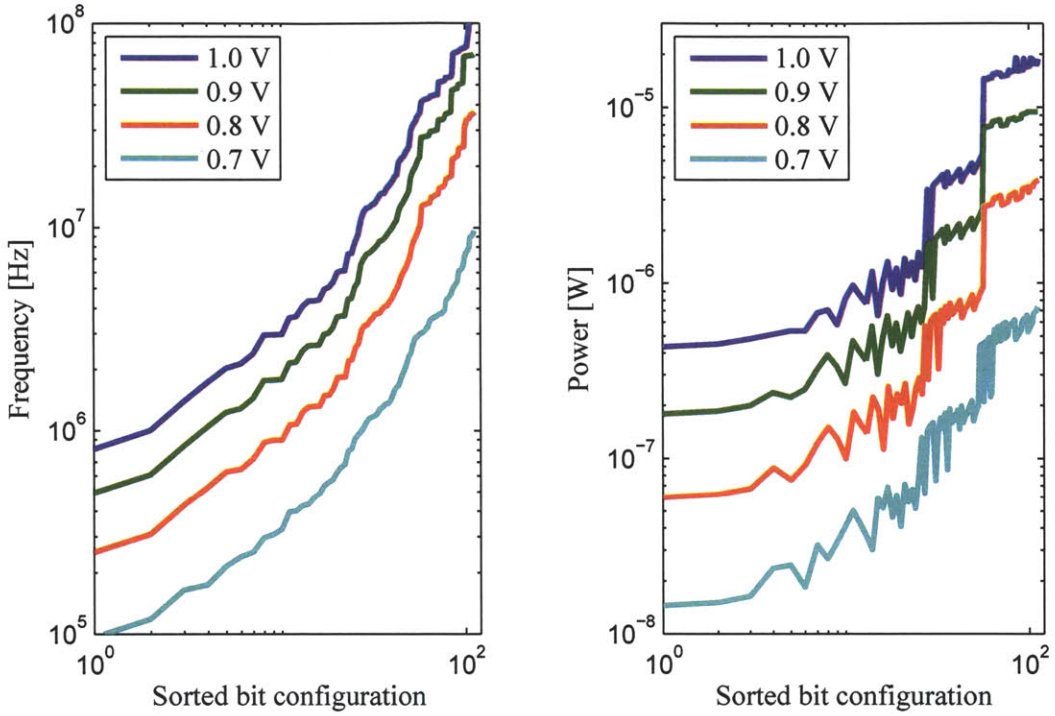

(a) Measured ring oscillator output frequency for different values of V_{DD}.

(b) Measured ring oscillator power consumption for different values of V_{DD}, sorted in the same order as panel (a).

Figure 3-41: Ring oscillator frequency and power results, sorted in order of increasing frequency.

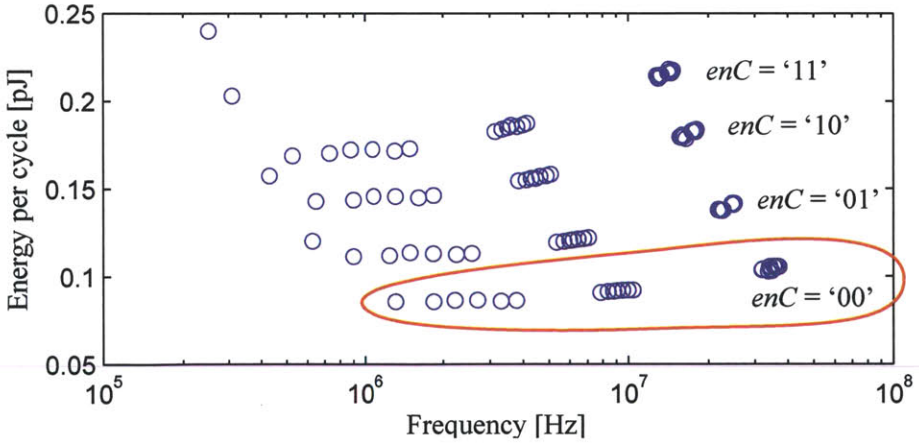

Figure 3-42: Measured energy required for every cycle of the ring oscillator at $V_{DD} = 0.8$ V.

falling somewhere in between the typical and fast corners.[26] As with the boost converter, low-current measurements were performed using a Keithley 6430 sourcemeter together with low-leakage tri-axial cables. Interestingly, it was found that the board had to be mounted onto nylon spacers for these measurements; otherwise, supplies would "short" across the ESD mat on which the board was resting. The impedance of the mat was measured to be approximately 2.5 GΩ between probes spaced 10 cm apart, which is enormous in normal testing environments and typically of little concern. However, at 0.8 V, this results in 320 pA of current, which dwarfs the entire transmitter power budget and was therefore carefully avoided.

Table 3.6: Measured transmitter standby-mode power breakdown at various supply voltages compared to simulated results.

	Standby power consumption [pW]				
V_{DD} [V]	PO	Ring Osc.	Digital	V_{PUMP}	Total
0.8 (simulated TT)	0.6	7.8	1.0	9.1	18.7
0.8 (simluated FF)	1.3	27.2	3.3	29.4	61.4
0.8 (measured)	0.7	16.5	4.7	14.8	39.7
0.9 (measured)	0.8	18.8	5.1	17.6	45.8
1.0 (measured)	0.9	21.1	5.9	22.2	60.3

Figure 3-43 plots the transmitter standby power as it scales with V_{DD}. Note that in this measurement, V_{PUMP} was also varied to its naturally settling value for each value of V_{DD}. At a supply voltage of approximate 1.1 V, the high-V_t devices begin to approach their threshold voltages and therefore the standby power of the transmitter begins to increase at an exponential pace.

At a supply voltage of 0.8 V, a data rate of 5 Mbps, and a radiated output power of approximately -29 dBm, the transmitter consumes 191 μW of active power, resulting in an energy efficiency of 38 pJ/bit. Combining this active-mode data point together

[26]This is somewhat of a surprising result, since for simulation results to be accurate, the transistor models themselves required accuracy down into the low femtoamp range. A discussion with the foundry revealed that models were corroborated with measurements down to 100 fA; it was therefore initially unclear how well the models extrapolated beyond these current levels.

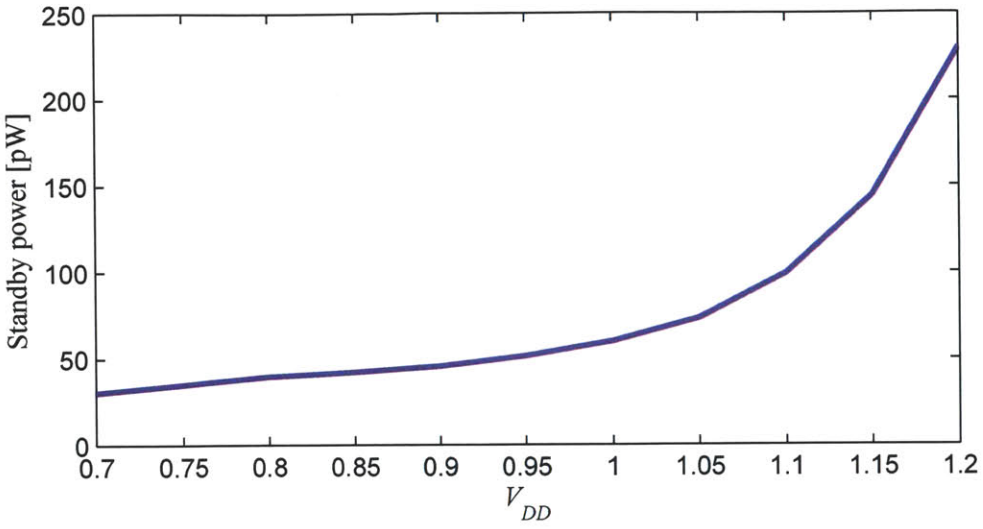

Figure 3-43: Measured standby power of the radio transmitter plotted versus various system supply voltages.

with the 0.8 V leakage power consumption (39.7 pW), as suggested by Equation 3.4, results in the total average transmitter power consumption, $P_{TX,avg}$. The result of this equation is plotted in Figure 3-44 and compared to other previously published work. Although references [17, 141] are indeed optimized for ultra-low leakage, there are currently no published reports of transmitters that have standby powers below the desired power budget of 250 pW, much less when transmitting actual data. At an average data rate of 1 bps, the presented transmitter consumes an average power of 83 pW, which is over 100X lower than previous work, and well below the desired power budget. In fact, the transmitter can achieve average data rates up to 5X higher while maintaining an average power consumption below 250 pW. Although this does not sound like a very high transmission rate, Sections 3.6 and 5.2 discuss several potentially transformational applications that can benefit from these data rates. Also, recall that this is a *duty-cycled* data rate; that is, a short packet of information is sent at the instantaneous active-mode data rate of 5 Mbps in this case, after which the transmitter goes into its ultra-low-leakage sleep state.

Interestingly, not only is the standby-mode power the lowest reported, the active-mode energy efficiency is also the lowest reported amongst narrowband transmitters

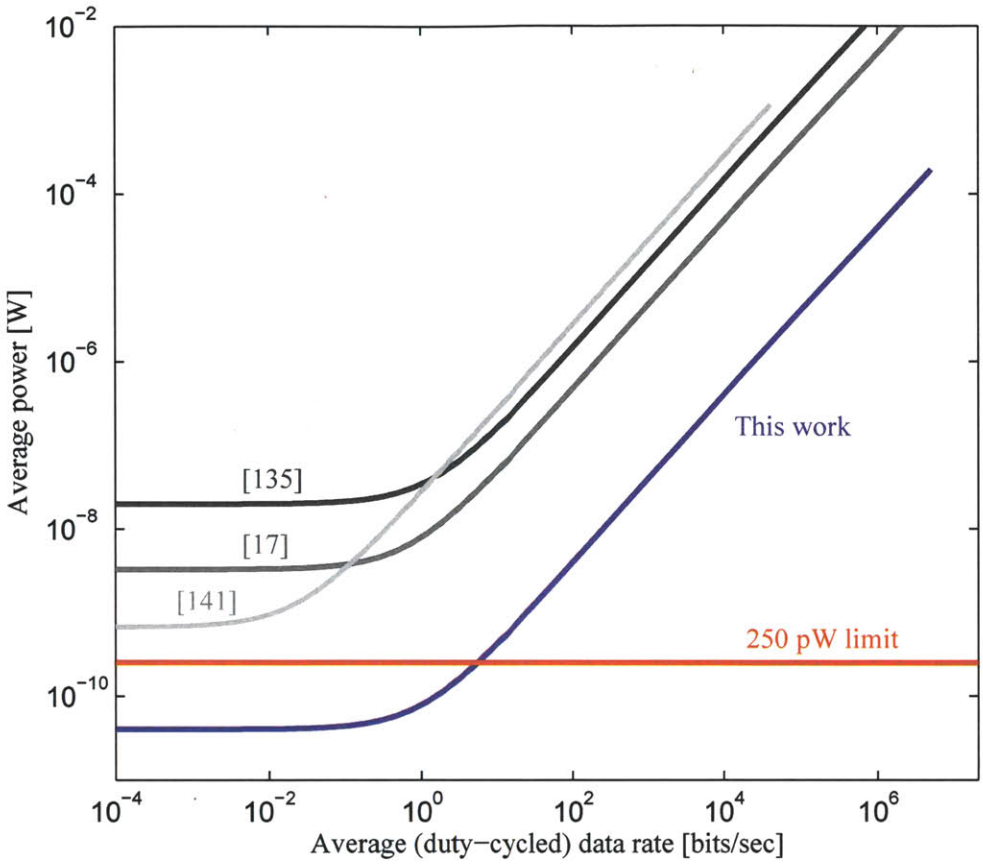

Figure 3-44: Average power of the radio transmitted plotted over an extremely wide range of duty-cycled data rates, compared to other work.

operating at data rates less than or equal to 10 Mbps. Figure 3-45 shows the energy required to transmit a single bit of information over an extremely wide range of duty-cycled data rates, compared to other energy-efficient transmitters that publish leakage power consumption results. Table 3.7 summarizes the measurement results from this work and compares its performance to other previously published narrowband transmitters. To be fair, it is important to keep in mind that the radiated output power of this work is generally less than others. However, low output power is a necessary consequence of the low-complexity direct-RF power oscillator that offers the desired ultra-low leakage power demanded by this particular application. This is an enabling trade-off that is acceptable in practice under the asymmetric link budget.

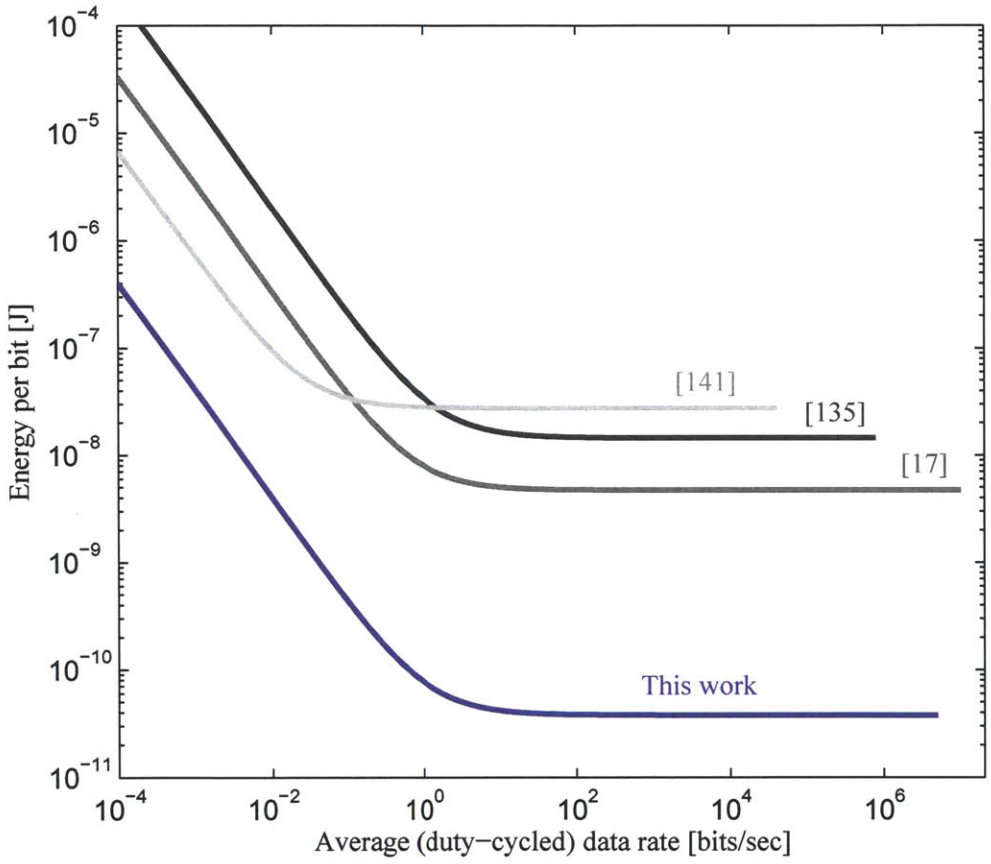

Figure 3-45: Energy consumed per transmitted bit of the radio transmitted plotted over an extremely wide range of duty-cycled data rates, compared to other work.

Table 3.7: Comparison of previously published energy efficient and/or low power narrowband transmitters.

Reference	Frequency [MHz]	Data rate [Mbps]	P_{out} [dBm]	Energy/bit [pJ]	Standby power [pW]
[69]	400	0.12	−16	2900	–*
[17]	570/690	10	−10	4700	3,300
[135]	400	0.8	−4.5	< 14,400	≈ 20,000
[136]	1900	0.33	0.8	4050	–*
[137]	433	3/10	−12.7	187/52	–*
[139]	900	1	−11.4	3800	–*
[140]	2400	1/10	−10	483/48	–*
[141]	2400	0.042	−45	29,000	< 675
[151]	900	5	−10	140	–*
This work	**2400**	**5**	**> −29**	**38**	**39.7**

*Most transmitter publications do not report standby/leakage power.

3.5.2 Clinical Measurements

The preceding subsection described measurement results performed at MIT in a standard electronics laboratory testing environment. For clinical testing, the endoelectronics chip was interfaced with an animal's endocochlear potential which, after an initial start-up energy packet, acted as the only source of power into the system. This section describes the results of these experiments, showing the first-ever demonstration of energy harvesting from a mammalian electrochemical potential. Experiments were performed at the Massachusetts Eye and Ear Infirmary; surgeries were performed by Andrew C. Lysaght with the approval of the institutional Animal Care Committee (protocol # 09-09-026).

To access the endocochlear potential, a surgical procedure was performed to expose the round window on a Hartley Albino *Cavia porcellus* (guinea pig). Although the cochlea is generally encased with bone, the round window presents a natural opening into the cochlea, therefore no drilling was required. To externally access the round window, the auricle and neighboring musculature were reflected ventrally to expose the external auditory meatus and bulla. The lateral wall of the bulla, up to the caudal edge of the tympanic ring, was then removed, exposing the round window. A photograph of the exposed round window is shown in Figure 3-46. Glass microelectrodes were then advanced through the round window, with the perilymphatic electrode resting in the *scala tympani* chamber of fluid. The endolymphatic electrode passed through the basilar membrane until it entered the *scala media* chamber, as illustrated in Figure 3-3. For precise control, micromanipulators were used to advance the electrodes.

With the electrodes tips in place, the half-cells[27] of the electrodes were interfaced to the boost converter input of the endoelectronics chip. For initial experimentation, the chip was located external to the animal, as shown in Figure 3-47. The experiment proceeded as follows. The endoelectronics chip was first initialized by placing the antenna of the wireless energy delivery circuit close to the chip. At the same time,

[27]The half-cells employ the use of Ag/AgCl exchange pellets. The electrolyte was composed of a solution of 2 M KCl.

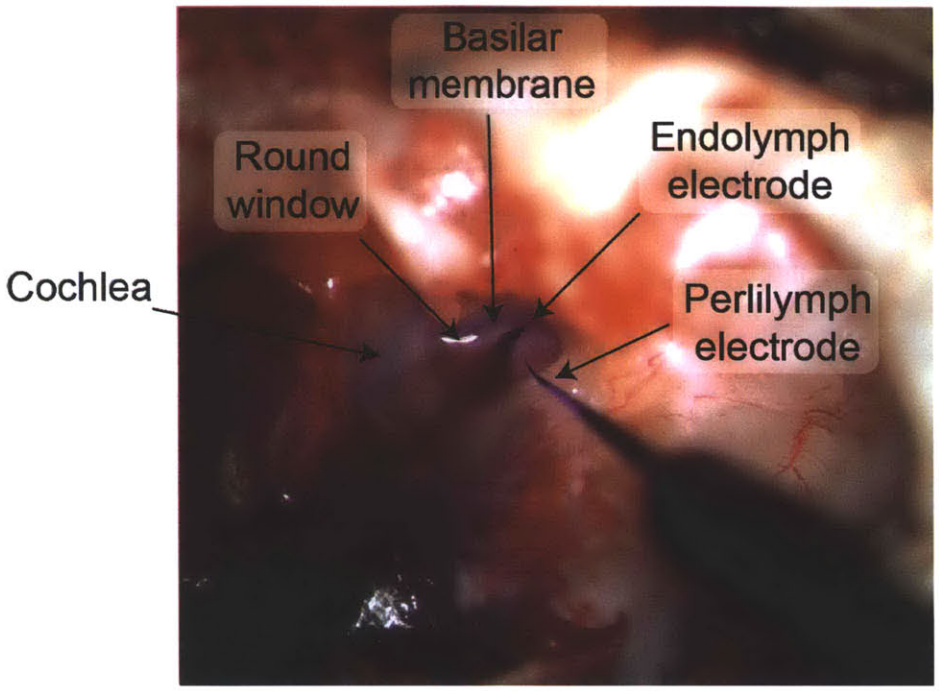

Figure 3-46: Photograph of electrode insertion through the round window of a guinea pig in order to interface with the endocochlear potential.

a Keithley Instruments 2602 dual-channel sourcemeter monitored both the V_{DD} and V_{PUMP} supplies. The sourcemeter was set to source zero-current (i.e. it was in a high-impedance mode), and was only used to measure voltages. The instrument was additionally set to measure purely differential results, without reference to earth ground. In other words, it was used as a purely floating voltmeter that did not inject any charge into the system. Once the sourcemeter confirmed that the chip was initialized (i.e. the V_{DD} measurement exceeded 0.8 V), the wireless energy delivery circuit was removed, and the chip's supplies continued to be monitored via the sourcemeter. An additional high-impedance multimeter was used to monitor the input to the boost converter, V_{in}. Finally, an external antenna, low-noise amplifier, and mixer were used to demodulate wirelessly received packets for display and analysis on a TDS3064B oscilloscope from Tektronix Inc., Beaverton, OR.

Figure 3-48 shows a recording of the supply voltages V_{DD} and V_{PUMP} throughout the duration of a single experiment. At time zero, wireless energy was delivered to the circuit, raising V_{DD} to 1.43 V. When the wireless energy source was removed,

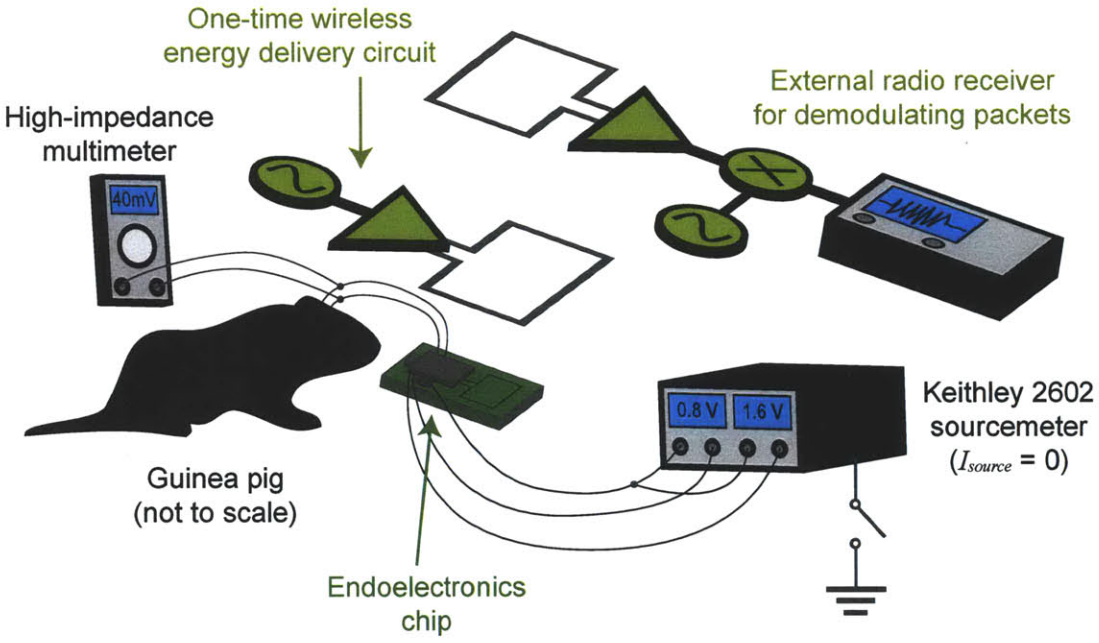

Figure 3-47: Simplified illustration of the clinical experiment setup. The endoelectronics chip was initialized with a one-time wireless energy packet, after which the system extracted energy from the endocochlear potential. High-impedance multimeters monitored V_{DD}, V_{PUMP}, and V_{EP} while an external radio demodulated wirelessly received packets.

V_{DD} fell until it reached steady-state at approximately 1 V, where the combination of quiescent power and active radio power on average exactly canceled out incoming energy from the endocochlear potential. The system sustained itself for the duration of the five hour experiment, with the endocochlear potential acting as the only source of energy into the system. This was the very first demonstration of an electronic system powered from an electrochemical potential that exists naturally in mammals.

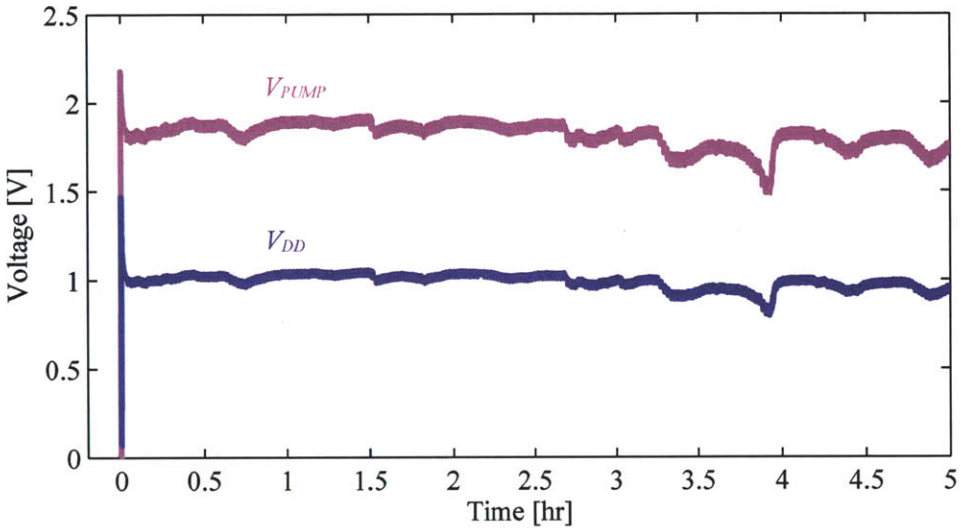

Figure 3-48: Clinical measurement result showing the first demonstration of an electronic system sustaining itself with the endocochlear potential acting as the only source of energy into the system.

A zoomed-in version of the V_{DD} trace of Figure 3-48 is shown together with two other experimental results on two separate guinea pigs in Figure 3-49. Here, the characteristic energy buffering behavior first described in Figure 3-11 can be seen. Wirelessly transmitted packets cause rapid and substantial drops in V_{DD}, after which the transmitter enters its low-leakage sleep mode. At this point, energy begins to buffer back onto capacitor C_{DD}, until the energy consumed by the previous transmission fully recovers.

As can be seen from Figure 3-49, the natural V_{DD} settling and energy recovery slope of the system will vary, depending on the actual endocochlear potential of each individual guinea pig and the realized electrode impedances. The configurable packet

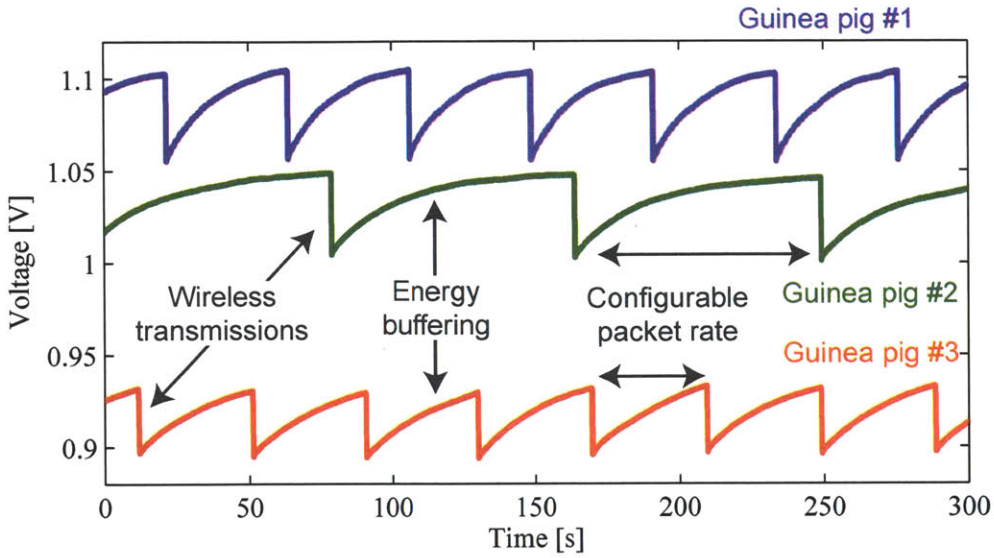

Figure 3-49: Clinical measurement result showing three separate V_{DD} traces for three separate experiments. The average DC-value of each trace, along with its energy recovery slope is determined by the individual animal's endocochlear potential, the realized electrode impedances, and the configurable packet rate (the packet rate only affects the average DC level, not the energy recovery slope).

rate will also affect the natural V_{DD} settling. Higher values of V_{DD} will cause higher active transmitter current consumption, requiring more energy for each transmitted packet. For example, the experiment with guinea pig #1 produced voltage drops of 48 mV, while the experiments with guinea pigs #2 and #3 produced drops of 45 mV and 36 mV, respectively. The average DC level of V_{DD} will only sustain if these voltage drops are recovered by the energy harvesting circuit. In other words, a higher V_{DD} causes a larger voltage drop, which in turn requires additional energy from the endocochlear potential to sustain the average V_{DD} level. Experimental results indicated that electrode impedances could vary by as much as 30%, while the endocochlear potential could vary by upwards of 20% between animals. The approximately 18% variation seen in Figure 3-49 falls within this range and was not unexpected.[28]

[28] On-demand wireless transmission could instead be used to keep V_{DD} at a fixed, regulated level. Such a design is not strictly necessary (and in fact, increases the receiver complexity), while precluding the design of the built-in wireless endocochlear potential sensor described in the following paragraph.

As described in Section 3.4.5, the endocochlear potential is related to the instantaneous transmitter data rate. Capturing and analyzing wirelessly received data from the TDS3064B revealed that it was indeed possible to monitor relative changes in $V_{in} \approx V_{EP}/2$, using data rate as a proxy. A representative demodulated packet is shown in Figure 3-50. Demodulated data was found to be correct and as expected. Figure 3-51 illustrates the wireless sensor results. Voltage V_{in}, plotted in light gray, was directly measured using a high-impedance Agilent U1253A multimeter. The instantaneously wirelessly received data rate was scaled and offset-adjusted, and then plotted in black and overlaid on top of the direct measurement. Measurement results track natural changes in V_{in} very well over the duration of the 2.5 hour experiment, with an RMS error of 0.45 mV. This is not only the first demonstration of a sensor that can wirelessly monitor the endocochlear potential, but is also the first demonstration of one that is self-powered.

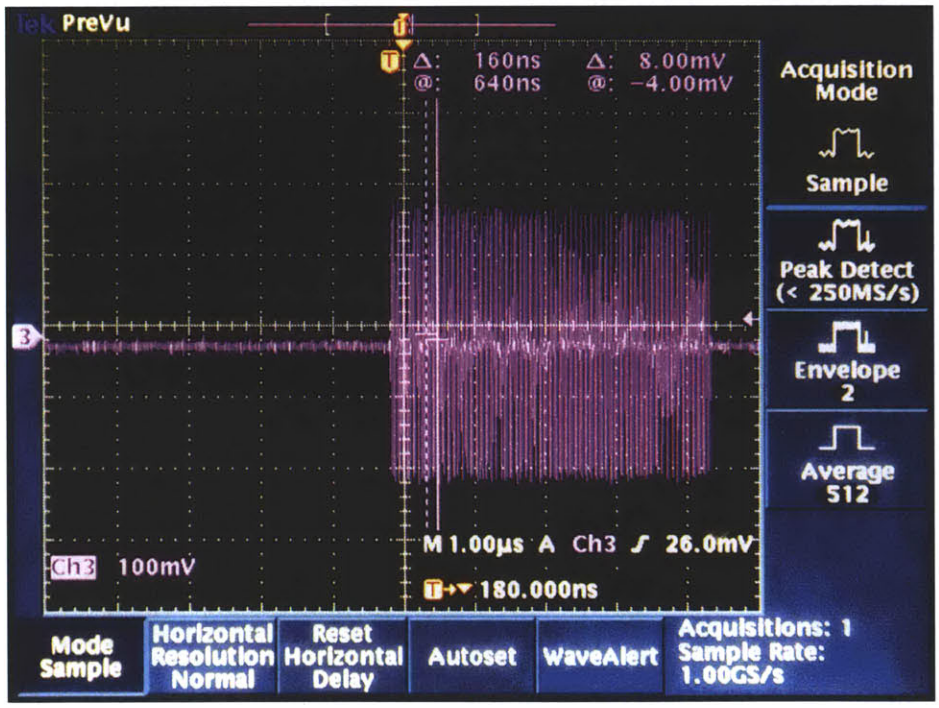

Figure 3-50: Transient measurement of a representative wirelessly received and demodulated packet.

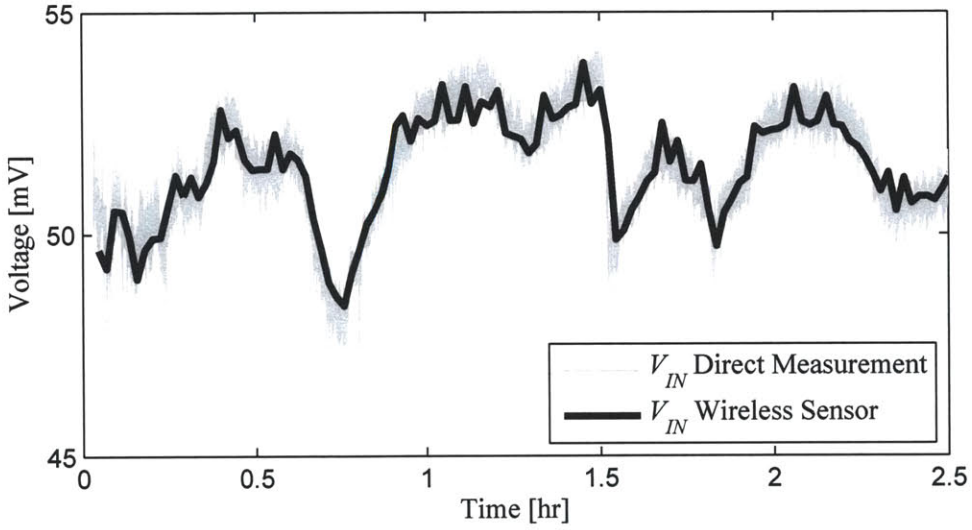

Figure 3-51: Results showing that the instantaneously received data rate can be used as an accurate proxy to measure relative changes in the endocochlear potential.

3.6 Summary and Conclusions

This chapter has presented circuit and system solutions for extracting energy from the endocochlear potential and using this energy to power a wireless sensor. Although there are many forms of energy available to harvest from the human body, none have been developed or demonstrated in the vicinity of the ear, eye, or brain. This area of the body contains many interesting and important organs that present tremendous opportunities to install monitoring or therapeutic actuation devices.

For instance, it is not current possible to biopsy the inner ear without causing permanent hearing damage. As a result, nothing has ever been chronically measured in the inner ear of freely behaving mammals. Consequently, the underlying causes of sensorineural hearing loss[29] are often not known. A self-powered sensor using the technology developed in this thesis provides a new window of opportunity to monitor chemical concentrations or molecular biomarkers completely autonomously without requiring implanted chemical batteries that eventually require surgical replacement. Even taking such measurements a few times per day, which can certainly fit within the power budget of the harvesting system, can potentially offer transformative insight into inner-ear biochemistry. Such expanded insight can create unique opportunities to develop novel diagnostics or therapies.

Although the surgical approach used in this work is not currently suitable for humans, surgical implantation of similarly-sized devices are routinely performed in patients today. For example, stapes prosthetics or cochlear implants, which help restore conduction-based or sensorineural-based hearing loss in profoundly deaf patients, respectively, have minimal risk of damaging residual hearing [152, 153]. Thus, with continued work on inner ear surgical approaches and advances in electrode geometries, it is not out of the realm of possibility to envision human applications of endocochlear potential harvesting systems.

In order to extract net positive energy from the endocochlear potential, it was nec-

[29]Sensorineural hearing loss is the most common form of hearing loss, and typically refers to the any form of hearing loss that involves neural degeneration. This is in contrast to conductive hearing loss, which affects mechanical motion of the ear, for instance in the ossicular chain.

essary to develop electronics that consumed orders of magnitude lower power than existing work. Specifically, a boost converter was designed that operated with a quiescent power consumption of 490 pW at 0.8 V and a power train efficiency approaching 55%. Similarly, a radio transmitter was developed that consumed 39.7 pW in standby mode and required 38 pJ to transmit a single bit of information. Operating at a duty ratio of 0.0001% and transmitting an average of 1 bps, the transmitter achieved an average power consumption of 83 pW, which is over 100X lower than previously published work. Design of the fully-functional system was enabled in part through very careful transistor sizing, extensive leakage gating and management techniques, reduced complexity architectures, comprehensive electromagnetic simulations, and use-case engineering. The endoelectronics chip was fabricated in a 0.18 μm CMOS process and was directly wirebonded to a circuit board containing a printed antenna, and three external passives. During clinical experiments, the endoelectronics system sustained itself with the endocochlear potential acting as the only source of energy into the system. This was the first demonstration of an electronic system powered from an electrochemical potential that exists naturally in mammals. Further exciting future research directions stemming from these results are discussed in the thesis conclusions in Section 5.2.

Chapter 4

Rapid Wireless Ultra-Capacitor Charging

Current implantable systems are almost universally operated using either continuous power delivery from an external wireless energy source, or periodic recharging of an implanted battery. As discussed in Section 1.3, wireless power transfer techniques have issues in aesthetics and usability, while implanted batteries have both limited energy densities and limited number of re-charge cycles before surgical re-implantations are required. To overcome these constraints, new energy sources or application-specific use-cases are necessary.

Chapter 3 described a method to harvest energy from the endocochlear potential in order to autonomously power an implant in the vicinity of the ear, eye, and brain without either of the aforementioned issues. The extractable amount of power was, however, extremely limited, and was only suitable for powering energy buffering devices that executed tasks (e.g. sense or communicate) once every few minutes. While there is a large range of tremendously useful tasks one can accomplish on such power budgets, there is an even larger class of implanted applications that can only operate with substantially higher power consumption.

This chapter presents a wireless energy delivery scheme for implantable devices requiring higher power densities than what was discussed in Chapter 3. Specifically, a once-per-day charging paradigm is proposed that leverages the effectively unlimited

number of recharge cycles offered by current and emerging ultra-capacitor technologies to produce implanted systems with essentially unlimited device lifetimes. A technique to rapidly charge such ultra-capacitors is also presented in order to alleviate the patient burden of system energy maintenance.

4.1 Target Applications: Fully-Implanted Devices

Characteristic examples of implantable systems requiring more energy than is extractable from the endocochlear potential are cochlear stimulation devices, vestibular prosthetics, retinal implants, neural recorders, and deep-brain stimulators. Typically, such devices continuously consume on the order of tens of microwatts to several milliwatts of power. Today, almost all such devices rely on continuous wireless power transfer for chronic operation. This requires the use of a potentially large and obtrusive external device that has both aesthetic and functional concerns. For example, should the external source be remove (for instance, while showering or swimming), implant functionality is lost.

Use-case engineering can be employed to address this issue. As discussed in Chapter 3, there are no other sufficiently powerful sources of energy to harvest from the body in the vicinity of the ear, eye, and brain. Consequently, the only alternative use-case that obviates the need for a semi-permanent external wireless power transfer device is to periodically charge an implanted energy storage element. Rechargeable batteries are generally a logical choice for energy storage, though they will eventually require invasive surgical replacement once their internal chemistry wears out. Just as important to consider is the patient use-case: batteries take a long time to charge, typically a *minimum* of one hour. This is a long period of time to wear an external device that was, by design, supposed to be completely eliminated in the first place. Although one can envision a wireless power transfer system integrated into a patient's pillow for autonomous charging during sleep, efficient charging typically requires very close proximity between the external and implantable coils. At large separations, extremely high transmitter output powers are required, raising very difficult tissue

heating and specific absorption rate (SAR) issues.

Ultra-capacitors, on the other hand, offer energy storage densities that are becoming increasingly comparable to batteries, with the significant advantage of having an effectively unlimited number of recharging cycles. Importantly, ultra-capacitors can charge to full capacity in orders of magnitude less time than conventional batteries. Thus, this chapter proposes a once-per-day charging use-case with ultra-capacitors as the energy storage element. By delivering up to several hundred milliwatts of instantaneous power to the implant, charging times can be reduced to a few minutes. This work can additionally leverage the large number of exciting research results in the ultra-capacitor space, such as graphene-based devices [154]. Table 4.1 compares some of the key characteristics of batteries and ultra-capacitors.

Table 4.1: Comparison of energy storage elements. Estimated values come from a 1 cm^3 energy storage element.

	Energy density [J/cm^3]	Operational lifetime (at 1 mW)	Charging time (at < 200 mW)
Coin cell battery [155]	337	94 hours	>> 1 hour
Solid-state battery [156]	33*	9.2 hours	≈1 hour
Commercial ultra-capacitor [157]	11	3 hours	0.9 minutes
Research ultra-capacitor [154]	205†	57 hours	17 minutes (3.6 minutes for 12 hour operation)

*Based on an estimated height of 0.6 mm.
†Estimated using 1.5 g = 1.0 cm^3.

Although ultra-capacitors can in theory charge as fast as ESR permits, there are biological implications of tissue heating through electromagnetic radiation and resistive losses that ultimately limit charging times. Appendix A discusses these limits in more detail.

The purpose of this chapter is to investigate techniques to accelerate charging time. Since an ultra-capacitor's voltage drops as it is discharged, other power electronics circuitry will be necessary in order to provide stable supplies to load circuits. Reference [158] describes a technique to overcome this drooping effect, and could easily be applied to the charging system developed in this chapter.

4.2 Inductive Coupling

4.2.1 Overview

Near-field inductive coupling is the most popular approach to deliver wireless power to an implantable device. It has applications in cochlear stimulation devices, retinal prostheses, neural stimulation implants, cardiac pacemakers, endoscopy pill-cams, and many other exciting bio-electronics applications. A schematic of a typical wirelessly-powered device is shown in Figure 4-1.

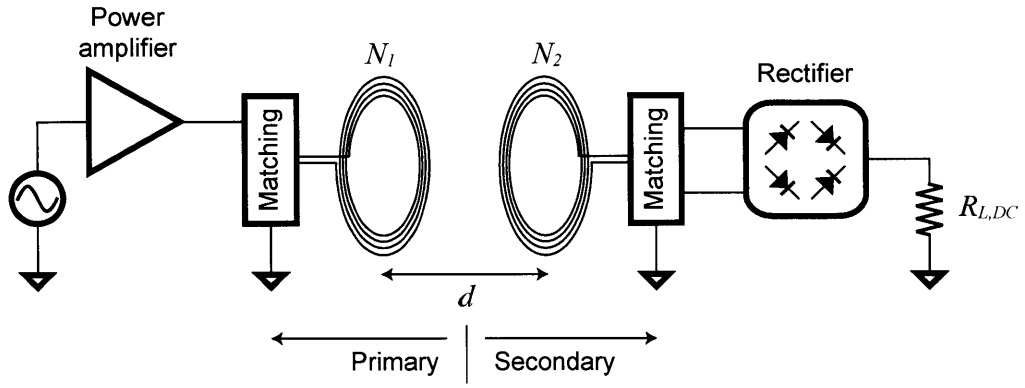

Figure 4-1: An introductory schematic overview of a typical inductively-coupled system.

The circuit operates as follows: a power amplifier, with an RF voltage-source input, sends power through a primary-side coil with N_1 turns. Some form of matching is used to tune-out the inherent loop inductance in order to decrease loading effects on the power amplifier. So long as the operational wavelength is much less than the physical dimension of the coils and their separation, energy will be contained

solely in near-field magnetics. In other words, the coils look like antennas that are *extremely* electrically small, as specified in Section 3.4.4. Thus, the secondary-side coil, composed on N_2 turns and spaced a distance d from the primary-side coil, receives energy from the transmitter's produced time-varying magnetic field. The RF output of the secondary-side matching network then passes through a rectifier, converting the AC energy into DC energy used to power the load, in this case modeled by resistor $R_{L,DC}$. There are many excellent references that discuss the electromagnetic properties of such a system, as well as analytical formulae for predicting inductance and other parameters in more detail [100, 159].

A more detailed circuit diagram of a typical inductive coupled system is shown in Figure 4-2. Inductors L_1 and L_2 model the primary and secondary loop reactances, respectively. The inductors are not perfect, however, as they each both have finite quality factors. Specifically, the quality factor of each coil is given by $Q = \omega L/R$, where ω is the operating frequency and R represents the parasitic series loss resistance. Current sources Mi_2 and Mi_1 model the mutual coupling effects between the coils, where M is the mutual coupling factor, while capacitors C_1 and C_2 provide resonant matching with the inductors. The coil coupling coefficient, k, is defined by the following equation:

$$k \equiv \frac{M}{\sqrt{L_1 L_2}}. \tag{4.1}$$

It can be shown that k is dependent only on coil separation distance d and individual coil geometries [100]. Importantly, it should be noted that k varies between 0 (no coupling) and 1 (perfect coupling), and decreases with d. Most transcutaneous implanted systems have separation distances ranging from a few millimeters to 20 mm, resulting in $0.03 < k < 0.3$ for coils with centimeter-sized diameters.

The primary side is driven by a voltage source, V_s, that has a series resistance, R_s. The secondary side is loaded by a resistor, R_L. Note that the actual load circuits are always found at the output of the rectifier. However, it can be easily shown that, with respect to the schematic in Figure 4-1, $R_L \approx R_{L,DC}/2$ [100].

Finally, an important definition that will be useful for analysis is the turns ratio

of an ideal transformer, assuming perfect coupling:

$$n \equiv \sqrt{\frac{L_2}{L_1}}. \tag{4.2}$$

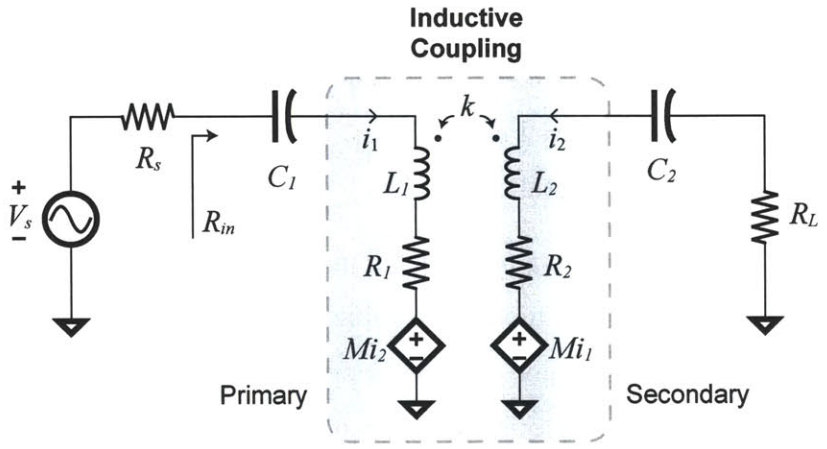

Figure 4-2: Schematic model of an inductively coupled system. In this case, series capacitors C_1 and C_2 are used to resonate with inductors L_1 and L_2.

Most wireless power transfer designs endeavor to maximize power transfer efficiency in order to minimize the size of the external power source. It can be shown that resonating the inductors with capacitors helps to achieve maximal power transfer efficiency. This has been shown using traditional circuit analysis techniques, preferred by electrical engineers, as well as coupled-mode theory, preferred by physicists [160]. As it turns out, both approaches provide the same results for high quality factor coils at large separation distances [161]. Circuit analysis, however, is more accurate over a wider range of cases.

Unlike in conventional systems, however, **maximizing power transfer efficiency is not the primary goal of this work**. Recall that in the application use-case, the external device is only worn for a few minutes during ultra-capacitor charging. Consequently, the physical size of the external charging device is not particularly important relative to devices designed for chronic wireless power delivery. Instead, **a metric of greater importance is charging time**. From a design

perspective, maximizing charging time is equivalent to maximizing the amount of power delivered to the load circuit (in this case a capacitor) over a short period of time, given source and system constraints. It makes sense to refer to this scheme as wireless *energy* transfer, operating instantaneously at a maximum power transfer condition.

In many cases, maximizing efficiency is not the same as maximizing power transfer to the load. To better understand this, consider the classic resistive divider circuit in Figure 4-3. The power transfer efficiency of this circuit is given by:

$$\eta = \frac{R_L}{R_L + R_s}, \tag{4.3}$$

which is maximized when the load resistance, R_L, is large relative to the source resistance, R_s. However, the power delivered to the load is given by:

$$P_L = \frac{V_s^2 R_L}{(R_L + R_s)^2}. \tag{4.4}$$

A large R_L implies low current from the source, which means low amounts of power are being delivered to the load. In the limit that R_L tends to infinity, η tends to 100%, yet P_L tends to zero. The classic maximum power transfer theorem states that the load resistance should be matched to the source resistance in order to deliver the maximum amount of power possible to the load. In other words, $R_L = R_s$ for maximum power transfer. Naturally, if the designer has the ability to make the source impedance arbitrarily small (as in many power amplifier design cases), both high efficiency and high output power can be achievable from a given voltage source. Maximum power transfer of course still applies, but if the source impedance can be made sufficiently low such that "enough" power is extracted from the source, high efficiency can still be achieved at the desired output power.

In the case of inductively-coupled links, however, it is often not possible to change the impedance seen before the load due to finite coil quality factors. Therefore, given a fixed voltage source, it is difficult to achieve both high efficiency and high power delivery. Consequently, it is worthwhile analyzing in greater detail what the

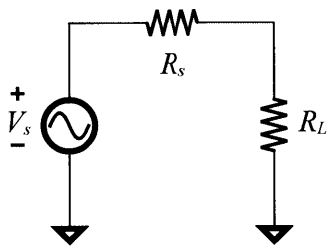

Figure 4-3: Resistive divider circuit.

fundamental limitations are in order to gain insight into any circuit solutions that can approach these limits.

4.2.2 Reflected Load Analysis

Inductive coupling theory has been well-studied in the past, and many excellent references describe analytical expressions that can accurately predict the maximum achievable efficiency of a given link [100, 159]. However, **the new problem formulation of requiring maximum power transfer requires new analysis to determine optimal design conditions**. Building on existing work, this section derives new analytical results for predicting maximum power transfer conditions.

Transformer Model

The simplest way to analyze inductively-coupled circuits using circuit theory is by reflected load analysis. It is well-known that circuit elements can be reflected across the terminals of an ideal transformer, modulated by a factor of $1/a^2$, where a is the turns ratio of the transformer. A pair of inductively coupled coils as shown in Figure 4-2, can be thought of as a loosely-coupled transformer (i.e., with $k < 1$), and can be modeled with an ideal transformer as one of its circuit elements. One such model is shown in Figure 4-4, employing an ideal transformer with a turns ratio of $a = n/k$. Thus, any load on the secondary side can be reflected to the primary side, multiplied by a factor of $(k/n)^2$. It is important to know that reflected impedances must be seen in parallel to L_2 for reflection to be valid in this case.

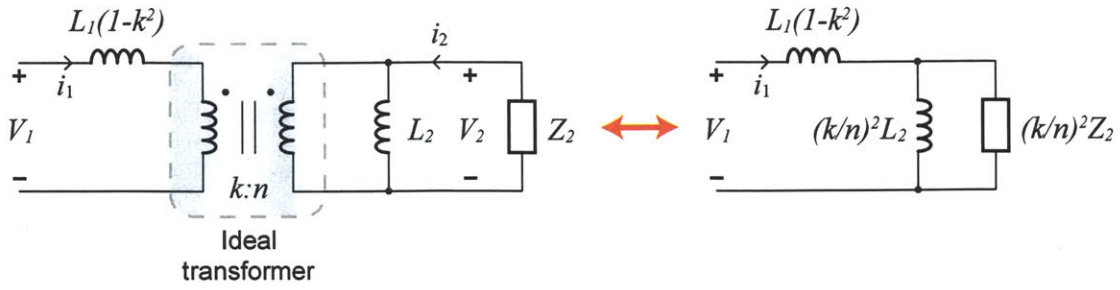

Figure 4-4: Circuit model of a loosely-coupled transformer, and its load-reflected equivalent.

Capacitor Tuning Options

There are four primary topological options for resonating out inductors L_1 and L_2: the combinations of series or parallel capacitors on both the primary and secondary coils, as illustrated in Figure 4-5. Series tuning on the primary is typically used to decrease loading effects of voltage-based sources, while parallel tuning is equivalently used for current-based sources. Since most drivers or power amplifiers effectively operate as voltage sources, series tuning in the primary is almost universally employed in the design of transcutaneous inductive links.

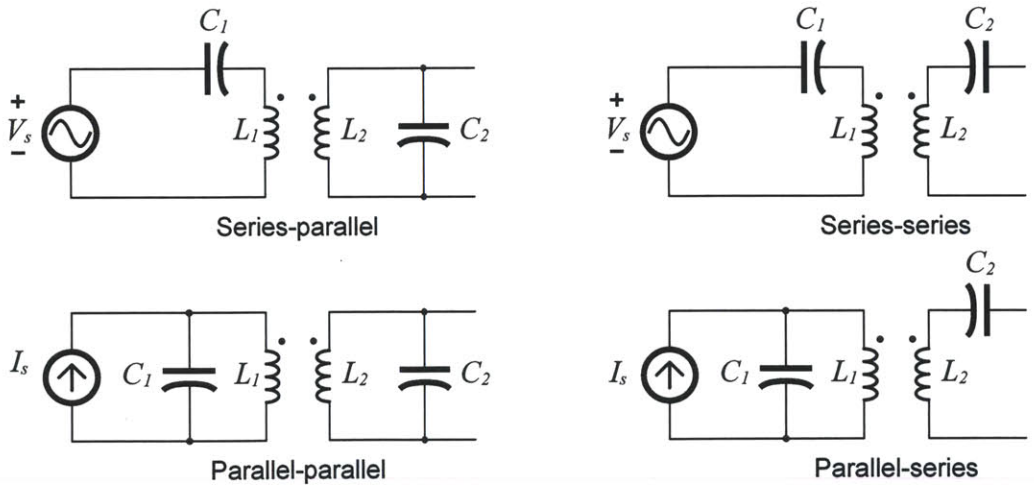

Figure 4-5: The four basic options for resonant tuning of inductively coupled coils.

The choice of secondary-side tuning depends greatly on the application. It is

well known that using a parallel secondary tuning capacitance induces a voltage multiplication factor, making rectifier diodes easier to turn-on.[1] This makes a series-parallel link configuration ideal for low-power (i.e., high R_L) applications, where it is difficult to generate sufficient voltage to activate non-linear rectifiers. At high powers (i.e., low R_L), the voltage multiplication factor may present voltages that go far beyond CMOS compatibility, limiting its utility. Instead, a series-tuned secondary is preferred for high power applications, where increased power is generated through Q-multiplied current rather than voltage.

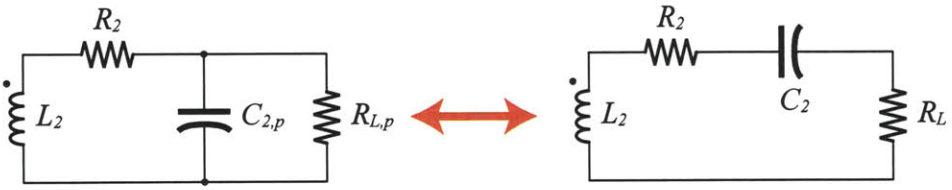

Figure 4-6: Converting a parallel-tuned secondary to a series-tuned secondary.

Since the purpose of this work is to deliver high power to an implanted device, a series-tuned secondary is employed. Regardless, the analysis that is presented in the following subsections can be easily applied to parallel-tuned secondaries by first transforming the parallel-tuned circuit to look like a series-tuned circuit as shown in Figure 4-6 and through the following relationships:

$$Q_L = \omega C_{2,p} R_L \tag{4.5}$$

$$R_L = R_{L,p}(1 + Q_L^2) \tag{4.6}$$

$$C_2 = C_{2,p}\left(\frac{1 + Q_L^2}{Q_L^2}\right). \tag{4.7}$$

[1]This is somewhat confusing, since parallel LC resonators exhibit a *current* multiplicative factor. However, from the perspective of the dependent voltage source Mi_1 in Figure 4-2, a parallel tuning capacitor ends up looking like it is in series with the inductor.

Note that the resonant frequency of a series-tuned load is given simply by:

$$\omega_o = \frac{1}{\sqrt{L_2 C_2}} = \frac{1}{\sqrt{L_1 C_1}}, \tag{4.8}$$

assuming the primary network is tuned to the same frequency. The case is not as simple for the parallel-tuned secondary, as the resonant frequency depends on the load:

$$\omega_o = \sqrt{\frac{1}{L_2 C_2} - \frac{1}{R_{L,p}^2 C_2^2}}. \tag{4.9}$$

This is in fact an additional reason to choose a series secondary for high power cases. If $R_{L,p}$ is small, then it's possible that:

$$\frac{1}{R_{L,p}^2 C_2^2} > \frac{1}{L_2 C_2}, \tag{4.10}$$

thereby indicating that there is no parallel resonate matching condition that will reflect as a real impedance to the primary. As a result, others have described primary circuits that sense this condition, and shift their driving frequency to compensate [162]. As will be shown in Section 4.3.1, the instantaneous resistance of a charging capacitor can change dramatically from start to finish. A series-tuned secondary avoids the need to track any resonance shifts in this case, thereby simplifying circuits, while also being inherently well suited for high power applications in the first place.

Optimal Load Analysis for Maximum Power Transfer

In order to determine what conditions permit transfer of maximum power to the load, it is necessary to obtain workable expressions for simplified, though equivalent circuits. For example, the circuit in Figure 4-7(a) is an accurate representation of an inductively coupled system with a series-resonant secondary. To gain design insight through simplified yet equivalent circuits, the total non-inductive secondary impedances are grouped together such that they exist in parallel to L_2 for reflection to the primary side. The total secondary impedance is given by Equation 4.11 and is

shown reflected to the primary side in Figure 4-7(b).

$$Z_{2T} = R_2 + R_L + \frac{1}{j\omega C_2} \tag{4.11}$$

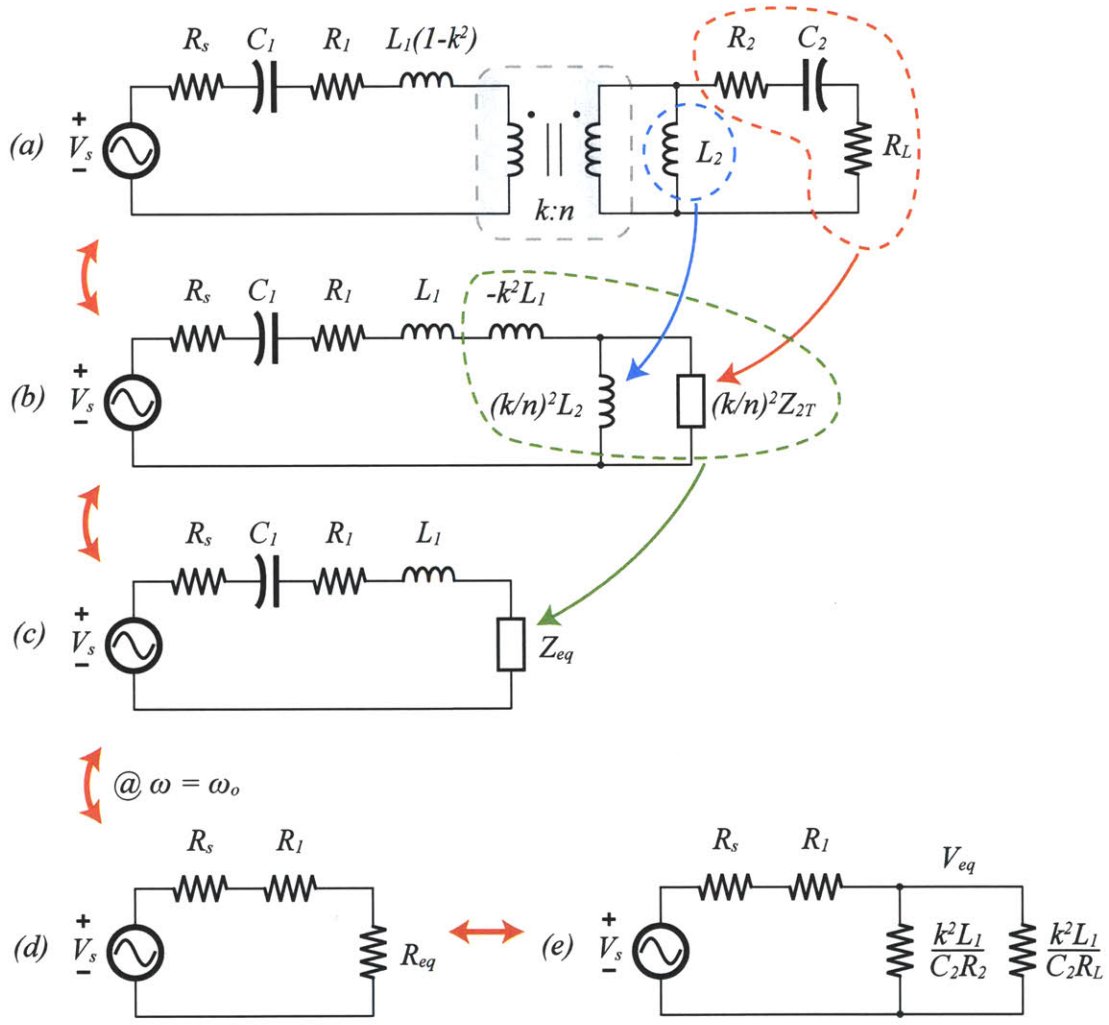

Figure 4-7: Equivalent circuits for a series-turned secondary.

Due to the parallel combination of an inductance and complex impedance, Figure 4-7(b) is still too cumbersome for practical analysis. Mapping the values in Figure 4-7(b) to Figure 4-7(c) is the next step in enabling useful analysis. This can be done

using equivalency mapping as follows:

$$Z_{eq} = -j\omega k^2 L_1 + \frac{1}{\frac{1}{j\omega(k/n)^2 L_2} + \frac{1}{(k/n)^2 Z_{2T}}}$$

$$= -j\omega k^2 L_1 + \frac{1}{\frac{1}{j\omega k^2 L_1} + \frac{1}{(k/n)^2 Z_{2T}}}$$

$$= \frac{\omega^3 k^2 L_1 L_2 C_2 \left[\omega C_2 (R_L + R_2) + j(1 - \omega^2 L_2 C_2)\right]}{\omega^2 C_2^2 (R_L + R_2)^2 + (1 - \omega^2 L_2 C_2)^2} \tag{4.12}$$

These results were initially shown in [159], and subsequently independently verified. Equation 4.12 is complicated and not very useful for analysis. Fortunately, the expression simplifies considerably at resonance (i.e., $\omega = \omega_o = 1/\sqrt{L_2 C_2}$):

$$Z_{eq}|_{\omega_o} = \frac{k^2 L_1}{C_2 (R_L + R_2)} = R_{eq}. \tag{4.13}$$

What is critical to note here is that this is a purely real impedance. If the primary and secondary are set to resonate at the same frequency, the entire inductive coupling circuit looks purely resistive! The equivalent circuit under this resonant condition is shown in Figure 4-7(d). Note that in this series-tuned configuration, capacitors C_1 and C_2 must only be tuned with respect to their adjacent inductors, without regard for any other element in the circuit. The same cannot be said for parallel-tuned secondaries, where the tuning of C_2 must also take into account the load impedance per Equation 4.9. If the load changes, as is most certainly the case for a charging capacitor, either C_2 must be dynamically compensated, or the driving frequency must be modulated as described earlier.

The expression for R_{eq} can be split into two different components as follows:

$$\begin{aligned} R_{eq} &= \frac{k^2 L_1}{C_2(R_L + R_2)} \\ &= \frac{k^2 L_1}{C_2}\left(\frac{R_L R_2}{R_L + R_2}\right)\frac{1}{R_L R_2} \\ &= \left(\frac{k^2 L_1}{C_2 R_2}\right) /\!/ \left(\frac{k^2 L_1}{C_2 R_L}\right) \end{aligned} \tag{4.14}$$

A circuit with these two separated components is shown in Figure 4-7(e). Given that there is an isolated component proportional to the load resistor, the power consumption seen at the load can be found using the following set of equations:

$$\begin{aligned} P_{out} &= V_{eq}^2\left(\frac{C_2 R_L}{k^2 L_1}\right) \\ V_{eq} &= V_s\left(\frac{R_{eq}}{R_s + R_1 + R_{eq}}\right) \\ &= V_s\left(\frac{k^2 L_1}{C_2(R_s + R_1)(R_L + R_2) + k^2 L_1}\right) \\ P_{out} &= V_s^2\left(\frac{k^2 L_1 C_2 R_L}{(k^2 L_1 + C_2(R_s + R_1)(R_L + R_2))^2}\right). \end{aligned} \tag{4.15}$$

Solving Equation 4.16 can lead to the load impedance that maximizes power transfer, given all other inductive coupling conditions.

$$\frac{\partial P_{out}}{\partial R_L} = 0. \tag{4.16}$$

The solution to this equation is shown here:

$$R_{L,opt} = R_2 + \frac{k^2 L_1}{C_2(R_s + R_1)} \tag{4.17}$$

Setting $R_s = 0$, which is a somewhat reasonable assumption given good practice

power amplifier design[2], and substituting R's for Q's further simplifies the equation:

$$\begin{aligned} R_{L,opt} &= \frac{\omega L_2}{Q_2} + \frac{k^2 Q_1}{\omega C_2} \\ &= \frac{1}{Q_2}\sqrt{\frac{L_2}{C_2}} + k^2 Q_1 \sqrt{\frac{L2}{C_2}} \\ &= \boxed{\sqrt{\frac{L_2}{C_2}}\left(\frac{1 + k^2 Q_1 Q_2}{Q_2}\right)} \end{aligned} \tag{4.18}$$

Equation 4.18 shows that the ideal load impedance (i.e., the value of R_L that maximizes power transfer to itself) changes with the distance between coils (i.e., k). It is also dependent on the ratio of secondary reactance values and the coil quality factors. Thus, the optimal impedance depends on the coil separation, as well as their geometry. Figure 4-8(a) plots the optimal load impedances across all practical values of k for the particular inductive parameters indicated in the figure caption. In this example, R_L varies from a minimum of 3.6 Ω at $k \approx 0$, to a maximum of 17 kΩ at $k = 1$. Interestingly, the optimal R_L at low coupling coefficients is exactly equal to the parasitic resistance of the secondary coil, R_2, as can be inferred by Equation 4.17. This makes sense, since the state of the secondary circuit has almost no bearing on the primary circuit under low coupling conditions (i.e., its reflected impedance to the primary is negligible). Thus, a maximum power matching circuit on the secondary is the configuration that extracts the most power. At higher levels of coupling, reflected impedances are no longer negligible. Thus, matching R_L to R_2 would significantly load the primary circuit, thereby falling out of a maximum power transfer condition.

Figure 4-8(b) shows the extractable output power from the same inductive coupling setup as described in Figure 4-8(a), but this time plotted for varying output loads and coupling coefficients. Also shown is the theoretically maximum attainable output power and the associated load resistances for k varying from 0.001 to 0.5. At low coupling coefficients, the optimal R_L is small, as is the maximum ex-

[2]Alternatively, R_s can be lumped into the definition of the primary quality factor: $Q_{1,mod} = \omega L_1/(R_s + R_1)$.

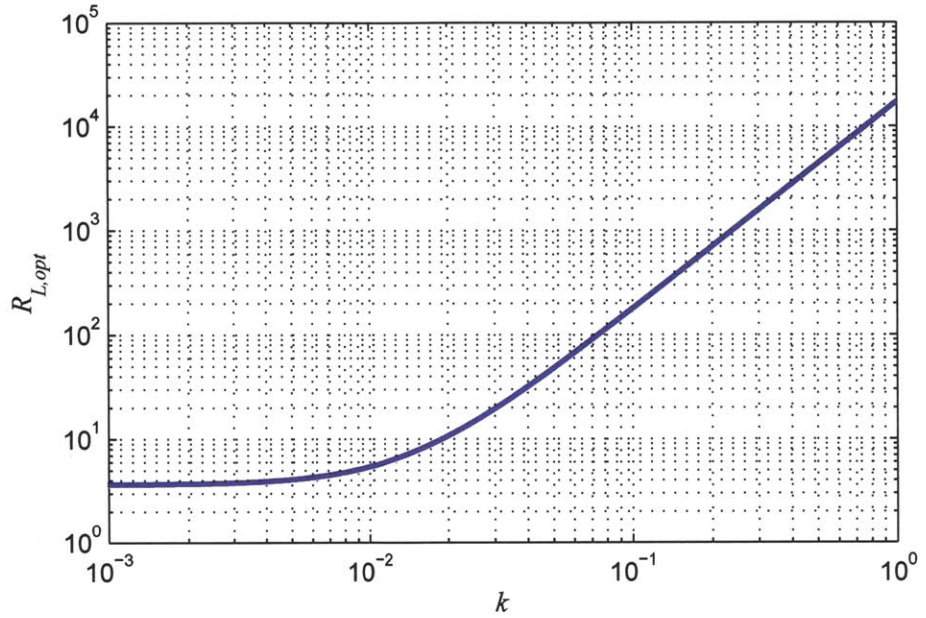

(a) Load impedances that maximize power transfer plotted across all practically useful coupling coefficients.

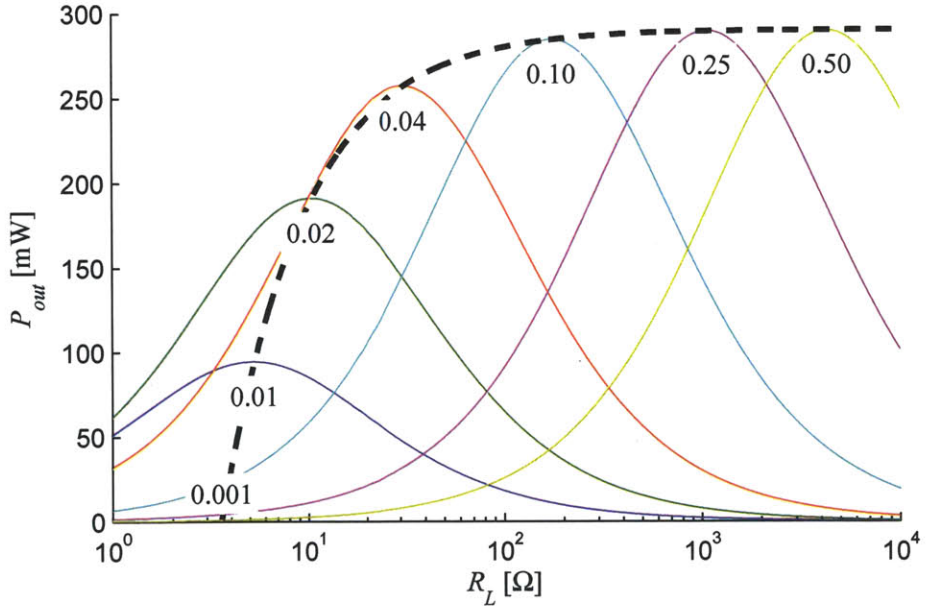

(b) Amount of extracted output power plotted across a range of load resistances for various values of k (whose values are annotated in plain text on the figure). The solid dashed line represents the maximum extractable power for a given k, while also lining up with the associated optimal R_L for the given k.

Figure 4-8: Load impedances that maximize power transfer. In this example, $V_s = 3.3$ V_{p-p}, $f = 6.78$ MHz, $L_1 = 3.3$ μH, $L_2 = 6.7$ μH, $Q_1 = 60$, and $Q_2 = 80$.

tractable power. As k increases, the optimal R_L and associated extractable power increases. Although $R_{L,opt}$ continues to increase with k, $P_{out,max}$ sees diminishing returns, eventually plateauing beyond coupling coefficients greater than 0.2. This also matches intuition very well – at high values of k, the reflection coefficient becomes large, requiring a large R_L (due to the inverse relationship) to create an impedance that matches $R_2 + R_s$. At this point, the reflected $k^2L_1/(C_2R_2)$ becomes very large relative to $k^2L_1/(C_2R_L)$, making its effects negligible. Thus, the maximum power transfer theory can be simply applied here: $k^2L_1/(C_2R_L) = R_2 + R_s$, resulting in 50% power transfer efficiency. In this example, 300 mW is thus the source-limited maximum power available to be delivered to the load.

It is important to note here that these curves are very setup-specific. For example, imagine designing an inductive link for a coupling coefficient of 0.1 and a load impedance of 170 Ω. At these conditions, 285 mW would be delivered to the load. If the coupling coefficient was increased to 0.25, perhaps because a different patient has a thinner skin thickness, then for the same load impedance the extractable power drops by 2X to 137 mW. As a result of this sensitivity, inductive systems are typically either designed for a worst-case scenario, having on-board regulators dissipating any excess received power, or they are designed with some sort of feedback communication system in order to modulate the amount of delivered power.

Note that the analysis presented in this section is specifically geared towards maximizing power transfer. Appendix B describes how the presented analysis can also be applied to instead determine the conditions for maximum power transfer efficiency.

Summary

This section has shown how to analyze inductively coupled links for the purposes of deriving theoretical maximal limits on efficiency and power transfer. It was shown that extracting maximum power depends on the load impedance, the coupling coefficient, and the ratio of secondary reactances. As will be shown in Section 4.3.1, the problem of charging a capacitor involves dynamically changing load impedances. The

analysis provided in this section will give insight as to what circuit or architectural solutions may be appropriate for solving the varying impedance problem.

4.3 Wireless Capacitor Charging Challenges and Solutions

4.3.1 Charging a Capacitor - Instantaneous Resistance

AC to DC converters employ the use of non-linear elements such as diodes to perform rectification. This makes rectifier modeling challenging, as large-signal analysis is typically required. Although solutions may exist under steady-state conditions, capacitor charging is by definition a transient event. Thus, it is very difficult to derive precise analytical expressions that provide design insight.

Instead, design insight can be attained by observing the behavior of analogous circuits. Consider, for example, a simple RC circuit in Figure 4-9, where the capacitor is charged from a step voltage. If the input step occurs at time $t = 0$, the output voltage is given by:

$$V_{out}(t) = V\left(1 - e^{-t/RC}\right), \quad t \geq 0. \tag{4.19}$$

Similarly, the loop current is given by:

$$I(t) = \frac{Ve^{-t/RC}}{R}, \quad t \geq 0. \tag{4.20}$$

So at $t = 0$, $V_{out} = 0$ and $I = V/R$, while at $t = \infty$, $V_{out} = V$ and $I = 0$. The *instantaneous resistance* can then be found by dividing $V_{out}(t)$ by $I(t)$:

$$R_{C,inst}(t) = \frac{V_{out}(t)}{I(t)} = R\left(e^{t/RC} - 1\right), \quad t \geq 0. \tag{4.21}$$

At $t = 0$, the instantaneous resistance of the capacitor is zero; that is, the capacitor is able to sink as much current as limited by R. At $t = \infty$, the instantaneous resistance becomes infinite; that is, no current is able to enter the capacitor. Figure 4-10 shows

the transient results of a representative example.

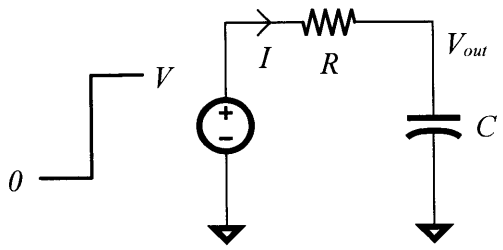

Figure 4-9: Charging a capacitor at DC with a voltage step.

This situation is analogous to charging a capacitor from an AC source – at $t = 0$ the capacitor is fully discharged, and can accept as much current as possible, limited only by rectifier losses. In other words, its instantaneous resistance is zero. Provided there is no resistive load in parallel, the capacitor cannot be further charged once steady-state is reached at $t = \infty$, and therefore its effective impedance is infinite.

Another way to think about this problem is by considering AC-charging a capacitor that is so large it can effectively be modeled by a DC voltage source over sufficiently short periods of time, as in Figure 4-11. Then, using the same averaging technique as used for the boost converter in Section 3.4.2, the rectifier can be modeled with an effective resistance, R_D.[3]

On average, the current flowing into the rectifier is given by:

$$I_{in} = \frac{V_{in} - V_{out}}{R_D}. \tag{4.22}$$

Thus, the average input resistance of the circuit is:

$$R_{in} = \frac{V_{in}}{I_{in}} = \frac{V_{in} R_D}{V_{in} - V_{out}}, \tag{4.23}$$

[3]This resistance implicitly includes a conduction angle factor based on the fact that the diodes do not conduct all the time. A different model could include a resistance in series with a voltage source, modeling the average diode drop. Regardless, this analysis is not meant to be quantitative or extremely precise, but is instead used to offer a more qualitative understanding.

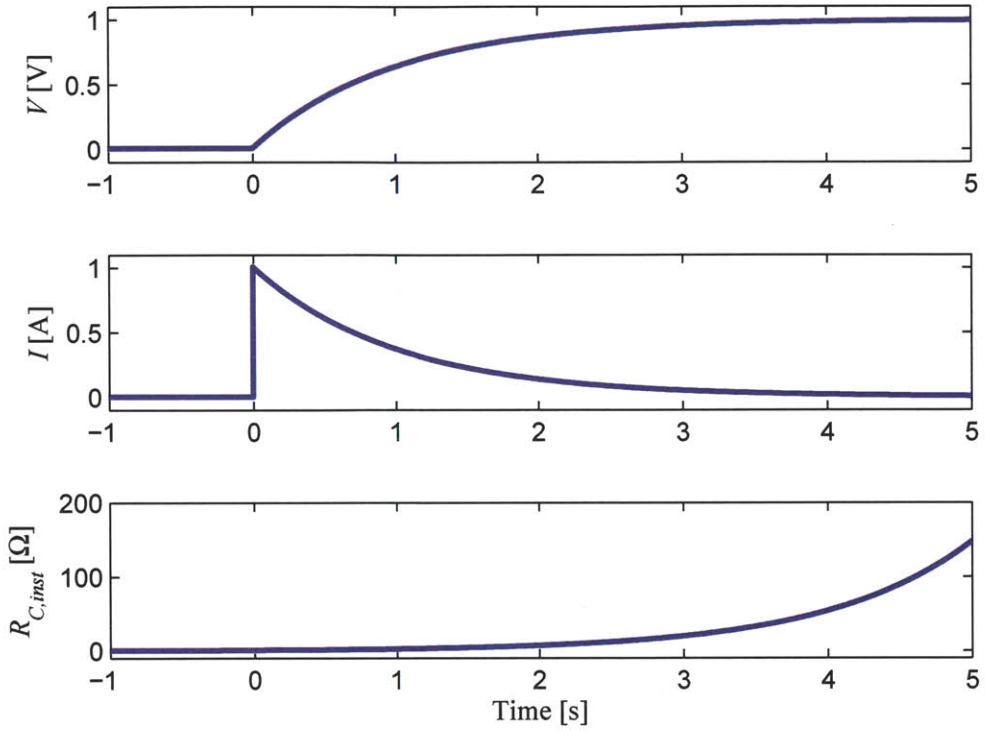

Figure 4-10: Transient results of charging a 1 F capacitor from a 1 Ω source impedance to 1 V.

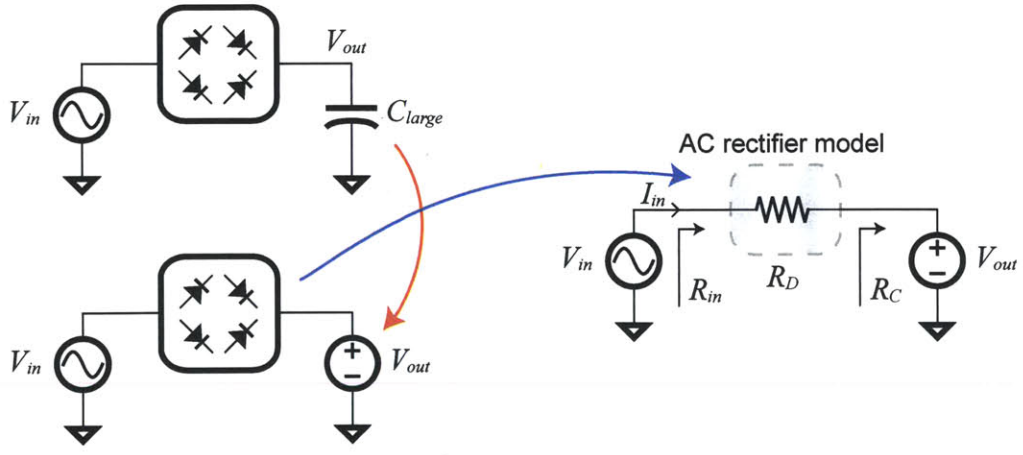

Figure 4-11: Model used to calculate instantaneous charging capacitor resistance.

and the instantaneous capacitor impedance can be given by:

$$R_C = R_{in} - R_D = \frac{V_{in}R_D}{V_{in} - V_{out}} - R_D = \frac{V_{out}R_D}{V_{in} - V_{out}}. \tag{4.24}$$

As with the step-response analysis, the instantaneous resistance of the capacitor is zero when its voltage is zero. Similarly, when its voltage is equal to V_{in}, its instantaneous resistance is infinite. In between, the capacitor's instantaneous resistance depends not only on the output voltage, but also the input voltage, and the effective diode resistance, which in itself will also likely change with voltage (or current). Further modeling of these effects are certainly possible, though for the following analysis, it is sufficient to only qualitatively understand this phenomenon.

The Main Issue for Inductive Coupling

As discussed in Section 4.2.2, given an inductive coupling setup fully defined in terms of L's, C's, R's, and k, there exists an optimal load resistance that maximizes the power transfer to said load. Unfortunately, the instantaneous resistance of a charging capacitor changes with its own voltage. As a result, there will only be a single point in time when conventional wireless energy delivery circuits are delivering maximum power to the implanted capacitor. To overcome this issue and provide maximum power for larger portions of the charging time, a proposed solution should either alter the effective load impedance in some way, or alter the setup of the inductive coupling circuit in some manner. Importantly, the ideal load impedance should be tunable not only to address changes in instantaneous capacitor resistance, but also to support robustness against coil separation distance (i.e., k).

Appendix C proposes several methods to alter the load impedance to match the ideal impedance, given coil geometry and k. However, since there are pitfalls associated with all proposed approaches, the following section discusses an alternative technique that instead alters the characteristic inductive coupling equations.

4.3.2 Proposed Solution: Multi-tap Secondary

Theory

Equations 4.18 and B.2 suggest that for given coil geometrical parameters and separation distances, there exists an optimal load impedance that either maximizes the total amount of power delivered to the load or maximizes power transfer efficiency. The solutions proposed in Appendix C served to modify the load impedance (in this case, the instantaneous resistance of a charging capacitor) to match the optimization criteria. This impedance modulation can be performed dynamically to provide robustness to dynamically changing load impedances, or it can be performed semi-statically to provide robustness against variations in coil separation distances. Unfortunately, all of the proposed solutions have pitfalls in terms of efficiency, charging-time degradation, or practicality.

Fortunately, there is an alternate knob that can be used to adjust the system. Equations 4.18 and B.2 show that the optimal impedance also depends on the ratio of secondary reactances: $\sqrt{L_2/C_2}$. Under resonant conditions, L_2 and C_2 are naturally related by the following relation: $\omega_o = 1/\sqrt{L_2 C_2}$. Thus, the optimal impedance for maximum power transfer shown in Equation 4.18 can be re-written in terms of either C_2 or L_2, the latter of which is shown here:

$$R_{L,opt} = \omega_o L_2 \left(\frac{1 + k^2 Q_1 Q_2}{Q_2} \right). \tag{4.25}$$

Changing the value of L_2 (and, correspondingly, C_2) can therefore change $R_{L,opt}$ for a given k. For example, Figure 4-12 illustrates $R_{L,opt}$ plotted versus k for three separate values of L_2. With this design insight, a circuit that can change L_2 and C_2 can, at any point in time and for any k, change $R_{L,opt}$ to equal the charging capacitor's instantaneous resistance (R_C) at that precise instance in time. This directly solves the underlying issue – it would be possible to ensure the circuit is always delivering energy either at the maximum transfer point, or while operating with the highest possible efficiency.

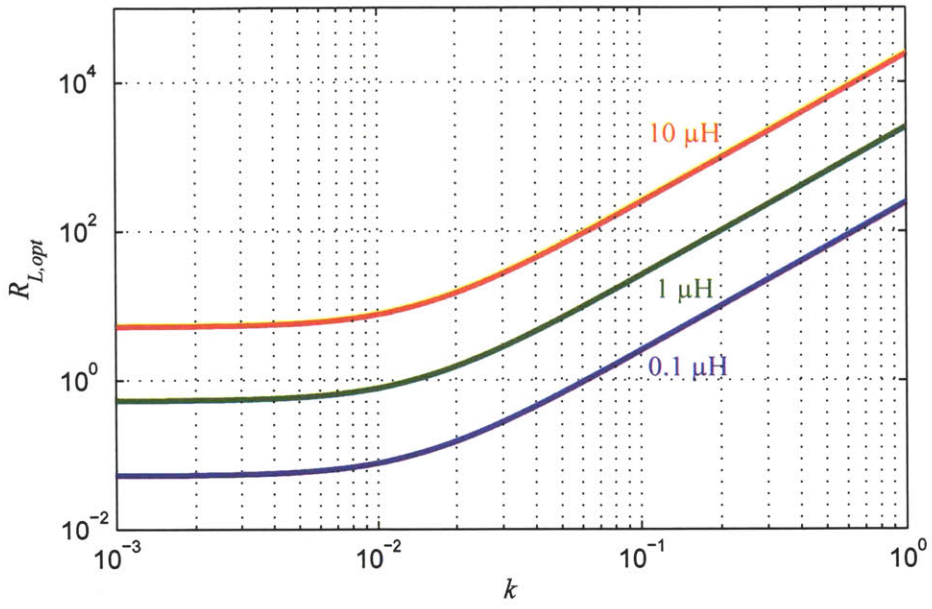

Figure 4-12: Plot of $R_{L,opt}$ over all practical values of k for three different values of L_2. In this example, $V_s = 3.3$ V_{p-p}, $f = 6.78$ MHz, $L_1 = 3.3$ μH, $Q_1 = 60$, and $Q_2 = 80$. The maximum output power is identical to the power-optimized curve shown in Figure B-1(b).

Naturally, the complication here is that tunable inductors are difficult to implement. However, others have described tunable inductors for RFIC applications by using interesting bridge topologies [163] or multi-tap structures [164]. Even an inductor with three taps (i.e., three quantized inductance values) can provide substantial performance benefits. For example, Figure 4-13 details analytical results of power delivered to R_L for various values of k typically found in transcutaneous charging applications. Specifically, each plot contains three curves for three separate values of L_2: 0.1 μH, 1 μH, and 10 μH in blue, green, and red, respectively. These results show that even with only three taps, a wide-range of $R_{L,opt}$ can be covered over the applicable range of k. Additionally, L_2 can be dynamically changed for a given k: as the capacitor charges, R_C increases, and the appropriate value of L_2 can be used such that instantaneously R_C is as close as possible to the selected value of $R_{L,opt}$.

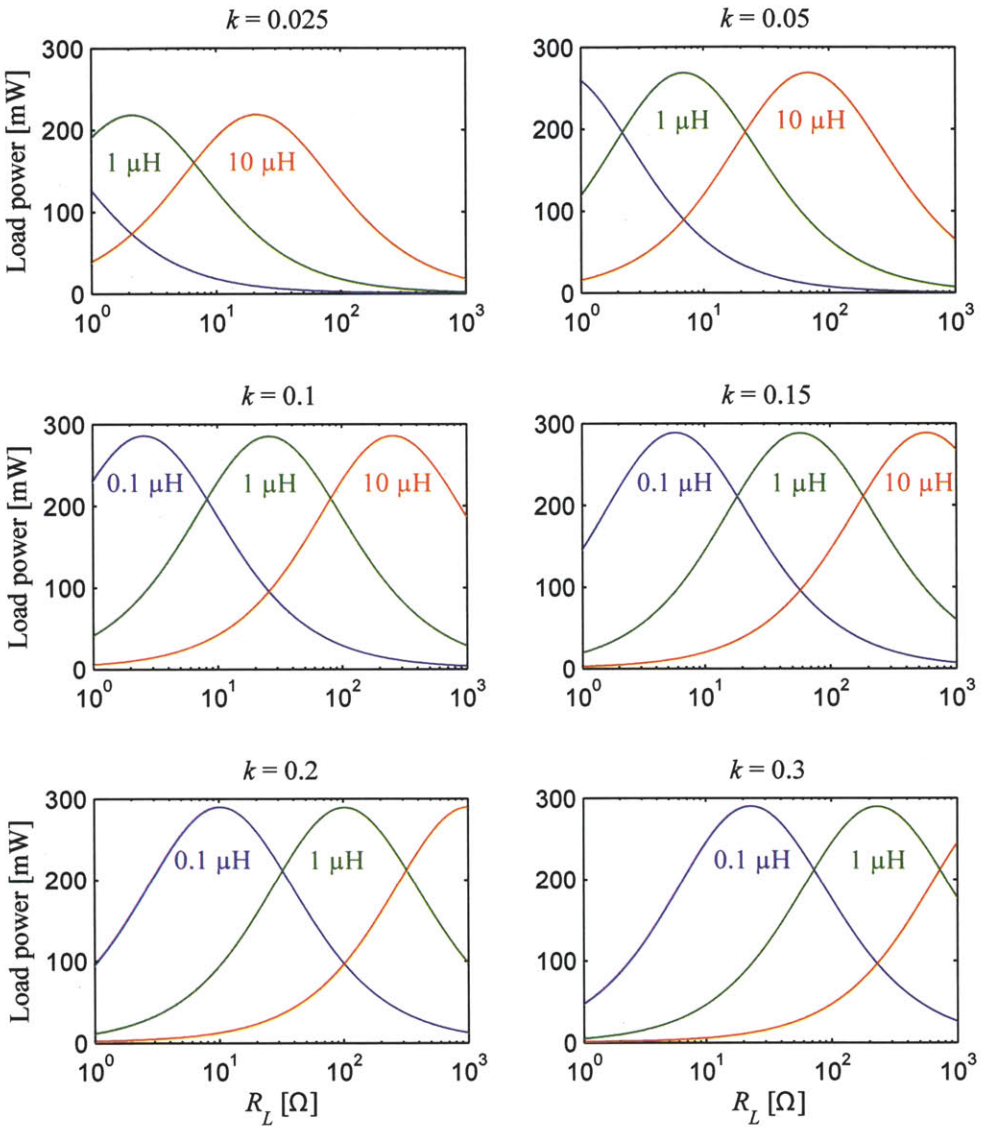

Figure 4-13: Power delivered to R_L across various values of R_L and a few select values of k. In these plots, the blue, green, and red curves correspond to secondary inductances of 0.1 μH, 1 μH, and 10 μH, respectively. Additionally, $V_s = 3.3$ V_{p-p}, $f = 6.78$ MHz, $L_1 = 3.3$ μH, $Q_1 = 60$, and $Q_2 = 80$.

Architecture

The architecture of the proposed multi-tap-secondary inductive coupling system for rapid wireless capacitor charging is shown in Figure 4-14. The secondary coil is designed as a single large coil with inductance L_{23}. Two smaller inductances, L_{22} and L_{21}, are created by tapping into fewer turns of the coil. Each tap is allocated a single series capacitor used to resonate with the effective inductance seen at the output of the tap. The output of the series capacitors are connected to series switches, used to select a single tap configuration at a time. For an initial proof-of-concept demonstration, this architecture was implemented as a discrete prototype.

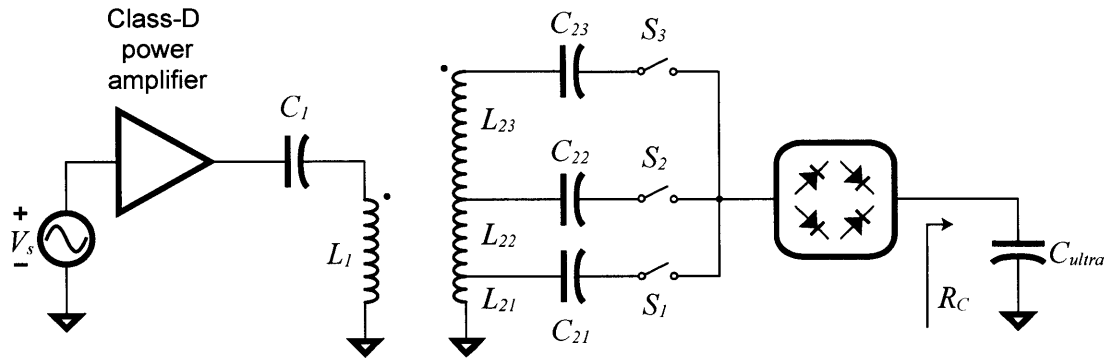

Figure 4-14: Architecture of the proposed multi-tap-secondary rapid wireless capacitor charger.

Design of the series switches is challenging. To have minimal effect on the inductor quality factors, the switch should be designed with as low on-resistance as possible. However, low-impedance switches typically have large associated parasitic capacitances. This presents a classic engineering trade-off: should resources be allocated to minimizing switch on-resistance or parasitic capacitance? Additionally complicating the matter is the need for high voltage-blocking capabilities. To appreciate this issue, consider the following scenario: switch S_1 is on, and switches S_2 and S_3 are off. Inductor L_{21} is resonating with capacitor C_{21}, and current is flowing through the rectifier, thereby charging C_{ultra}. Due to series resonance, the voltage at the node connecting L_{21} and C_{21} is Q multiplied. Since switches S_2 and S_3 are off, current in

those branches are zero. As a result, the voltages at the inputs to S_2 and S_3 are at the same Q-multiplied level at the node connecting L_{21} and C_{21}. Since intrinsic Qs can be high – upwards of 100 for example – this appears to be a major issue. However, actual realized Qs are always much lower due to the loading effects of the rectifier and R_C. That being said, it is still important to maximize switch voltage-blocking capabilities for reliable operation.

As discussed in more detail in the following subsection, the discrete prototype design employs the use of a secondary inductor that is 25 mm in diameter. At this size, a total of 20 turns achieves an approximate inductance of less than 10 μH. At an operational frequency of 6.78 MHz, this results in a minimum series tuning capacitance of approximately 50 pF. To avoid disrupting resonant conditions, a switch should be selected such that its parasitic capacitance resides below this value. Thus, a Panasonic AQY221R2V solid-state optoelectronic relay was chosen as the switching element for this discrete prototype. Its specifications meet the requirement of this application: its on-resistance is 0.75 Ω, its parasitic capacitance is 12.5 pF, and it can safely block 40 V. When turned on, the relay requires approximately 5 mW to operate.

Many inductively-coupled applications employ the use of class-E power amplifiers on the primary circuit for high efficiency [165]. However, a class-E amplifier requires very precise knowledge of the load impedance in order to operate properly (and therefore at high efficiency) [40]. As previously discussed, inductive coupling systems operating with varying k and R_C conditions can present wildly varying impedances as seen by the primary, making the design of uncompensated class-E amplifiers impractical for these cases. To combat this issue, others have described interesting control loops to provide robustness against load variations that offer promising potential [166]. On the other hand, class-D amplifiers can operate reasonably efficiently without significant regard for load impedances. Consequently, such an amplifier was chosen for this initial proof-of-concept. Specifically, the amplifier was implemented as an inverter structure with NDS351AN and FDN360P NMOS and PMOS transistors, respectively.

The rectifier is composed of four Panasonic DB2S205 Schottky diodes in a bridge configuration.

Coil Design

The primary and secondary coils in the discrete prototype are both designed as printed inductors on an FR-4 substrate circuit board. The primary coil is an $N = 8$ turn design, while the secondary coil is an $N = 18$ turn design with an additional two taps after turns 2 and 5. Both coils are printed using 2-oz copper with a trace width/spacing of 0.2 mm. In terms of size, the primary coil is designed with a diameter of 30 mm, while the secondary coil is designed to be slightly smaller at 25 mm for robustness to mis-alignment. These types of sizes are often found in existing cochlear stimulation devices.

Electromagnetic simulations were performed using Mentor Graphics IE3D to extract inductance and mutual coupling information. A 3D visualization of the simulation setup of the five-port network is shown in Figure 4-15, and a summary of parameters are shown in Table 4.2.

Table 4.2: Simulated coil parameters.

	L_1	L_{21}	L_{22}	L_{23}
N	8	2	5	18
L [μH]	3.31	0.28	1.25	6.73
R_{series} [Ω]	2.02	0.47	1.10	3.07
Q	70	26	48	93
C_{tune} [pF]	167	1954	443	82

The quality factor is simulated to be higher for inductors with larger turns ratios. This matches theory well, as inductance increases with the square of the number of turns, while resistance increases only linearly with the number of turns [100]. Figure 4-16 shows the coupling coefficient of the structure, simulated across several different coil separation distances. Interestingly, the coupling coefficient is greater

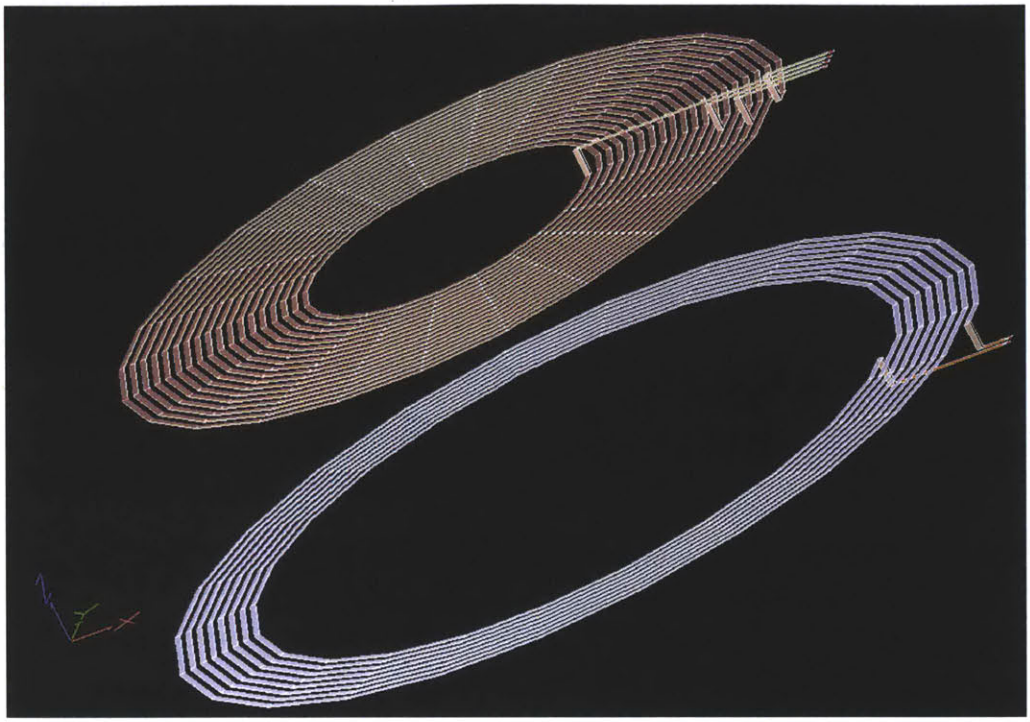

Figure 4-15: Electromagnetic simulation setup of the multi-tapped secondary and conventional primary coils.

for the larger secondary inductances. This is purely due to the non-overlapping trace geometry occupying a larger area for a larger number of turns. Since the skin effect for such trace thickness is negligible, simulation results found that 2-oz copper increased the quality factor of the coils by 2X over 1-oz copper, as expected. A photograph of the manufactured secondary coil is shown in Figure 4-17.

To set more realistic expectations, the results originally shown in Figure 4-13 are re-calculated using the actual realized inductance values and quality factors. In addition, a 0.9 Ω source resistance was included in the calculation of Q_1, while a 0.75 Ω switch resistance and 3 Ω equivalent rectifier resistance was included in the calculation of Q_2. The results of these analytical calculations are shown in Figure 4-18. At low values of R_L, I^2R losses in the secondary parasitics consume a large fraction of the total available power to the load, thereby limiting the effectiveness of this technique. However, this effect is most pronounced at low k with low secondary inductances; the small amount of passive gain from the inductive turns ratio limit the

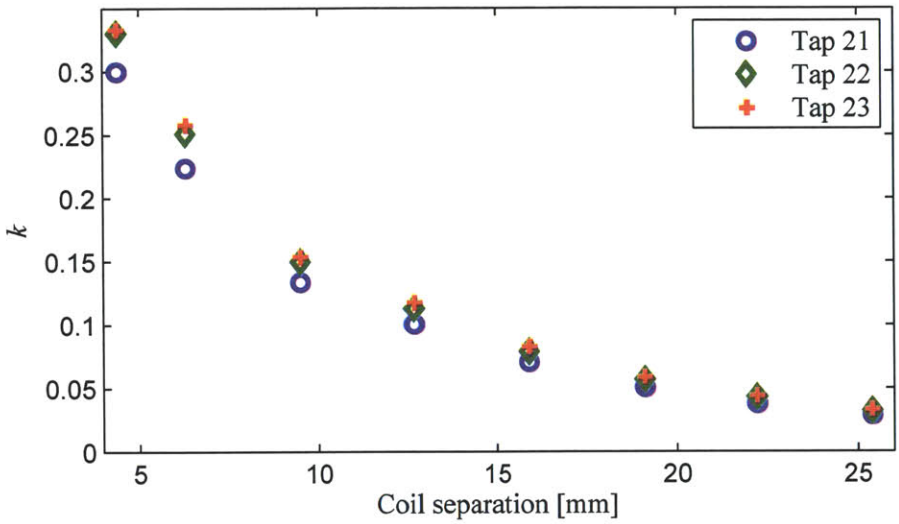

Figure 4-16: Simulated coupling coefficients for various coil separation distances.

Figure 4-17: Photograph of the secondary three-tap coil.

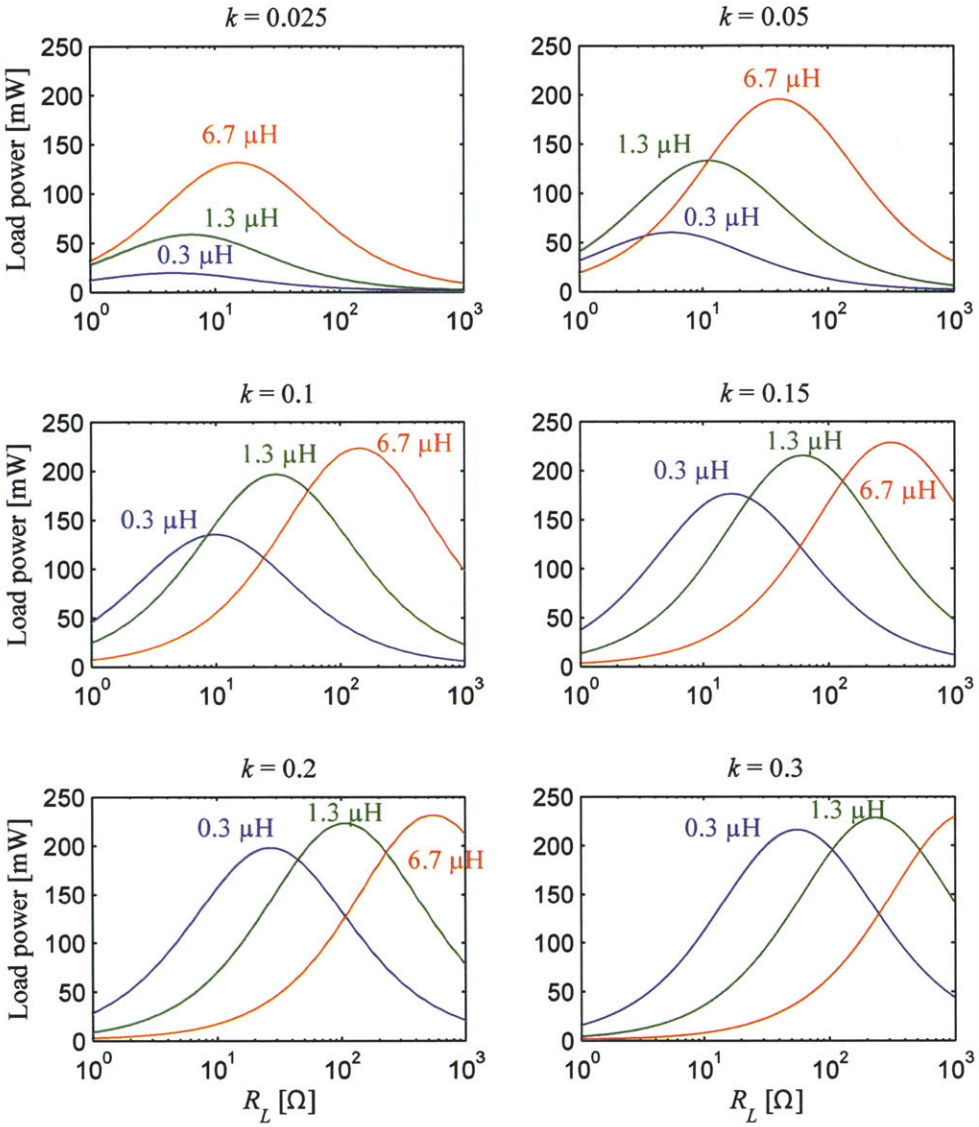

Figure 4-18: Power delivered to R_L across various values of R_L and a few select values of k. In these plots, the blue, green, and red curves correspond to secondary inductances of 0.28 μH, 1.25 μH, and 6.73 μH, respectively. Additionally, $V_s = 3.3$ V_{p-p}, $f = 6.78$ MHz, $L_1 = 3.3$ μH. $Q_{1,eff} = 48$, $Q_{21,eff} = 2.8$, $Q_{22,eff} = 11$, and $Q_{23,eff} = 42$.

usefulness of this configuration anyway. Thus, at low-k, it is almost always beneficial to use a high value of L_2, resulting in a higher $R_{L,opt}$ and therefore a lower proportion of I^2R losses relative to delivered load power. On the other hand, this technique permits much higher power delivery at high-k configurations over a wide range of load impedances.

4.4 Discrete Prototype Measurement Results

The discrete prototype was tested in a regular electronics lab environment using nylon board-spacers of various lengths to separate the primary and secondary coils. A photograph of the testing setup is shown in Figure 4-19. Voltage and power monitoring are simultaneously performed using a Keithley 2400 sourcemeter at the output of the rectifier.

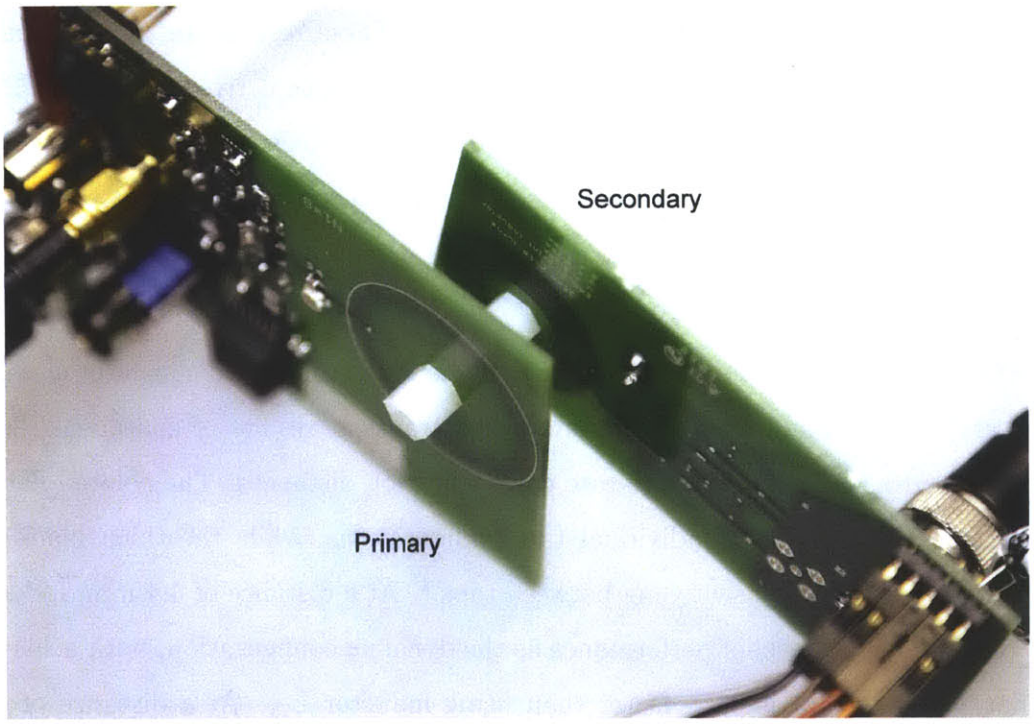

Figure 4-19: Photograph of the testing setup for the rapid wireless capacitor charger.

Figure 4-20 demonstrates the benefits of using a multi-tapped secondary coil. Across various distances and output capacitor voltages, it is clear that not a single

tap configuration offers the best performance. At close coil separation distances (i.e., high-k), inductor L_{21} delivers the most power to the load, while inductor L_{23} delivers the most power to the load at long distances (low-k). At intermediate distances, dynamically switching between secondary coil configurations as the output capacitor voltage increases can achieve superior power delivery results.

Also shown in Figure 4-20 are measurement results from a board that did not include the series switches; instead, the output of the second tap (i.e., L_{22} and C_{22}) was directly connected to the rectifier. Since the overall extractable power is not significantly higher in this configuration, these measurement results demonstrate that a multi-tap secondary is still beneficial, even when taking into account series switch losses and activation power consumption.

Since it is difficult to analytically model a rectifier feeding a DC voltage source, the x-axis shown in Figure 4-20 is converted to resistance values by dividing the output capacitor voltage by its incoming current. These results are then compared in Figure 4-21 to analytical predictions using the equations derived in Section 4.2.2, under the same conditions as stated in Figure 4-18. Measured results match the theoretically predicted behavior very closely for all tap configurations. Note that the measured output resistance is limited under certain tap and distance configurations due to output capacitor voltage limits.

The discrete prototype was also used to demonstrate improved capacitor charging time and range. Figure 4-22 shows measured transient results of charging a 2.5 F ultra-capacitor to 5V for two separate coil separation distances. The colored dashed lines correspond to static individual tap configurations, while the thick black line corresponds to dynamic switching between taps.[4]. At a distance of 4.4 mm, inductor L_{21} offers the same level of performance as the dynamic configuration, both achieving a charging time that is 3.7X faster than using inductor L_{23}. At a distance of 12.7 mm, however, inductor L_{21} requires an estimated 26 minutes to reach 5V, which is 10.3X slower than the dynamic configuration.

[4]A Keithley 2400 sourcemeter was used to measure the power of each tap at output intervals of 0.5 V to dynamically determine the optimal configuration

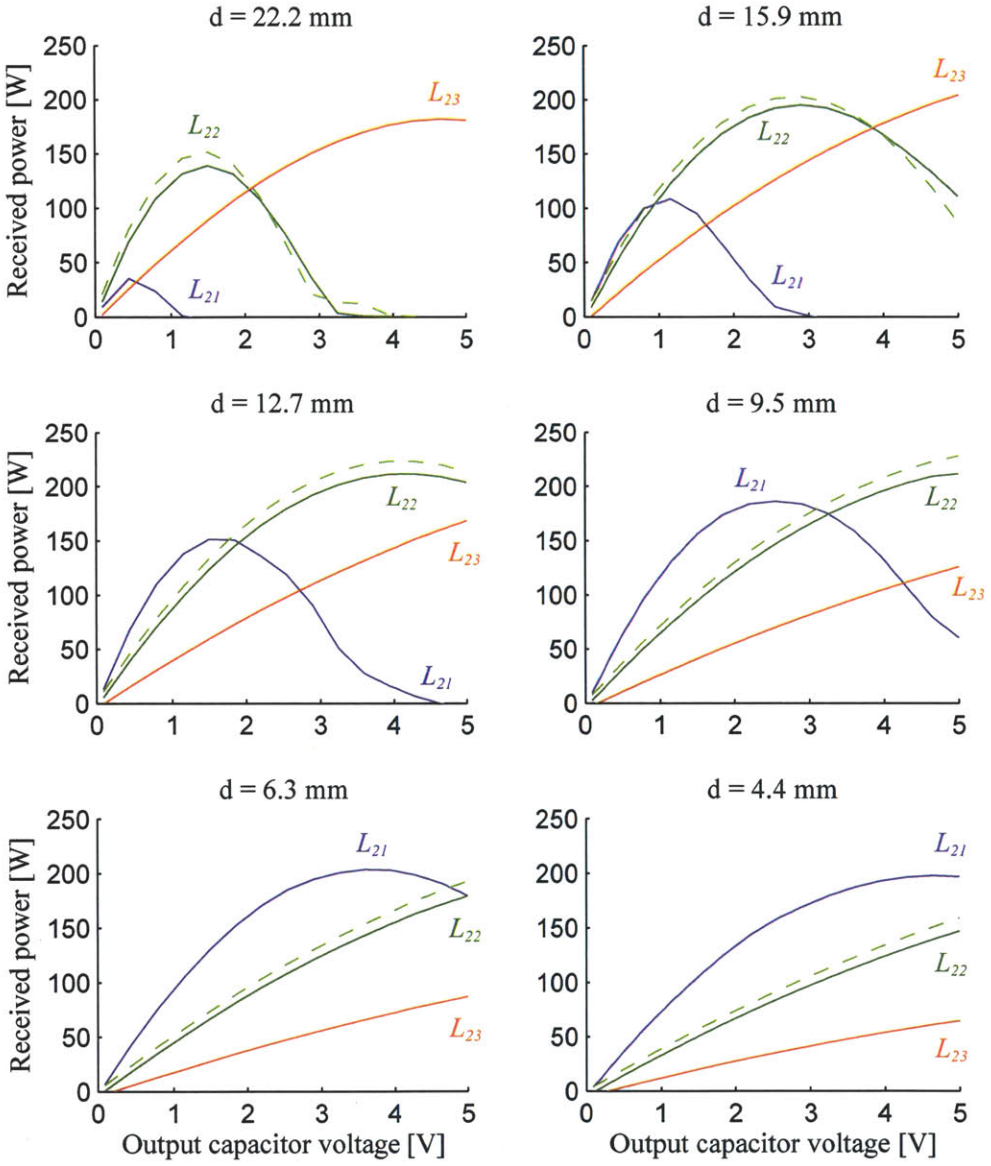

Figure 4-20: Power delivered to a Keithley 2400 sourcemeter set at fixed voltage values for a few select distances. In these plots, the overlaid solid blue, green, and red curves correspond to inductors L_{21}, L_{22}, and L_{23}, respectively. The light dashed green line corresponds to a fixed secondary tap configuration (i.e., without any series switches). Here, $V_s = 3.3$ V_{p-p} and $f = 6.78$ MHz.

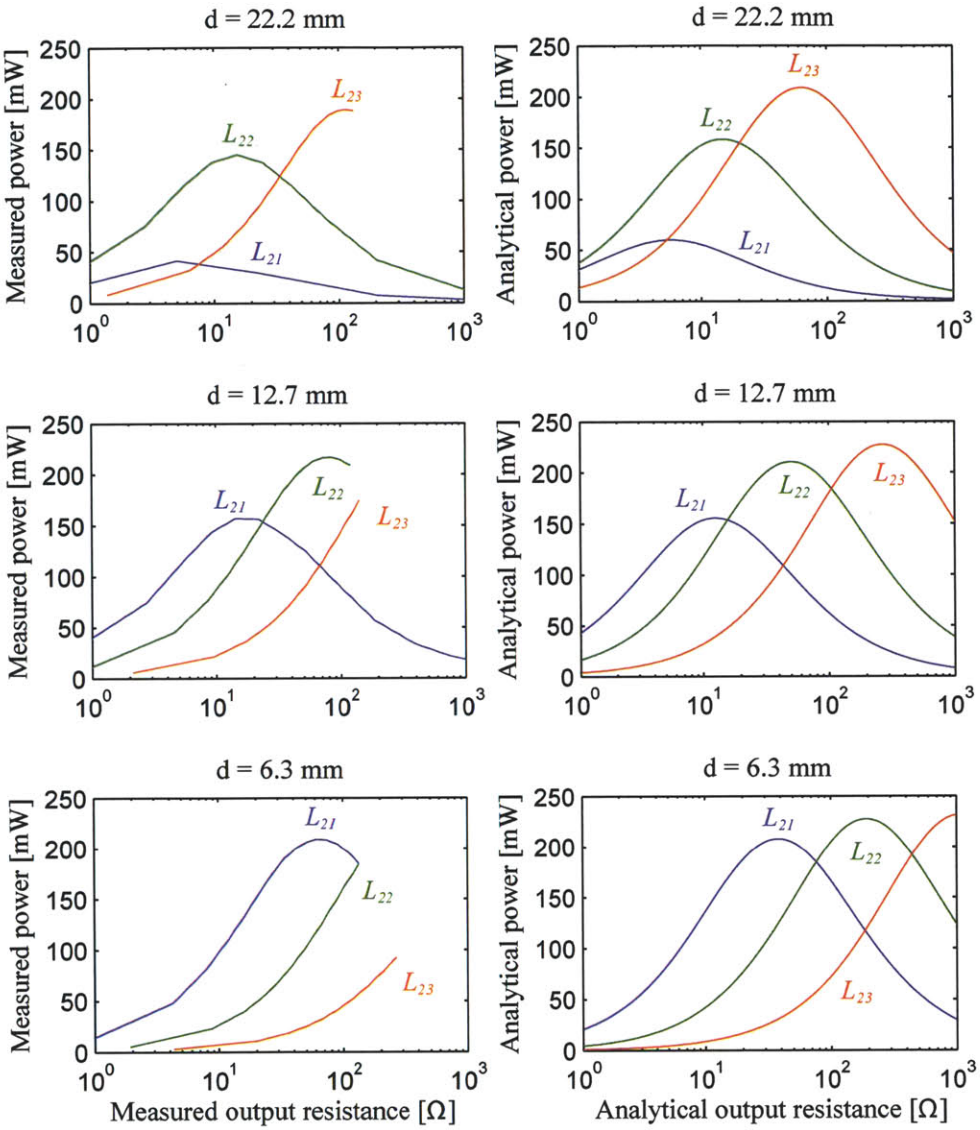

Figure 4-21: Measured power delivery compared to analytically predicted power delivery under the same conditions as in Figures 4-18 and 4-20.

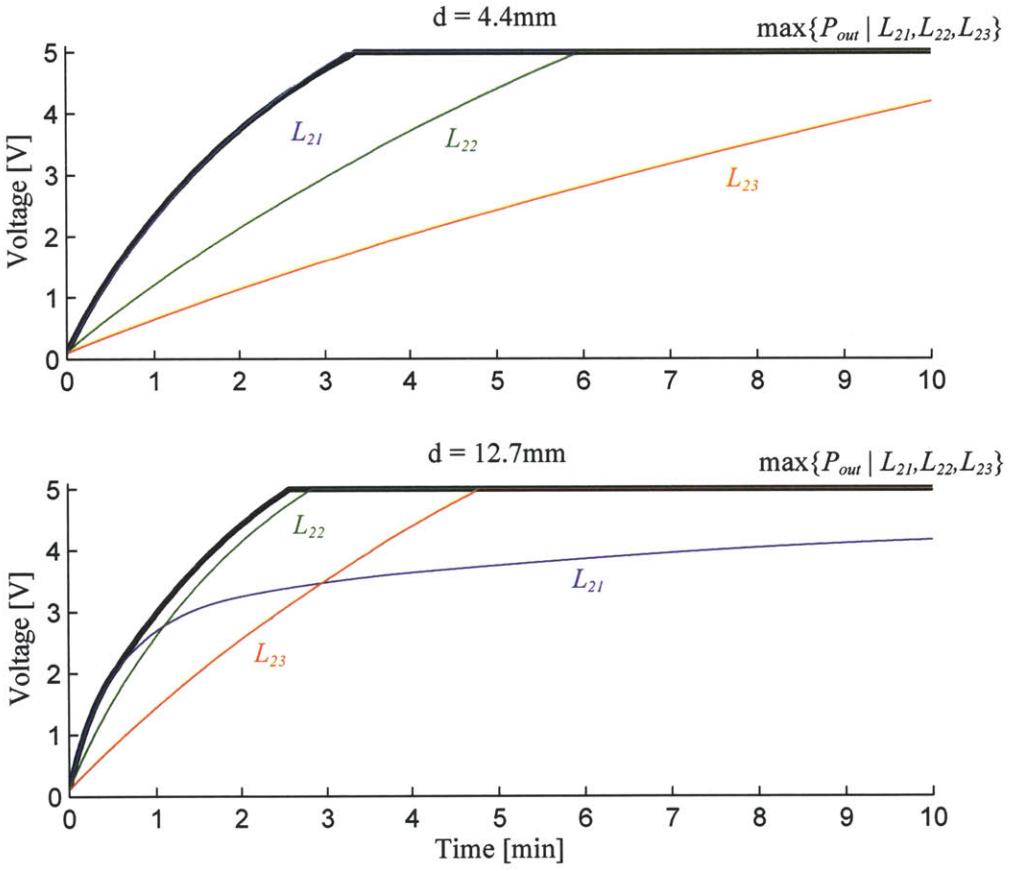

Figure 4-22: Transient measurement of charging a 2.5 F ultra-capacitor to 5 V. The thin blue, green, and red lines corresponds to exclusive use of inductors L_{21}, L_{22}, and L_{23}, respectively, while the thick black line corresponds dynamic switching between them.

Figure 4-23 summarizes charging time results plotted versus coil separation distance. As was observed from Figure 4-20, inductor L_{21} provides the best performance at small coil separations distances, inductor L_{22} at medium distances, and inductor L_{23} are long distances. Dynamically switching between taps offers the fastest charging time at essentially all distances, while also expanding the operational range by up to 2.5X.

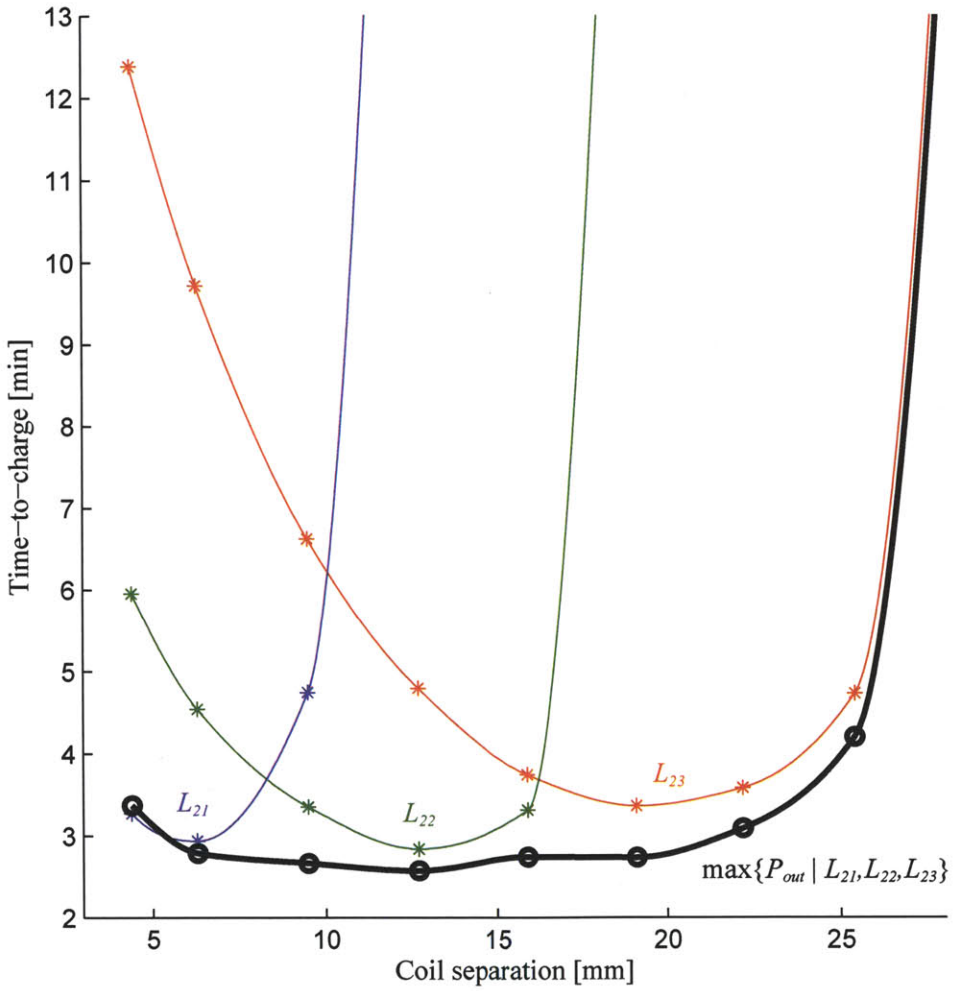

Figure 4-23: Charging time for a 2.5 F, 5 V ultra-capacitor. The thin blue, green, and red dashed lines corresponds to exclusive use of inductors L_{21}, L_{22}, and L_{23}, respectively, while the thick black line corresponds dynamic switching between them.

4.5 Conclusions

4.5.1 Summary

In order to achieve essentially unlimited device lifetime for implantable systems that have high power requirements, an ultra-capacitor is proposed for use as an implanted energy storage element. Since ultra-capacitors have lower energy densities than batteries, a wireless charging system is employed that provides sufficient energy for day-long operation under a once-per-day charging use-case. Wireless power transfer efficiency, which is optimized in nearly all inductive power transfer links, is in actuality a secondary concern to capacitor charging time under this particular use-case.

As a result, this chapter developed analytical circuit theory used to predict the value of load impedance that maximizes power transfer in a near-field inductive link. With insight derived from the developed equations, a multi-tap secondary circuit was proposed in order to alter the optimal load condition depending on coil-to-coil separations and the instantaneous resistance of a charging capacitor. A rapid wireless capacitor charging system was designed using the proposed techniques, demonstrating charging times that are up to 3.7X faster and operate over a 2.5X larger coil separation distance than conventional approaches.

4.5.2 Future Work: Power Monitor Circuit

The discrete prototype in this work utilized a Keithley 2400 sourcemeter to act as a power monitor in order to determine which of the three taps achieved the highest level of received power at various intervals in time during capacitor charging. For future integration work, there is need for a CMOS-compatible power monitor with low energy overhead. Fortunately, the design of such a circuit appears to be feasible. Figure 4-24 suggests a low-complexity architecture to achieve this goal. At certain intervals in time, which can be determined using either a counter or a voltage monitor, C_{ultra} is removed as the rectifier load, and one of three test capacitors are inserted in its place. Each of the test capacitors can be charged in succession for each tap

configuration, with charging occurring over either a fixed period of time or voltage. The C_{test} charging times or voltages can then be compared to see which of the three taps offers the highest level of performance. Given a power monitor on the primary side in addition to bi-directional communication, it is also possible to use such an architecture to maximize power transfer efficiency, should it be favorable over power transfer, given the specific application.

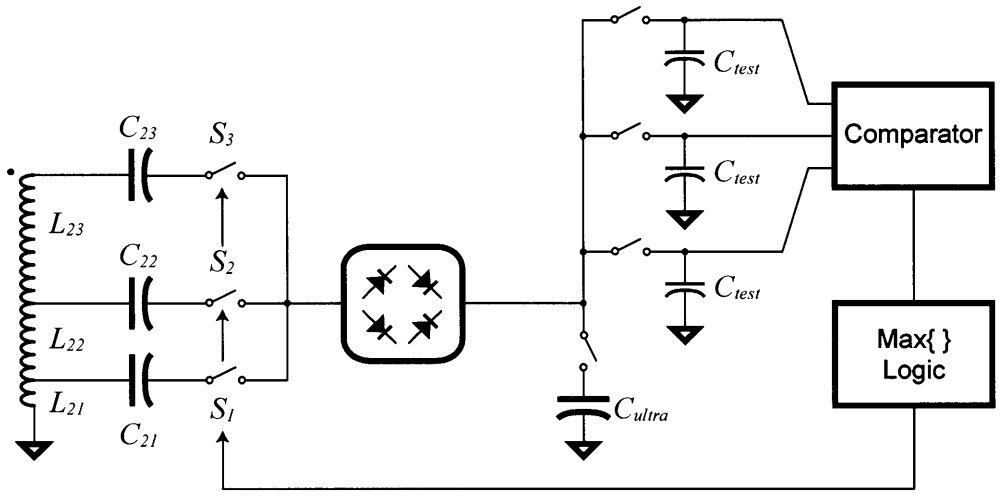

Figure 4-24: Block diagram of a simple power monitoring circuit which can be used to select which of the three taps offers the highest power transfer.

Chapter 5

Conclusions and Future Directions

5.1 Conclusions and Brief Summary of Contributions

The design of personalized biomedical devices present a tremendous opportunity for electrical engineers, biotechnologists, and clinicians to make significant contributions to society through the development of economic value, and by helping people live better, healthier lives. With today's aging population and skyrocketing medical costs, it is certainly an opportunistic time to undertake research and development of such devices.

In particular, many envisioned devices are currently not feasible in practice, fundamentally due to anatomical size constraints. Such size constraints limit the available volume of energy storage elements, thereby limiting the power consumption and therefore the functionality of underlying circuits for reasonable operational lifetimes. There are two proposed methods to combat this problem: 1) increasing total system energy efficiency, thereby providing sufficient functionality under extreme energy storage constraints, or 2) introducing energy into the system from other ambiently available energy sources.

The ability to increase efficiency or harvest ambient energy was primarily enabled using three hierarchically-related techniques. The first technique, *use-case engineer-*

ing, examined system usability issues from a patient's perspective. It was often found that the system energy allocation landscape could be dramatically altered for minor use-case changes or considerations. For example, employing as communication substrates textiles that patients already wear saved dramatic energy costs in body-area networks compared to existing wireless solutions. Deciding to harvest energy from the natural inner-ear battery was an example of use-case engineering in itself, as was the decision to provide a wireless start-up packet which obviated the requirement of sub-70 mV start-up circuitry. Also, designing a once-per-day charging use-case for high-power implanted systems created a new problem formulation: rather than optimize efficiency of wireless power transfer links, how can power transfer itself be maximized in order to minimize charging time?

Such use-case engineering ideas often led directly into the second employed technique: *architectural optimizations*. Maximizing wireless power transfer given coil separation parameters required a new inductive coupling architecture: a multi-tapped secondary circuit to dynamically switch between high-power transfer states. Similarly, extracting energy from the endocochlear potential required significant simplifications in the wireless transmitter architecture to achieve system-enabling levels of leakage power consumption. Employing a two-wire eTextiles interface not only permitted energy-efficient body-area network communication abilities, but also enabled efficient body-*energy*-network capabilities.

The final important technique employed to increase energy efficiency or enable ambient energy harvesting involved *circuit optimizations* at the bottom of the design hierarchy. For example, efficient supply-rail-coupled drivers, samplers, and analog-to-digital converters together with low-voltage digital design enabled an ultra-low-power eTextiles communication and power-delivery interface IC. Similarly, ultra-careful optimization of transistor leakage and active power consumptions enabled a transmitter and energy harvester IC that could operate with the endocochlear potential acting as the only source of energy into the system. Finally, careful coil design, selection of switches, and diodes enabled initial concept demonstration of the multi-tapped secondary coil architecture for rapid ultra-capacitor charging applications.

These techniques coalesced together to improve important system or sub-block metrics by 3–100X, while also enabling unique application opportunities. The following section discusses future implications and research directions of the presented work.

5.2 Future Directions

There are currently a great many unknown and potentially transformative applications that can be enabled through research and development of anatomically-scaled sensing and actuation systems. Such systems can offer new views into natural biological processes and can manufacture unique possibilities to administer closed-loop therapies for treatment of illness and disease. The opportunities in these areas are incredibly vast.

To create these opportunities, there are many exciting research challenges that must be solved in the area of electronics and in the life sciences. With regard to electronics, nearly universal requirements for personalized biomedical devices are the ability to communicate information and to manage their energy efficiently. Since the sub-systems that perform these tasks often dominate the power budget of these biomedical devices, this thesis examined the design of energy efficient communication and power management circuits and systems. It was found that circuits operating with sufficiently low power can enable unique system functionalities. There are many opportunities for future work in the specific areas covered in this thesis.

Body-Area Networks

The work presented in Chapter 2 demonstrated 1 m eTextiles communication circuits that consumed orders of magnitude lower energy than previously reported body-area networking systems. At such low-levels, communication circuits no longer dominate sensor-node power budgets. As a result, given an eTextiles medium, emerging research on body-sensing systems should instead focus on increasing sensing and processing efficiencies.

That being said, there are some practical considerations with regard to eTextiles that remain to be explored. For instance, built-in calibration routines could be developed to control and monitor transmitter voltage swings and receiver comparator thresholds for dynamic network-compensating adjustments. Although the snap-button interface was very simple and effective, it was still somewhat cumbersome to patients. Future work could investigate band-aid sensor nodes that wirelessly communicate over a centimeter range to an eTextiles node as in [55], which could then efficiently relay data over the body using the techniques developed in this thesis. Such wireless links could also be repurposed to simultaneously deliver power to the sensor node.

The ultimate goal of body-area networking is to relay data around the human body using the least amount of energy possible. In this regard, it would be beneficial to develop a BAN communication platform that dynamically changes its network configuration, similar in concept to a frequency-hopping cognitive radio system. For instance, the communication platform would always choose to use an eTextiles network should one be present. However, not all patients will necessarily wear the proper eTextiles clothing at all times. Thus, if an eTextiles network was not available, the platform could attempt both BCC and/or wireless communication at different frequencies to try to determine which medium and/or channel offers the best performance. Once a channel is selected, dynamic output power scaling should be employed depending on the channel characteristics in order to communicate with the minimum amount of power possible. The development of such network architectures requires innovation in the communication sub-systems and network protocols, presenting exciting research opportunities.

Wireless Energy Delivery

The rapid wireless capacitor charging system implemented in Chapter 4 is only a preliminary prototype. Based on measurement results it does, however, validate both its architectural motivation and the theory behind its operation. There are several interesting challenges in moving from a discrete prototype to a fully integrated sys-

tem. Although the prototype operates well below any SAR or FCC radiation limits as described in Appendix A, there is much research to be done on transient resistive tissue heating effects in order to determine what ultimately limits power delivery. Irrespective of these limits, an integrated power monitor circuit would be required as mentioned in Section 4.5.2. Of equal importance is design of the series switches selecting between various inductor taps. Although the employed optoelectronics relays can be manufactured in miniaturized packages, for system footprint reasons it would still be beneficial to investigate integrated switch designs. Also, as previously mentioned, an output voltage regulator would be required for load circuit compatibility. Preliminary research indicates that this is a problem that can indeed be solved [158].

Communication circuits, either employing back-scattered load modulation or an active radio should also be investigated in order to program the implanted device. A bi-directional communication system could potentially provide an opportunity to deliver maximally efficient energy to the charging ultra capacitor using the theory and techniques developed in this thesis. Additionally, it may be possible to achieve both high efficiency and power transfer by configuring the multi-tapped secondary in a maximum efficiency setting, while dynamically modulating the voltage of the primary power amplifier in order to deliver the requisite amount of power to the implant.

The ability to use an ultra-capacitor as an implanted energy storage element is increasing with improving energy densities. Although commercially-available devices do not yet offer sufficient energy density for day-long operation of a 1 mW load, future research directions indicate preliminary feasibility, particularly using carbon nanotubes or graphene [154, 167]. Beyond implanted systems, there is a potentially large market for rapid-charging ultra-capacitors, particularly in applications where charging times are critical. It may be possible, for example, to extend some of the research developed in this thesis to wireless capacitor charging applications in vehicular or consumer electronics.

Ultra-Low-Duty-Cycle Electronics and Energy Harvesting

The radio transmitter developed in Chapter 3 attained record-setting low power consumption primarily through significant leakage-power reduction techniques and aggressive duty-cycling. Radio transmitters are, however, only one block typically used in sensing platforms. Considerable research efforts can be envisioned in the design of other blocks such as sensor interfaces, analog front-ends, analog-to-digital converters, signal processors, and radio receivers. It is of particular interest to maintain energy efficiencies of such blocks down to ultra-low (i.e., less than once-per-minute) sampling rates. With additional leakage management efforts, previous work indicates preliminary feasibility - for example, an ADC that was not necessarily optimized for ultra-low-leakage achieved a 200 nW power consumption at a 500 S/s sampling rate [62].

Given the feasibility of extremely-duty-cycled, low-power sensing platforms, it is worthwhile re-visiting some of the energy harvesting sources discussed in Section 3.1. Although the available power from several of these sources such as ambient RF or microscale vibrations are both small and inherently intermittent, the development of sub-nW systems can considerably expand the available application spaces. It may still not be possible to use these sources to power devices that require continuous energy delivery such as pacemakers or cochlear stimulators; however, it may be possible to use these energy sources to power devices that monitor slowly varying biological signals. For example, sensing signals such as blood pressure, stomach pH, or blood sugar levels even a few times an hour can offer clinicians a new and extremely valuable view into how the human body functions under normal transient conditions while potentially avoiding the white coat effect [168]. The battery-less bio-compatibility of such energy autonomous systems is another significant advantage.

For bio-compatibility reasons, further developments in electrochemical energy harvesting systems requires additional innovations in electrode design. As briefly discussed in Chapter 3, the employed electrodes are still too large to completely avoid cellular damage during insertion. Transitioning to metallic electrodes using elements

such as platinum can potentially offer sufficiently low impedances while minimizing junction potentials. Alternatively, it may be possible to draw inspiration from electrodes used for neural recordings or stimulation that use carbon nanotubes or PEDOT coatings for improved impedance characteristics [169, 170].

On the other hand, sub-nW electronics together with ambient energy harvesting also offers a blueprint for the development of truly ubiquitous computing and sensing environments. Requiring such little power and system size, it is possible to envision distributed monitoring systems integrated with wallpaper, furniture, automotive frames, or clothing. Such "connected everything" networks can be used for a wide variety of applications, from smart-buildings to personal health monitoring.

The energy harvesting results in Chapter 3 demonstrated that it is possible to extract energy from a naturally-generated electrochemical potential in the inner-ear. Interestingly, most cells throughout the body have non-zero resting membrane potentials that, although not strictly at DC, are at similar voltage levels to the endocochlear potential. It is thus not out of the realm of possibility to envision cell-scale nano-robot sensing devices that harvest energy from these intracellular membrane potentials. An autonomous network of devices could be distributed throughout the body, with each unit navigating through space, extracting energy from cells, performing measurements or computations, all while communicating amongst each other. Figure 5-1 shows an illustration of a representative device.

Although this idea seems far-fetched, it is in fact very similar in concept to the endocochlear potential harvesting system presented in this thesis. Back-of-the-envelope power consumption estimations validate the possibility of such systems when combined with future electronics power reduction. For example, the approximately 22 billion neuron cells in brain of an average-sized human consumes a total of 14.6 W, which is approximately 660 pW per cell [100, 171, 172]. Similarly, the approximately 10 trillion cells in the human consume an average of 150 W, resulting an an average power consumption of 150 pW for *every cell in the human body.* Considering that the transmitter required only 83 pW to transmit packets once-per-minute, these numbers indicate system feasibility together with future research and development efforts.

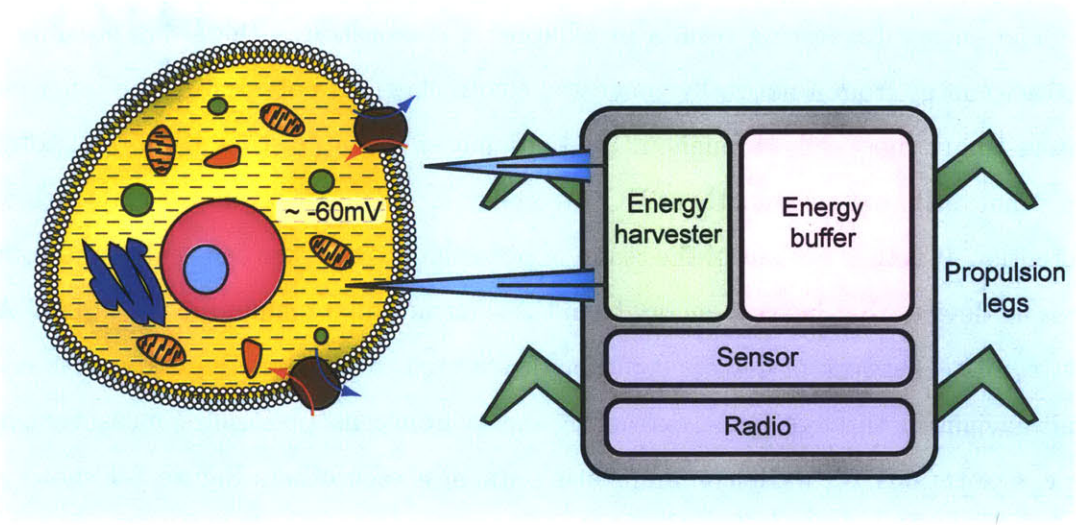

Figure 5-1: Diagram of a nanorobot harvesting energy from intracellular potentials.

Appendix A

Limits to Wireless Power Transfer in Biological Tissue

The purpose of this appendix is to briefly discuss wireless power transfer limits in the presence of biological tissue. The subsequent discussion is by no means a complete and exhaustive treatment of the complicated issue of tissue heating; however, several design guidelines and rules-of-thumb specifically tailored to the coils proposed in Section 4.3.2 will be introduced.

FCC Radiation Regulations

A coil with N turns and circumference l operating at a wavelength λ has a radiation resistance that can be modeled by:

$$R_{rad} = Z_o N^2 \frac{\pi}{6} \left(\frac{l}{\lambda}\right)^4, \tag{A.1}$$

where Z_o is the radiation resistance of free space (377 Ω). Operating at 6.78 MHz, a coil with 8 turns and a diameter of 3 cm therefore has a radiation resistance of 0.26 $\mu\Omega$. Using Equation 3.9, the resistive loss component for the same coil is approximately 2 Ω.

The maximum radiated power in an FCC-designated ISM band is 4 W. Thus, the

maximum power that can be delivered into a primary source coil is:

$$P_{1,max_{FCC}} = \frac{P_{rad,max_{FCC}}}{\eta_{rad}} = \frac{4 \text{ W}}{\frac{0.26\mu\Omega}{0.26\mu\Omega+2\Omega}} = 30 \text{ MW}. \tag{A.2}$$

Since this is the same amount of power as a power plant, clearly tissue heating effects will be limited before FCC radiation regulations are reached.

FCC SAR Regulations

The FCC also regulates the specific absorption rate (SAR) of wireless devices to be less than 1.6 W/kg over 1 g of tissue [173]. SAR is calculated using:

$$SAR = \frac{\sigma E^2}{\rho}, \tag{A.3}$$

where E is the electric field, and σ and ρ are the conductivities and mass densities of the tissues in question, respectively. Note that SAR calculations are performed exclusively using electric fields, as magnetic fields have little impact on biological tissue.

The electric field originating from a coil is given by:

$$E = \sqrt{\frac{Z_o D_o P_{rad}}{4\pi r^2}}, \tag{A.4}$$

where D_o is the antenna gain (= 1.5 for a loop antenna), and r is the distance from the coil [100]. Thus, the maximum primary power dissipation under FCC SAR regulation can be found using:

$$P_{1,max_{SAR}} = \frac{4\pi r^2 \rho(\text{SAR}_{max})}{\sigma Z_o D_o \eta_{RAD}}. \tag{A.5}$$

Using this equation to calculate for skin ($\rho = 1050$ kg/m^3, $\sigma = 0.2$ S/m) at a distance of 1 mm results in a maximum primary power consumption of 1.4 kW. This is the same amount of power consumed by a typical toaster; thus it is clear that other tissue heating effects will dominate before SAR regulations are exceeded.

Resistive Tissue Heating

Since it appears that the electromagnetic radiation at MHz-frequencies does not have a substantial effect on tissues at reasonable power levels, the only other concerning heating mechanism stems from resistive losses. For example, an implanted circuit consuming power is by definition dissipating energy as heat. There are several resources to determine what constitutes "safe" power dissipation. For example, the IEC 6060-1 standard suggests that medical devices should not raise the surface temperature of the skin by 6°C [174] when the device is used for 10 or more minutes. On the other hand, [175] suggests that a power density of approximately 50 mW/cm^2 causes an acceptable 1°C temperature increase in the brain, while [176] suggests that a heat flux of 80 mW/cm^2 can cause necrosis in muscle tissue.

Using the most conservative of the aforementioned rules-of-thumb, a maximal power density of 50 mW/cm^2 translates to a maximum power consumption of 250 mW for a $\pi r^2 = \pi(1.5 \text{ cm})^2 = 5 \text{ cm}^2$ implanted coil. Naturally, this assumes power dissipation occurs solely in the implanted coil. More complex modeling of the actual implantable-sized circuit implementations will be required to get a better understanding of fundamental tissue heating limits.

Based on these preliminary calculations, however, it appears that the approximately 200 mW of power delivered to the secondary device in Chapter 4 is appropriate. Note that of the 200 mW delivered to the secondary, most of that power is instantaneously being used to charge up the ultra-capacitor. Since in this case energy is being stored and not dissipated, there is less generated heat than if an equivalent resistive load was used. In fact, the actual amount of dissipated heat can be calculated by multiplying the secondary received power by the secondary efficiency, η_2, which depending on the coil separation, is often designed to be much higher than 50%.

Appendix B

Optimal Inductively-Coupled Load Analysis for Maximum Power Transfer Efficiency

The maximum power transfer analysis developed in Section 4.2.2 can be easily leveraged to also derive optimal efficiency criteria. It is certainly possible to take the P_{out} result in Equation 4.15 and divide it by the input power to derive an expression for efficiency; however, this does not provide much analytical insight. Instead, total link efficiency can be broken out into two separate components: primary and secondary efficiencies. Specifically, the circuits in Figures 4-7(d) and 4-7(a) can be used to calculate the primary and secondary efficiencies at resonance, respectively.

$$\begin{aligned}
\eta_{tot} &= (\eta_1) \times (\eta_2) \\
&= \left(\frac{R_{eq}}{R_{eq} + R_s + R_1}\right) \times \left(\frac{R_L}{R_L + R_2}\right) \\
&= \text{...(ignoring } R_s\text{, or lumping together with } Q_1\text{)...} \\
&= \frac{k^2 Q_1 \omega C_2 R_L}{\left(\omega C_2 R_L + k^2 Q_1 + \frac{1}{Q_2}\right)\left(\omega C_2 R_L + \frac{1}{Q_2}\right)}
\end{aligned} \tag{B.1}$$

Taking the derivative of efficiency with respect to R_L and equating to zero will yield the load impedance that maximizes power transfer efficiency:

$$\boxed{R_{L,\eta_{opt}} = \sqrt{\frac{L_2}{C_2}}\left(\frac{\sqrt{1+k^2Q_1Q_2}}{Q_2}\right)} \tag{B.2}$$

Similar results were also derived in [100,159], though the result in [100] is only applicable for reasonably large k. For completeness, the optimal efficiency given this result is shown here:

$$\eta_{opt} = \frac{1+k^2Q_1Q_2}{(1+\sqrt{1+k^2Q_1Q_2})^2}. \tag{B.3}$$

What is very interesting to note here is that the $R_{L,\eta_{opt}}$ expression is identical to the $R_{L,opt}$ expression for maximum power transfer, with the only difference being the square root of $(1+k^2Q_1Q_2)$ in the numerator. It should also be mentioned that this expression is exact for both series- and parallel-tuned secondaries.

As shown in Figure B-1(a), efficiency can theoretically approach 100%, given large quality factors and high coupling. This is in constrast to links optimized for maximum power transfer, which in good agreement with theory, approach a maximum limit of 50%. However, as shown in Figure B-1(b), a highly-efficient link at high k delivers very little power compared to a link optimized for maximum power transfer. At low coupling coefficients, links designed for maximum efficiency or power transfer have the same behavior. This follows intuition nicely: as at low coupling coefficients, reflected impedances are minimal, as previously described. Thus, no matter how much power is consumed in the primary, it is always beneficial to match R_L to R_2 for low values of k.

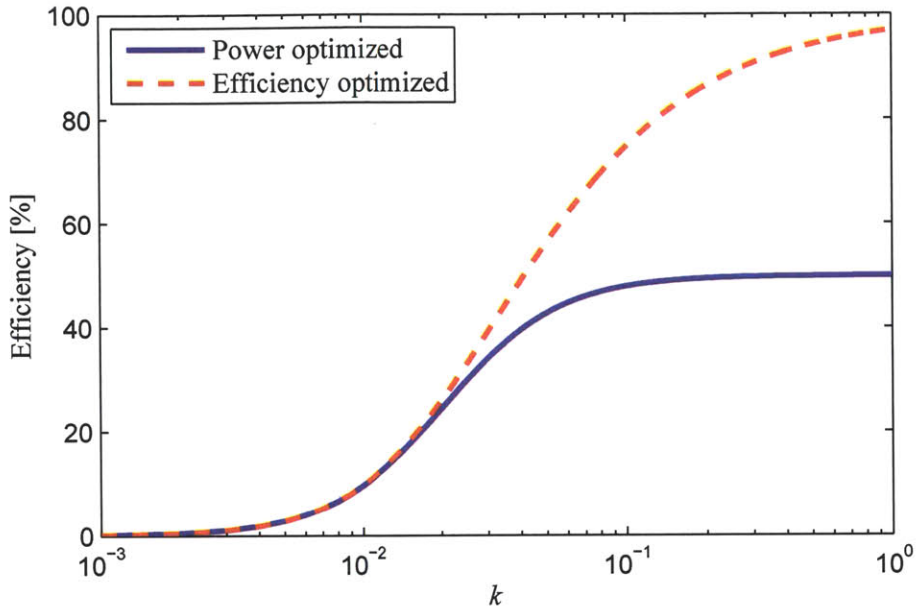

(a) Maximum achievable efficiency for all practical values of k, found by optimizing the load impedance for each value of k.

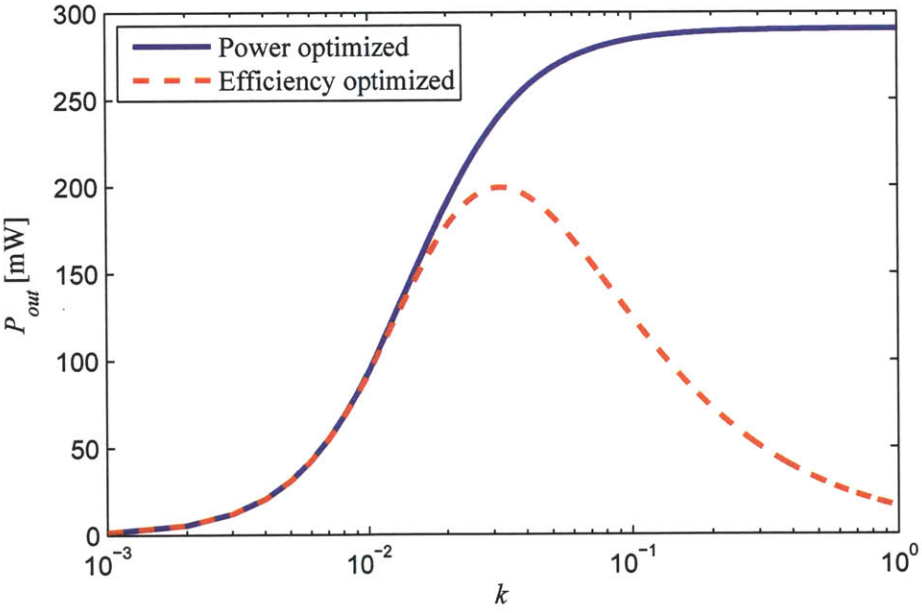

(b) Maximum achievable load power for all practical values of k, found by optimizing the load impedance for each value of k.

Figure B-1: Efficiency and load power delivery for a power-transfer-optimized link and an efficiency-optimized link. In this example, $V_s = 3.3$ V_{p-p}, $f = 6.78$ MHz, $L_1 = 3.3$ μH, $L_2 = 6.7$ μH, $Q_1 = 60$, and $Q_2 = 80$.

Appendix C

Changing the Effective Impedance of Wireless Power Transfer Links

There are many other ways to attempt to modify the standard inductive coupling circuit in Figure 4-1 to support varying instantaneous capacitor resistances and coupling coefficients. One of the most straightforward approaches is to attempt to change the effective ultra-capacitor resistance, at least as seen from the point of view of the inductive coupling circuit. The basic concept is shown in Figure C-1. Such an approach can be used either semi-statically, to provide robustness against varying k, or dynamically, to provide robustness against varying R_C.

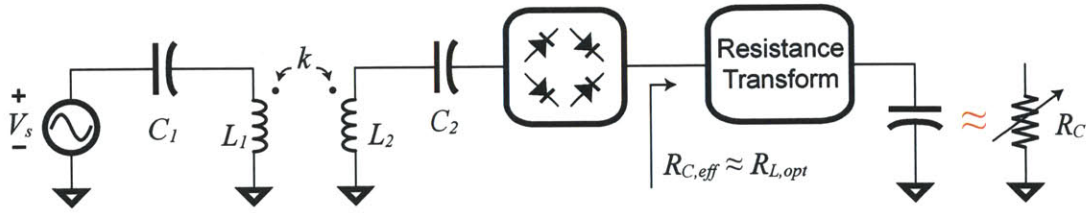

Figure C-1: Generalized circuit to modify the effective instantaneous capacitor resistance, $R_{C,eff}$ to look like the optimal load resistance, $R_{L,opt}$, for maximum power transfer.

DC/DC Converter

One of the most straightforward approaches to modulate $R_{C,eff}$, irrespective of R_C, is to replace the resistance transform block in Figure C-1 with a DC/DC converter. The converter can be a switched capacitor converter, or a magnetic-based converter, the latter of which is illustrated in Figure C-2. As shown in Section 3.4.2, it is possible to modulate the average input impedance of a boost converter by simply switching the pulse width $\Phi 1$.

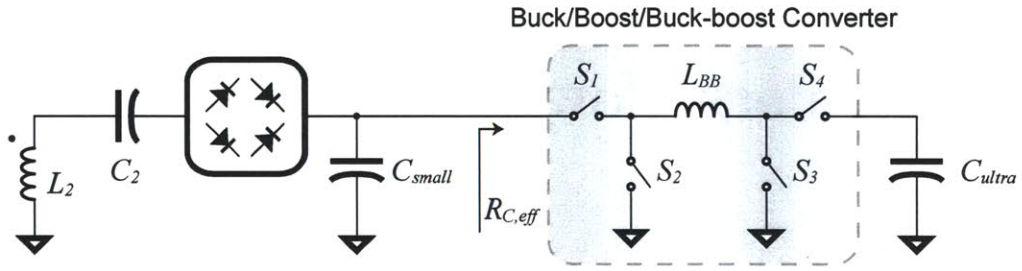

Figure C-2: Modulating $R_{C,eff}$ using a DC/DC converter.

For efficiency and functionality reasons, it is necessary to ensure the voltage conversion ratio of the converter matches the voltages present at its input and output. For example, given a constant input voltage, the converter output voltage setting should ramp up as the capacitor charges. Depending on the way the inductive link is configured, this may require the use of buck, boost, and buck-boost methods of control.

Although this approach is directly able to set the input impedance, providing robustness against dynamically changing R_C and semi-static but potentially varying k, the circuit has high overhead. For instance, simplified linear expressions for input impedance only apply when the voltage conversion ratio is high in boost or buck modes. A more complex method of control would be necessary in buck-boost modes. Perhaps more importantly, it is exceedingly difficult to design a converter that operates efficiently over such a wide range of voltage conversion factors. Since the DC/DC converter is directly in-line with the output, any losses due to finite efficiency will di-

rectly affect charging time. On a positive note, the converter can be run in reverse to regulate load voltages after charging is complete. Others have described circuits with lower complexity to perform the same task [158].

Although promising, an approach involving an in-line DC/DC converter suffers from several pitfalls and is therefore not further studied. It is certainly within the realm of possibility for future research to solve some of the outstanding issues, however.

Matching Network

It is well known in RF and microwave electronics that passive elements can provide impedance matching abilities at AC. Since the inductive link operates at AC prior to the rectifier, passive impedance matching circuits may be a logical choice to attempt to shape R_C. For example, the circuit in Figure C-3 uses a π network to convert the impedance seen at the input of the rectifier. The π-network capacitors can be varied in order to provide dynamic matching capabilities.

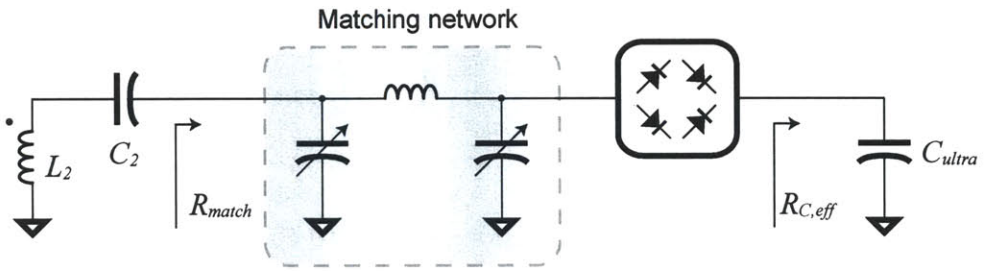

Figure C-3: Using a matching network to convert resistances.

Unfortunately, passive matching networks have limited utility in this particular situation. The primary reason is that such matching network must use components that have finite quality factors, thereby limiting the achievable impedance transformation range. As shown in Figure 4-8(a), the optimal impedance for maximum power transfer of the particular link example varies by several orders of magnitude for various k. Such a large impedance transformation range is simply not attainable with

practical matching networks.

Resistance Compression Network

Resistance compression networks (RCNs) are a special class of matching networks that not only perform impedance matching, but also compress output impedance changes as seen at their input [177]. For example, a resistance compression network has been demonstrated to compress the input impedance of an energy recovery rectifier in an outphasing power amplifier design [178]. Figure C-4 illustrates how a resistance compression network can be used for inductive coupling applications. Compression efficiencies can often approach 20X - meaning a 100:1 change in resistance at the output results in a 5:1 ratio at the input.

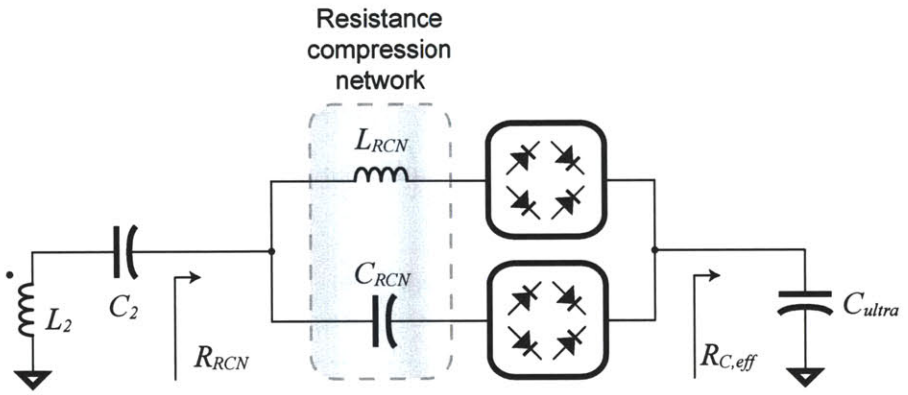

Figure C-4: Using a resistance compression network to convert and normalize resistances.

A resistance compression network can mitigate the effects of dynamically changing R_C in capacitor charging applications by compressing R_{RCN} to be closer to the optimal $R_{L,opt}$. However, the effective input impedance of the RCN is nominally centered around a single value: $R_{RCN,nom} = Z_0 = \sqrt{L_{RCN}/C_{RCN}}$. Thus, use of a resistance compression networks only benefits inductive coupling applications at a single value of k. The RCN can be made tunable to overcome this issue, but as was the case for matching networks, finite passive quality factors limit the range of achievable nominal resistances.

Appendix D

List of Acronyms

ADC analog-to-digital converter 51

AES advanced encryption standard 38

ATP adenosine triphosphate 86

BAN body-area network 29

BCC body-coupled communication 40

BER bit error rate 53

CSMA carrier-sense multiple-access 66

CMOS Complimentary Metal Oxide Semiconductor 24

CW continuous wave 102

DAC digital-to-analog converter 113

DCM discontinuous conduction mode 96

ECG electrocardiography 25

EEG electroencephalography 31

EM electromagnetic 38

ESD electrostatic discharge 110

ESR effective series resistance 127

eTextiles electronic textiles 37

EP endocochlear potential 74

FCC Federal Communications Commission 110

FSK frequency-shift keying 40

MSB most significant bit 136

MSK minimum-shift keying 115

OOK on-off keying 105

PC personal computer 22

PCB printed circuit board 44

PO power oscillator 104

POR power-on-reset 122

OFDM orthogonal frequency-division multiplexing 103

PA power amplifier 29

RCN resistance compression network

RF radio-frequency 22

RFIC radio frequency integrated circuit

RFID radio frequency identification 73

SAR specific absorption rate 157

SoC system-on-chip 30

STI shallow trench isolation 95

TDMA time-domain multiple-access 44

UWB ultra-wideband 67

ZCS zero current switching 98

Bibliography

[1] T. N. Jackson, "Organic Semiconductors: Beyond Moore's Law," *Nature Materials*, pp. 581–582, 2005.

[2] S. McCartney, *ENIAC: the triumphs and tragedies of the world's first computer.* Walker & Company, 1999.

[3] C. Mims, "Does the Space Shuttles Computer Really Run on Just One Megabyte of RAM?" *Popular Science*, Feb. 2009.

[4] E. Rogers, *Diffusion of innovations.* Free Press, 1995.

[5] H. Wang, *Delivering Quality Healthcare to the Digital Home: 2010 Update.* Parks Associates Industry Report, 2010.

[6] W. Greatbatch, "Medical Cardiac Pacemaker," U.S. Patent 3,057,356, Oct., 1962.

[7] M. A. Wood and K. A. Ellenbogen, "Cardiac pacemakers from the patients perspective," *Circulation*, vol. 105, pp. 2136–2138, 2002.

[8] M. Arndt, "Rewiring the body," *Business Week*, pp. 74–82, Mar. 2005.

[9] "Cochlear Implants," *NIH Publication No. 11-4798*, 2011.

[10] B. Calogero and A. M. Halfmann, "Will the Baby Boom Bust Healthcare?" *Tefen USA Whitepaper*, 2006.

[11] S. P. Keehan, A. M. Sisko, C. J. Truffer, J. A. Poisal, G. A. Cuckler, A. J. Madison, J. M. Lizonitz, and S. D. Smith, "National Health Spending Projections Through 2020: Economic Recovery And Reform Drive Faster Spending Growth," *Health Aff*, Jul. 2011.

[12] T. F. Geithner, H. L. Solis, K. Sebelis, M. J. Astrue, C. P. Blahous, R. D. Reischauer, and D. M. Berwick, *2011 Annual Report of the Boards of Trustees of the Federal Hospital Insurance and Federal Supplementary Medical Insurance Trust Funds*, 2011.

[13] A. Shoeb, A. Kharbouch, J. Soegaard, S. Schachter, and J. Guttag, "A machine-learning algorithm for detecting seizure termination in scalp EEG," *Epilepsy & Behavior*, vol. 22, pp. S36–S43, 2011.

[14] K. Boahen, "Neuromorphic microchips," *Scientific American*, vol. 292, no. 5, pp. 56–63, 2005.

[15] S. Weinzimer, G. Steil, K. Swan, J. Dziura, N. Kurtz, and W. Tamborlane, "Fully automated closed-loop insulin delivery versus semiautomated hybrid control in pediatric patients with type 1 diabetes using an artificial pancreas," *Diabetes Care*, vol. 31, no. 5, pp. 934–939, 2008.

[16] N. Verma, A. Shoeb, J. Bohorquez, J. Dawson, J. Guttag, and A. P. Chandrakasan, "A micro-power EEG acquisition SoC with integrated feature extraction processor for a chronic seizure detection system," *IEEE J. Solid-State Circuits*, vol. 45, no. 4, pp. 804–816, 2010.

[17] G. Chen, H. Ghaed, R. Haque, M. Wieckowski, Y. Kim, G. Kim, D. Fick, D. Kim, M. Seok, K. Wise *et al.*, "A cubic-millimeter energy-autonomous wireless intraocular pressure monitor," in *IEEE ISSCC Dig. Tech. Papers*, Feb. 2011, pp. 310–312.

[18] M. Pedram and J. Rabaey, *Power Aware Design Methodologies.* Kluwer Academic Publishers, 2002.

[19] P. P. Mercier, M. Bhardwaj, D. C. Daly, and A. P. Chandrakasan, "A low-voltage energy-sampling IR-UWB digital baseband employing quadratic correlation," *IEEE J. Solid-State Circuits*, vol. 45, no. 6, pp. 1209–1219, 2010.

[20] P. Hudson and J. Meindl, "A monolithic micropower command receiver," *IEEE J. Solid-State Circuits*, vol. 7, no. 2, pp. 125–135, 1972.

[21] R. White and J. Meindl, "The impact of integrated electronics in medicine," *Science*, vol. 195, no. 4283, pp. 1119–1124, 1977.

[22] G. Williams, K. Doughty, and D. Bradley, "A systems approach to achieving CarerNet–an integrated and intelligent telecare system." *IEEE Trans. Inf. Technol. Biomed.*, vol. 2, no. 1, pp. 1–9, Mar. 1998.

[23] R. Wootton, S. Dimmick, and J. Kvedar, *Home telehealth: Connecting care within the community.* RSM Press, 2006.

[24] A. P. Chandrakasan, R. Min, M. Bhardwaj, S. Cho, and A. Wang, "Power aware wireless microsensor systems," in *Proc. IEEE European Solid-State Circuits Conf.*, Sep. 2002, pp. 47–54.

[25] N. Cho, J. Bae, and H.-J. Yoo, "A 10.8 mW Body Channel Communication/MICS Dual-Band Transceiver for a Unified Body Sensor Network Controller," *IEEE J. Solid-State Circuits*, vol. 44, no. 12, pp. 3459–3468, Dec. 2009.

[26] M. Sahin and Y. Tie, "Non-rectangular waveforms for neural stimulation with practical electrodes," *J. Neural Eng.*, vol. 4, pp. 227–233, 2007.

[27] M. Steyaert and W. Sansen, "A micropower low-noise monolithic instrumentation amplifier for medical purposes," *IEEE J. Solid-State Circuits*, vol. 22, pp. 1163–1168, Dec. 1987.

[28] R. Harrison and C. Charles, "A low-power low-noise cmos amplifier for neural recording applications," *IEEE J. Solid-State Circuits*, vol. 38, no. 6, pp. 958–965, Jun. 2003.

[29] J. D. Weiland, W. Liu, and M. S. Humayun, "Retinal Prothesis," *Annual Review of Biomedical Engineering*, vol. 7, no. 1, pp. 361–401, 2005.

[30] G. Suaning and N. Lovell, "CMOS neurostimulation ASIC with 100 channels, scaleable output, and bidirectional radio-frequency telemetry," *IEEE Trans. Bio-Med. Eng.*, vol. 48, no. 2, pp. 248–260, 2001.

[31] J. Klassen, "A description of cymbet battery technology and its comparison with other battery technologies," *White Paper, Cymbet Corporation. Available: http://www.cymbet.com.*

[32] Y. Nishi, "Lithium ion secondary batteries; past 10 years and the future," *Journal of Power Sources*, vol. 100, no. 1, pp. 101–106, 2001.

[33] A. Zuger, "The 'Other' Drug Problem: Forgetting to Take Them," *The New York Times*, June 2 1998.

[34] A. Burke, "Ultracapacitors: why, how, and where is the technology," *Journal of Power Sources*, vol. 91, no. 1, pp. 37–50, 2000.

[35] E. Shi and A. Perrig, "Designing secure sensor networks," *IEEE Wireless Commun. Mag.*, vol. 11, no. 6, pp. 38–43, Dec. 2004.

[36] M. Feldhofer, J. Wolkerstorfer, and V. Rijmen, "AES implementation on a grain of sand," *IEE Proc. Inf. Security*, vol. 152, pp. 13–20, Oct. 2005.

[37] H. Friis, "A note on a simple transmission formula," *Proc. IRE*, vol. 34, no. 5, pp. 254–256, May 1946.

[38] J. Ryckaert, P. De Doncker, R. Meys, A. de Le Hoye, and S. Donnay, "Channel model for wireless communication around human body," *Electronics letters*, vol. 40, no. 9, pp. 543–544, Apr. 2004.

[39] E. Reusens, W. Joseph, B. Latré, B. Braem, G. Vermeeren, E. Tanghe, L. Martens, I. Moerman, and C. Blondia, "Characterization of on-body communication channel and energy efficient topology design for wireless body area networks," *IEEE Trans. Inf. Technol. Biomed.*, vol. 13, no. 6, pp. 933–945, Sep. 2009.

[40] T. H. Lee, *The Design of CMOS Radio-Frequency Integrated Circuits, 2nd ed.* Cambridge, UK: Cambridge University Press, 2004.

[41] D. C. Daly, P. P. Mercier, M. Bhardwaj, A. L. Stone, Z. N. Aldworth, T. L. Daniel, J. Voldman, J. G. Hildebrand, and A. P. Chandrakasan, "A pulsed UWB receiver SoC for insect motion control," *IEEE J. Solid-State Circuits*, vol. 45, no. 1, pp. 153–166, Jan. 2010.

[42] "CC2540F128, CC2540F256 2.4-GHz Bluetooth low energy System-on-Chip," Data Sheet, Texas Instruments, Nov. 2011.

[43] T. Zimmerman, "Personal area networks (PAN): Near-field intra-body communication," M.S. thesis, Massachusetts Institute of Technology, 1995.

[44] N. Cho, J. Yoo, S. Song, J. Lee, S. Jeon, and H.-J. Yoo, "The human body characteristics as a signal transmission medium for intrabody communication," *IEEE Trans. Microw. Theory Tech.*, vol. 55, no. 5, pp. 1080–1086, May 2007.

[45] T. Schenk, N. Mazloum, L. Tan, and P. Rutten, "Experimental characterization of the body-coupled communications channel," in *Proc. IEEE Int. Symp. on Wireless Comm. Systems*, Oct. 2008, pp. 234–239.

[46] S. Song, N. Cho, and H.-J. Yoo, "A 0.2-mW 2-Mb/s digital transceiver based on wideband signaling for human body communications," *IEEE J. Solid-State Circuits*, vol. 42, no. 9, pp. 2021–2033, Sep. 2007.

[47] A. Fazzi, S. Ouzounov, and J. van den Homberg, "A 2.75mW wideband correlation-based transceiver for body-coupled communication," in *IEEE ISSCC Dig. Tech. Papers*, Feb. 2009, pp. 204–205.

[48] N. Cho, L. Yan, J. Bae, and H.-J. Yoo, "A 60 kb/s–10 Mb/s Adaptive Frequency Hopping Transceiver for Interference-Resilient Body Channel Communication," *IEEE J. Solid-State Circuits*, vol. 44, no. 3, pp. 708–717, Mar. 2009.

[49] H. Kim, Y. Kim, B. Kim, and H.-J. Yoo, "A Wearable Fabric Computer by Planar-Fashionable Circuit Board Technique," in *Proc. IEEE Int. Work. on Wearable and Implantable Body Sensor Net.*, Jun. 2009, pp. 282–285.

[50] S. Park, K. Mackenzie, and S. Jayaraman, "The wearable motherboard: A framework for personalized mobile information processing (PMIP)," in *Proc. IEEE Design Automation Conf.*, Jun. 2002, pp. 170–174.

[51] L. Buechley and M. Eisenberg, "Fabric PCBs, electronic sequins, and socket buttons: techniques for e-textile craft," *Journal of Personal and Ubiquitous Computing*, vol. 13, no. 2, pp. 133–150, Feb. 2009.

[52] E. Scilingo, A. Gemignani, R. Paradiso, N. Taccini, B. Ghelarducci, and D. De Rossi, "Performance evaluation of sensing fabrics for monitoring physiological and biomechanical variables," *IEEE Trans. Inf. Technol. Biomed.*, vol. 9, no. 3, pp. 345–352, Sep. 2005.

[53] H. Kim, Y. Kim, Y. Kwon, and H.-J. Yoo, "A 1.12 mW continuous healthcare monitor chip integrated on a planar-fashionable circuit board," in *IEEE ISSCC Dig. Tech. Papers*, Feb. 2008, pp. 150–151.

[54] J. Yoo, S. Lee, and H.-J. Yoo, "A 1.12 pJ/b Inductive Transceiver With a Fault-Tolerant Network Switch for Multi-Layer Wearable Body Area Network Applications," *IEEE J. Solid-State Circuits*, vol. 44, no. 11, pp. 2999–3010, Nov. 2009.

[55] J. Yoo, L. Yan, S. Lee, Y. Kim, and H.-J. Yoo, "A 5.2 mW Self-Configured Wearable Body Sensor Network Controller and a 12μW 54.9% Efficiency Wirelessly Powered Sensor for Continuous Health Monitoring System," *IEEE J. Solid-State Circuits*, vol. 45, no. 1, pp. 178–188, Jan. 2010.

[56] P. P. Mercier and A. P. Chandrakasan, "A Supply-Rail-Coupled eTextiles Transceiver for Body-Area Networks," *IEEE J. Solid-State Circuits*, vol. 46, no. 6, pp. 1284–1295, Jun. 2011.

[57] E. Liu, Y. Gao, G. Samdani, O. Mukhtar, and T. Korhonen, "Broadband characterization of indoor powerline channel and its capacity consideration," in *Proc. IEEE Int. Conf. Comm.*, vol. 2, 2005, pp. 901–905.

[58] M. Lee, R. Newman, H. Latchman, S. Katar, and L. Yonge, "HomePlug 1.0 powerline communication LANsprotocol description and performance results," *International Journal of Communication Systems*, vol. 16, no. 5, pp. 447–473, 2003.

[59] R. Ho, T. Ono, R. Hopkins, A. Chow, J. Schauer, F. Liu, and R. Drost, "High Speed and Low Energy Capacitively Driven On-Chip Wires," *IEEE J. Solid-State Circuits*, vol. 43, no. 1, pp. 52–60, Jan. 2008.

[60] D. Schinkel, E. Mensink, E. Klumperink, E. van Tuijl, and B. Nauta, "Low-power, high-speed transceivers for network-on-chip communication," *IEEE Trans. VLSI Syst.*, vol. 17, no. 1, pp. 12–21, Jan. 2009.

[61] P. P. Mercier, D. C. Daly, and A. P. Chandrakasan, "An Energy-Efficient All-Digital UWB Transmitter Employing Dual Capacitively-Coupled Pulse-Shaping Drivers," *IEEE J. Solid-State Circuits*, vol. 44, no. 6, pp. 1679–1688, Jun. 2009.

[62] N. Verma and A. P. Chandrakasan, "An Ultra Low Energy 12-bit Rate-Resolution Scalable SAR ADC for Wireless Sensor Nodes," *IEEE J. Solid-State Circuits*, vol. 442, no. 6, pp. 1196–1205, Jun. 2007.

[63] R. Llopis and M. Sachdev, "Low power, testable dual edge triggered flip-flops," in *Proc. IEEE Int. Symp. on Low Power Electron. and Design*, 1996, pp. 341–345.

[64] J. Montanaro, R. Witek, K. Anne, A. Black, E. Cooper, D. Dobberpuhl, P. Donahue, J. Eno, W. Hoeppner, D. Kruckemyer *et al.*, "A 160-MHz, 32-b, 0.5-W CMOS RISC Microprocessor," *IEEE J. Solid-State Circuits*, vol. 31, no. 11, pp. 1703–1714, Nov. 1996.

[65] W. Ellersick, C. Yang, M. Horowitz, and W. Dally, "GAD: A 12-GS/s CMOS 4-bit A/D converter for an equalized multi-level link," in *Proc. IEEE Symp. VLSI Circuits*, Jun. 1999, pp. 49–52.

[66] M. Lee, W. Dally, and P. Chiang, "Low-power area-efficient high-speed I/O circuit techniques," *IEEE Journal of Solid-State Circuits*, vol. 35, no. 11, pp. 1591–1599, Nov. 2000.

[67] N. Verma and A. P. Chandrakasan, "A 256 kb 65 nm 8T Subthreshold SRAM Employing Sense-amplifier Redundancy," *IEEE J. Solid-State Circuits*, vol. 43, no. 1, p. 141, Jan. 2008.

[68] N. Van Helleputte, M. Verhelst, W. Dehaene, and G. Gielen, "A Reconfigurable, 130 nm CMOS 108 pJ/pulse, Fully Integrated IR-UWB Receiver for Communication and Precise Ranging," *IEEE J. Solid-State Circuits*, vol. 45, no. 1, p. 69, Jan. 2010.

[69] J. L. Bohorquez, A. P. Chandrakasan, and J. L. Dawson, "A 350μW CMOS MSK Transmitter and 400μW OOK Super-Regenerative Receiver for Medical Implant Communications," *IEEE J. Solid-State Circuits*, vol. 44, no. 4, pp. 1248–1259, Apr. 2009.

[70] R. Want, "RFID: A key to automating everything," *Scientific American*, vol. 10, 1991.

[71] K. Finkenzeller *et al.*, *RFID handbook: Fundamentals and applications in contactless smart cards, radio frequency identification and near-field communication.* Wiley, 2010.

[72] T. Starner and J. Paradiso, "Human generated power for mobile electronics," pp. 1–35, 2004.

[73] G. Brooks, T. Fahey, T. White *et al.*, *Exercise physiology: Human bioenergetics and its applications.* Mayfield publishing company, 1996, no. Ed. 2.

[74] T. Starner, "Human-powered wearable computing," *IBM systems Journal*, vol. 35, no. 3.4, pp. 618–629, 1996.

[75] J. Donelan, Q. Li, V. Naing, J. Hoffer, D. Weber, and A. Kuo, "Biomechanical energy harvesting: generating electricity during walking with minimal user effort," *Science*, vol. 319, no. 5864, pp. 807–810, 2008.

[76] H. Johnson and B. Trattner, "Self-contained hand held portable lantern-flashlight consisting of a manually operated generator and rechargeable batteries," Nov. 23 1982, US Patent 4,360,860.

[77] M. Liao, "Cellular phone with built-in generator," Nov. 5 2002, US Patent App. 10/287,648.

[78] L. Wu, A. Zachas, R. Harley, T. Habetler, and D. Divan, "Design of a portable hand crank generating system to power remote off-grid communities," in *IEEE Power Engineering Society Conference and Exposition in Africa*, 2007, pp. 1–8.

[79] N. Shenck and J. Paradiso, "Energy scavenging with shoe-mounted piezoelectrics," *IEEE Micro*, vol. 21, no. 3, pp. 30–42, 2001.

[80] J. Antaki, G. Bertocci, E. Green, A. Nadeem, T. Rintoul, R. Kormos, and B. Griffith, "A gait-powered autologous battery charging system for artificial organs," *ASAIO Journal*, vol. 41, no. 3, 1995.

[81] D. Bayerl and X. Wang, "Three-Dimensional Kelvin Probe Microscopy for Characterizing In-Plane Piezoelectric Potential of Laterally Deflected ZnO Micro-/Nanowires," *Advanced Functional Materials*, 2012.

[82] Z. Dolezal and U. Hof, "Thermoelectrically-powered wrist watch," Jul. 22 1980, US Patent 4,213,292.

[83] L. Mateu, C. Codrea, N. Lucas, M. Pollak, and P. Spies, "Energy harvesting for wireless communication systems using thermogenerators," in *Proc. Conf. on Design of Circuits and Integrated Systems (DCIS)*, 2006.

[84] Y. K. Ramadass and A. P. Chandrakasan, "A battery-less thermoelectric energy harvesting interface circuit with 35 mV startup voltage," *IEEE J. Solid-State Circuits*, vol. 46, no. 1, pp. 333–341, 2011.

[85] E. J. Carlson, K. Strunz, and B. P. Otis, "A 20 mV input boost converter with efficient digital control for thermoelectric energy harvesting," *IEEE J. Solid-State Circuits*, vol. 45, no. 4, pp. 741–750, 2010.

[86] J. Paradiso and T. Starner, "Energy scavenging for mobile and wireless electronics," *IEEE Pervasive Computing*, vol. 4, no. 1, pp. 18–27, 2005.

[87] C. Sun, J. Shi, D. Bayerl, and X. Wang, "PVDF microbelts for harvesting energy from respiration," *Energy Environ. Sci.*, vol. 4, no. 11, pp. 4508–4512, 2011.

[88] S. Chaudhuri, D. Lovley *et al.*, "Electricity generation by direct oxidation of glucose in mediatorless microbial fuel cells," *Nature Biotechnology*, vol. 21, no. 10, pp. 1229–1232, 2003.

[89] F. Scholz, U. Schröder *et al.*, "Bacterial batteries," *Nature Biotechnology*, vol. 21, no. 10, pp. 1151–1152, 2003.

[90] N. Mano, F. Mao, and A. Heller, "Characteristics of a miniature compartmentless glucose-O2 biofuel cell and its operation in a living plant," *Journal of the American Chemical Society*, vol. 125, no. 21, pp. 6588–6594, 2003.

[91] S. Barton, J. Gallaway, P. Atanassov *et al.*, "Enzymatic biofuel cells for implantable and microscale devices," *Chemical Reviews*, vol. 104, pp. 4867–4886, 2004.

[92] R. Drake, B. Kusserow, S. Messinger, and S. Matsuda, "A tissue implantable fuel cell power supply," *ASAIO Journal*, vol. 16, no. 1, p. 199, 1970.

[93] M. Rasmussen, R. Ritzmann, I. Lee, A. Pollack, and D. Scherson, "An implantable biofuel cell for a live insect," *Journal of the American Chemical Society*, 2012.

[94] P. Cinquin, C. Gondran, F. Giroud, S. Mazabrard, A. Pellissier, F. Boucher, J. Alcaraz, K. Gorgy, F. Lenouvel, S. Mathé *et al.*, "A glucose biofuel cell implanted in rats," *PLoS One*, vol. 5, no. 5, p. e10476, 2010.

[95] L. Halámková, J. Halámek, V. Bocharova, A. Szczupak, L. Alfonta, and E. Katz, "Implanted biofuel cell operating in a living snail," *Journal of the American Chemical Society*, 2012.

[96] J. Rabaey, M. Mark, D. Chen, C. Sutardja, C. Tang, S. Gowda, M. Wagner, and D. Werthimer, "Powering and communicating with mm-size implants," in *Proc. IEEE Design, Automation, and Test in Europe Conference*, 2011, pp. 1–6.

[97] E. Reilly and P. Wright, "Modeling, fabrication and stress compensation of an epitaxial thin film piezoelectric microscale energy scavenging device," *Journal of Micromechanics and Microengineering*, vol. 19, p. 095014, 2009.

[98] E. Yeatman, "Advances in power sources for wireless sensor nodes," in *Proc. Intl Workshop Wearable and Implantable Body Sensor Networks*, 2004, pp. 20–21.

[99] N. Mano, "A 280 μw/cm^2 biofuel cell operating at low glucose concentration," *Chemical Communications*, no. 19, pp. 2221–2223, 2008.

[100] R. Sarpeshkar, *Ultra Low Power Bioelectronics: Fundamental, Biomedical Applications, and Bio-Inspired Systems.* Cambridge University Press, 2010.

[101] H. Hibino, A. Inanobe, K. Furutani, S. Murakami, I. Findlay, and Y. Kurachi, "Inwardly rectifying potassium channels: their structure, function, and physiological roles," *Physiological Reviews*, vol. 90, no. 1, pp. 291–366, 2010.

[102] H. Kurokawa and R. Goode, "Sound pressure gain produced by the human middle ear," *Otolaryngology–Head and Neck Surgery*, vol. 113, no. 4, p. 349, 1995.

[103] P. Wangemann, "K+ cycling and the endocochlear potential," *Hearing Research*, vol. 165, no. 1-2, pp. 1–9, 2002.

[104] S. Mandal, S. Zhak, and R. Sarpeshkar, "A bio-inspired active radio-frequency silicon cochlea," *IEEE J. Solid-State Circuits*, vol. 44, no. 6, pp. 1814–1828, 2009.

[105] J. Stock and M. Orna, "Electrochemistry, past and present," Washington, DC (USA); American Chemical Society, Tech. Rep., 1989.

[106] G. V. Békésy, "Dc resting potentials inside the cochlear partition," *The Journal of the Acoustical Society of America*, vol. 24, p. 72, 1952.

[107] ——, "Resting potentials inside the cochlear partition of the guinea pig," *Nature*, vol. 169, pp. 241–242, 1952.

[108] I. Tasaki, C. Spyropoulos *et al.*, "Stria vascularis as source of endocochlear potential," *J. Neurophysiology*, vol. 22, no. 2, pp. 149–155, 1959.

[109] A. Salt, I. Mleichar, and R. Thalmann, "Mechanisms of endocochlear potential generation by stria vascularis," *The Laryngoscope*, vol. 97, no. 8, pp. 984–991, 1987.

[110] P. Wangemann and J. Schacht, "Homeostatic mechanisms in the cochlea," *The Cochlea*, pp. 130–185, 1996.

[111] S. Takeuchi and M. Ando, "Voltage-dependent outward K+ current in intermediate cell of stria vascularis of gerbil cochlea," *American Journal of Physiology-Cell Physiology*, vol. 277, no. 1, pp. C91–C99, 1999.

[112] S. Takeuchi, M. Ando, and A. Kakigi, "Mechanism generating endocochlear potential: role played by intermediate cells in stria vascularis," *Biophysical Journal*, vol. 79, no. 5, pp. 2572–2582, 2000.

[113] I. Quraishi and R. Raphael, "Generation of the endocochlear potential: a biophysical model," *Biophysical Journal*, vol. 94, no. 8, pp. L64–L66, 2008.

[114] H. Hibino, F. Nin, C. Tsuzuki, and Y. Kurachi, "How is the highly positive endocochlear potential formed? the specific architecture of the stria vascularis and the roles of the ion-transport apparatus," *Pflügers Archiv European Journal of Physiology*, vol. 459, no. 4, pp. 521–533, 2010.

[115] M. Gratton, R. Schmiedt, and B. Schulte, "Age-related decreases in endocochlear potential are associated with vascular abnormalities in the stria vascularis," *Hearing Research*, vol. 94, no. 1-2, pp. 116–124, 1996.

[116] P. Dallos, "Some electrical circuit properties of the organ of corti. i. analysis without reactive elements," *Hearing Research*, vol. 12, no. 1, pp. 89–119, 1983.

[117] R. Patuzzi, "Ion flow in cochlear hair cells and the regulation of hearing sensitivity," *Hearing Research*, 2011.

[118] E. Cheung and D. Corey, "Ca2+ changes the force sensitivity of the hair-cell transduction channel," *Biophysical Journal*, vol. 90, no. 1, pp. 124–139, 2006.

[119] S. Johnson, M. Beurg, W. Marcotti, and R. Fettiplace, "Prestin-driven cochlear amplification is not limited by the outer hair cell membrane time constant," *Neuron*, vol. 70, no. 6, pp. 1143–1154, 2011.

[120] W. Brownell, P. Manis, M. Zidanic, and G. Spirou, "Acoustically evoked radial current densities in scala tympani," *The Journal of the Acoustical Society of America*, vol. 74, p. 792, 1983.

[121] R. Swanson and J. Meindl, "Ion-implanted complementary MOS transistors in low-voltage circuits," in *IEEE ISSCC Dig. Tech. Papers*, Feb. 1972, pp. 192–193.

[122] P. Chen, K. Ishida, X. Zhang, Y. Okuma, Y. Ryu, M. Takamiya, and T. Sakurai, "0.18-V input charge pump with forward body biasing in startup circuit using 65nm CMOS," in *Proc. IEEE Custom Integr. Circuits Conf.*, 2010, pp. 239–242.

[123] B. Mishra, C. Botteron, and P. A. Farine, "A 120 mV startup circuit based on charge pump for energy harvesting circuits," *IEICE Electronics Express*, vol. 8, no. 11, pp. 830–834, 2011.

[124] M. Hwang, A. Raychowdhury, K. Kim, and K. Roy, "A 85mV 40nW Process-Tolerant Subthreshold 8x8 FIR Filter in 130nm Technology," in *Proc. IEEE Symp. VLSI Circuits*, 2007, pp. 154–155.

[125] P. Chen, K. Ishida, K. Ikeuchi, X. Zhang, K. Honda, Y. Okuma, Y. Ryu, M. Takamiya, and T. Sakurai, "A 95mV-startup step-up converter with Vth-tuned oscillator by fixed-charge programming and capacitor pass-on scheme," in *IEEE ISSCC Dig. Tech. Papers*, Feb. 2011, pp. 216–218.

[126] J.-P. Im, S.-W. Wang, K.-H. Lee, Y.-J. Woo, Y.-S. Yuk, T.-H. Kong, S.-W. Hong, S.-T. Ryu, and G.-H. Cho, "A 40mV transformer-reuse self-startup boost converter with MPPT control for thermoelectric energy harvesting," in *IEEE ISSCC Dig. Tech. Papers*, Feb. 2012, pp. 104–106.

[127] N. Lotze and Y. Manoli, "A 62 mV 0.13 μm CMOS Standard-Cell-Based Design Technique Using Schmitt-Trigger Logic," *IEEE J. Solid-State Circuits*, vol. 47, no. 1, pp. 47–60, Jan. 2012.

[128] F. Zhang, Y. Zhang, J. Silver, Y. Shakhsheer, M. Nagaraju, A. Klinefelter, J. Pandey, J. Boley, E. Carlson, A. Shrivastava, B. Otis, and B. Calhoun, "A Batteryless 19μW MICS/ISM-Band Energy Harvesting Body Area Sensor Node SoC," in *IEEE ISSCC Dig. Tech. Papers*, Feb. 2012.

[129] K. Kadirvel, Y. Ramadass, U. Lyles, J. Carpenter, V. Ivanov, V. McNeil, A. Chandrakasan, and B. Lum-Shue-Chan, "A 330nA energy-harvesting charger with battery management for solar and thermoelectric energy harvesting," in *IEEE ISSCC Dig. Tech. Papers*, Feb. 2012, pp. 106–108.

[130] M. Mason, "Middle ear structures in fossorial mammals: a comparison with non-fossorial species," *Journal of Zoology*, vol. 255, no. 4, pp. 467–486, 2001.

[131] S. Hanson, M. Seok, Y. Lin, Z. Foo, D. Kim, Y. Lee, N. Liu, D. Sylvester, and D. Blaauw, "A low-voltage processor for sensing applications with picowatt standby mode," *IEEE J. Solid-State Circuits*, vol. 44, no. 4, pp. 1145–1155, 2009.

[132] S. Chung and T. Li, "An analytical threshold-voltage model of trench-isolated mos devices with nonuniformly doped substrates," *IEEE Trans. Electron Devices*, vol. 39, no. 3, pp. 614–622, 1992.

[133] J. Mandelman and J. Alsmeier, "Anomalous narrow channel effect in trench-isolated buried-channel P-MOSFET's," *IEEE Trans. Electron Devices*, vol. 15, no. 12, pp. 496–498, 1994.

[134] K. Roy, S. Mukhopadhyay, and H. Mahmoodi-Meimand, "Leakage current mechanisms and leakage reduction techniques in deep-submicrometer CMOS circuits," *Proceedings of the IEEE*, vol. 91, no. 2, pp. 305–327, 2003.

[135] P. Bradley, "An ultra low power, high performance medical implant communication system (mics) transceiver for implantable devices," in *Proc. IEEE Bio-Med. Circuits Syst. Conf.*, 2006, pp. 158–161.

[136] Y. Chee, A. Niknejad, and J. Rabaey, "An ultra-low-power injection locked transmitter for wireless sensor networks," *IEEE J. Solid-State Circuits*, vol. 41, no. 8, pp. 1740–1748, 2006.

[137] M. Raja and Y. Xu, "A 52 pJ/bit OOK transmitter with adaptable data rate," in *Proc. IEEE Asian Solid-State Circuits Conf.*, 2008, pp. 341–344.

[138] M. Vidojkovic, X. Huang, P. Harpe, S. Rampu, C. Zhou, L. Huang, J. van de Molengraft, K. Imamura, B. Busze, F. Bouwens *et al.*, "A 2.4 GHz ULP OOK single-chip transceiver for healthcare applications," *IEEE Trans. Bio-Med. Circuits Syst.*, vol. 5, no. 6, pp. 523–534, 2011.

[139] D. C. Daly and A. P. Chandrakasan, "An energy-efficient ook transceiver for wireless sensor networks," *IEEE J. Solid-State Circuits*, vol. 42, no. 5, pp. 1003–1011, 2007.

[140] A. Paidimarri, P. M. Nadeau, P. P. Mercier, and A. P. Chandrakasan, "A 440pJ/bit 1Mb/s 2.4GHz TX with Multiple Channels of operation using FBARs and an Integrated Pulse-shaping PA," in *Proc. IEEE Symp. VLSI Circuits*, Jun. 2012.

[141] E. Chow, S. Chakraborty, W. Chappell, and P. Irazoqui, "Mixed-signal integrated circuits for self-contained sub-cubic millimeter biomedical implants," in *IEEE ISSCC Dig. Tech. Papers*, Feb. 2010, pp. 236–237.

[142] S. O'Driscoll, A. Poon, and T. Meng, "A mm-sized implantable power receiver with adaptive link compensation," in *IEEE ISSCC Dig. Tech. Papers*, Feb. 2009, pp. 294–295.

[143] A. Poon, S. O'Driscoll, and T. Meng, "Optimal frequency for wireless power transmission into dispersive tissue," *IEEE Trans. Antennas Propag.*, vol. 58, no. 5, pp. 1739–1750, 2010.

[144] D. Miron, *Small antenna design.* Newnes, 2006, vol. 1.

[145] IEEE Standard for Local and metropolitan area networks – Part 15.6: Wireless Body Area Networks, Feb. 2012. [Online]. Available: http://www.ieee802.org/15/pub/TG6.html

[146] G. Vendelin, *Design of amplifiers and oscillators by the S-parameter method.* New York, Wiley-Interscience, 1982, vol. 1.

[147] N. Pletcher and J. Rabaey, "A 100 μW, 1.9 GHz oscillator with fully digital frequency tuning," in *Proc. IEEE European Solid-State Circuits Conf.*, 2005, pp. 387–390.

[148] J. M. Rabaey, A. P. Chandrakasan, and B. Nikolic, *Digital Integrated Circuits.* Prentice-Hall, 1996.

[149] M. Ercegovac and T. Lang, "Binary counter with counting period of one half adder independent of counter size," *IEEE Trans. Circuits Syst.*, vol. 36, no. 6, pp. 924–926, 1989.

[150] M. Stan, A. Tenca, and M. Ercegovac, "Long and fast up/down counters," *IEEE Trans. Comput.*, vol. 47, no. 7, pp. 722–735, 1998.

[151] J. Bae, L. Yan, and H. Yoo, "A low energy injection-locked FSK transceiver with frequency-to-amplitude conversion for body sensor applications," *IEEE J. Solid-State Circuits*, vol. 46, no. 4, pp. 928–937, 2011.

[152] J. Fayad, M. Semaan, J. Meier, and J. House, "Hearing results using the SMart piston prosthesis," *Otology & Neurotology*, vol. 30, no. 8, p. 1122, 2009.

[153] S. Mowry, E. Woodson, and B. Gantz, "New frontiers in cochlear implantation: acoustic plus electric hearing, hearing preservation, and more." *Otolaryngologic Clinics of North America*, vol. 45, no. 1, p. 187, 2012.

[154] C. Liu, Z. Yu, D. Neff, A. Zhamu, and B. Jang, "Graphene-based supercapacitor with an ultrahigh energy density," *Nano Letters*, vol. 10, pp. 4863–4868, 2010.

[155] "ML2020 Data Sheet," Panasonic, 2005.

[156] "EnerChip CBC050 Data Sheet, DS-72-01 Rev B," Cymbet Corporation, 2010.

[157] "UltraCap8 Series ESHSR-0003C0-002R7 Data Sheet," NessCap Ultracapacitors, 2008.

[158] W. Sanchez, C. Sodini, and J. Dawson, "An energy management IC for bioimplants using ultracapacitors for energy storage," in *Proc. IEEE Symp. VLSI Circuits*, 2010, pp. 63–64.

[159] K. Van Schuylenbergh and R. Puers, *Inductive Powering: Basic Theory and Application to Biomedical Systems.* Springer, 2009.

[160] A. Kurs, A. Karalis, R. Moffatt, J. Joannopoulos, P. Fisher, and M. Soljačić, "Wireless power transfer via strongly coupled magnetic resonances," *Science*, vol. 317, no. 5834, pp. 83–86, 2007.

[161] M. Kiani and M. Ghovanloo, "The Circuit Theory Behind Coupled-Mode Magnetic Resonance-Based Wireless Power Transmission," *IEEE Trans. Circuits Syst. I*, no. 99, pp. 1–1, 2012.

[162] K. Van Schuylenbergh and R. Puers, "Self-tuning inductive powering for implantable telemetric monitoring systems," *Sensors and Actuators A: Physical*, vol. 52, no. 1, pp. 1–7, 1996.

[163] A. Tanabe, K. Hijioka, H. Nagase, and Y. Hayashi, "A Novel Variable Inductor Using a Bridge Circuit and Its Application to a 5–20 GHz Tunable LC-VCO," *IEEE J. Solid-State Circuits*, vol. 46, no. 4, pp. 883–893, 2011.

[164] C. Fu, C. Ko, C. Kuo, and Y. Juang, "A 2.4–5.4-GHz wide tuning-range CMOS reconfigurable low-noise amplifier," *IEEE Trans. Microw. Theory Tech.*, vol. 56, no. 12, pp. 2754–2763, 2008.

[165] M. Paernel, "High-efficiency transmission for medical implants," *IEEE Solid-State Circuits Magazine*, vol. 3, no. 1, pp. 47–59, 2011.

[166] M. Baker and R. Sarpeshkar, "Feedback analysis and design of RF power links for low-power bionic systems," *IEEE Trans. Bio-Med. Circuits Syst.*, vol. 1, no. 1, pp. 28–38, 2007.

[167] J. Schindall, "The charge of the ultracapacitors," *IEEE Spectrum*, vol. 44, no. 11, pp. 42–46, 2007.

[168] A. R. Feinstein, "On white-coat effects and the electronic monitoring of compliance," *Archives of Internal Medicine*, vol. 150, no. 7, p. 1377, 1990.

[169] S. Cogan, "Neural stimulation and recording electrodes," *Annu. Rev. Biomed. Eng.*, vol. 10, pp. 275–309, 2008.

[170] M. Abidian, K. Ludwig, T. Marzullo, D. Martin, and D. Kipke, "Interfacing Conducting Polymer Nanotubes with the Central Nervous System: Chronic Neural Recording using Poly (3, 4-ethylenedioxythiophene) Nanotubes," *Advanced Materials*, vol. 21, no. 37, pp. 3764–3770, 2009.

[171] L. Aiello, "Brains and guts in human evolution: the expensive tissue hypothesis," *Brazilian Journal of Genetics*, vol. 20, 1997.

[172] C. Koch, *Biophysics of computation: information processing in single neurons.* Oxford University Press, USA, 2005.

[173] F. C. Commission *et al.*, "Questions and answers about biological effects and potential hazards of radiofrequency electromagnetic fields," *OET Bulletin*, vol. 56, 1999.

[174] "IEC 60601-1, Medical electrical equipment – Part 1: General requirements for safety and essential performance," 1995.

[175] S. Kim, P. Tathireddy, R. Normann, and F. Solzbacher, "Thermal impact of an active 3-D microelectrode array implanted in the brain," *IEEE Trans. on Neural Systems and Rehabilitation Engineering*, vol. 15, no. 4, pp. 493–501, 2007.

[176] T. Seese, H. Harasaki, G. Saidel, and C. Davies, "Characterization of tissue morphology, angiogenesis, and temperature in the adaptive response of muscle tissue to chronic heating," *Laboratory investigation*, vol. 78, no. 12, pp. 1553–1562, 1998.

[177] Y. Han, O. Leitermann, D. Jackson, J. Rivas, and D. Perreault, "Resistance compression networks for radio-frequency power conversion," *IEEE Trans. Power Electron.*, vol. 22, no. 1, pp. 41–53, 2007.

[178] P. Godoy, D. Perreault, and J. Dawson, "Outphasing energy recovery amplifier with resistance compression for improved efficiency," *IEEE Trans. Microw. Theory Tech.*, vol. 57, no. 12, pp. 2895–2906, 2009.